# Modelling and analysis of amplitude, phase and synchrony in human brain activity patterns

**Maria Botcharova**

Centre for Mathematics and Physics in the Life Sciences and Experimental Biology (CoMPLEX)
University College London

A thesis presented for the degree of Doctor of Philosophy
August 2014

I, Maria Botcharova, confirm that the work presented in this thesis is my own. Where information has been derived from other sources, I confirm that this has been indicated in the thesis.

# Abstract

The critical brain hypothesis provides a framework for viewing the human brain as a critical system, which may transmit information, reorganise itself and react to external stimuli efficiently. A critical system incorporates structures at a range of spatial and temporal scales, and may be associated with power law distributions of neuronal avalanches and power law scaling functions. In the temporal domain, the critical brain hypothesis is supported by a power law decay of the autocorrelation function of neurophysiological signals, which indicates the presence of long-range temporal correlations (LRTCs).

LRTCs have been found to exist in the amplitude envelope of neurophysiological signals such as EEG, EMG and MEG, which reveal patterns of local synchronisation within neuronal pools. Synchronisation is an important tool for communication in the nervous system and can also exist between disparate regions of the nervous system. In this thesis, inter-regional synchronisation is characterised by the rate of change of phase difference between neurophysiological time series at different neuronal regions and investigated using the novel phase synchrony analysis method. The phase synchrony analysis method is shown to recover the DFA exponents in time series where these are known. The method indicates that LRTCs are present in the rate of change of phase difference between time series derived from classical models of criticality at critical parameters, and in particular the Ising model of ferromagnetism and the Kuramoto model of coupled oscillators. The method is also applied to the Cabral model, in which Kuramoto oscillators with natural frequencies close to those of cortical rhythms are embedded in a network based on brain connectivity. It is shown that LRTCs in the rate of change of phase difference are disrupted when the network properties of the system are reorganised.

The presence of LRTCs is assessed using detrended fluctuation analysis (DFA), which assumes the linearity of a log-log plot of detrended fluctuation magnitude. In this thesis it is demonstrated that this assumption does not always hold, and a novel heuristic technique, ML-DFA, is introduced for validating DFA results.

Finally, the phase synchrony analysis method is applied to EEG, EMG and MEG time series. The presence of LRTCs in the rate of change of phase difference between time series recorded from the left and right motor cortices are shown to exist during resting state, but to be disrupted by a finger tapping task. The findings of this thesis are interpreted in the light of the critical brain hypothesis, and shown to provide motivation for future research in this area.

# Acknowledgements

First and foremost I would like to thank my supervisors, Dr Luc Berthouze and Dr Simon Farmer, for their guidance, inspiration and their never-ending sense of fun.

I would also like to thank my collaborators at University College London: Laurence Aitchison, Dr Holly Rossiter, Dr Marco Davare and Professor Gareth Barnes; and at the University of Nottingham: Dr Matthew Brookes. I would like to thank Dr Joana Cabral for helpful comments and for providing her Matlab implementation of the Cabral model. I would like to thank Drs Cédric Ginestet, Aaron Clauset and Manfred Kitzbichler for useful discussions and suggestions, and Dr Leon James and Dr Julian O'Kelly for allowing us to use their recordings of EEG data, and all EEG, EMG and MEG subjects for their willing participation.

I would like to acknowledge my departments - my third supervisor Professor Roger Lemon, the Sobell Department and the Institute of Neurology; and the Centre for Mathematics and Physics in the Life Sciences and Experimental Biology (CoMPLEX) as well as their funding bodies (including the EPSRC and BHF) without which this work would not have been possible.

Outside of neuroscience I would most of all like to thank my parents, Dr Victor Botcharov and Kira Fomenko, my grandmother Dr Natalya Lesnik and close family friend Professor Yuri Safarov for their unfailing support and belief in me, without which I could never have managed.

I would also like to thank my colleagues Dr Caroline Hartley, Nish Malalasekera, Dr Bruno Miranda, Andrew James Watson, Dr Laurence Hunt, Dr Himanshu Tyagi, Lianne McCombe, Professor Peter Dayan, Hedi Young, Deborah Hadley, Dr Chris Seers, Anna Gray, Dr Mhoriam Ahmed, Jonathan Henton and Luke Harding for their advice, lively discussions and essential distractions.

I would like to thank all my friends, and especially George and Katherine Pender, Dr Samuel Rabin, James Sharpe, Anna Sanderson, James Green, Dr Rebecca Burrell, Adrian Hodgson, Alice Soulieux and Nicola McCabe for making me feel like myself again when I most needed it.

Finally, I am grateful to the National Theatre, the Royal Opera House, the Coningsby and Athenaeum clubs and The Guardian for providing sustenance and entertainment.

I would like to dedicate my thesis to my grandparents who are no longer here - Vadim Fomenko, Dr Galina Botcharova and Yevgeny Botcharov.

# Contents

# List of Figures

# List of Tables

## List of Publications

1 M. Botcharova, S.F. Farmer, and L. Berthouze, **Power-law distribution of phase-locking intervals does not imply critical interaction**, *Physical Review E*, 2012, **86**(5), 051920, doi:10.1103/PhysRevE.86.051920.

2 M. Botcharova, S.F. Farmer, and L. Berthouze, **A maximum likelihood based technique for validating detrended fluctuation analysis (ML-DFA)**, *ArXiv*, 2013, arXiv:1306.5075.

In preparation

1 M. Botcharova, L. Berthouze, M.J. Brookes, G.R. Barnes and S.F. Farmer, **Resting state MEG oscillations show long-range temporal correlations of phase synchrony that break down during finger-tapping**,*NeuroImage*, ready for submission by March 2014.

2 M. Botcharova, S.F. Farmer, and L. Berthouze, **A marker of criticality in the rate of change of phase synchronisation**, *Frontiers in Neuroscience (Systems Neuroscience)*, to be submitted in April 2014.

# Chapter 1

# Introduction

The human nervous system can coordinate muscles in the body with astonishing efficiency. In order to perform even a simple task such as balancing a ping pong ball between two fingers, a wide range of judgements must be made. Its weight, surface friction and fragility need to be assessed in order not to drop, or crush it. The brain is able to perform such analysis almost instantaneously, and moreover, to impel the relevant muscles into executing the task with seamless coordination. We can only begin to imagine the complex interactions needed between components of the nervous system in order to execute something as precise and powerful as an artist's brush-stroke or a ballet dancer's leap.

Any task performed by the nervous system depends on a coordinated sequence of firing amongst the billions of neurons from which it is formed. During the resting state preceding the execution of a task, the nervous system must therefore be ready to facilitate a rapid coordination of the neural network. The organisational principles by which this neuronal coordination is achieved, both between distant and proximal neurons, are an intriguing open question. However, we do understand some of the mechanistic processes involved. Neuronal firing can be coordinated when a single neuron causes a connected neighbour to also fire, but more extensively when the activity of a large group of neurons synchronise in a process that is coordinated by global changes in the network [256]. Due to mechanisms of the neuronal cells and their networks, synchronised activity is quasi-rhythmic and can produce an oscillatory signal with a sufficiently large amplitude to be detected macroscopically at various defined frequency bands. We can record the electric field produced by a localised pool of synchronised neurons by electroencephalography (EEG) and magnetoencephalography (MEG) from the cortex, or by electromyography (EMG) from neurons in muscles. The fluctuations of amplitude and phase of these signals, known collectively as neurophysiological signals,

or neurophysiological time series, provides a window into the local neural synchronisation.

However, synchronisation is not only a local phenomenon, and indeed, the term is more commonly used to describe the synchronisation that is observed between different neural networks located at different sites in the nervous system. Such long-range synchronisation is evidenced by a weak oscillatory synchrony between neurophysiological signals, which is commonly quantified by the coherence measure [215]. It has been argued that coherence plays a critical role in information processing, storage and transmission [89, 90]. Importantly, physiological synchronisation is weak, it varies over time, and with task. Furthermore, signals coming in and out of phase, which are not necessarily synchronous are also of importance and a potential mechanism for information transfer. The idea that the networks characterised by signals such as EEG, EMG and MEG may come in and out of synchronisation with each other, and that synchronisation lends salience to a signal, has led to the hypothesis of 'communication through coherence' [89, 91, 250].

The coherence measure provides a single time-averaged scalar value of oscillatory synchronisation, used to correlate components in the frequency domain [280]. However, as synchronisation is a dynamic quantity, it is also of interest to quantify its evolution with time. This can be done using for example, a windowed coherence [216], a wavelet transform [215] or more recently optimal spectral tracking coherence [37], all of which provide time-varying windowed measures. There are also a number of instantaneous measures of synchronisation such as the instantaneous phase difference, where the phase is a quantity used to describe the position of an oscillatory signal in its cycle [270]. These measures will be formally introduced in Section 1.1.6.3 and compared in Chapter 6.

#### Characterising time-varying synchronisation

A number of techniques are therefore available that allow us to quantify the dynamics of neural synchronisation between neural networks. We have also seen that the amplitude (power) of oscillatory neurophysiological time series such as the EEG, EMG and MEG can be used to quantify 'local' synchronisation. We may next ask how we can best characterise the properties of these time-varying measures of synchronisation.

Signals such as EEG, EMG and MEG are quasi-rhythmic and contain oscillations. We can therefore say that they contain some order, or correlation across time, and we would not expect them to consist of a series of random and unrelated innovations. This may also be expected of a measure of neural synchronisation

between more distant regions of the nervous system if they are communicating with each other [90].

On the other hand, we would not expect for a time series of neural synchronisation to be a perfectly ordered oscillatory signal, such as a sine function. If a neurophysiological time series was of this form, then the value of the signal at one time point would be perfectly determined by its previous time point. The neuronal system would therefore have no freedom to respond to incoming external stimuli, which is essential for action and learning. Indeed, EEG, EMG and MEG time series are not perfectly oscillatory other than in certain pathological situations such as during some epileptic seizures, or in pathological tremor (for example Parkinson's disease), where these time series become much more ordered [246, 257, 309]. Similarly, a sinusoidal time series of global neural synchronisation would not permit the two underlying neural networks to influence each other [158].

We may therefore expect that the human nervous system operates somewhere between these two extremes of order and disorder. One metric that would allow us to distinguish these situations is the autocorrelation function, which is a measure of the correlation between values taken by a time series at different time lags [232].

#### Temporal correlations

For a time series of white noise, the autocorrelation function is a Dirac delta function (see Figure 1.13) [25, 83, 198]. This indicates that at any time lag different from zero, the values taken by the time series have a zero correlation and are completely independent of each other. An autocorrelation function of a sine function will have the form of a cosine with peaks at integer multiples of the oscillation period (see Figure 1.12).

A time series with a richer temporal structure will have a slowly decaying autocorrelation with non-zero correlation values for a broad range of time lags. Such a time series will have a strong relationship between the values it takes at time points close to each other, but also retain correlations across longer time periods. This property is called long-range dependence [25, 133, 268].

Long-range dependence has properties that would be advantageous to time series of neural synchronisation. For example, we might expect that a neural system with the ability to retain information for short as well as long time series would show long-range dependence [54, 157, 192, 254, 296]. We might also suppose that the transmission of information between short and long distances would proceed over variable time periods, so that a time-varying measure of synchronisation

between different neural networks would show correlations at a range of time lags [12, 51, 154, 250].

The slow decay of the autocorrelation function may take a number of functional forms. Power law decay has recently attracted particular attention in neuroscience [119, 178, 203, 204, 212]. Power laws have also been identified in the distribution of neuronal avalanches [23, 254], and scaling properties of the human nervous system [80, 88, 229, 240]. In particular, power laws in the decay of an autocorrelation function define a time series that is said to contain long-range temporal correlations (LRTCs) [59, 105]. Empirically LRTCs have been detected in various natural phenomena (see [249] for a review). In neuroscience, they have been found in the amplitude envelope of EEG time series [28, 178].

Computationally, time series with variations in long-range temporal correlations can be constructed using the Fractionally Integrated Moving Average (FARIMA) model. FARIMA models will be formally introduced in Section 1.1.8.8, and will be used in this thesis to study processes with different forms of temporal correlations.

#### Significance of LRTCs and the critical brain hypothesis

Particular importance has been attributed to LRTCs because they are defined by a power law function, which has been found to describe quantities derived from classical systems in a state of criticality. These include supercritical fluids in physics and the Ising model of ferromagnetism. These two systems and their properties will be formally introduced in Section 1.1.7.

A system at criticality consists of a large number of interacting elements and is at a point of transition between a state of order and disorder. This has already been mentioned as a desirable property for the amplitude of neurophysiological signals and for time-varying neural synchronisation. The idea that the brain is in a state of criticality is known as the 'critical brain hypothesis', for which evidence has been found at single neuron, LFP and surface signal level [23, 54, 77, 158, 254, 261, 284]. The properties of a critical system would be particularly advantageous for the nervous system in a resting state because the neural system must remain organised, but also have the flexibility to respond and adapt to subsequent tasks.

In this thesis, the evidence for LRTCs in the amplitude envelope of neurophysiological time series will be reviewed, and their presence in EEG and EMG time series across age will be investigated (see Chapters 3 and 4).

The authors of a recent paper find that the dynamics of network interaction in the human brain possess properties of criticality across a wide range of frequency

scales [158]. The authors of this latter paper identify power law distributions in two measures of time-varying neural synchronisation [158]. In this thesis, the methodologies used in [158] will be critically assessed and it will be demonstrated that they contain some weaknesses. A novel and alternative method for assessing power law statistics in a time-varying measure of synchronisation will be developed for neurophysiological signals, which will be referred to as the phase synchrony analysis method. This method will be used to analyse the time-varying interaction between signals obtained from an oscillator model of the brain, and between neurophysiological time series during resting state, when a movement task is executed, and in subjects of different ages.

#### Detecting LRTCs

The presence of LRTCs in a time series is commonly assessed by applying the detrended fluctuation analysis (DFA) technique for quantifying the related property of self-similarity [212, 214]. DFA is used to quantify the relationship between the detrended fluctuation size in a time series and the window size over which these fluctuations are measured. The concepts of LRTCs, self-similarity and their relationship to each other are introduced and discussed in Sections 1.1.8.2-1.1.8.7.

The application of DFA relies on a number of assumptions of the signal that do not hold for all time series. In its current form, DFA provides no mechanism for determining whether these assumptions can be justified. Although DFA is used extensively in the literature, it is not always clear whether valid conclusions can be drawn from its results for this reason. In this thesis, the ML-DFA technique will be introduced, which may be used to determine whether the model that best describes the relationship between detrended fluctuation size and window size, is linear. This in turn determines whether there is power law scaling, and whether the exponent derived from DFA should be accepted.

A further methodological consideration in DFA comes from the fact that the choice of window sizes are set individually by the experimenter. The effects of choosing different window sizes for DFA will be investigated in Chapter 4.

In the next section, the concepts and measures that have been mentioned in the introduction are formally introduced and discussed and a more detailed review of the relevant literature is given.

## 1.1 Background

### 1.1.1 Neurophysiology

The nervous system is the network of nerve cells (neurons) in the body, supported and protected by glial cells. It can be thought of as consisting of two main parts. The central nervous system (CNS) includes the brain and spinal chord, and the peripheral nervous system (PNS), which includes the neural networks that connect the CNS to sensor and effector organs and the peripheral and autonomic nervous systems.

The brain is the largest hub of neurons in the body and the cerebral cortex is its outer layer. The cortex contains approximately $10^{10}$ nerve cells, each of which may be connected to between $10^3$ and $10^5$ other neurons [205]. The surface of the cortex can be broadly divided into regions that are responsible for particular functions or processes, although these are not fully understood for the whole cortex. In the latter stages of this thesis, MEG recordings of subjects at rest will be compared with those of a movement task. The EMG of subjects will also be analysed, which only shows a signal when there is muscle activity. It is therefore mentioned here that the major cortical regions involved in voluntary movement are the primary motor and somatosensory cortices [241]. The locations of these two regions are indicated in a schematic diagram in Figure 1.1.

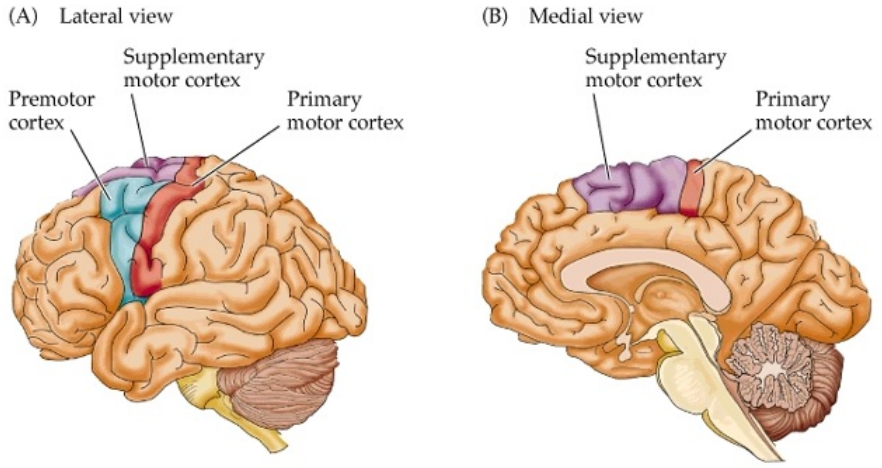


FIGURE 1.1: A schematic illustration of the motor cortical areas in the cortex. Taken from [234].

#### 1.1.1.1 Single neuron physiology action potentials

The primary function of a single nerve cell, or neuron, is to receive and transmit signals to and from different parts of the body.

A neuron typically consists of three compartments (see Figure 1.2). It has a cell body (soma), which contains the nucleus of the cell and sustains it. It has an axon, which is used to transmit electrical messages and it has a tree-like structure called a dendrite, which acts like an antenna and receives incoming messages from other neurons.

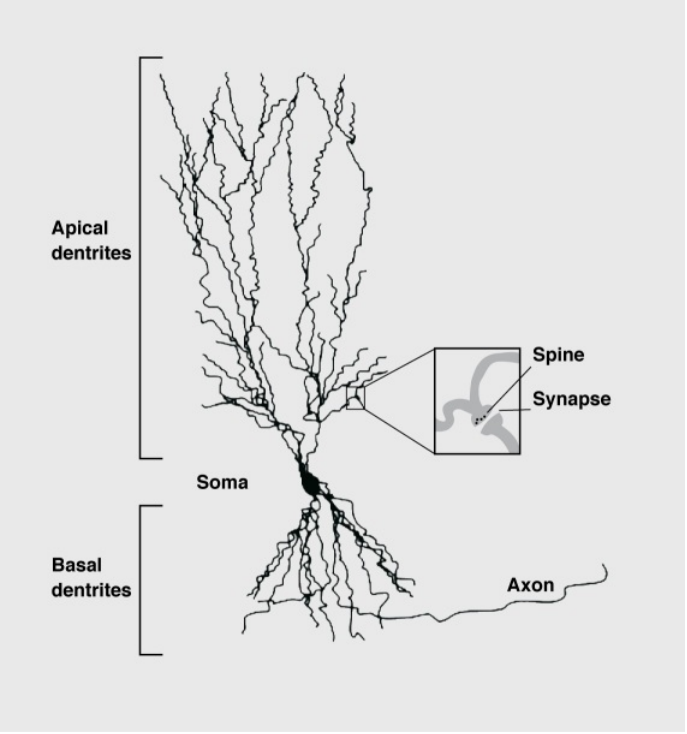


FIGURE 1.2: A schematic illustration of a neuron. Taken from [93].

The inside of a neuron and the space surrounding it is filled with charged particles, or ions. These are primarily positively charged sodium ($Na^+$), potassium ($K^+$), although calcium ($Ca^2+$) and negatively charged chlorine ($Cl^-$) are also involved. These are represented in brackets by their chemical symbols in the previous sentence. Ions enter and leave the cell through ion channels that are specific to the type of ion that they let through.

The potential of the cell membrane of a neuron is controlled by properties of the ion channels located on this membrane. When no signal is being transmitted, a neuron is at an approximately constant potential of $-70$ mV (millivolts) (see

Figure 1.3). There are relatively more sodium ions outside the cell and more potassium ions inside the neuron in this resting state.

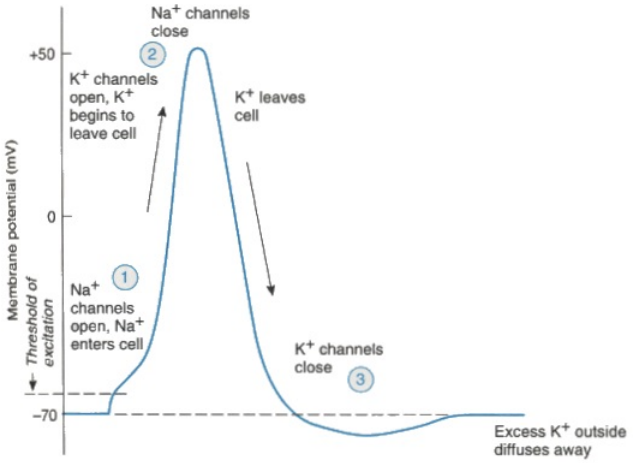


FIGURE 1.3: A schematic illustration of an action potential . Taken from http://www.mindcreators.com/neuronbasics.htm. Viewed on 1st March 2014.

If a neuron receives an electrical signal at its dendrite, its membrane potential is caused to increase by an influx of sodium though its sodium channels. If the membrane potential rises sufficiently, typically above a value of $-55$ mV, the neuron releases an 'all-or-nothing' electrical spike and is said to 'fire'. The incoming electrical signal also triggers the opening of potassium channels, but these take longer to open (see Figure 1.3). When they do, potassium flows out of the cell, causing the membrane potential to decrease and the neurons to re-polarise. At around this time, sodium channels begin to close so that no more positive charge enters the cell. The membrane potential returns to its starting value of $-70$ mV, following a small 'overshoot' caused by the fact that potassium channels do not close immediately.

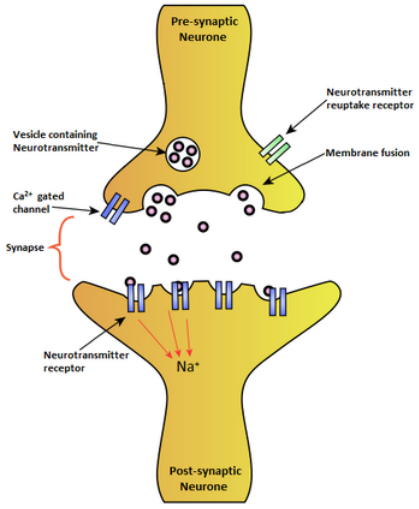


FIGURE 1.4: A schematic illustration of a synapse between the axon of one neuron and the dendrite of another. Taken from http://psychonautwiki.org/. Viewed on 1st March 2014.

When a cell fires, the electrical signal is transmitted from the cell's axon. It may be received by another neuron whose dendrite is divided from it by a small gap called a synapse (see Figure 1.4). The next step in this process is the transmission of the electrical signal across the synapse. When an action potential is emitted, molecules called neurotransmitters, are released from the axon, into the synaptic gap. Examples of these include glutamic acid (glutamate), gamma-aminobutyric acid (GABA), acetylcholine (ACh), dopamine, serotonin and others. A cell with dendrites that access this synapse detects the molecules, which may bind to its dendritic receptors. This leads to a tiny alteration in the cell membrane's potential, promoting the opening of voltage-gated ion channels, causing either a small depolarisation called an excitatory post synaptic potential (EPSP), or a small hyperpolarisation called an inhibitory post synaptic potential (IPSP). The combination of EPSPs and IPSPs may allow this cell to also fire in the same way as the first one.

An individual neuron can be excitatory, or inhibitory so that it may either promote or prevent the firing of a neuron to which it is connected, respectively.

In addition to a synaptic connection, neurons can also be joined at gap junctions. Gap junctions are collections of intercellular channels that permit the direct transfer of ions and small molecules between neighbouring cells [103]. They can be responsible for causing electrical coupling between cells in humans.

Being able to record neural activity is fundamental to understanding the principle by which synchronisation can occur. In the next section, a number of methods for recording the activity of the nervous system are introduced.

### 1.1.2 Recordings of neurophysiological activity

There are a number of ways in which the neuronal activity can be recorded.

It is possible to record individual action potentials (also known as spikes) directly using a fine-tipped microelectrode, which records the rate of change of voltage across time (recall that neurons will fire due to a change in their potential, or voltage). Such a recording is an invasive procedure, performed in humans only in exceptional clinical circumstances.

Non-invasive recordings of electrical activity can also be made. Action potentials themselves do not usually produce an observable electric field because individual spikes generate currents that flow in opposite directions whose electric fields cancel out inside an approximately spherical skull [46]. However, current that flows along the dendrite of synchronously firing neurons can produce a flow of extracellular electrical current, which may be detected outside the cortex and skull (see Figure 1.7).[1] By Ohm's law, this current produces a voltage difference which is called the local field potential (LFP). Spatially and temporally summated LFPs can be detected using electroencephalography (EEG).

#### 1.1.2.1 Electroencephalography (EEG)

The EEG is a recording of the voltage difference between between two electrodes, or channels, on the surface of the scalp (see Figure 1.7). An example of an EEG recording is shown in Figure 1.9.

The values of a potential has no physical meaning in itself unless it is evaluated as a potential difference with a 'reference' point. This is what a voltmeter measures. The reference should be a point that is distant from any sources of potential. Because we do not always know the precise locations of the sources of electric field that we are measuring, it is not obvious where this reference should be [205]. One natural suggestion may be to place the reference electrode on the floor or a wall of the room, but this will in itself contain some intrinsic noise, which may distort the recording. In practice, the reference is another electrode, which is typically placed at the ear lobes, the mastoid (base of skull) or at other sites on the scalp.

Following the recording, EEG signals are re-montaged, or re-referenced according to a desired scheme. The most common techniques for this are to use the Laplacian, bipolar or common average referencing montages [79]. In this thesis, the common average reference is used, in which the average of the recorded potential differences is divided by the number of channels and subtracted from a channel of

[1] Action potentials tend to occur at the point of negative peaks in the oscillatory field [241].

interest [205]. This montage is sometimes called a 'reference-free' technique and is used to reduce the signal-to-noise ratio [205].

EEG is typically recorded using between 32 and 64 channels or electrodes, some of which are shown in Figure 1.5, and in particular channels C3 and C4 correspond roughly to the locations of the left and right motor cortices. These are referred to again in Chapters 3 and 9. A single electrode typically records the activity that occurs under around 10 $cm^2$ of scalp surface, which will typically contain the activity generated by millions of neurons [46].

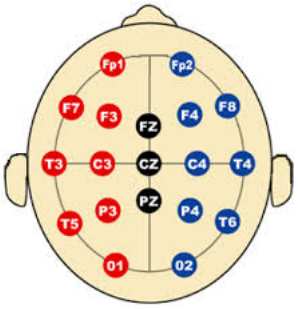


FIGURE 1.5: A schematic illustration of the major positioning sites of electrodes during recording of EEG data. The channels focused on in this analysis are C3 (red) and C4 (blue). Image taken from http://www.biomedical-engineering-online.com. Viewed on 1st March 2014.

One weakness of EEG recordings is that they can have a poor signal-to-noise ratio since the voltage recordings of the brain also contain noise from cortical regions surrounding those of interest, or be distorted by the skull, hair, and other tissues that separate the measuring equipment from the cortex. Noise from the latter regions can be minimised by reducing the resistance of the path along which current flows through the voltmeter. This is done by coating the electrode with gel before placing it on the skin, and by removing any dead skin from the surface of the scalp, which do not permit a flow of current [140, 205].

The EEG was first recorded in 1928 by Hans Berger in order to test his theory that electrical signals from the brain were the source of telepathy. Since then, it has been used to detect brain tumours, diagnose epileptic conditions, infectious diseases, head injury, drug overdose and brain death [205, 246, 308, 309].

Neuronal electrical activity can also be recorded directly at sites of the peripheral nervous system such as the muscles. These recordings are called electromyography (EMG).

#### 1.1.2.2 The Electromyography (EMG)

The electromyogram (EMG) is a recording of the potential difference between two electrodes along a muscle, which results from the electrical activity of neurons connected to that muscle (see Figure1.6).

The first examples of EMG date back to 1666 by Francesco Redi, who found the electricity-generating muscle of the electric eel. In 1792, Luigi Galvani showed that electricity could generate the contraction of muscles. Over half a century later, in 1849, Emil du Bois-Reymond demonstrated that the electrical activity generated by voluntary movement could be recorded, and the first recording was then performed in 1890 by Étienne-Jules Marey, who termed the technique electromyography. With increasingly developed technology, EMG recordings have improved in quality until the 1960s, when surface EMG began to be used.

EMG is generally performed using a bipolar recording. The EMG of a person at rest is silent (although a neuromuscular junction is sometimes spontaneously active). As the muscle is activated, motor units are recruited both through increased firing rate and increased action potential size and action potentials begin to be observed. The surface EMG is a non-invasive recording that consists of superimposed action potentials that have been subject to spatial and temporal averaging. Needle EMG is invasive and recorded directly from a muscle, while surface EMG is recorded from the skin. The former can detect activity of individual motor units, the latter an interference signal. The amplitude of the rectified EMG initially scales linearly with muscle force output.

Most experts recommend that the surface EMG is filtered and rectified before any further analysis is applied to it [112, 292], and this is done in this thesis. In rectification, the amplitude of the signal is squared [112]. This is useful as it gives a better indication of the power of motor-neuron activity, which may otherwise cancel out due to the positive and negative components of individual action potentials (see Figure1.6). Rectification has further been shown to improve the detection of motor unit coherence in some frequency bands [292].

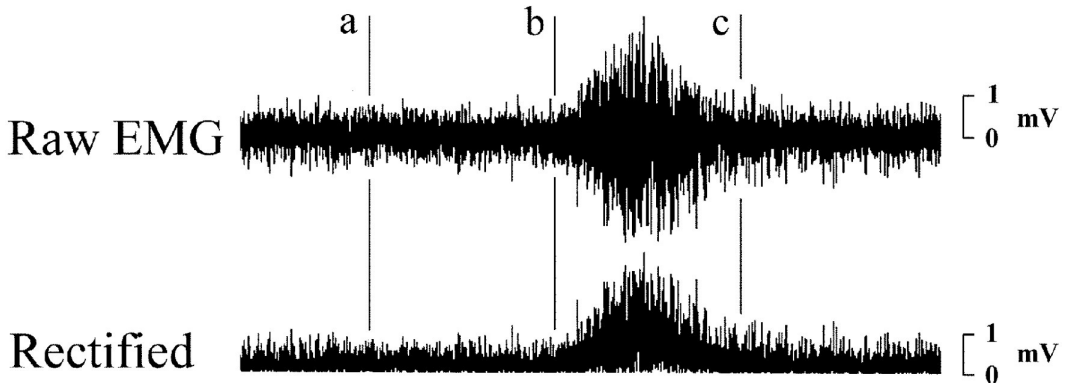


FIGURE 1.6: A raw and rectified EMG signal. Adapted from [173].

Due to the fact that an EMG can be recorded directly from a muscle, it typically has a lower signal-to-noise ratio than EEG.

#### 1.1.2.3 Magnetoencephalography (MEG)

Following Maxwell's laws, an electric current will induce an orthogonal magnetic field, and a set of synchronised dendritic neuronal currents will induce a weak magnetic field much like those in a set of parallel wires (see Figure 1.7).

The magnetic field is weaker than the electric field, however, it can be measured using a very sensitive magnetometer called a superconducting quantum interference device (SQUID). Technological difficulties in making such sensitive equipment meant that MEG was developed only relatively recently. The use of magnetoencephalography (MEG) was first recorded in 1968 as a technique for imaging neural activity [60]. Since the development of high-density sensor grids in the 1990s, MEG has been widely used [116].

To generate an MEG signal that is detectable, the activity of approximately 50,000 neurons is needed [304]. The recording is typically made in a shielded room to reduce interference from background magnetic noise.

The MEG sensors are organised in a slightly different configuration to EEG (see Figure 1.8).

Collectively, EEG, EMG and MEG time series will be referred to as neurophysiological signals.

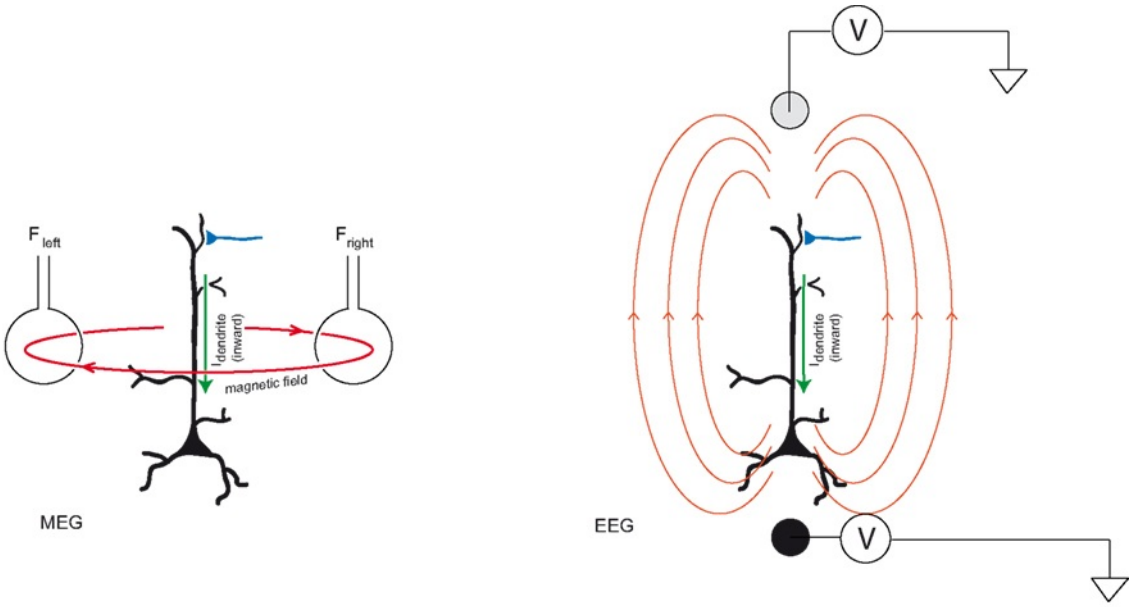


FIGURE 1.7: Electric and magnetic fields produces by current flow in neuronal pallisades. MEG signals measured outside the human scalp are thought to be produced by magnetic fields induced by dendritic intracellular currents ($I_{dendrite}$) in neuronal cells. EEG detects the differences in scalp potentials arising from these currents. Taken and adapted from [190].

#### 1.1.2.4 Some differences between EEG and MEG recordings

A simultaneous recording of the EEG and MEG of a single subject is shown in Figure 1.9.

The benefit of MEG over EEG is that magnetic fields are not distorted as strongly by physiological tissue such as the skull, skin and hair between the brain and the sensor. This means that the spatial and temporal resolution of MEG is better than in EEG [116]. The MEG is also a reference free measure of brain activity.

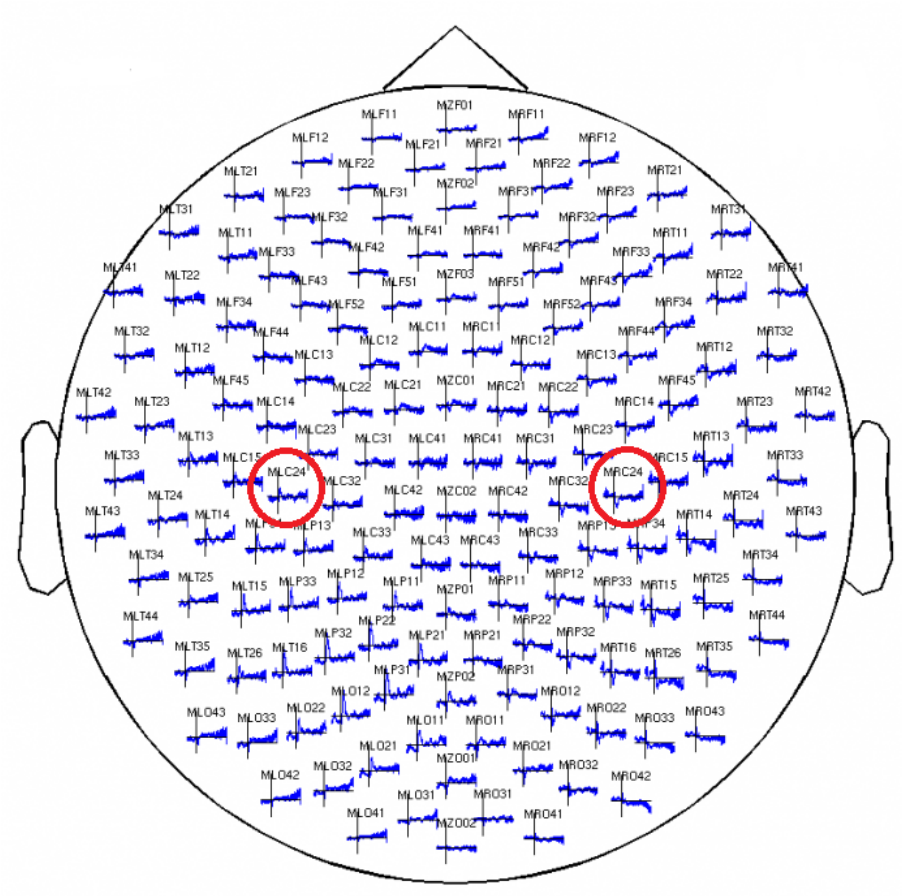


FIGURE 1.8: A schematic illustration of the positioning of MEG channels with examples of recordings plotted at each location. The channels corresponding to the motor cortices are MRC24 for the right motor cortex and MLC24 on the left. These are indicated by red circles. Image taken from FieldTrip toolbox http://fieldtrip.fcdonders.nl/. Viewed on 29th July 2014.

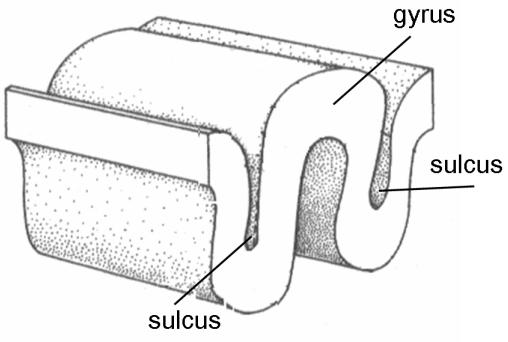


FIGURE 1.10: A diagram to illustrate the gyri and sulci of the cortex. Taken from http://www.quora.com/. Viewed on 10th December 2013.

The MEG sensors are very close to the magnetic fields that they are designed to

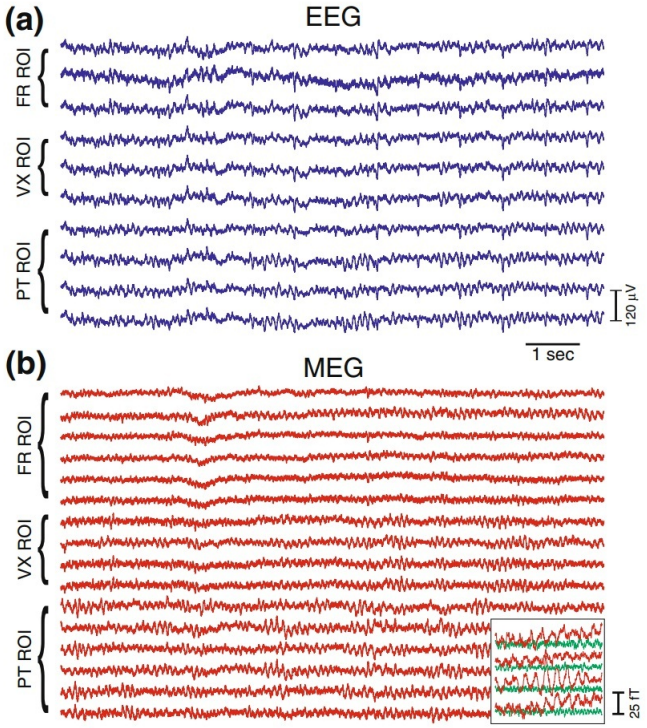


FIGURE 1.9: A comparison of the EEG and MEG recorded simultaneously from the same subject. Image taken from [69].

record because conductivity varies essentially radially. However, because MEG detects mainly the tangential components of neural activity, it is dominated by sulcus (cortex furrow) activity (see Figure 1.10). EEG, on the other hand, is sensitive to both tangential and radial components of a current source and can therefore detect activity from both the convex ridges (gyri) and sulci of the cortex. This means that EEG may also be more sensitive to deeper brain activity.

In general, the magnetic field decays more rapidly than electric, so that MEG may be more sensitive to superficial cortical activity [116].

#### 1.1.2.5 Functional Magnetic Resonance Imaging (fMRI)

Functional magnetic resonance imaging (fMRI) [17, 170] is not discussed in great depth in this thesis, because fMRI data is not analysed here. The work in this thesis is primarily focused on the temporal structure of neurophysiological time series and compared to EEG and EMG, fMRI has poorer temporal resolution. However, a number of studies that have applied their techniques to fMRI will be discussed, so that this imaging method is mentioned here. fMRI is a neuroimaging technique which uses the patterns of blood flow in the brain to identify those regions that are activated at a given time point. It depends on the fact that brain

regions that are active will need an increased inflow of blood in order to sustain their activity. fMRI has poor temporal resolution because blood flow and the measured response is much slower than neuronal firing. One of the weaknesses of fMRI is that brain regions do not always receive blood at the same rate, so that the order in which increased blood flow is observed is not necessarily identical to the order of activation.

#### 1.1.2.6 Default Mode Network

We have mentioned already that the human brain can alter its activity in response to external stimuli or with the performance of a specific task, however, neurophysiological activity is also not constant when a person is completely at rest. When no specific activity is being undertaken, and a subject is in a resting and wakeful state, a number of regions, named the default mode network (DMN) have been observed to be active [68, 267]. The existence of such activity was demonstrated by Marcus Raichle and his team in 2001 [237]. It has been suggested that this activity corresponds to the 'self-referential thoughts', daydreaming, creativity or retrieving memories [44]. The DMN will later be mentioned in relation to a model of the human brain at resting state [47].

### 1.1.3 Oscillations in neurophysiology

The visual inspection of the MEG and EEG time series shows that they are characterised by oscillations of fluctuating amplitude and frequency which are intermixed in a complex fashion with non-oscillatory activity. The power of the oscillatory components that are present in such a time series can be quantified using the Fourier-based power spectrum. A power spectrum is formally defined in the next section (Section 1.1.4), but for the purposes of the present discussion, it is simply stated that it quantifies the contribution of different frequency (spectral) components to a signal. The frequency $f$ is defined as the number of cycles that an oscillation completes in a given time period. Typically, this time period is taken to be 1 second, in which case the unit of frequency is Hertz (Hz).

The power spectra of neurophysiological time series can be characterised by a number of distinct spectral peaks, which often sit on a $\frac{1}{f}$-like decay that is sometimes referred to as $\frac{1}{f}$ noise [46]. See Figure 1.11 for an example for EEG and EMG time series.

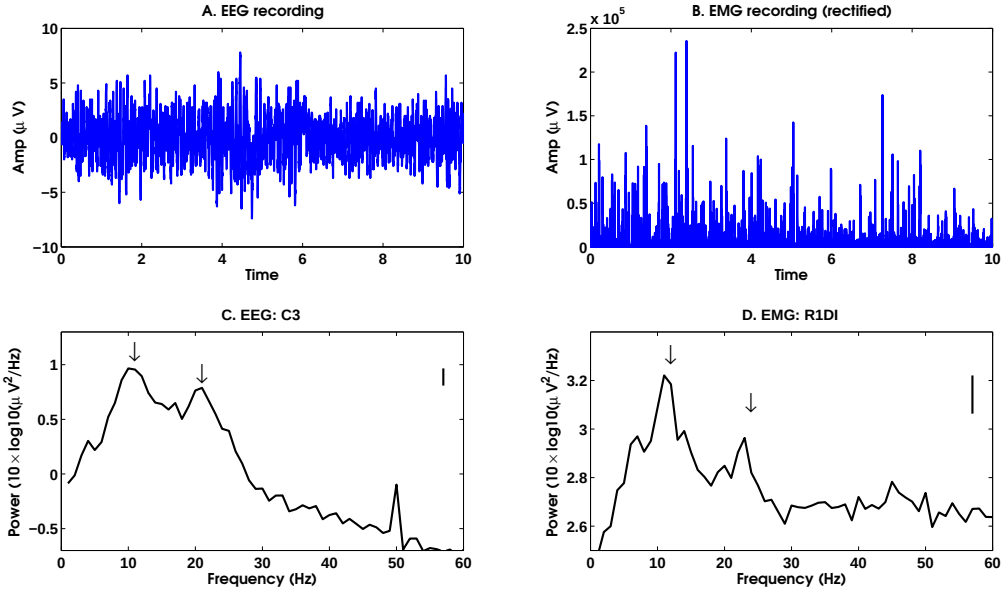


FIGURE 1.11: A-B. An example of a 10 second recording of EEG and EMG. The EMG has been rectified. C-D. The power spectra of the EEG and EMG time series. We may observe an approximate $\frac{1}{f}$ decrease in the power at higher frequencies, but also peaks in the EEG power spectrum at approximately 10 Hz and a more subtle increase at approximately 20 Hz. These are indicated by arrows. There is an artefact at 50 Hz due to mains noise. In the EMG, there are also peaks at approximately 10 Hz and 23 Hz indicated by arrows. The EEG is taken from channel C3 (see Figure 1.5 and the EMG was taken from the first dorsal interosseous muscle of the right hand (R1DI). A common average montage was used. This data was recorded with a sampling rate of 512 Hz and bandpass filtered at 4-256 Hz before the power spectra were calculated.

In EEG and MEG, the frequencies at which spectral peaks occur can vary with sensor location and task performed, but in general peaks of spectral power can occur in frequency ranges of $4-7$ Hz, $7-14$ Hz, $16-32$ Hz and $>30$ Hz. These are referred to as the $\theta$, $\alpha$, $\beta$ and $\gamma$ bands, respectively [26, 46, 60, 116, 241]. Peaks in slower frequencies of $<4$ Hz are also sometimes observed, and referred to as the $\delta$ band. The upper-$\alpha$ band or $\mu$-band ($8-13$ Hz) in the motor control literature is defined separately to the whole $\alpha$ band [218, 223]. The relative mixture of powers in the different frequency bands is state-dependent. Slow frequencies dominate in sleep, while faster frequencies dominate in the alert brain.

At a single unit level, the EMG consists of action potentials which, during weak, steady contraction fire at $\approx$ 10Hz and show up in an oscillatory process. There may be superimposed modulating frequencies above and below 10 Hz (for example 20 Hz frequencies which are strongly associates with motor unit synchrony [82]. Spectral analysis emphasises these oscillatory components.

Oscillations of different frequencies have been associated with different functional properties, and these are discussed in Section 1.1.3.3.

So far in this section,the emergence of quasi-oscillatory rhythms in individual time series recorded by EEG, EMG and MEG have been discussed. Oscillations occur locally as a result of the synchronous activity of neural networks [46], and this phenomenon has been referred to as short-range, or local synchronisation [218, 219]. However, the term 'synchronisation' is also used to describe the long-range, or global synchronisation, which occurs between individual neurons or neuronal assemblies located at different areas of the brain. The mechanisms and properties of synchronisation both at short and long ranges will be discussed in the next section.

#### 1.1.3.1 Neural synchronisation

Neuronal firing is an important mechanism by which neurons can respond to external stimuli. Individual neurons have been observed to alter their firing rate when specific stimuli are presented. This phenomenon, known as 'rate coding' was first observed in 1926 (published in 1928) by Edgar Douglas Adrian and the subject is reviewed for example in [242]. Synchronisation between such individual neurons may occur because they share a connection at a synapse. This means that when an upstream neuron fires, its neighbour is more likely to fire as a result. Such a mechanism for synchronisation is not deterministic, as the firing of the downstream neuron also depends on electrical input from a large number of other upstream cells. Thus the progress of an action potential in this way will depend on the structural connectivity of the nervous system, which may form when neurons with a common function fire synchronously and connect to each other during development [76, 121].

A subset of neurons in the cortex, called chattering cells, were found to fire regularly at a specific frequency, and it was suggested that the propagation of these firing patterns may be the source of the oscillatory structure of neurophysiological time series [106]. However, these phenomena are not explored further in this thesis.

The quasi-oscillatory rhythms visible in neurophysiological signals have also been proposed to result from synchronisation among larger neuronal pools [291]. Pools of neurons can synchronise because of the collective interactions of excitatory and inhibitory neurons present within them [7]. Inhibitory neurons are crucially important to generating oscillatory rhythms because they can create a temporal window during which firing cannot occur, and this temporal window reoccurs rhythmically due to the feedback connections between neurons [7, 291].

The rhythmic firing of neuronal networks will result in changes to the collective membrane potentials of these neurons, which can be detected by EEG or MEG. These membrane potential alterations are not the same as the firing patterns of neurons because they also include sub-threshold potentials, which are not sufficient to cause a spike. However, membrane potential oscillations are thought to be able to coordinate synchronous firing at a global level, although individual neurons rarely fire regularly, or precisely in time with oscillatory peaks [74]. For this reason, neurophysiological signals are not perfectly rhythmic, but sometimes said to be quasi-oscillatory. It has been suggested that oscillations may promote neuronal binding into assemblies by increasing the saliency of groups of neurons relative to each other [81, 256]. It has been also proposed that synchronisation can occur in this way both between proximal and distal neuronal pools that have a similar function [81, 256].

The attention of this thesis is now turned to long-range or global synchronisation in particular.

#### 1.1.3.2 Communication through coherence

One measure of long-range oscillatory synchronisation is coherence, which can be used to quantify the synchronisation relationship between observable frequencies in two separate time series [81]. Because EEG, EMG and MEG signals are not perfectly oscillatory, the coherence between them is weak. Coherence is introduced mathematically in Section 1.1.4.

Significance has been attached to the coherence between neuronal groups in the nervous system. It has been argued by Pascal Fries that variations in coherence across time represent 'communication', or the transfer of information, between different pools of neurons in the nervous system [89, 91, 250]. Fries suggests that when the neurons of a particular group are active, they introduce temporal windows for communication, and if two neuronal pools have windows that correspond in time, they can interact more effectively.

It was demonstrated that subjects' reaction time correlated with the coherence between neurons of the motor cortex and the spinal chord [250]. Fries also demonstrated his hypothesis through defining a 'hazard rate' for a task, which represented the likelihood of the presentation of a stimulus if it had not yet appeared in a particular time frame [89]. When the hazard rate was high, and the stimulus was very likely to appear, subjects responded quickly. This strongly correlated with the magnitude of cortico-spinal coherence (MEG-EMG) in the $\gamma$ frequency band. The hazard rate was thus suggested as a quantification of the means by which the

system of motorneurons prepared for action and therefore by which components of this system 'communicated' with each other.

Fries further argued that variation in the coherence between different neuronal pools is an essential property that allows cognitive flexibility [89]. Collectively, these ideas are referred to as the 'communication through coherence' hypothesis.

#### 1.1.3.3 Functional significance of oscillations

Neurophysiological oscillations at different frequencies are associated with particular functions. Some of the main features of the individual frequency bands will be stated in this section.

**$\alpha$ frequencies** Oscillations in the $\alpha$ band correspond to relaxed wakefulness [26].

A rhythm of 7-10 Hz is also the main rhythm observed during slow finger tapping due to 8-10 Hz discontinuities in the descending motor command [278].

**$\beta$ frequencies** Oscillations in the $\beta$ band characterise the active, wakeful brain [142] and they have particular relevance to the motor system [81, 248, 291].

In particular, increased peaks in the $\beta$ and also the $\mu$ bands are associated with preparation for movement, and are observed in sustained muscle contraction, but not associated with movement itself. These tend to decrease in power at the onset of activity in a process that was studied extensively by Pfurtscheller et al. and called event-related de-synchronisation (ERD) [218]. When movement ceases, $\beta$ and $\mu$ band peaks tend to increase again with event-related synchronisation (ERS) [219]

Coherence between cortical motor neurons (recorded with MEG and EEG) and those found in the muscle (recorded with EMG) has been observed at around 20 Hz during sustained muscle contraction [61, 111], which disappears during movement ([15] and modelled in [301]).

**$\gamma$ frequencies** Oscillations in the $\gamma$ band are associated with arousal and attention. A peak in $\gamma$ frequencies is seen at the initiation of movement, but not during sustained muscle contraction [143]. When a trained action is performed, $\gamma$ oscillations tend to weaken, which suggests that they are particularly important in the learning process [241]. They can dominate in cortico-muscular coherence during strong motor contractions [41], and during walking [217].

**Slower frequencies** The $\theta$ band is associated with sleep, drowsiness and disinterest the $\delta$ band with depressed consciousness [308, 309].[2]

#### 1.1.3.4 The Kuramoto model

In this section so far, the prevalence of oscillations in neurophysiological time series such as EEG, EMG and MEG has been discussed. The synchronisation between neurophysiological time series recorded at different spatial locations of the cortex was also discussed, and between cortex and muscle. The classical Kuramoto model of oscillators is now introduced, which incorporates a mechanism for exploring synchronisation onset through a coupling constant [2, 56].

The Kuramoto model has been widely used to study the oscillatory behaviour of biological systems such as the sleep and body temperature cycles in humans [228, 265], heart pacemaker cell firing [2, 228, 265], neuronal firing [36, 158, 228] and fire-fly flashing [2, 228, 265, 265].

The Kuramoto model describes the phase behaviour of a system of mutually coupled oscillators with a set of differential equations. Each of $N$ oscillators in the system rotates at its own natural frequency $\{\omega_i, i = 1, ..., N\}$, drawn from some distribution $g(\omega)$. However, it is attracted out of this cycle through coupling $K$, which is globally applied to the system and the sine coupling function. Time is represented by $t$. The differential equation to describe the phase of an oscillator is [167–169]:

$$\dot{\phi}_i(t) = \omega_i(t) + \frac{K}{N}\sum_{j=1}^{N}\sin(\phi_j(t) - \phi_i(t)) \tag{1.1}$$

Kuramoto [167] showed that the evolution of any phase $\phi_i(t)$ can be re-expressed using two mean field parameters, which result from the combined effect of all oscillators in the system. Namely, we may say:

$$\dot{\phi}_i(t) = \omega_i + Kr(t)\sin(\psi(t) - \phi_i(t)) \tag{1.2}$$

where $\psi(t)$ is the mean phase of the oscillators, and $r(t)$ is their phase coherence, so that:

[2] Although humans in these states are clearly at rest, these frequencies are not typically referred to as being associated with the 'resting state' because they are not associated with a readiness to react or perform a task. The 'resting state' is a state of wakeful rest.

$$r(t)e^{i\psi(t)} = \frac{1}{N}\sum_{j=1}^{N} e^{i\phi_j(t)} \tag{1.3}$$

This crucially indicates that each oscillator is coupled to the others through its relationship with mean field parameters $r(t)$ and $\psi(t)$, so that no single oscillator, or oscillator pair drives the process on their own. The mean field $\psi(t)$ is the average phase of the oscillators, and $r(t)$ describes the strength of synchronisation, sometimes referred to as the extent of order in the system [32, 266]. When $r(t) = 0$, no oscillators are synchronised with each other. When $r(t) = 1$, all oscillators are entrained with each other.

One solution to Equation 1.2 is $r \equiv 0$ for all time and coupling, leaving each oscillator to evolve independently at its own natural frequency. Using a limit of $N \to \infty$, some further deductions can be made, including the fact that when the natural frequency distribution $g(\omega)$ is unimodal and symmetric, another solution can be found for $\omega_i$, with $r(t)$ not equivalent to 0 [167]. A critical bifurcation occurs for sufficiently high coupling, during which the order parameter, $r(t)$, evolves continuously. The coupling at the bifurcation is referred to as the critical coupling value $K_c$ [75]. Further ideas on and properties of a system at criticality will be discussed in greater detail in Section 1.1.7.

In an infinite Kuramoto model, criticality is defined through this bifurcation. For a finite system, however, the critical coupling can only be approximated by this theoretical value. One defining characteristic of the critical coupling is that as $K_c$ is approached the Kuramoto system is in a state of flux as oscillators come in and out of synchronisation with each other over time. If the coupling value is increased to a value above $K_c$, then some the oscillators will synchronise and remain synchronised as time evolves. Indeed, as $K$ is increased further, the critical coupling $K_c$ is that at which the the greatest rate of change of synchronisation, with respect to the coupling value $K$, occurs.

However, in this thesis, only finite-sized systems of the Kuramoto model are considered. For this reason, a marker of criticality is extracted and used when the theoretical value may not apply. Specifically, this is a marker of the greatest rate of change of order [193]. This is the change in the 'effective mean-field coupling strength', $\Delta(Kr)$. If the value of $Kr$ exceeds the difference between the natural frequency and the mean phase $\omega_i - \psi$ (in modulus) i.e. $|\omega_i - \psi| < Kr$, then oscillator $i$ will synchronise to the mean field [193]. Thus the value of $K$ at which $Kr$ increases maximally is the coupling value at which the greatest number of oscillators are drawn into the mean field, i.e., a defining feature of the critical point in the system.

The evolution of phase in the Kuramoto model is smooth. A richer structure can be created if noise is added to the system [47]. This procedure is studied in greater detail later in the thesis in Section 6.11. The Kuramoto model has also been recently used by Joana Cabral and colleagues to create a more physiologically accurate model of neurophysiological signals for the human brain in a resting state, which will be referred to in this thesis as the Cabral model. This model will be introduced in Chapter 7. The Cabral model includes variable connectivity between oscillators, based on empirical estimate of connectivity. It also includes a time delay matrix for the activity of one oscillator to reach the others.

### 1.1.4 Signal processing techniques

In the previous section, the fact that neurophysiological time series such as EEG, EMG and MEG are characterised by oscillations, which can be observed at different frequencies was discussed. A common method for quantifying the power of particular frequency band in a signal is to look at its power spectrum. In this section, the power spectrum and also the coherence are defined mathematically. In order to provide the definitions of these two measures, a number of metrics must be introduced first, both because they are used in the calculation of the power spectrum and coherence, and because they can be used in their own right to extract important information about a signal. One of these is the autocorrelation function, which is used to calculate the relatedness of a time series with itself across different time lags. The autocorrelation function is also essential to our understanding and definition of LRTCs (see Section 1.1.8.2). Another important function is the cross-correlation function, which quantifies the correlation between two different time series across time lags. This is the time-domain analogue of the cross-spectral density function, which can be normalised to give the coherence.

The Fourier transform is first defined, which is a necessary tool for the calculation of both a power-spectrum and a coherence.

#### 1.1.4.1 The Fourier transform

The Fourier transform is an important tool in signal processing. It was developed following the theory presented by Joseph Fourier that any function, whether continuous or not, may be decomposed into a series of sine and cosine curves. It is a mathematical operation that transforms a signal from the time to the frequency domain. The Fourier transform is given by:

$$\mathcal{F}\left\{x(t)\right\} = X(f) = \int_{-\infty}^{\infty} x(t)e^{-2\pi itf}dt \tag{1.4}$$

which evaluates the strength of the frequencies present as a function of frequency $f$.

Its inverse may also readily be calculated:

$$x(t) = \mathcal{F}^{-1}\left\{X(f)\right\} = \int_{-\infty}^{\infty} X(f)e^{2\pi itf}df \tag{1.5}$$

#### 1.1.4.2 Auto-correlation function

The autocorrelation function is a measure of the relatedness of the innovations in the signal as a function of their temporal separation. It can be used to identify periodic components or the harmonics of a signal [232].

For a signal $x(t)$, the autocorrelation is defined by:

$$\rho_{xx}(\tau) = \int_{\infty}^{-\infty} x(t+\tau)\bar{x}(t)dt \tag{1.6}$$

where $\tau$ is the time lag between points, and $\bar{x}(t)$ denotes the the complex conjugate of $x(t)$. It is noted that, if $x(t)$ is real, then $\bar{x}(t) = x(t)$.

For a discrete time series $x_i$, the autocorrelation can be adapted to the following form:

$$\rho_{xx}(j) = \sum_i x_i\bar{x}_{i-j} \tag{1.7}$$

where $j$ is the lag, and $\bar{x}_i$ is the complex conjugate of $x_i$.

Infinitely long sine and cosine signals will have an autocorrelation function that is a cosine curve (see Figure 1.12). The peaks in this autocorrelation function will occur with a frequency equal to that of the original signal.[3]

[3]The autocorrelation function of a finite sine or cosine signal will have peaks that decay slowly with time lag.

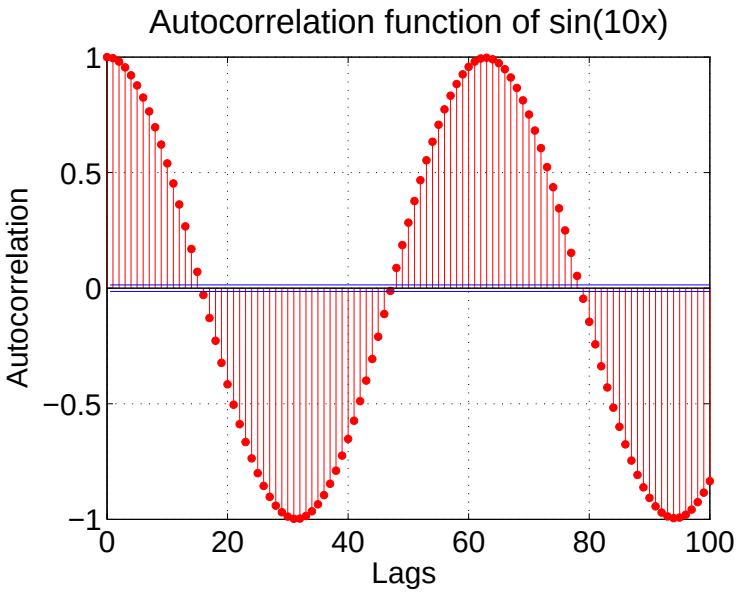


FIGURE 1.12: The autocorrelation function of $\sin(10x)$. The autocorrelation function is periodic. The blue lines are upper and lower bound confidence intervals.

White noise is a time series that is made up of independent random variables. A time series of any white noise has an autocorrelation function that is a Dirac delta function (see Figure 1.13). Due to the independence of its elements, it will be correlated to itself at a time lag of 0, but have no correlations at any other time lag.

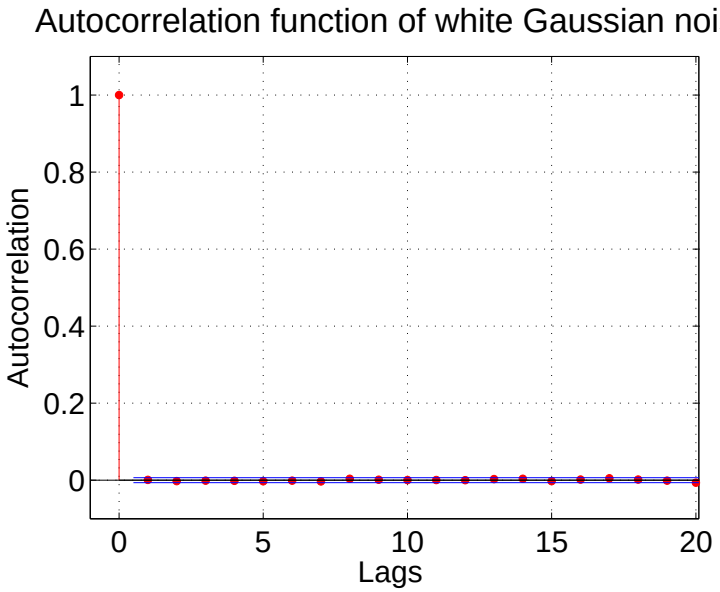


FIGURE 1.13: The autocorrelation function of white noise. The autocorrelation is a Dirac delta function with a values of 1 at time lag 0 and a value of zero for all other time lags. The blue lines are upper and lower bound confidence intervals.

**A note on noise** A Gaussian white noise time series is a white noise time series that is constructed by taking innovations from a Gaussian process at each time point. It is possible to use alternative probability distributions for the selection of variables, but these will not be called Gaussian. Throughout this thesis, when white noise is used, it is generated by a Gaussian process.

#### 1.1.4.3 Cross-correlation function

The cross-correlation function measures the relatedness between the innovations in two distinct signals as a function of the time lag between them. Its definition extends naturally from that of the autocorrelation, but it is applied to two signals, which are labelled $x(t)$ and $y(t)$. The cross-correlation is defined as:

$$\rho_{xy}(\tau) = \int_{\infty}^{-\infty} x(t+\tau)\bar{y}(t)dt$$

For a discrete time series, it is:

$$\rho_{xy}(j) = \sum_{i} x_i \bar{y}_{i-j}$$

For example, two sine curves that are shifted copies of each other will have peaks in their cross-correlation function at the value of their temporal shift, and its integer multiples.

#### 1.1.4.4 Power spectrum

The power spectrum of signal $x(t)$ is defined as the Fourier transform of its autocorrelation function:

$$G_{xx}(f) = \int_{\infty}^{-\infty} \rho_{xx}(\tau)e^{-2\pi i f\tau}d\tau \tag{1.8}$$

where $f$ is frequency. This measure is also known as the power spectrum of a time series, the spectral density, power spectral density, or energy spectral density depending on the context. Intuitively, the spectrum decomposes the content of a stochastic process into the different frequencies present [280].

Due to the presence of spectral peaks in neurophysiological time series (see Section 1.1.3), we are often interested in isolating and investigating a specific range of frequencies. This may be done using a procedure called filtering, and it is performed

using a Fourier transform. The Fourier transform $\mathcal{F}\{x(t)\}$ of the signal, $x(t)$ is first taken (Equation 1.4). This transforms the signal from the temporal to the frequency domain. The necessary range of frequencies may then be isolated from the transformed data, and the inverse Fourier transform taken to return it to the temporal domain (Equation 1.5).

More detail on filters and filter types is given in Section 1.1.4.5.

#### 1.1.4.5 Filtering

A filter is a technique that removes unwanted components of a signal. They are used when a specific band of frequencies need to be isolated.

Filters are typically either lowpass, highpass or bandpass. A lowpass filter will allow frequencies lower than a certain selected value and block (attenuate) frequencies higher than this value. A highpass filter will allow high frequencies and block low frequencies. A bandpass filter will retain the frequencies within a certain band that is bounded both above and below. The effect that a filter will have on the power spectrum of a signal is defined by its frequency response curve. The 'ideal' bandpass filter would be a perfect rectangle with boundaries at the two limits of the bandpass range (see Figure 1.14). Using such a bandpass filter, the power of the signal would be perfectly preserved at the required frequencies, and the power of all other frequencies would be perfectly zero.

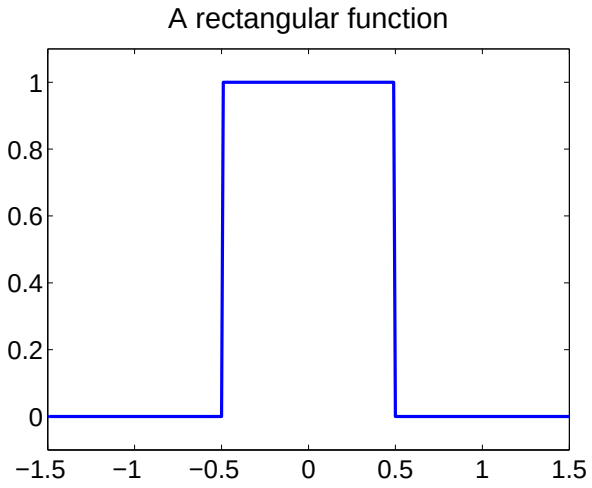


FIGURE 1.14: A rectangular function. The ideal filter may be thought of as a rectangular function.

The practicalities of designing such a filter can be understood by looking at its impulse response function. An impulse is a Dirac delta function, and the impulse

response shows the effect of a filter on this function. The Dirac delta function is used because its Fourier transform is equal to 1 for all frequencies. This means that in applying a filter to this function, we may see the effect that the filter will have on all possible frequencies. The result of applying a filter to an impulse function is called its impulse response.

The impulse response of a perfect rectangle is the sinc($t$) function defined by:

$$\text{sinc}(t) = \frac{\sin(\pi t)}{\pi t}$$

The shape of a sinc function is shown in Figure 1.15.

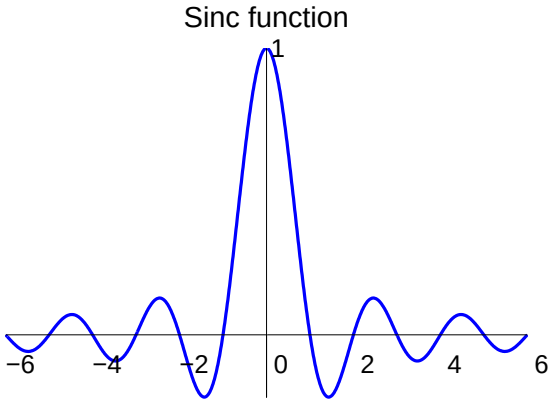


FIGURE 1.15: A sinc function with time on the $x$-axis. A sinc function takes non-zero values both at positive and negative time. Indeed, it can take non-zero values at infinite values of time.

The sinc function has non-zero values at both negative and positive time. As the sinc function is non-zero at negative time, its application to a signal relies on knowledge about that signal prior to the beginning its record. This is not possible in practical applications. An ideal bandpass filter can therefore not implemented.

In practice, two classes of filter are commonly used. These are finite and infinite impulse response filters. Finite response filters are so defined because their impulse response function is zero after a finite time period. Infinite response functions have a slowly decaying impulse response function that does not shrink to zero.

Examples of frequency response curves for lowpass, highpass and bandpass infinite

impulse response filters are shown in Figure 1.16.[4]

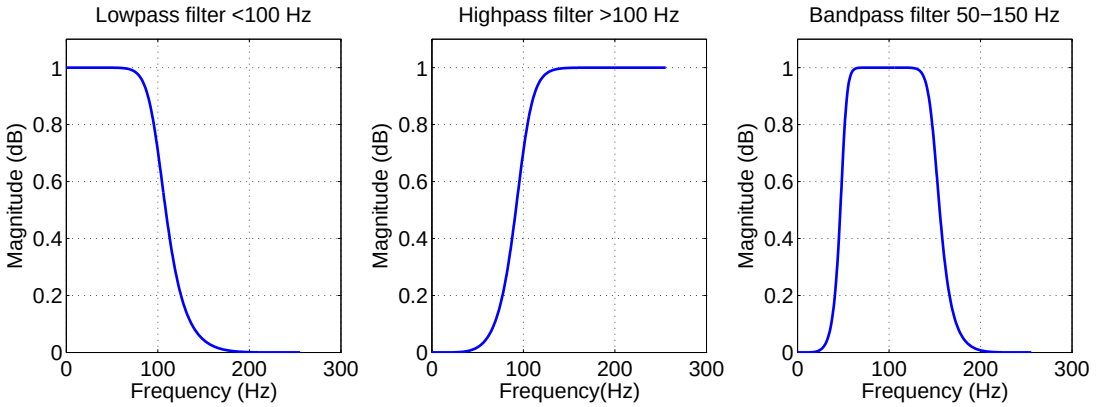


FIGURE 1.16: The magnitude of the frequency response of one example of a lowpass, highpass and bandpass filter.

Finite response filters are typically more computationally intensive, however they are more straightforward to apply, and are less prone to errors [232]. In most modern computational languages, algorithms for computing FIR filters have been optimised. For these reasons, a finite response filter will be used to bandpass filter neurophysiological data in this thesis. In particular, the filter is constructed so that the sum of squared differences between its frequency response and that of the ideal filter is minimised. The frequency response of such a filter for a frequency range of 16-24 Hz is shown in Figure 1.17.

[4]The filter used to generated the plots in Figure 1.16 was a Butterworth filter, which is a classical infinite impulse response filter. Other classical filters include the Chebyshev Types I and II, elliptic, and Bessel filters amongst others. These filters have different characteristics. The Butterworth filter has a smooth decay and the magnitude of its response away from the 'cutoff' point approximate the ideal filter well as seen in Figure 1.16. These are called the 'passband' and 'stopband' regions. Other filters have 'ripples' in their frequency response functions, but have other advantages such as Chebyshev filters which are characterised by a minimum difference between their frequency response and that of the ideal filter in either the passband or the stopband regions.

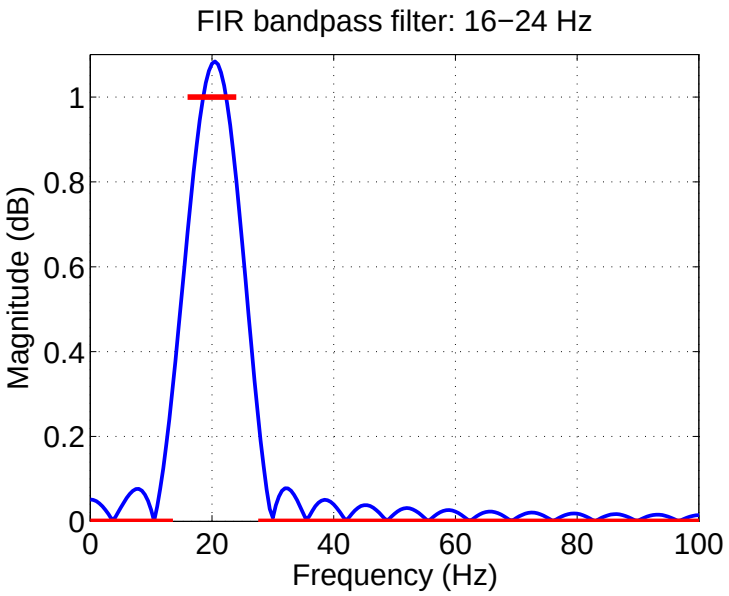


FIGURE 1.17: The magnitude of the frequency response of a FIR 16-24 Hz bandpass filter. The red lines indicate the magnitude of the ideal frequency response for a bandpass filter of 16-24 Hz.

An important property of FIR filters is the filter order. The filter order determines how quickly the impulse response of a filter decays to zero. It is typically set to a value that is equal to several cycles of the lower-frequency component of the band. Unless stated otherwise, the filter order is set to 3 times the lower bandpass filter limit in this thesis. A similar approach has been used in many recent studies [117, 177–179].

#### 1.1.4.6 Coherence

The coherence is a measure of the relationship between the different frequency components contributing to two time series [280]. In order to calculate coherence, the auto-spectral density is required, but also the cross-spectral density, which is the Fourier transform of the cross-correlation function of signals $x(t)$ and $y(t)$.

The cross-spectral density is defined as:

$$G_{xy}(f) = \int_{\infty}^{-\infty} \rho_{xy}(\tau) e^{-2\pi i f \tau} d\tau \tag{1.9}$$

The coherence between the two signals $x(t)$ and $y(t)$ can now be defined as:

$$C_{xy}(f) = \frac{|G_{xy}|^2}{G_{xx} G_{yy}} \tag{1.10}$$

In calculating $C_{xy}(f)$ the cross-spectra (numerator) are normalised by the autospectra (denominator). This is important to ensure that one signal doesn't dominate another. If one of the signals had a very strong component in one frequency and another was weak and noisy, a strong coherence would be returned without this normalisation.

Coherence takes a value $\in [0, 1]$. A value of one indicates that $y(t)$ is an exact functional from of $x(t)$ and can be written as $h(t) * x(t)$ where $*$ denotes convolution, defined by the following integral:

$$(f * g)(t) = \int_{-\infty}^{\infty} f(\tau)g(t - \tau)d\tau$$

A value of zero indicates that the signals are completely unrelated [232]. It can be thought of as a normalised mean of the correlation between two signals at a given frequency.

The cross spectrum has a real and imaginary component, which means that its amplitude and phase may be studied independently (see Section 1.1.6.1 for more details). The amplitude component is used to derive the coherence (see Equation 1.10). The phase component is not considered in detail in this section, but it has also been studied (for example [37]). The phase is a measure of the position of an oscillatory signal in its cycle.

In order to demonstrate the measures in this section, they are applied to some example data of an EEG and an EMG signal recorded simultaneously from a human subject (information about the recording is provided later in Section 2.2). These are plotted alongside each other with their respective power spectra (Equation 1.8), and their coherence (Equation 1.10) in Figure 1.18. A typical value for coherence between the cortical EEG and muscular EMG is of the order of 0.05-0.1 [16].

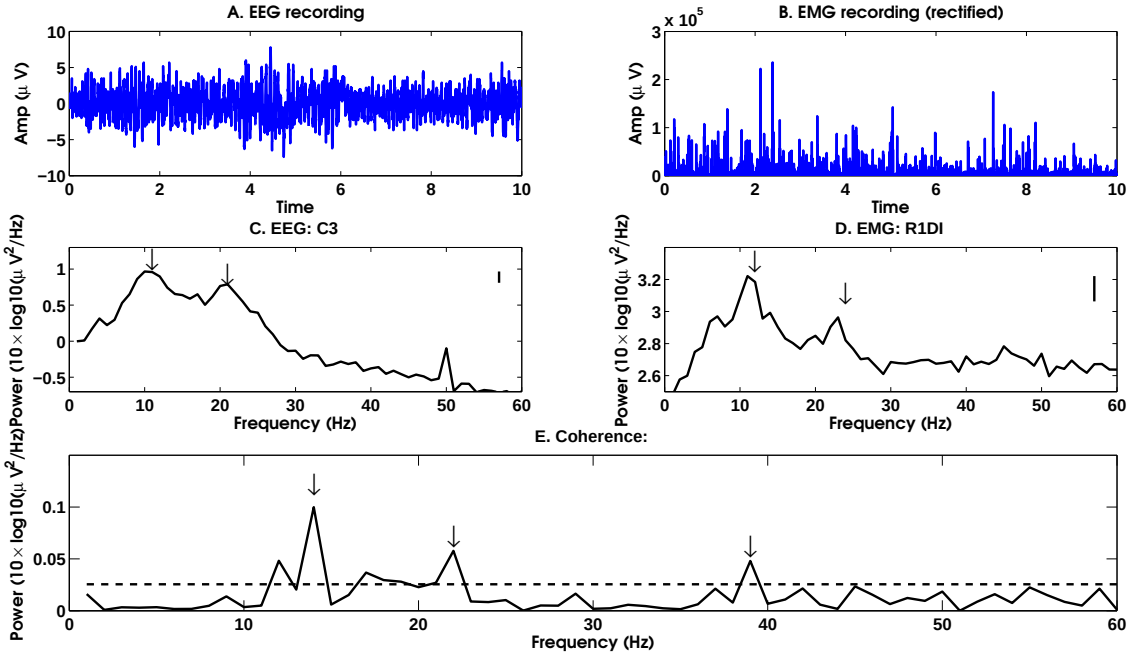


FIGURE 1.18: A-B. An example of 10 seconds of an EEG and EMG signal from a single subject. C-D. The EMG signal is first rectified [112, 292] but the EEG is not, then the power spectra are shown for both. The EEG signal shows a peak in the $\alpha$ rhythm frequency of 8-12 Hz (arrow), and near 20 Hz (arrow), in the $\beta$ rhythm range. There is an artefact at 50 Hz due to mains noise. The EMG shows features consistent with $\alpha$ rhythms near 10 Hz (arrow) and with $\beta$ rhythms at $\approx$ 23 Hz (arrow). E. The coherence between the two signals is shown as a function of frequency. The dashed line in the coherence plot is a confidence level of significance. The coherence levels surpass confidence levels in the $\approx$ 14 Hz region (arrow) and at $\approx$ 39 Hz (arrow) [37]. The EEG is taken from channel C3 (see Figure 1.5 and the EMG was taken from the first dorsal interosseous muscle of the right hand (R1DI). This data was recorded with a sampling rate of 512 Hz and bandpassfiltered to a range of 4-256 Hz before the power spectrum was calculated.

Coherence is a time-averaged measure, and it provides a single, scalar quantification of the oscillatory synchronisation between two time series at each frequency. However, the synchronisation between neuronal pools does not typically remain constant over time. It is observed that neurophysiological time series can synchronise and desynchronise over time. The coherence measure may obscure these time-varying properties in providing an average value. It is useful, therefore, to also consider time-varying measures of synchronisation.

### 1.1.5 Time-varying measures of synchronisation

In the previous section, a number of classical signal processing measures were defined, which can be used to quantify time-averaged properties of a signals. A number of time-varying measures of synchronisation are based on the division of

the time series into windows and application of the metrics defined in Section 1.1.4, amongst others, to individual windows. In one such method, which is described in Section 1.1.5.1, the Fourier transform is applied to segments of a time series. The optimal spectral tracking framework is a recent framework in which such techniques have been developed and optimised (Section 1.1.5.2). Another methodology is that of wavelet coherence (Section 1.1.5.3).

#### 1.1.5.1 Fourier transform methods

A Fourier transform is classically applied to a whole signal, and can be used to obtain a measure of coherence (see Section 1.1.4.6). Time-varying measures can be obtained by applying the Fourier transform to shorter windows in a time series, or to sliding windows in a technique called the short-time Fourier transform. A Fourier transform is an integral, so that by definition it cannot be applied instantaneously. The resolution of such time-varying synchronisation measures is therefore limited by the size of the window (see Figure 1.19).

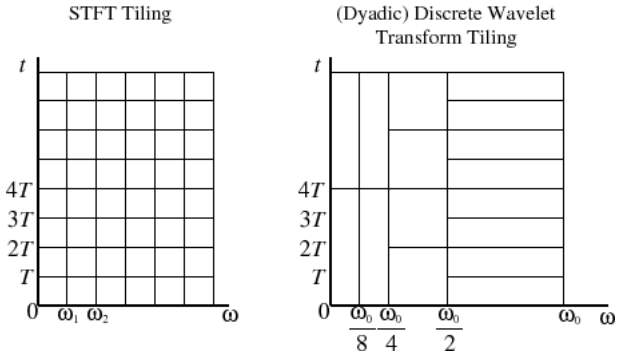


FIGURE 1.19: In Fourier-based methods, windows are regular (left hand panel short-time Fourier transform (STFT)) and in wavelet-based methods, they are such that higher frequencies have a greater temporal resolution (right hand panel). Here $T$ represents time, and $\omega$ represents frequency. Taken from http://www.dsprelated.com/dspbooks/sasp/Discrete_Wavelet_Filterbank.html. Viewed on 6th March 2014.

#### 1.1.5.2 Optimal spectral tracking (OST)

A recent framework was developed by Brittain et al. to characterise measures such as time-varying coherence and phase alongside their confidence intervals [37]. The framework is called Optimal Spectral Tracking (OST), and it does not assume that the signal is stationary. It is straightforward to apply to any time series including neurophysiological data.

OST is used to reproduce the spectrum of two individual signals, the coherence between them, and the phase spectrum as a function of the temporal and spectral domains. The phase spectrum is a measure indicating whether the two time series are in phase in a particular frequency band, and it can be calculated by finding the phase component of the cross-spectral density. A phase spectrum with a near-constant zero value means that the two time series are almost phase locked.

In order to perform OST, the time series is first divided into a number of temporal segments, of $N$ data points each. The cross-spectral density between the two signals is obtained for each window (see Equation 1.9). This is done using the Fourier transform (Equation 1.4) as described in Equation 1.9. The Fourier transform is estimated using a periodogram, which is evaluated at equally spaced Fourier frequencies, $f_n = n/(N\delta t)$, $\{n = 0, ..., \lfloor N/2 \rfloor\}$, where $\delta t$ is the sampling interval and $\lfloor N/2 \rfloor$ means that the floor of $N/2$ should be taken. Both time and frequency-varying coherence estimates are performed over some range of temporal and spectral values. As a result, a trade-off emerges between the number of temporal and spectral divisions made. An example of these measures is shown in Figure 1.20, it is possible to observe the blocks of segmentation in both domains of the time and frequency-varying spectrum of an EEG signal. This is an important restriction in dealing with short data sets, where relatively few temporal data points are available.

After calculating the periodogram, the logarithm of the periodogram is taken. A number of normalising techniques are also applied, for details of which, see [37]. The next step requires the spectral estimators to undergo tracking by applying filtering procedures. This is performed using a Kalman filter, chosen for its optimality for a data set where Gaussian noise input is assumed [37]. Its main aim is to improve a noisy estimate of a signal, and produce values that should be closer to the true values of the data. A value is predicted for the true value of the signal, and its uncertainty is estimated. This predicted value and the actual measured value are then combined using a weighted average based on this uncertainty. More weight is given to a value with less uncertainty. Tracking is performed on the log-spectra of all the segments making up the spectral estimates.

#### 1.1.5.3 Wavelet coherence

Wavelet coherence requires the application of a wavelet transform $\gamma(s, \tau)$, which is obtained by a convolution of a signal $x(t)$ with a family of functions called wavelets $\Psi^*_{s,\tau}(t)$:

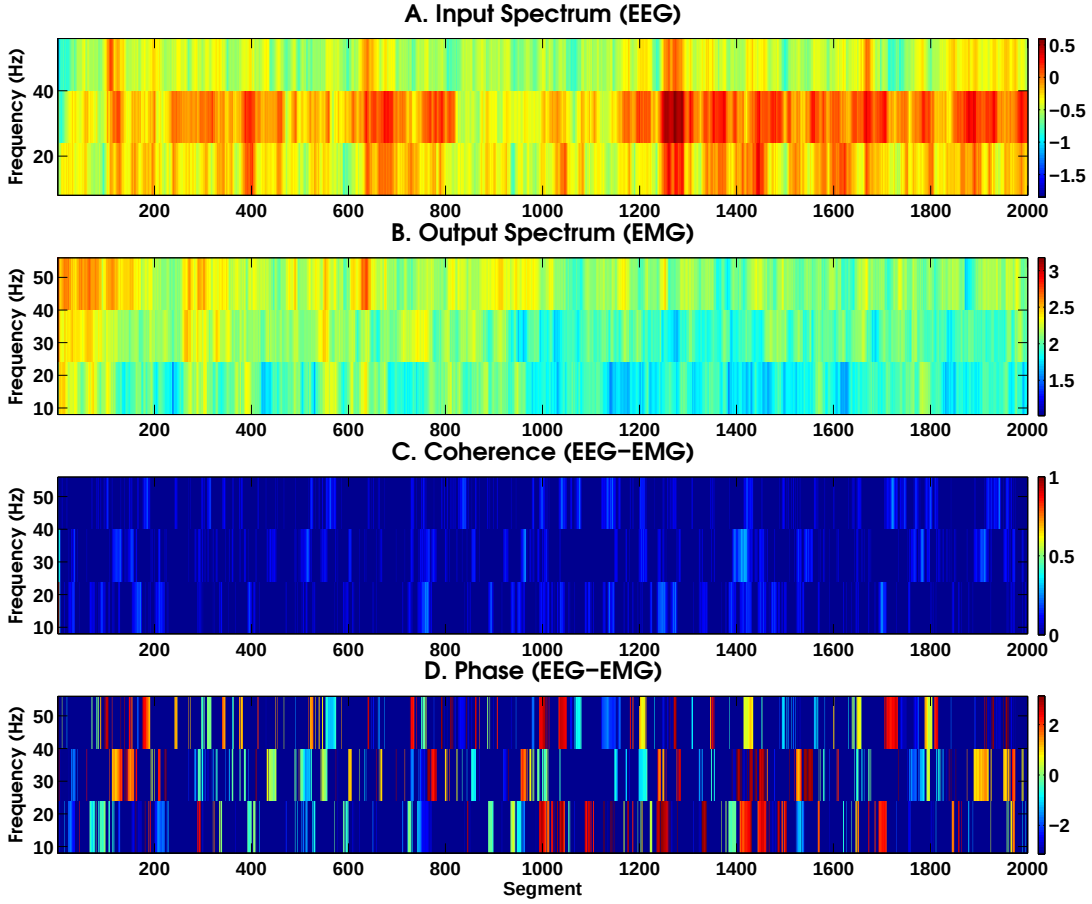


FIGURE 1.20: Panels A-D. show 2-dimensional plots of OST analysis of left motor cortex EEG (input) and right-hand EMG (output) data for a representative data set using the OST method [37]. Time is shown on the $x$-axis and frequency is shown on the $y$-axis. While the temporal axis is divided into segments of 0.0625 seconds, the spectral axis is divided into bands of 16 Hz in width spanning 1-15, 16-31 and 32-47 Hz. A. The periodogram for the EEG time series corresponding to the selected subject. B. The periodogram of the EMG time series corresponding to the same subject. C. The time-varying coherence of EEG and EMG. D. The phase spectrum.

$$\gamma(s,\tau) = \int x(t)\Psi^*_{s,\tau}(t)dt$$

A wavelet is defined as:

$$\Psi_{s,\tau}(t) = \frac{1}{\sqrt{s}}\Psi\left(\frac{t-\tau}{s}\right)$$

where parameters $s$ and $\tau$ can be used to scale and shift the wavelet and $*$ indicated the complex conjugate [215]. The function $\Psi(t)$ is called the mother wavelet, and can be a number of different functions. The mother wavelet must satisfy some

basic properties. Its integral across time must be zero, the integral of its square must equal 1 and it must also possess a property called 'admissibility', which allows the original signal to be constructed from its wavelet transform [215]. A number of standard forms exist for $\Psi(t)$. In continuous space, these include the Morlet wavelet, the Haar wavelet and the Daubechies wavelet.

Wavelet coherence is obtained using a technique similar to classical, or Fourier, coherence (see Section 1.10), but the integrals in Equations 1.8 and 1.9 are performed using a mother wavelet instead.

In wavelet-based measures, because the mother wavelet can be re-scaled, the windowing is not regular as in Fourier based methods (see Figure 1.19), so that high frequencies are represented with a greater temporal resolution. A general review of wavelet methods can be found in [215, 307].

The practical application of wavelet coherence to continuous neural signals was developed by Jean-Philippe Lachaux [172]. An example of the result of applying wavelet coherence is shown in Figure 1.21.

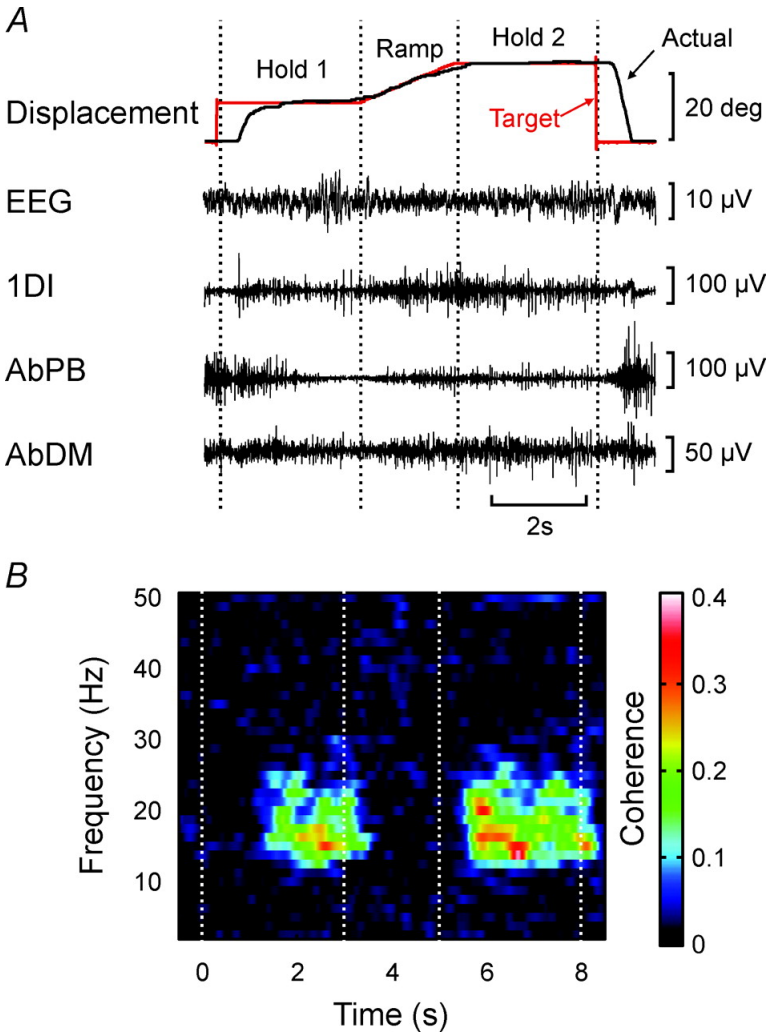


FIGURE 1.21: An example of wavelet coherence for human data. A. raw traces from one subject of EEG. Top trace shows both the target position (red) and the actual lever position (black) during a precision grip task. Other traces show EEG and the EMG signals from three intrinsic hand muscles. Dotted lines indicate two hold periods. B, time-resolved corticomuscular coherence plot for subject in A. Dotted lines indicate two hold periods. Increased EEG-EMG coherence can be seen during the precision grip tasks at $\approx$ 20 Hz. Taken from [302].

Wavelet transforms have been extensively used to quantify coherence between neurophysiological time series [38, 148, 159, 210, 216, 235, 245, 302].

### 1.1.6 Instantaneous signal processing techniques

Although windowed measures provide some information about the time-varying properties of a signal, they nevertheless require the signal to be segmented. There is a further class of metrics for deriving the properties of time series, which does

not require segmentation. These are called instantaneous measures and they can be used to obtain a measure of synchronisation called the phase difference. [5]

The phase difference quantifies the difference between the positions of two time series in their cycles, known as their phases. Intuitively, if the peaks and troughs of two time series are exactly aligned then they are 'synchronised' and 'in phase', and their phase difference will be exactly zero. If the peaks of one time series are precisely aligned with the troughs of another, then the time series are still considered to be synchronised because their phase difference will not change, however they are now 'out of phase' (see bottom panel in Figure 1.22 from the work of Pascal Fries). Typically, neurophysiological time series will not have a constant value of phase difference for very long, but one that varies, as discussed. Phase relationships between neurophysiological time series are an important mechanism for communication in the nervous system [89, 90].

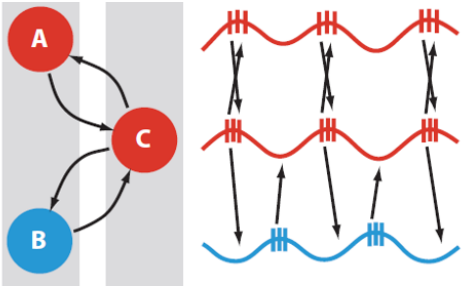


FIGURE 1.22: A schematic diagram of two signals that are synchronised in phase (red) and signals that are synchronised and out of phase (red and blue). The signals in this figure represent neurophysiological signals, which are recorded from brain regions, or 'oscillators' shown as circles on the left of the figure. Illustration taken from [90].

Prior to defining an instantaneous phase difference, it is necessary to define an instantaneous phase. One method of deriving the instantaneous phase of a time series $x(t)$ involves creating an associated complex signal called an analytic signal $x_a(t)$. This provides a means of calculating an instantaneous phase because any complex number $z$ is defined to have a phase and an amplitude (see Section 1.1.6.1). If the analytic signal $x_a(t)$ can be defined uniquely for a signal $x(t)$, then it can be used to produce a unique and instantaneous value of phase for $x(t)$.

The analytic signal $x_a(t)$ is created through the application of the Hilbert transform. An array of alternative techniques exist for calculation of instantaneous phase properties [30, 31, 99, 101, 104, 130, 153, 166, 176, 209]. However, it has been demonstrated that results obtained from the Hilbert transform and other methods are comparable, and in particular, in the analysis of neural synchrony

[5] The term phase synchrony incorporates all phase relationships including synchronous ones.

[235]. An additional reason for using the analytic signal and the Hilbert transform is that it is straightforward to apply to any time series.

The use of $x_a(t)$ also provides a means of calculating the amplitude envelope of a signal, which is also an instantaneous measure, which quantifies how the amplitude peaks of the signal evolve over time. Visually, the amplitude envelope is obtained by tracing a line between each of the peaks of the time series to form a convex hull [154]. In a single neurophysiological time series, the amplitude envelope is a smooth signal which smooths the very rapid oscillations. The amplitude envelope of the bandpass filter of an example EEG time series is shown in Figure 1.23. [6]

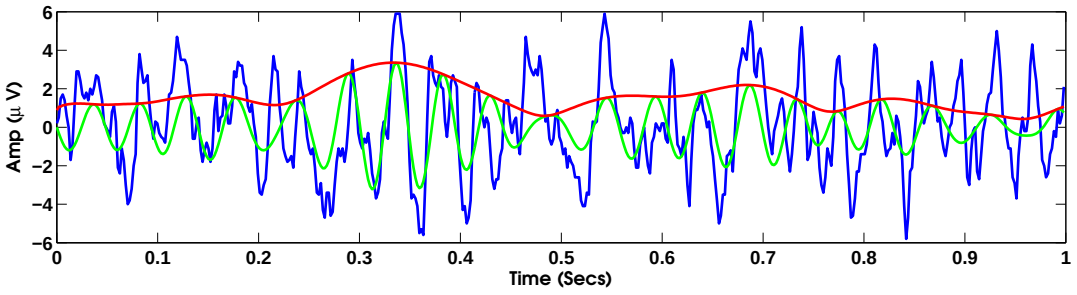


FIGURE 1.23: An extract of an EEG signal of length 1 second (blue), also showing the same signal bandpass filtered between 16 and 24 Hz (green). The amplitude envelope of the bandpass filtered time series is shown in red.

One further useful measure can be derived from the analytic signal, and this is the instantaneous frequency. The frequency, or speed of oscillation in neurophysiological time series will typically vary in time and this can be calculated as the instantaneous frequency.

#### 1.1.6.1 Obtaining the phase and amplitude of a complex number

Any complex number $z$ can be written as $z = a + ib$ where $i$ is the imaginary unit $i = \sqrt{-1}$ (see Figure 1.24). It can also equivalently be written as $z = Ae^{i\phi}$ where $A$ is the amplitude of $z$ and $\phi$ is the phase. These quantities can be visualised as in Figure 1.24.

[6] The amplitude envelope always takes positive values, which is a useful property in case we need to take logarithms of a signal, but this is not immediately relevant here.

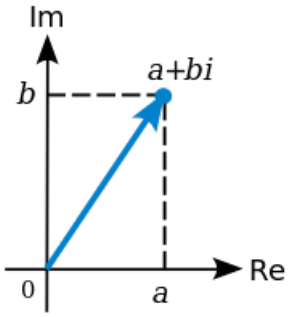


FIGURE 1.24: A complex number $z$ can be written as $z = a + ib$. This number can be visualised on two axes representing the real (Re) and imaginary (Im) parts of $z$ where $a$ is real and therefore on the $x$-axis, and $b$ is imaginary and therefore on the $y$-axis. The amplitude $A$ of $z$ is the length of the blue line from the origin to the point ($a$,$b$). The phase $\phi$ is the angle between the $x$-axis and the blue line. Taken from http://en.wikipedia.org/wiki/File:Complex_number_illustration.svg. Viewed on 4th March 2014.

The amplitude $A$ can be recovered from the values of $a$ and $b$ by $A = \sqrt{a^2 + b^2}$ and the phase $\phi = \tan^{-1}\frac{b}{a}$.

#### 1.1.6.2 The analytic signal

The analytic signal $x_a(t)$ for any signal $x(t)$ is a unique time series of complex values. For each of these complex values, the amplitude and phase may be computed, and two time series can be constructed from these values - that of the amplitude envelope and the instantaneous phase of signal $x(t)$.

The analytic signal was first defined by Gabor and Ville [94, 285]. It can be created as a result of the observation that the Fourier transform of $x(t)$ is symmetric about the origin, so that the negative frequency components of a signal are redundant (see Section 1.1.4.1). These negative frequencies can be discarded by combining the Fourier transform $X(f)$ with a Heaviside step function $u(f)$, which has value 1 for all $f > 0$ and a value of 0 for all $f < 0$ by definition. This is done with the following multiplication:

$$X_a(f) = X(f) \cdot 2u(f) \tag{1.11}$$

$X_a(f)$ therefore only takes non-zero values for $f > 0$. The advantage of this formulation is that this new Fourier transform does not lose any information from the original signal, but performing an inverse Fourier transform and returning to the temporal domain now yields a unique complex time series for any $x(t)$, defined as $x_a(t)$:

$$x_a(t) = \mathcal{F}^{-1}\left\{X_a(f)\right\} \tag{1.12}$$
$$= \mathcal{F}^{-1}\left\{X(f) \cdot 2u(f)\right\} \tag{1.13}$$
$$= \mathcal{F}^{-1}\left\{X(f)\right\} * \mathcal{F}^{-1}\left\{2u(f)\right\} \tag{1.14}$$

where the final line follows as a standard rule of Fourier transforms and the symbol $*$ indicates a convolution. Therefore, the analytic signal is given by:

$$x_a(t) = x(t) + i\left[x(t) * \frac{1}{\pi t}\right] \tag{1.15}$$

The function $x(t) * \frac{1}{\pi t}$ can therefore be written as $\int_{-\infty}^{\infty} s(\tau)\frac{1}{\pi(t-\tau)}d\tau$, which is the Hilbert transform.

#### 1.1.6.3 The Hilbert transform

The Hilbert transform $\mathcal{H}(s(t))$ of a signal $x(t)$ is defined as:

$$\mathcal{H}(x(t)) = \text{p.v.} \int_{-\infty}^{\infty} x(\tau)\frac{1}{\pi(t-\tau)}d\tau \tag{1.16}$$

where the term p.v. indicates that the Cauchy principal value is taken. The Cauchy principal value is a way of defining the integral uniquely. This is necessary because $\frac{1}{\pi t}$ is not integrable (it is indefinite), and therefore the integrals defining the convolution do not converge. The use of a Cauchy principal value allows for a value to be assigned to such an integral.

The formal formulae for the amplitude envelope, instantaneous phase and instantaneous frequency will now be given using these definitions.

#### 1.1.6.4 Amplitude envelope

The amplitude envelope $A(t)$ of a signal $x(t)$ is given by $A(t) = \sqrt{x(t)^2 + \mathcal{H}(x(t))^2}$.

#### 1.1.6.5 Instantaneous phase

The instantaneous phase $\phi(t)$ of a signal $x(t)$ evolves by a value of $2\pi$ upon the completion of a cycle. It increases in proportion to the fraction of an oscillation that the signal completes. The instantaneous phase is found by:

$$\phi(t) = \tan^{-1}\left(\frac{\mathcal{H}(s(t))}{s(t)}\right) \tag{1.17}$$

When a new cycle begins, the phase drops back to its starting value, so that the phase looks similar to a sawtooth, such as that shown in Figure 1.25. In Figure 1.25 the phase evolves between $-\pi$ and $\pi$, but the phase can equally be visualised as an evolution between any two values with a separation of $2\pi$.

The most common range for the phase is $[-\pi, \pi]$, but it also often defined to be $\in [0, 2\pi]$.

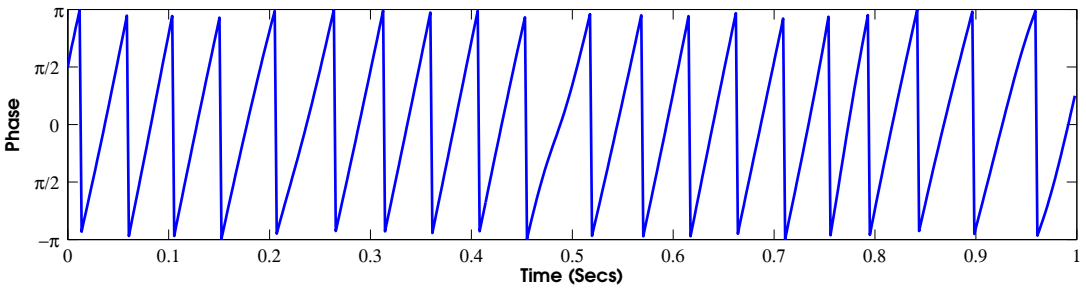


FIGURE 1.25: The phase of the Hilbert transform for a short extract of the band-pass filtered EEG signal for a single example subject.

#### 1.1.6.6 Instantaneous phase difference as a measure for synchronisation

The difference between the phases of two distinct signals provides a measure of the relationship between them. As seen in Figure 1.25, the phase of a signal is a sawtooth function. If we simply subtract one such time series from another, we will obtain errors near the point at which the jump occurs. In a situation where one signal has phase just below $2\pi$ and the other has a phase just above zero, they have a very small phase difference as they will be close to each other in their positions on a cycle. However, their phase difference as taken from a straightforward difference of the two sawtooth functions will be large, equalling almost $2\pi$. To rectify this, it is necessary to 'unwrap' each phase so that the jumps in the sawtooth receive an addition of $2\pi$, making the phase into a continuous function [85–87]. This is demonstrated for an example signal in Figure 1.26.

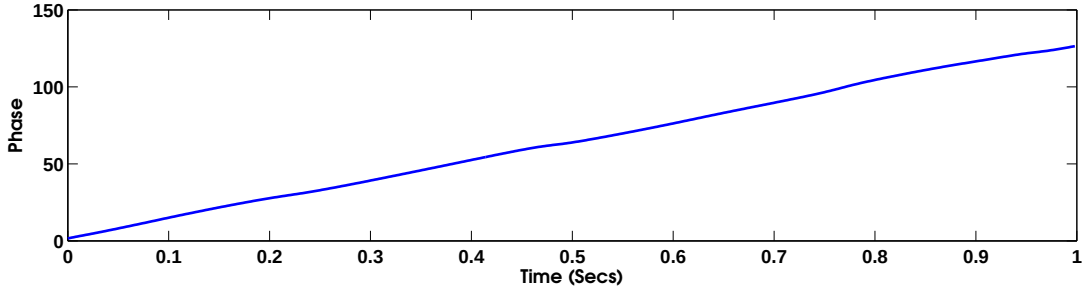


FIGURE 1.26: The unwrapped phase of the Hilbert transform for a band-pass filtered EEG signal for a single example subject.

Equivalently, the phase difference can be calculated using a measure formulated in [228], which avoids the need to unwrap. For two phases $\phi_1(t)$ and $\phi_2(t)$ of signals $x_1(t)$ and $x_2(t)$, which have Hilbert transforms $\mathcal{H}(x_1(t))$ and $\mathcal{H}(x_2(t))$, $\phi_1(t) - \phi_2(t)$ is defined as:

$$\phi_1(t) - \phi_2(t) = \tan^{-1}\left(\frac{\mathcal{H}(s_1(t))s_2(t) - s_1(t)\mathcal{H}(s_2(t))}{s_1(t)s_2(t) + \mathcal{H}(s_1(t))\mathcal{H}(s_2(t))}\right) \tag{1.18}$$

Figure 1.27 shows an example of the instantaneous phase difference between two EEG signals.

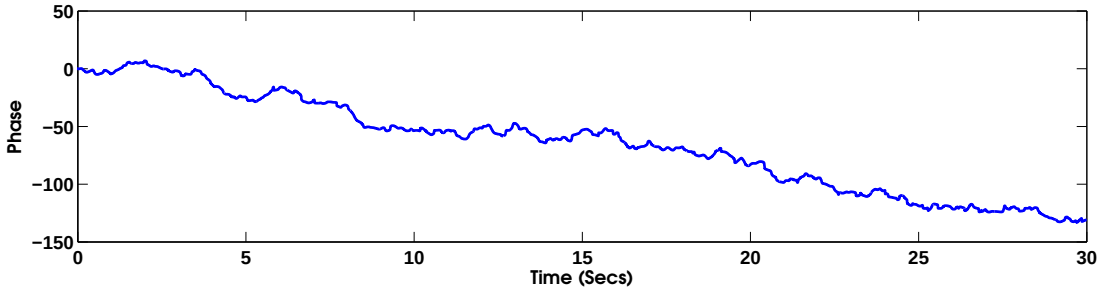


FIGURE 1.27: The difference between the unwrapped phases of two band-pass filtered EEG signals for a single example subject.

#### 1.1.6.7 Instantaneous frequency

The definitions of the phase $\phi(t)$ and the instantaneous frequency $f(t)$ of a signal are closely connected. The position of an oscillator in its cycle will be the integral of the oscillatory speed at which it has travelled over a time period. The phase is therefore the integral of the frequency:

$$\phi(t) = 2\pi \int_0^t f(t)dt \tag{1.19}$$

Conversely, frequency is the rate of change of the phase [29]:

$$f(t) = \frac{1}{2\pi}\frac{d\phi(t)}{dt} \tag{1.20}$$

The instantaneous frequency for an example of a signal is shown in Figure 1.28. In this figure, it is possible to observe some of the typical characteristics of such a time series. The instantaneous frequency remains close to zero indicating that the speed of the underlying oscillators remains close to a constant on average.

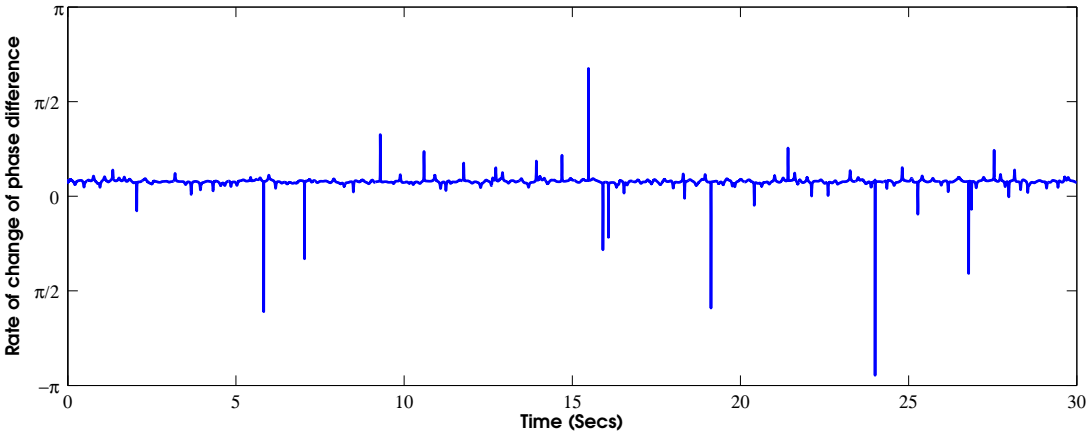


FIGURE 1.28: The time derivative of the unwrapped phase of a band-pass filtered EEG signal. This is also called the instantaneous frequency.

Most deviations from the mean are typically smooth, as seen in an enlarged example of the time series in Figure 1.29. They represent the periods during which the oscillator is attracted away from its natural cycle by its interaction with other oscillators either to slow down (below the zero line) or speed up (above the zero line). The smoothness of these transitions indicates that they are not artefacts of the Hilbert transform or other signal processing steps, as such effects would produce jagged discontinuities (see Figure 1.32).

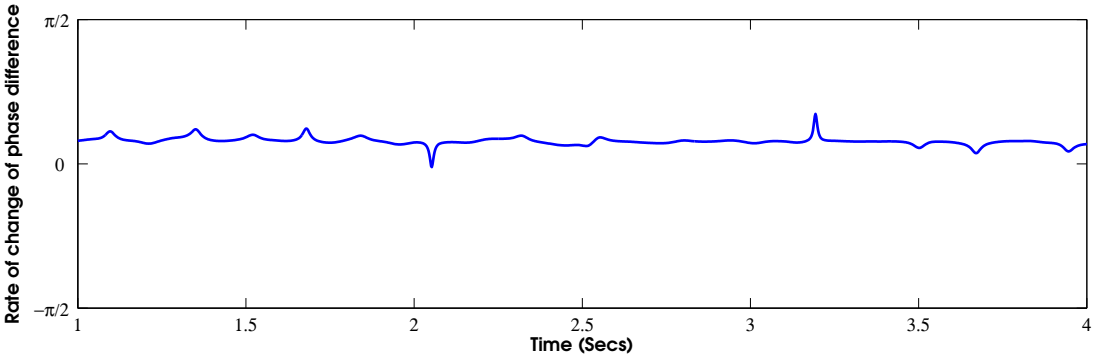


FIGURE 1.29: The time derivative of the unwrapped phase of a band-pass filtered EEG signal. This is also called the instantaneous frequency.

Further to Figures 1.28 and 1.29, some specific features of the instantaneous frequency time series are highlighted in Figure 1.30. In this figure, it is possible to observe the sharper 'spikes' evident in the instantaneous frequency which correspond to a more sudden and larger shift in speed with which an oscillator adjusts its progress. However, even such large jumps are not completely instantaneous (there is an increase in frequency just prior to the jump), and therefore are unlikely to be artefactual.

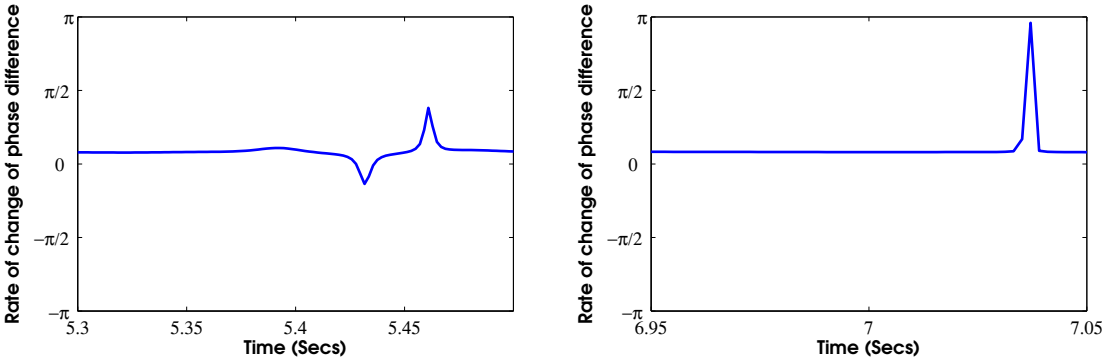


FIGURE 1.30: The time derivative of the unwrapped phase of a band-pass filtered EEG signal. This is also called the instantaneous frequency.

In addition to the rate of change of phase of a single signal, which encodes its speed of traversing an oscillatory cycle, it is possible to calculate the rate of change of the phase difference between two distinct signals. This time series represents the instantaneous adjustment with which the underlying oscillators move towards (below the zero line) or away from (above the zero line) each other as a result of their interactions with each other and any other oscillators in the system. This quantity will be referred to again in Chapter 6 and discussed in greater detail.

It is sometimes convenient to describe the cycle of a signal in terms of its angular frequency, commonly denoted by $\omega$. The angular frequency is a measure of rotation

rate, and can be related to frequency by $\omega = 2\pi f$.

#### 1.1.6.8 Broadband signals

In this section, some problems that may arise during calculation of amplitude and phase are discussed.

For time series with constant frequency, the amplitude envelope and time-varying phase components are straightforward to find and interpret [29, 146]. If we consider a pure sine wave, then its frequency is a constant value because this function always returns to its zero point upon completion of a cycle, and its speed of oscillation is straightforward to calculate. The amplitude envelope consists of a horizontal line at 1. However, for a signal with an uneven trend it is not always clear where different cycles begin or end [21]. This can cause difficulties in interpreting the results obtained from the Hilbert transform.

In order to demonstrate these difficulties, an example signal constructed multiplicatively from two simple cosine curves is used, with different but constant frequencies $f_1$ and $f_2$:

$$x(t) = \cos(2\pi f_1 t)\cos(2\pi f_2 t)$$

If we try to formulate the analytic signal for $x(t)$ and write it in the form $A(t)e^{i\phi(t)}$, it is intuitively unclear whether the signal has a phase dictated by $\cos(2\pi f_1 t)$ and an amplitude dictated by $\cos(2\pi f_2 t)$ or vice versa, or whether both phase and amplitude would be some combination of the two [29]. Indeed, the degree to which an instantaneous phase and amplitude can be meaningfully calculated from EEG, EMG and MEG signals has been richly discussed [29, 132, 208, 243, 277].

In practice, when the Hilbert transform is applied to such a signal, the higher of the two frequencies is dominant in determining the phase modulator [29]. This becomes more ambiguous when the two frequencies $f_1$ and $f_2$ are similar, and the power spectra of $\cos(2\pi f_1 t)$ and $\cos(2\pi f_2 t)$ overlap.

A straightforward way of ensuring that the phase of a signal is separable from the amplitude, is therefore to restrict it to a narrow band of frequencies [29]. This is typically achieved by band-pass filtering the signal before applying the Hilbert transform (see Section 1.1.4.4).

A bandpass filter of very narrow range, however, can also cause problems for Hilbert transform application. In particular, restricting the signal to a band in which there is no intrinsic activity in the signal may lead to spurious phase or

amplitude components, that arise simply through the interactions of other underlying processes, at unrelated phases and amplitudes [49]. For instance, an example signal will be considered:

$$x(t) = \sin(2\pi f_1 t) + \sin(2\pi f_2 t)$$

By trigonometric transformation, the signal may be written as

$$x(t) = 2\cos\left(\frac{2\pi t}{2}(f_1 - f_2)\right)\sin\left(\frac{2\pi t}{2}(f_1 + f_2)\right)$$

If we assume that $f_2 > f_1$, but that the difference between $f_2$ and $f_1$ is very small so that $f_2 = f_1 + \delta$ and $e \ll f_1, f_2$. Then it is possible to approximate

$$x(t) \approx 2\cos\left(\frac{2\pi t}{2}(\delta)\right)\sin\left(2\pi t(f_1)\right)$$

An inspection of the power spectrum of such a signal, shows that there will be a strong frequency component evident at a value of $\frac{\delta}{2}$ Hz (Figure 1.31).

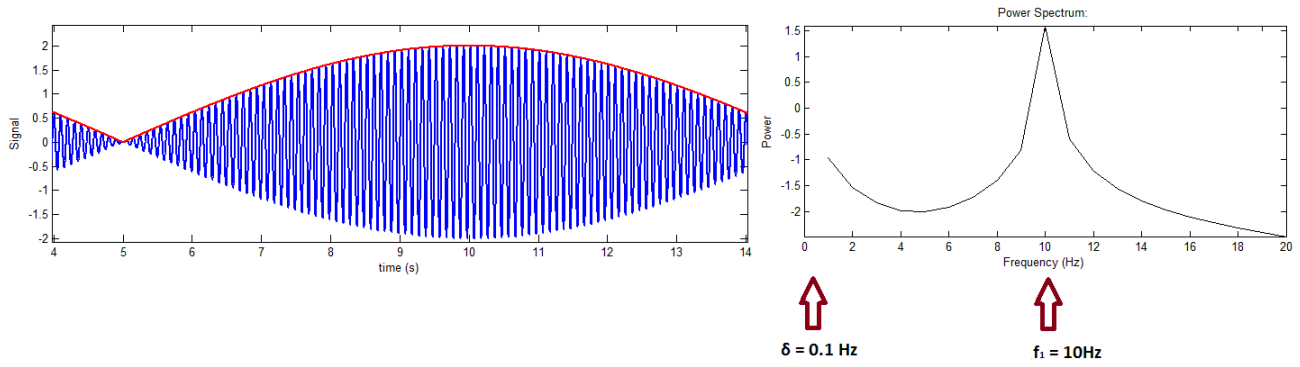


FIGURE 1.31: A plot of the signal $x(t) = \sin(2\pi f_1 t) + \sin(2\pi f_2 t)$ as given in the example mentioned is in blue. The red line indicates its amplitude envelope. The frequency $f_1 = 10$Hz and $f_2 = 10.1$ Hz. The plot on the right is the power spectrum of the signal, with a component at 10Hz and also one at low frequencies near 0.1Hz.

It has proved useful to link the bandpass filtering limits to the power spectra of data [160]. However, as demonstrated by Figure 1.31, it is also important to understand the processes that might be governing a broadband physiological signal before bandpass filtering.

**Edge effects of the Hilbert transform** Another known limitation of the Hilbert transform is that it may give rise to artefacts at the start and end of instantaneous

phase or amplitude recovered from a signal (see Figure 1.32).

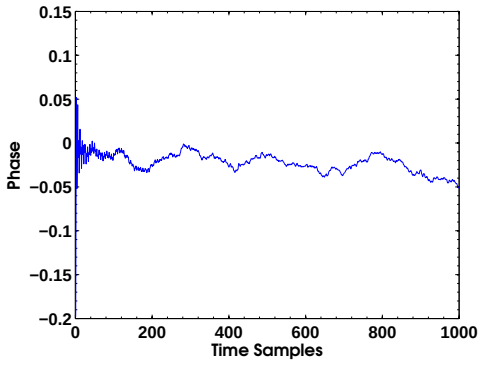


FIGURE 1.32: A plot of the phase of a time series recovered by the Hilbert transform. The first 200-300 time samples show artefacts.

These effects are typically corrected by inspecting the results obtained from the Hilbert transform and cutting the segments of data where artefacts are observed. This is done in this thesis.

In the next section a property of systems, known as criticality will be discussed, the characteristics of which may be advantageous to the human nervous system, and have been discussed in relation to the brain. The evidence for critical behaviour in the brain has been investigated by studying measures such as the amplitude envelope and phase, both of which have been described in this section.

### 1.1.7 Criticality

In the previous three sections, techniques that can be used to assess a variety of signal properties were introduced and discussed. These include measures of individual signals, such as the autocorrelation function, the power spectrum, the amplitude envelope and the instantaneous phase and frequency. They also include measures of synchronisation between two different time series such as the cross-correlation function, coherence, wavelet coherence, OST coherence and phase difference. Each of these techniques can be and has been applied to neurophysiological time series. We may next ask what values or characteristics we might expect these measures to show when applied to time series recorded from the brain.

One hypothesis that has recently generated much academic enthusiasm in neuroscience is that of the brain as a critical system [24, 55, 258, 260, 297]. The discussions in this field revolve mostly around the brain in particular, but in fact, many ideas can be applied to the nervous system as a whole. In this section, two systems will therefore be referred to interchangeably.

The term 'criticality' originated in physics to describe a system that is undergoing an abrupt change in its dynamics. One example of such a change occurs in the transition of materials from a liquid or a gas to a supercritical fluid.[7] Another example of such a change occurs when a non-magnetic material becomes magnetic. An abrupt change occurs in these system when some parameter of the system is modified so that it is above a certain threshold value. In the example of a supercritical fluid, such a change occurs at the 'critical point', which is caused by a change in the pressure or temperature of the system. Magnetism in a ferromagnetic material occurs when the energy (heat) of its constituent elements is reduced below the Curie point.

Measurements made from a these physical systems possess a common characteristic, which is the presence of power laws statistics at the critical point. A power law is a functional form, which will be defined mathematically in Section 1.1.7.1. Power laws are observed in the frequency distributions or in the scaling properties of metrics derived from these two systems at or near their critical point. This is a property belonging to one class of critical systems. The emergence of power laws will be discussed in Sections 1.1.7.2 and 1.1.7.3 for a supercritical fluid and in a model of ferromagnetism called the Ising model, which are two classical examples of criticality.

The link between systems at criticality and the human nervous system has been described as the 'critical brain hypothesis'. It has been argued that the nervous system displays properties consistent with a critical system, and that because there is no known external force that tunes the development of the nervous system, it must be in a state of self-organised criticality (SOC) in particular. In Section 1.1.7.4 the evidence for criticality in natural phenomena in general, and in the brain specifically will be discussed, and the arguments behind its self-organisation will be given.

#### 1.1.7.1 Power laws

A power law is a function between variables $y$ and $x$ defined by:

$$y(x) = Cx^{-\alpha} \tag{1.21}$$

where $C > 0$ and $\alpha \in (0, 1)$ are both constants.

Power law functions show scale invariance [59]. This means that if $x$ is altered to some multiple of $x$, say $Ax$, the corresponding value of $y$ will also be some multiple

[7] We shall see in Section 1.1.7.2 that this transition is not the same as a phase transition between a solid and liquid or a liquid and gas, which we tend to be more familiar with.

of $y$:

$$y(Ax) = C(Ax)^{-\alpha} \tag{1.22}$$
$$= CA^{-\alpha}x^{-\alpha} \tag{1.23}$$
$$= Dx^{-\alpha} \tag{1.24}$$

where $D$ is just another constant parameter. This property becomes especially interesting when it is seen in a frequency distribution, such that $y$ represents the frequency with which an event of size $x$ occurs. Scale invariance would mean that both 'small' and 'large' events have a finite probability of occurring [145] . For example, if we suppose that $x$ represents the amount of rainfall in a given day, then a power law distribution of $x$ would mean that without a change in the physics of the system, rarer 'large' events such as powerful storms can still occur amongst the much more frequent 'small' events of drizzle. Indeed, this is what observe in nature.

This contrasts with an exponential function $y(x) = Ce^{\alpha x}$, in which if $x$ is increased by a few orders of magnitude, the corresponding $y$ value quickly becomes so small as to be almost zero. If a frequency distribution has an exponential form then the probability of 'large' events happening would be infinitesimal.

#### 1.1.7.2 Supercritical fluids

One physical example of a critical phase transition is seen when a supercritical fluid is created. This occurs at the critical point (see Figure 1.33).

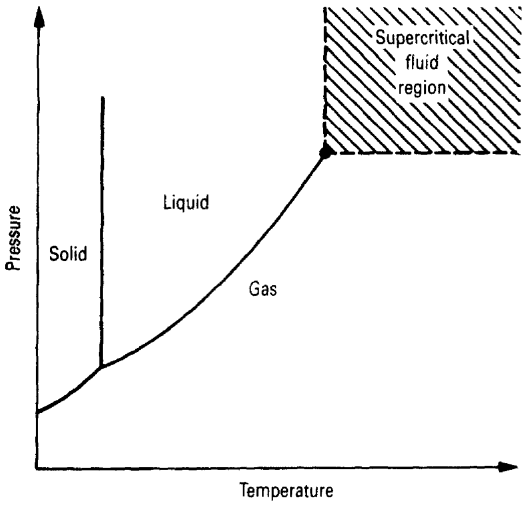


FIGURE 1.33: A schematic diagram which shows the phase transitions of a material as its temperature and pressure are altered. First order phase transitions between solid and liquid or liquid and gas are shown by lines. A supercritical fluid is created when the temperature of a liquid or the pressure of a gas is increased beyond a certain critical point. At this point, the heat capacity and viscocity of the material are predicted to have power law statistics [73]. A supercritical fluid has properties of both liquids and gases. Image taken from http://www.webapps.cee.vt.edu/ewr/environmental/teach/smprimer/sfc/sfc.html. Viewed on 4th March 2014.

This phase transition is different from a regular phase transition from solid to liquid and from liquid to gas because it is a second order phase transition. It is defined by a discontinuity in the second derivative of free energy, while the first derivative of the free energy remains continuous as a parameter (temperature or pressure in this case) is adjusted. An ordinary phase transition is a first order transition in which the first derivative of the phase transition, which is the density, is discontinuous.

In supercritical fluids, it is not possible to distinguish gas from liquid. Supercritical fluids are able to transfer thermal energy effectively (they have high diffusivity). The heat capacity and viscosity of supercritical fluids are predicted to be characterised by power laws [73].

#### 1.1.7.3 The Ising Model

The Ising model is a model of magnetism in two dimensions, which has been discussed extensively in the statistical mechanics literature. Some of the more recent examples include [11, 22, 95, 131]. It describes the dynamics of a collection of particles on a metal, each of which has a spin $s_i$ taking the time-varying value $+1$ (spin up) or $-1$ (spin down), which depends on the total energy of the system, and on the spins of its neighbouring elements. When the spins of the metal align,

the particles represent a magnetic state. In 1944, the solution to the Ising model in two dimensions was published [207]. More recently, the Ising model has been used to model a 2-dimensional network of connected and interacting neurons where the two different spin values are used to encode the fact that neurons are in the binary state of either firing or not firing [127, 158].

In two dimensions, the model is implemented on a lattice of elements with a temperature parameter $T$ that controls the collective magnetisation [207]. The collection of values making up their individual spins is referred to as a configuration $s$ with no index to indicate that it incorporates all the spins in the lattice. The energy of the system in a given configuration $s$, and with no external magnetic field, is determined by the Hamiltonian:

$$H(s) = -J\Sigma_{i,j=nn(i)}^{N} s_i s_j$$

where $J$ is a coupling constant and $j$ is an index for the four elements that are nearest neighbours $nn$ of each element $i$ of the square grid (Figure 1.34). The negative sign is included by convention, and encodes the fact that a lattice containing many neighbours with non-identical spins will have a high energy. The average energy of the system is then given by $E =< H >$ where the symbol <> indicates the expectation value.

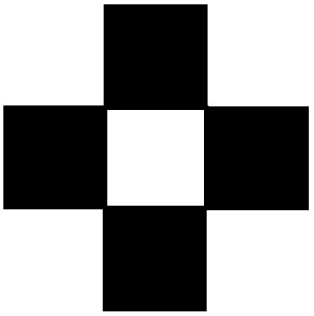

FIGURE 1.34: A schematic illustration of the 2-D nearest neighbours of the square (white) in the middle. For a 2-dimensional lattice, any square will have 4 nearest neightbours (black).

The probability of a given configuration occurring in a system is given by the Bolzmann distribution and is proportional to

$$\mathcal{P} = e^{-H(s)/kT}$$

where $T$ is the temperature parameter and $k$ is Boltzmann's constant. The probability is proportional to and not equal to $\mathcal{P}$ because it does not have a normalisation factor. $\mathcal{P}$ should be normalised with a division by the partition function $\sum_s e^{-E/kT}$, which is the sum across all possible configurations $s$.

The system will switch into a new configuration if the probability associated with this configuration is higher than or equal to that of the configuration that the system is currently in.[8]

If, for example, all the spins were identically equal to $+1$ or $-1$, then the Hamiltonian $H$ would be $H = -4JN$, meaning that the probability $\mathcal{P} \propto e^{4JN/kT}$ . If the lattice consisted of a chessboard of $+1$ and $-1$ spins, then $H = 4JN$ and $\mathcal{P} \propto e^{-4JN/kT}$. Although not normalised across configurations, these probabilities are nevertheless informative and are shown for varying temperature $T$ for these two spin configurations in Figures 1.35 and 1.36. The constants $k$ and $J$ are taken to be equal to 1 without loss of generality, and a sample lattice of size $N = 4 \times 4 = 16$ is used. It can be observed that at small temperatures the lattice of equal spins is by far the favourable state of the system as compared to the chessboard lattice 1.35. When the temperature is very high, the probabilities of the two states, and indeed any other states possible for the system become equal 1.36.

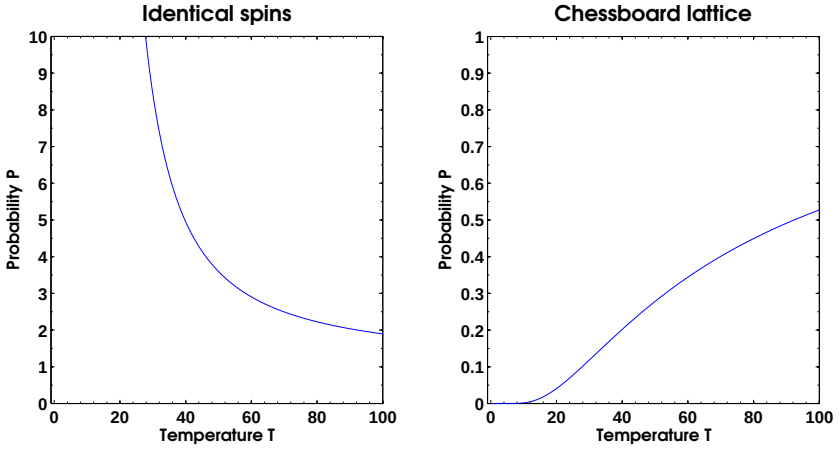


FIGURE 1.35: Plots of the unnormalised probability $\mathcal{P}$ of a lattice of identical spins and of a chessboard lattice (elements of the lattice alternate between being spin up and spin down) for different temprature values from 0 to 100. When the temprature is low, the lattice of identical spins has a much greater value of unnormalised probability associated with it, and it is more likely to occur. When temperature is $T = 100$, the unnormlised probability of the chessboard lattice increases, and that of the identical spins decreases.

[8] In practice the Ising model is evolved by selecting a configuration at random, checking whether it has a higher probability of occurring than the present one. If it does, then the system adapts the new configuration. If it doesn't then the old configuration is retained.

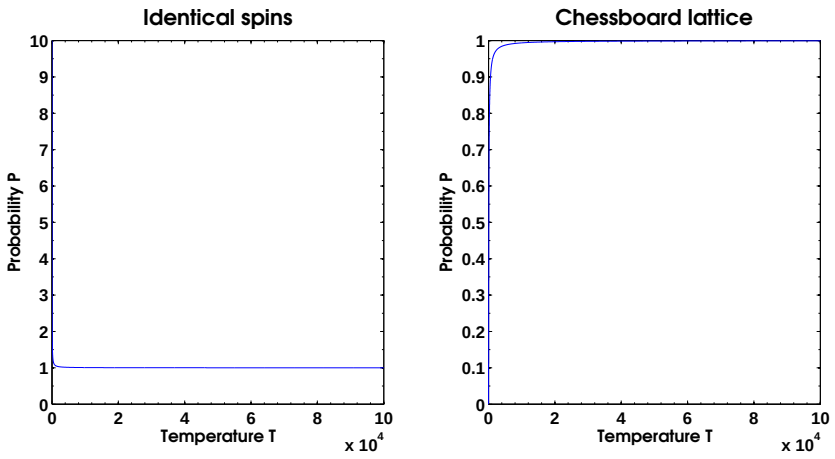


FIGURE 1.36: Plots of the probability $\mathcal{P}$ of a lattice of identical spins and of a chessboard lattice (elements of the lattice alternate between being spin up and spin down) for different temperature values from 0 to $10^5$. When the temprature is low, the lattice of identical spins has a much greater value of unnormalised probability associated with it, and it is more likely to occur. When temperature is $T = 10^5$, the unnormlised probability of the chessboard lattice, that of the identical spins, and indeed that of any other configuration (not shown) tend towards a single value, indicating that all configurations are equally likely to occur.

When the temperature is precisely zero, all the spins must be the same because this is the only configuration in which the exponent in the probability $\mathcal{P} \propto e^{-H(s)/kT}$ is positive and thus where $\mathcal{P}$ is non-zero. If temperature is increased slightly, then the grid will consist of large clusters of the same spin value and a new configuration of spins will only be adopted at the border between two clusters. The dynamics of the grid in this situation resemble a slow-moving lava lamp. This situation is shown in the Figure 1.37A, where spins of $+1$ and $-1$ are represented by black and white square respectively. Most elements in this situation are influenced only by the elements around them, and there is no evident interaction between the middle of one cluster and the middle of another, for example. This lattice represents a magnetic metal because the spins are largely aligned.

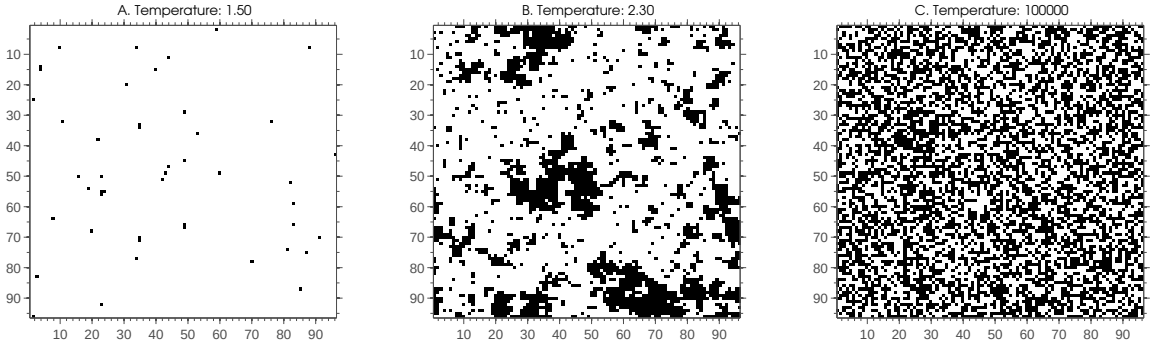


FIGURE 1.37: The Ising model lattice at a single time point once steady state has been reached for 3 different temperature parameter values. Panel A. shows the Ising mode at a cold temperature of 1.5. Almost all the spins are aligned, which is indicated by the fact that they are the same colour - white in this case. The black points in this panel indicate individual elements, or small clusters that differ in their spin value. The appearance of the panel changes very little with time. Panel C shows the Ising lattice at a high temperature of $T = 10^5$. The spins form a more or less random pattern across the lattice. Panel B is near critical temperature, $T = 2.3$. The lattice contains clusters of spins that are both small and large. Note that these images are temporal snapshots of the Ising model lattice. They are best apreciated when viewed as a time-varying video.

When the temperature parameter is extremely high, on the other hand, (Figure 1.37C), the spins in the lattice change rapidly because there is a lot of energy in the system and each element is less influenced by its neighbours. In this case, when spins are colour-coded in black and white, the grid looks similar to a malfunctioning TV screen. The lattice represents a metal that is not magnetic at high temperature $T$.

At an intermediate value of the temperature $T$ the transition between a non-magnetic and a magnetic material occurs [131]. As in the example of a supercritical fluid, this type of transition is a second order phase transition, as there is a discontinuity in the second derivative of the free energy $F$ in the system. The free energy $F$ in the Ising model is defined using the equation $e^{-F/kT} = \sum_s e^{-H(s)/kT}$. The order parameter is defined as the first derivative of the free energy. [9]

This transition is known as the critical point, and occurs at the critical temperature $T_c$. The value of $T_c$ can be found analytically for an infinite system, and is given by the solution to the equation [207]:

$$\sinh\left(\frac{2J}{kT_c}\right) = 1$$

Its numerical value is $T_c = 2.269$ when constants $k$ and $J$ are taken to be equal to 1, which is done from this point throughout this thesis.

[9] At this point, we recall the critical bifurcation of the Kuramoto model (Section 1.1.3.4). This also resembles a second-order phase transition [194] in which the order parameter ($r(t)$) leaves zero and grows continuously with coupling [75, 266]

At the critical temperature $T_c$, the range of cluster sizes present in the lattice increases vastly (Figure 1.37B for some idea of this). The larger clusters described for low $T$ become more fragmented and contain smaller clusters of their own, which in turn contain smaller clusters. The lattice contains clusters of a broad range of sizes, and the distribution of cluster sizes is such that there is no one characteristic size, but instead small and large clusters exist alongside each other. The distribution of large cluster sizes was shown to follow a power law [48].

A further consequence of the temperature being critical $T = T_c$ is that the spin values of elements in the system are influenced by other elements both a short and a long distance away from them. This implies that long-range correlations emerge at this temperature value, but these are spatial rather than temporal as in LRTCs. As a result correlations exist at arbitrarily large distances across the lattice. We can measure the correlation strength across a lattice using a quantity called the correlation length:

$$\xi =< s_i s_j > - < s_i >< s_j >$$

for each pair of sites $i$ and $j$. It can be shown that in the Ising model, this correlation length is given by:

$$\xi = \frac{-1}{\log(\tanh(\frac{k}{T}))}$$

If all the spins are identical in value, $\beta = \frac{k}{T} \to 0$ and $\xi \to 0$ exponentially because $T \to 0$. Similarly, when all the spins in the lattice are independent of each other, then the correlation length is equal to 0. At the critical temperature $T_c$, $\xi$ diverges and it has been shown that it does so with power law statistics:

$$\xi \propto (T - T_c)^{\alpha}$$

for some exponent $\alpha$ [66]. [10] The value of $\alpha$ tends to stay the same whether we approach the critical point from above or below, and often takes a similar value for different physical systems, which makes it particularly intriguing potential marker of criticality.

[10] The correlation length diverges only at a second order phase transition, but not at a first order phase transition where the first derivative of the free energy shows a discontinuity. Other quantities derived from the Ising model also diverge in the form of a power law such as the specific heat $\frac{\partial^s f}{\partial \beta^2}$, where $f$ is the free energy per element and $\beta = \frac{1}{kT}$, and the magnetisation $M =< \sum_i s_i >$. However, these arise as a result of the divergence of correlation length.

#### 1.1.7.4 Self-organised criticality (SOC)

In the Ising model, the temperature should be adjusted to a specific critical parameter $T = T_c$ for the system to be at criticality. Similarly, a supercritical fluid can only be created when the temperature and pressure of a material is set to a specific combination of values. There is another class of systems that show criticality, which do not need to be adjusted by an external force to reach their critical state, but evolve to criticality on their own. In other words, these are dynamical systems which have a critical point as an attractor. Such systems are said to display 'self-organised criticality' (SOC) [14].

The theory of self-organised criticality first emerged in 1987 with a letter published by Per Bak and two post-doctoral researchers [14]. They demonstrated this theory through the behaviour of a simple cellular automaton model, which could be used to produce complex behaviour with characteristics of SOC. Specifically, it showed the emergence of a power law distribution in avalanche sizes, which emerged without external tuning, for a wide range of starting parameters. The authors of [14] suggested that such systems were a plausible source for the complexity observed in nature.

Bak describes SOC as a phenomenon belonging to systems that are not at equilibrium, but in a state of imbalance, so that they are ready to respond to incoming stimuli [13]. This notion may be applied to the behaviour of a number of natural systems, one example of which is the weather system [13]. Indeed, Bak attributes the occurrence of sudden catastrophes and large scale events such as earthquakes and hurricanes to the existence of SOC.

In his book, entitled 'How Nature Works', Bak explains SOC using the analogy of a sandpile (see Figure 1.38 for an illustration). Grains of sand are dropped onto a flat surface to form a pile of sand. At first, the pile grows in size and very little happens. As more grains are added, however, some of them will slide along the sides of the pile and create small avalanches, taking down a stream of sand in their wake. As more sand is added, the pile of sand becomes unstable, so that it is no longer possible to predict whether adding a single grain will cause a build-up of sand, a small shift, or a large landslide, which may take with it the whole of the existing pile. So that, although the element we are adding is exactly the same, namely a grain of sand, the effect of its addition can only be understood when the whole system is considered together [12].

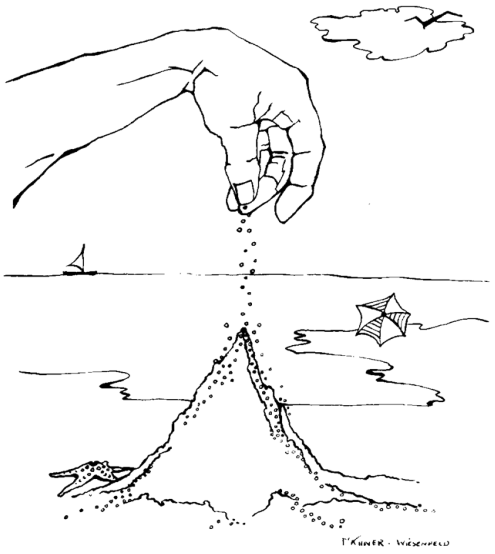

FIGURE 1.38: An illustration of a sandpile. Grains of sand that are dropped onto this pile can cause a range of different behaviours, which cannot be predicted by consiering the properties of individual grains of sand. Drawn by Ms. Elaine Wiesenfeld, taken from [13].

Intuitively, it may be natural to suppose that the brain displays critical behaviour. We know, for example, that the brain is capable of a wide range of behaviours, which involves large events (such as neuronal avalanches) and large scale oscillations (such as the sleep-wake cycle), as well as tiny bursts of activity (such as the firing of a single neuron). Such a dynamical range is also seen in the range of cluster sizes of the Ising model at its critical temperature. A broad dynamical range would also be a necessary condition for a well-functioning neuronal system, which should be able to communicate and benefit from information over a range of temporal and spatial scales [12, 51, 154, 250].

The organisational principles that cause the brain to show these behaviours are highly complex and not well understood. This is evidenced by the fact that the mechanism by which neurons work are fairly well known, and yet the interaction that allow thoughts and behaviour to arise from neurons is largely unexplained. This observation can also be made of the Ising model, in which the local rules by which neighbouring elements interact are simple, but globally, these interactions result in very complex patterns of correlation, which are complicated to describe.[11] Such properties are also seen in in Bak's cellular automaton model.

While the brain is in its resting state and disengaged from other activity, it must be ready to process and address any incoming stimuli efficiently. Such stimuli belong to the vast range of possible events in this universe so that a critical state should be associated with the ability to rapidly reconfigure in response to any one of these [254, 296]. If the brain was more ordered than a critical system, such as

[11] This can be evidenced for example by the near-impenetrability of the proof given in [66].

a cold Ising model, then its dynamics would be slow and correlations could not be transferred efficiently across the nervous system [13]. If, on the other hand the brain had a lot of energy such as the hot Ising model, the dynamics would be noisy, and the information transferred could not be organised [13].

Indeed, the advantages of criticality to the brain have been discussed extensively in neuroscience literature. Kitzbichler et al. [157, 158] argue that rapid state changes are crucial for the brain to deal with the environment it meets. They suggest that in some situations, an extensive cognitive effort is required and information transfer needs to be maximised between brain regions, and at other, relatively quiescent periods, the greater concern is minimising neuronal wiring costs [157]. A brain at criticality would allow the necessary rapid transitions in functional connectivity to occur quickly [126]. Werner [296] indicates that a neurophysiological system in a critical state is best able to learn and remember complex logical rules, by adapting its synaptic weights quickly. Meisel et al. [192] suggest that local events can spread rapidly through a system in such a state, and that remaining at criticality prevents the spread both from becoming uncontrollably large, and from dying away without effect. A single element hence has the ability to affect the entire system, which may be crucial to processing small external stimuli efficiently [54].

It has also been argued that network properties in the brain are crucial to producing critical behaviour [110, 259]. Studies have suggested that hubs and clusters are essential to producing critical synchronisation in neurophysiological systems [135]. Specifically, it has been argued that the brain at resting state shows evidence of criticality [50, 68, 109, 175, 267].

We do not know of any external force that tunes the organisational principles of the brain during its development. Indeed, different brains can develop in very different yet comparably efficient ways. This would imply a principle self-organisation based on interaction and complexity. However, the existence of the brain in a critical state is still an open question, and one which scientists still have the task of resolving [13].

#### 1.1.7.5 Summary

In this section, two examples of critical systems have been discussed, and in particular, a supercritical fluid, and the Ising model of ferromagnetism. A common characteristic of both of these systems was the presence of power laws, which were defined mathematically, and their properties as a power law frequency distribution were also given. The hypothesis that the nervous system may display self-organised criticality was considered. This relies on two points being true. The first is that

the brain does not have an external organising force, but that it organises itself. As far as we are aware, this statement is true. The second point is that the brain is critical. To date there is no known set of general characteristics that guarantee a system will display criticality [13]. Evidence for this has in large part relied on the observation of power laws in metrics and statistics in measures derived from the brain, or indeed the nervous system as a whole. However, while some classes of critical systems obey power law statistics, not all will show power laws [233]. Furthermore, a system that does show power laws is not necessarily critical [24]. The literature concerning criticality in the brain is substantial. A review of recent developments in the subject have been scheduled to appear in Frontiers in Neuroscience in April 2014, to which my supervisors Drs Simon Farmer and Luc Berthouze, and I will contribute.

This experimental and model evidence is considered in detail and some of the metrics which have been used to infer criticality of brain dynamics will be introduced and critiqued.

### 1.1.8 Power laws markers of criticality, long-range dependence and self-similarity

Notwithstanding the discussion above, the critical brain hypothesis is closely connected in academic literature with the identification of power laws in quantities derived from the brain. Several parallel lines of research have provided evidence of power law statistics in a number of measures calculated from the brain.

Power laws have been observed in distributions associated with neuronal avalanches, which are chains of neuronal firing that can be recorded by a network of electrodes above the cortex [23, 254]. Methods from statistical physics have been applied and spatio-temporal scaling functions were identified in fMRI [80, 229]. Furthermore, universal scaling functions such as those seen in the Ising model have been found in the activity of individual neurons [88, 240].

In time series analysis, evidence for the presence of criticality in the brain has emerged from the observation of power law statistics in the autocorrelation function. Specifically, the amplitude fluctuations of bandpass filtered EEG and MEG time series were found to have long-range temporal correlations (LRTCs) [178, 230]. The first study to do this was by the groups of Linkenkaer-Hansen who suggested that the presence of LRTCs contributed to the evidence for self-organised criticality in the brain and that LRTCs may be suggestive of a neural network that is capable of rapid reorganisation.

LRTCs are formally introduced in Section 1.1.8.2. They are defined by the presence of a power law decay in the auto-correlation function (see Equation 1.6). However, time series with long-range temporal correlations belong to a broader class of signals, which are said to possess long-range dependence (LRD) (Section 1.1.8.1). Rather than being specified by a power law decay, signals with LRD have an autocorrelation function with a decay that is slower than exponential (of which a power law is but one example).

The computational techniques that are used to assess the presence of LRTCs will be considered. In practice, it is not straightforward to determine the decay structure of an autocorrelation function. The most common method for assessing the presence of LRTCs is to estimate the Hurst exponent of a time series (see Section 1.1.8.3). The Hurst exponent was first calculated in 1951 by Harold Edwin Hurst, when he noticed that a time series he thought should be random had structure which he called long memory. In Section 1.1.8.3 the Hurst exponent is introduced. In section 1.1.8.4 it is shown that this can be found exactly for certain time series.

It was later proposed that the property of long memory was a manifestation of the related property of self-similarity [186]. This property is described in Section 1.1.8.5, and examples of objects and time series that possess this property are presented in Section 1.1.8.6. The presence of self-similarity can be assessed by a technique called detrended fluctuation analysis (DFA), which is introduced and the algorithm for which is described in Section 1.1.8.7. The advantages and weaknesses of DFA are discussed.

Finally, in Section 1.1.8.8 a model that may be manipulated to generate time series with known presence of LRTCs is introduced. This can be used to produce controllable results for DFA.

#### 1.1.8.1 Long-range dependence (LRD)

Long range dependence (LRD) in a time series is defined by an autocorrelation function that decays slowly. An example of the autocorrelation function for a signal with LRD is shown in Figure 1.39.

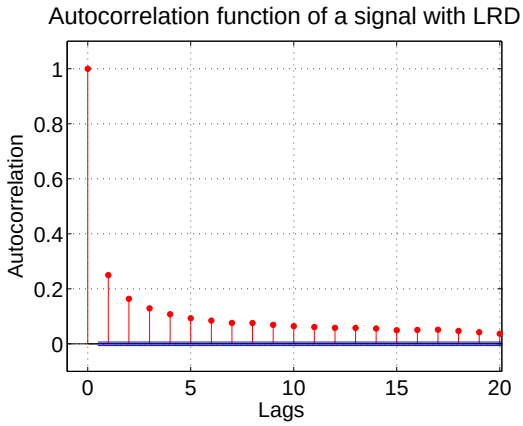


FIGURE 1.39: The autocorrelation function of a signal with LRD is shown in red. The slow decay can be compared to Figure 1.13. The blue lines are the upper and lower confidence intervals for the correlation values.

We may expect the brain to show some long-range dependence because neurophysiological time series are not white noise, and show dynamical integrity over time.

A power law decay in the autocorrelation function is considered in particular because power law statistics have been linked to the presence of criticality. The presence of LRTCs in particular have also been associated with critical state dynamics [178].

#### 1.1.8.2 Long-range temporal correlations (LRTCs)

A time series $x(t)$ is defined to have long-range temporal correlations (LRTCs) when its autocorrelation function $\rho_{xx}(\tau)$ has a power law decay:

$$\rho_{xx}(\tau) \sim C\tau^{-\alpha} \tag{1.25}$$

where $C > 0$, $\alpha \in (0, 1)$ is some exponent, and the symbol $\sim$ indicates asymptotic equivalence [59, 105]. The power law decay of a signal with LRTCs is displayed in log-log space in Figure 1.40 alongside that of a white noise signal.

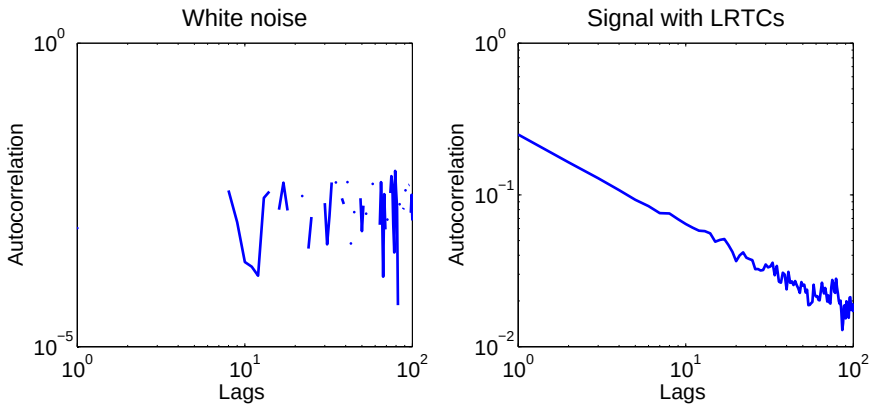


FIGURE 1.40: The autocorrelation functions of a white noise signal and a signal with LRTCs in log-log space. The power law decay can be seen as a linear function in log-log space. Data is missing in the autocorrelation function for white noise because the logarithm of a correlation value that is precisely zero is not defined.

Due to the power law form, LRTCs imply that the correlation of a time series to itself remains finite, even across large time lags (see Section 1.1.7.1). If the autocorrelation drops to zero after a certain time-lag, or it has an exponential decay, then the time series is said to have short-range or no dependence. In time series with LRTCs $\sum_{\tau=-\infty}^{\infty} \rho_{xx}(\tau)$ diverges.

LRTCs have been detected in a number of biological time series including inter-heartbeat intervals [212–214], DNA sequences [151] and walking patterns [120]; and natural phenomena including economics [244, 290], internet traffic [150], and geology [133, 283].

LRTCs may be equivalently defined through the Fourier transformation of Equation 1.25, to obtain the spectral density, which must also have a power law form:

$$G_{xx}(f) \sim Bf^{-\beta} \tag{1.26}$$

where $f$ represents frequency, $B$ is a constant, and $\beta = 1 - \alpha$ [59].

The values of $\alpha$ (or $\beta$) determine whether LRTCs are present. However, finding these exponents is often not straightforward for an arbitrary signal. In the time-domain, $\alpha$ is best approximated by the slope of the autocorrelation function in the infinite limit (i.e. for large values of the time lag), where measurement errors are also largest [59]. Similarly, in the frequency domain, $\beta$ is best approximated by the shape of the spectral density at large frequency shifts. Estimating the exponents in these ranges does not provide robust results.

Instead, for practical purposes, it is more straightforward to estimate the Hurst exponent $H$, which is related to $\alpha$ and $\beta$ by $H = \frac{2-\alpha}{2}$ and $H = \frac{1+\beta}{2}$, respectively.

#### 1.1.8.3 The Hurst exponent

The Hurst exponent was first calculated in 1951 by hydrologist Harold Edwin Hurst. When studying a time series of minimum water levels in the river Nile, he noticed that it did not appear 'random'.[12] Hurst noticed that the time series contained long periods when the minimum water level was below the average, followed by long periods in which observations were above the average. Indeed, the Nile River has been long known to be characterised by periods of drought followed by flooding, perhaps most colourfully described in the Egyptian Pharaoh's account of his dream to Joseph:

> Behold, there come seven years of great plenty throughout all the land of Egypt:
> And there shall arise after them seven years of famine;
> Genesis(41:29-30)

This is what Hurst observed. In 1969, Mandelbrot demonstrated that the property of long memory was not restricted only to hydrology, but can be seen in the spatial and temporal domains of a range of natural phenomena [187]. [13] However, unlike the biblical example, the periods observed by Hurst were not regular and periodic at seven years, but variable. The time series was stationary, which means its their average did not change in time. Hurst called this phenomenon 'long memory' [244].

Hurst's job as a hydrologist was to calculate the size of the reservoir needed to hold all the water flowing through a particular site along the Nile. In order to achieve this, he introduced a novel method for quantifying the variability of a time series called the re-scaled range $R/S$. The re-scaled range has been developed and adjusted to create the DFA technique.

In Section 1.1.8.4, some time series for which the Hurst exponent is known are presented, and the expected range of values of the Hurst exponent for some typical signal types are given.

#### 1.1.8.4 Known Hurst exponent values

Brownian noise is the cumulative sum of Gaussian white noise. It has a power spectrum of the form:

[12] In 1925, Omar Tousson published data that documented the minimum water levels of the Nile between the years 1007 and 1206. This formed part of a longer, historically available time series, which collectively listed the minimum water level of the Nile from 622 to 1281 A.D., making up 660 data points. This is the time series that Hurst studied.

[13] Mandelbrot later coined Hurst's observation as the 'Joseph effect' due to this Biblical reference [186].

$$G_{xx}(f) = Cf^{-2}$$

For Brownian noise, $H = 3/2$. Brownian noise derives its name from Robert Brown who discovered it, however, his fortuitously chromatic surname has contributed to a trend for naming noise with different Hurst exponents after colours such as pink noise, which is also of relevance to this thesis. It is defined by a power spectrum of:

$$G_{xx}(f) = Cf^{-1}$$

For pink noise, $H = 1$. Because of the reciprocal form of its spectral density, this is also sometimes referred to as $\frac{1}{f}$ noise. The name 'pink noise' comes from the appearance of white light after it has been filtered to have this power spectrum. $\frac{1}{f}$ noise is observed in the power spectra of neurophysiological time series underlying peaks in power at specific frequencies (see Section 1.1.3). Other colours of noise are defined and commonly used, but these three are the only ones referred to specifically in this thesis.

#### 1.1.8.5 Self-similarity

Hurst did not attempt an explanation of his findings himself, but Mandelbrot suggested that they were a manifestation of a self-similar process [186]. Indeed, it is a technique for assessing the self-similarity of a time series that is used in practice for estimating the Hurst exponent.

Self-similar time series will always have LRD, but not all processes with LRD are self-similar [249]. Self-similarity is a concept that can be applied to objects as well as time series and it is used to describe an entity that is made up of smaller versions of the whole.

The theory of self-similar processes was first introduced with this name by Kolmogorov in 1941 [25]. They first began to be used in statistics following Mandelbrot's 1968 paper [186], but they are not an entirely new concept. In his 1977 book, Mandelbrot refers to Leonardo da Vinci's use of self-similar objects to depict flowing air and water in his landscapes [184].

The properties of self-similar entities are explained by considering fractals, which are defined to possess self-similarity.

#### 1.1.8.6 Fractals

The fractal properties of an object can be characterised by its fractal dimension $D$. This is a ratio, equal to the number of scaled-down replicas of a shape that fit inside it, divided by the length scaling factor of the replicas. More precisely,

$$D = -\frac{\log N}{\log \epsilon} \tag{1.27}$$

where $N$ is the number of scaled-down replicas and $\epsilon$ is the scaling factor.

An example of a fractal is a Koch snowflake, such as that in Figure 1.41. To build the shape, we begin with a linear segment, of which a smaller segment is taken, with length scaling factor $\epsilon = \frac{1}{3}$. However, now each side of the snowflake will contain $N = 4$ lengths of this smaller shape. The (this time fractional) dimension therefore becomes $D = -\frac{\log_4}{\log_{\frac{1}{3}}} \sim 1.262$.

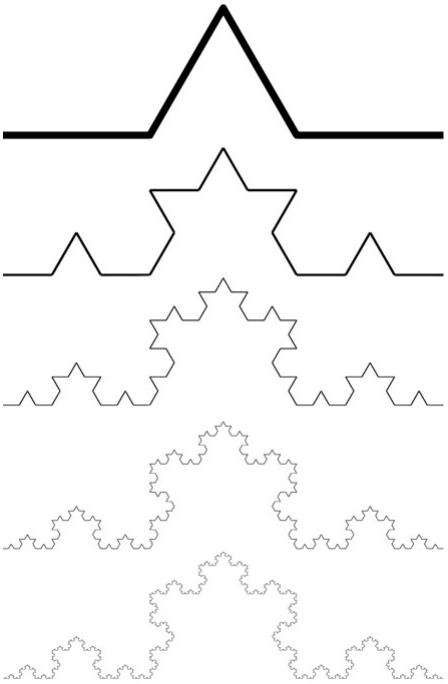

FIGURE 1.41: A Koch snowflake. The first five steps in generating the Koch snowflake. A smaller replica of the initial line is taken, and used to add two more short segments to it. This forms the next shape. A smaller replica of each linear segment is taken, and used to add two new sides to each side of this new constuction. The process is repeated an infinite number of times. Taken from [152].

It is also possible to consider the fractional dimension of a time series, such as Brownian noise. Its fractal dimension can be determined when a single time segment of length 1 is divided into $n$ smaller segments, each of length $1/n$ [3]. The length scaling factor of these is $\epsilon = \frac{1}{n}$. For each time segment $\frac{1}{n}$, the Brownian

motion process will grow by $\frac{1}{n^H}$. The area of a rectangular box corresponding to each time segment will therefore be $\frac{1}{n} \times \frac{1}{n^H} = \frac{1}{n^{H+1}}$.

Without the structure of Brownian noise, the area of the rectangle with horizontal length $\frac{1}{n}$ would be $\frac{1}{n^2}$ under the assumption that the vertical distance was also $\frac{1}{n}$.

The number of boxes of size $\frac{1}{n^2}$ required to fill an area of size $\frac{1}{n^{H+1}}$ will therefore be $\left[\frac{1}{n^{H+1}} / \frac{1}{n^2}\right] = \frac{1}{n^{H-1}}$.

There are $n$ intervals of length $1/n$ within the single time segment of length 1, so that the total number $N$ of smaller segments to fill the whole space will be:

$$N = n \times \frac{1}{n^{H-1}} = \frac{1}{n^{H-2}}$$

Thus the fractal dimension of Brownian motion is:

$$D_B = -\frac{\log N}{\log \epsilon} \tag{1.28}$$

$$= -\frac{\log \frac{1}{n^{H-2}}}{\log \frac{1}{n}} \tag{1.29}$$

$$= \frac{(2-H)\log(n)}{\log(n)} \tag{1.30}$$

$$= 2 - H \tag{1.31}$$

Lower Hurst exponents will therefore give rise to higher fractal dimensions. In general, for self-similar processes, the fractal dimension $D$ (Equation 1.27), is related to $H$ by $D + H = n + 1$ where $n$ is the dimension of the space. In 1-d space, $D + H = 2$ [185].

Mathematically, self-similarity is defined in terms of the distribution of the process [25]. Precise scale invariance is the manifestation of self-similarity. Therefore, in a self-similar process, the fluctuations grow with the window size as a power-law function. If the fluctuations at large window size are a power function of the window size, then an infinitely long self-similar time series must have infinite fluctuations and therefore be unbounded.

We can approximate the degree of self-similarity in a signal, such as a time-varying phase synchrony measure, using a method called detrended fluctuation analysis (DFA) [212, 214].

#### 1.1.8.7 Detrended fluctuation analysis (DFA)

The technique of detrended fluctuation analysis (DFA) is closely related to Hurst's $R/S$ statistic. The technique was adjusted by Chung-Kang Peng in 1994 to make it more suitable for analysing non-stationary signals, for which the Hurst exponent is not easily calculable [212, 214]. DFA is used to assess the rapidity of variation in a signal [232], which is a measure that indicates the presence of self-similarity in time series (Figure 1.42). DFA can be applied to both stationary and non-stationary data, avoiding artefactual dependencies [232]. A more extensive description of the DFA method can be found in [178, 215]. For a tutorial, see [117].

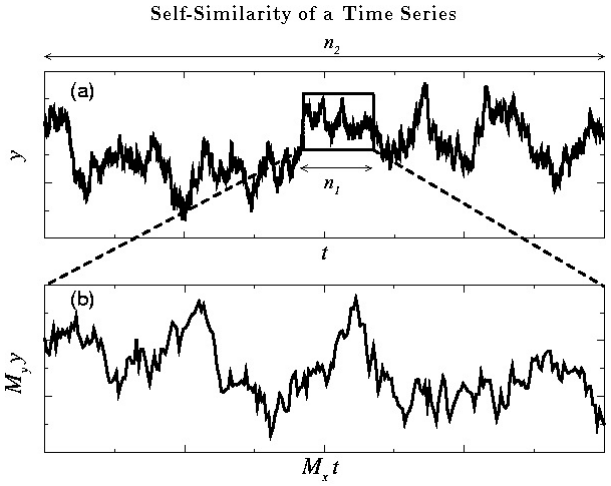


FIGURE 1.42: An illustration of the concept of self-similarity in a simulated signal. Two time scales are shown in (a) and (b), where (b) is a magnification of a section of (a). The fluctuations in the two images may be said to look 'similar' to each other from a distributional viewpoint. This is an example of a fractal time series (see Section 1.1.8.6). Taken from http://www.physionet.org/tutorials/fmnc/node3.html. Viewed on 23rd August 2010.

The application of DFA returns the value of an exponent $\gamma$, which is an estimate for the Hurst parameter, $H$ described above [133], and the value it takes characterises the order in the underlying data:

- If $0 < \gamma < 0.5$, anti-correlations are obtained so that large values are likely to be followed by small ones and vice-versa [25].
- There is no correlation between the innovations of a white noise time series. It therefore has an autocorrelation function that is zero for any lag time $j$ other than zero. It therefore has a constant power spectrum with $\beta = 0$ and the corresponding DFA exponent will be $\gamma = 0.5$ [3, 83, 198] (Figure 1.44).
- If $0.5 < \gamma < 1$, the correlations are persistent, and this corresponds to the presence of LRTCs, $\rho(\tau) \sim \tau^{-\alpha}$. This indicates that any time point of

the signal has a positive correlation with the level of the time series at the previous point. A signal value above the average level is therefore more likely to be followed by another above-average value at the next and there is order in the time series.

- If $\gamma = 1$, the time series is $\frac{1}{f}$ , or pink noise, which occurs widely in nature [162]. In the case of $\gamma > 1$, correlations will still exist, but the signal is non-stationary.
- $\gamma = 1.5$ indicates Brownian noise, which is an integrated white noise signal. Hence the value of the series at time $t + 1$ is fully dependent on its value at time $t$, and the series is correlated with itself across time. The DFA exponent obtained from a Brownian noise process is $\gamma = 1.5$ [231]. An example of Brownian noise alongside its DFA log-log plot is displayed in Figure 1.44.

The algorithmic method for obtaining this estimation using DFA is well described in [212, 214]. A brief overview of the method is provided here (Figure 1.43).

1. For a signal $x_i$, $\{i = 1, 2, ..., I\}$, the mean $x_{average}$, should be calculated and subtracted from each point $x_n$, and the cumulative sum taken at each step, to give $y(k)$:
$$y(k) = \sum_{n}^{k} x_i - x_{\text{average}}$$
This produces a time series that is unbounded. This action is illustrated in Figure 1.43(A)-(B) for an example of an MEG signal.
2. The signal is divided into a series of $I$ equally sized windows. For instance, 120 seconds of recorded data might be used, as in Figure 1.43(C).
3. For each one of these windows, a linear function is fitted to the data contained in it, by a least-squares method. For window $i$, $\{n = 1, 2, ..., N\}$, the linear trend, with coordinates $y_n$ is then subtracted from each data-point $y(k)$ in window $n$, as shown in Figure 1.43. (It is possible to fit alternative functions at this stage)
4. The root-mean-square error (RMSE), $E_N$ is calculated for the entire length of the data $RMSE_N = \sqrt{\frac{1}{I}\sum_{k}^{N}[y(k) - y_n]^2}$ where $y_n$ is specified by the window that $y(k)$ belongs to.
5. This process is repeated for a number of different window sizes, thereby examining a range of scales in the data. If the plot is well-described by a power law, then the log-log plot of window size against root-mean-square error would be linear, as indicated by the example in Figure 1.1.8.7(E). The

arrow indicates the window of size 120 seconds that was used as an example in this discussion. The root mean square error is plotted against window size on a log-log plot, and the slope of this line yields the DFA exponent, and in turn an estimate of the Hurst exponent.

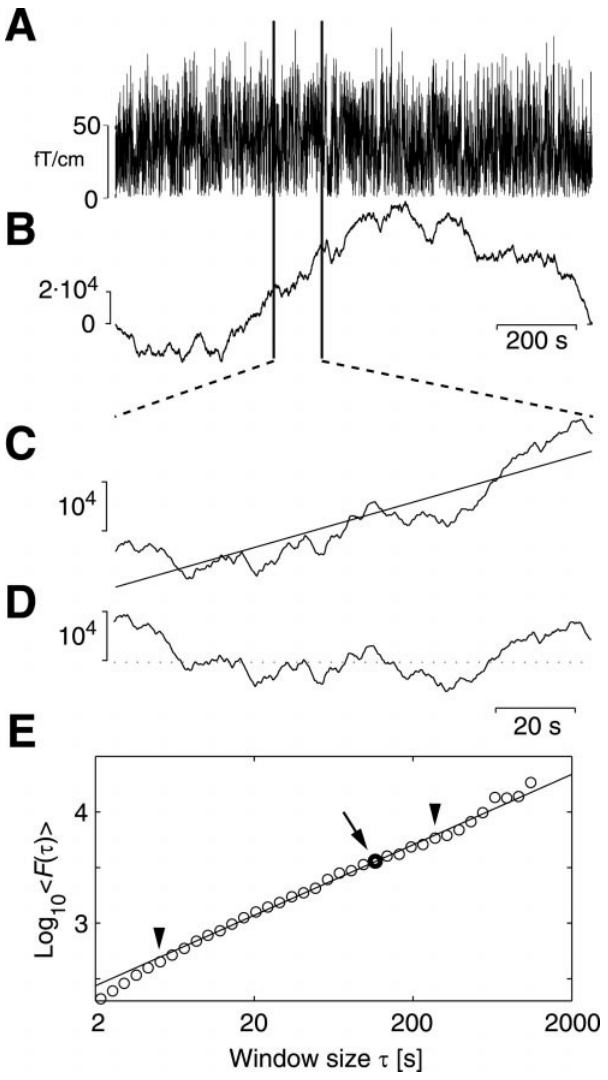


FIGURE 1.43: An example of the DFA method performed on MEG (magnetoencephalography) data from [178].The following steps are required for Detrended Fluctuation Analysis (image from [177]): A. The mean is subtracted from the signal, which is cumulatively summed. B. The data is divided into windows of a selected equal interval size. C. A least squares line is fitted to each window. D. The trend is subtracted in each window and average root mean square fluctuation calculated across all windows of this size. E. The process is repeated for a number of different window sizes. The root mean square error is then plotted against the window size on a log-log axis. A power law is indicted by a linear plot. The slope of such a linear plot is the DFA exponent, providing an estimation of the Hurst exponent.

Some examples of the log-log plots from which the DFA exponent has been calculated are shown in Figure 1.44, for white Gaussian noise, with exponent 0.5 and

for Brownian motion, with exponent 1.5.

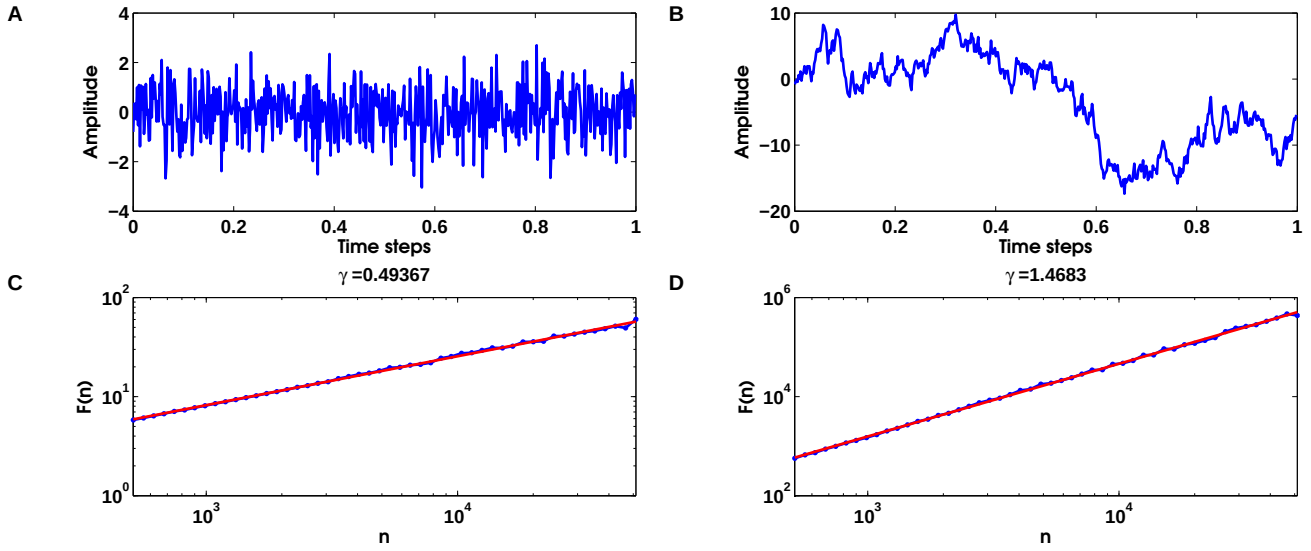


FIGURE 1.44: Some examples of white noise (left) and Brownian noise (right), above their DFA log-log plots, with corresponding exponents. As the time series on which the DFA is performed is finite, the DFA exponents are not precisely at 0.5 and 1.5, respectively, but approximate these values. The calculated DFA exponents are 0.49 and 1.47, respectively.

The selection of window lengths to be used is not always a trivial matter. The shortest window length should hold enough sample points to allow a reasonable calculation of the root-mean-square error for each window $i$ [117, 178].

The longest window length should be short enough to allow a sufficient number of them for a good estimate of the overall root-mean square error calculated in Equation 1.1.8.7. The original paper that proposes DFA [212] suggests that the largest segment size should be no longer than one tenth of the number of available data points, $I$. However, [117] and later [28] suggest that given the limitations of a short data set, power of interpretation is lost if the largest window size is restricted to a tenth of the length of the data. [28] confirmed that for their data (also that used in Section 2.2), it was permissible to use one quarter of $I$, by showing that there was good agreement between the exponents computed using both methods. This question is referred to again in Chapter 4.

**Known limitations of DFA** The estimation of the Hurst exponent provided by DFA can only be accurate if the time series to which DFA is applied is self-similar. If a time series is indeed self-similar, then the relationship between the magnitude of detrended fluctuations and the time scale over which they are measured can be

visualised as a *straight line* on a log-log fluctuation plot such as those in Figure 1.44 [212, 214]. DFA returns the slope of this plot.

Importantly, to date there is no mechanism within DFA to check that the slope that is returned comes from a plot is indeed linear. If the DFA fluctuation plot is not linear, then DFA will still return a value, but the underlying time series cannot be said to be self-similar, and the slope does not have an interpretable meaning. Specifically, a time series with a non-linear DFA fluctuation plot cannot be said to possess power law scaling. This makes it difficult to draw any conclusions regarding LRTCs and criticality within the underlying data, which is one major motivation for using DFA in the first place.

In Chapter 2, the evidential basis for these limitations is considered critically and a technique to overcome them is proposed.

Computationally, time series with different Hurst or DFA exponents can be generated using an Autoregressive Fractionally Integrated Moving Average (FARIMA) model [128]. FARIMA models can in fact be used more extensively to generate time series with varying combinations of both long-range and short-range temporal correlations. These time series can therefore be used to validate any technique for detecting the presence of LRTCs, such as DFA. For this reason, they are introduced in the next section 1.1.8.8.

#### 1.1.8.8 Fractionally Integrated Moving Average (FARIMA) models

The Autoregressive Fractionally Integrated Moving Average (FARIMA) model was introduced by Jonathan Hosking [128]. They are commonly used to generate a FARIMA process with short or long range temporal correlations.

To construct a FARIMA process a sequence of zero-mean white noise is first generated, which is typically taken to be Gaussian, and necessarily so to produce fractional Gaussian noise. The FARIMA process, $X_t$, is then defined by parameters $p$, $d$ and $q$, denoted FARIMA($p$,$d$,$q$) and given by:

$$\left(1 - \sum_{i=1}^{p} \phi_i B^i\right) (1 - B)^d X_t = \left(1 + \sum_{i=1}^{q} \theta_i B^i\right) \varepsilon_t. \tag{1.32}$$

$B$ is the backshift operator operator, so that $BX_t = X_{t-1}$ and $B^2 X_t = X_{t-2}$. Terms such as $(1 - B)^2$ are calculated using ordinary expansion, so that $(1 - B)^2 X_t = X_t - 2X_{t-1} + X_{t-2}$. While the parameter $d$ must be an integer in the

ARIMA model, the FARIMA can take fractional values for $d$. A binomial series expansion is used to calculate the result:

$$(1-B)^d = \sum_{k=0}^{\infty} \binom{d}{k} (-B)^k.$$

The left hand sum deals with the autoregressive part of the model where $p$ indicates the number of back-shifted terms of $X_t$ to be included, $\phi_i$ are the coefficients with which these terms are weighted. The right hand sum represents the moving average part of the model. The number of terms of white noise to be included are $q$, with coefficients $\theta_i$. In the range $|d| < \frac{1}{2}$, FARIMA processes are capable of modelling long-term persistence [128]. As we will only consider $p = 1$ and $q = 1$ throughout the manuscript, we will refer to $\phi_1$ as $\phi$ and $\theta_1$ as $\theta$. We set $|\phi| < 1$, $|\theta| < 1$ to ensure that the coefficients in Equation 1.32 decrease with increasing application of the backshift operator, thereby guaranteeing that the series converges, and $X_t$ is finite [128].

A FARIMA(0,$d$,0) is equivalent to fractional Gaussian noise with $d = H - \frac{1}{2}$ [128], where $p$=0 and $q$=0 in this case indicating that there are no $\phi$ or $\theta$ parameters. This produces a time series with a DFA fluctuation plot that has been shown to be asymptotically linear and have a DFA exponent of 0.5 [18, 268]. By manipulating the $\phi$ and $\theta$ parameters, the linearity of DFA fluctuation plots can also be distorted.

In a FARIMA(1,$d$,0) process, the $\phi$ parameter is non-zero (there is a single $\phi$ parameter as $p = 1$), and an autoregressive term is added to the process. In general, an increase in the $\phi$ coefficient at constant $\theta$ induces a decrease in fluctuations for small window sizes, and a concavity is seen in the fluctuation plot [199]. The value of $\phi$ increases the short-range exponent with an exponential relationship [199]. This means that the process at a given time point depends linearly on the previous values in the series, so that a single impulse would affect the rest of the process infinitely far into the future. The process is expected to behave like a FARIMA(0,$d$,0) time series in the long-term, but the short term behaviour will have short-term correlations, depending on the size of $\phi$ [128].

For a FARIMA(0,$d$,1) time series, the $\theta$ parameter is non-zero (there is a single $\theta$ parameter as $q = 1$), which indicates exponential smoothing and a time series with noisy fluctuations around a slowly-varying mean. The resulting DFA fluctuation plots have fluctuation levels that are above the expected regression line at large box sizes. An increase in $\theta$ for $\phi = 0$ induces convexity in the fluctuation plot.

## 1.2 Summary

The human nervous system is able to react and perform tasks with great efficiency in response to unexpected external stimuli. A nervous system at rest must therefore be in a state of readiness, which allows it to transfer information between its constituent neurons and neuronal pools both quickly and effectively when such a stimulus is presented. These processes will support perception and action. A system at criticality also possesses this characteristic. The 'critical brain hypothesis' has thus been suggested, which argues that the human nervous system is in a critical state, both in its individual constituent elements, and in their interactions.

The critical brain hypothesis may be considered both in terms of the amplitude of its activity and in its interactions, such as can be encoded by phase synchronisation between neurophysiological time series emerging from different regions. Evidence for the critical brain hypothesis has largely been based on the observation of power law statistics. Primarily, the evidence has relied on identifying power law distributions in neuronal avalanche size [23], but has been followed by the characterisation of power law scaling functions[80, 229, 240], and power law decay in the autocorrelation function (LRTCs)[178]. Emphasis has been placed on the power law form in particular because they are one known property of critical systems. In time series in particular, power law statistics have been identified by assessing the presence of LRTCs in amplitude envelopes of EEG and MEG time series [28, 178].

In this thesis, the critical brain hypothesis is tested in relation to both the activity of individual brain regions, and the interaction between distinct regions during resting state. It is hypothesised that the brain at rest will display evidence of a system at criticality because a resting brain that works efficiently should possess the properties typical of a critical system, such as the ability to react efficiently to incoming stimuli, learn and transfer information quickly. These latter properties should be evident both in the activity of individual regions, and in the interaction between regions of the brain. The hypothesis is tested by constructing, validating, and then applying a method that searches for the presence of LRTCs in either the amplitude envelope (individual region activity) or the rate of change of phase difference (region interaction) of neurophysiological signals.

In order to construct this method, a number of supporting steps are undertaken. Specifically, In Chapter 2 it is found that the technique of DFA, which is commonly used to assess the presence of LRTCs, suffers from methodological limitations, which call into question its ability to determine the presence of power law statistics. A heuristic technique, ML-DFA is developed and validated, which can be used to

assess the linearity of DFA fluctuation plots and to overcome these limitations. This technique is thenceforth applied at any point where DFA is used.

The amplitude envelope measure for neurophysiological time series reveals the characteristics of neuronal pools local to the position of their recording. Using ML-DFA and DFA together, the evidence for power law statistics in the amplitude envelope of EEG and EMG is evaluated in Chapters 3 and 4. In Chapter 3, the possible outcomes of analysing data from young subjects is considered. In Chapter 4, the potential pitfalls of using incorrect window sizes in DFA are investigated. These three mentioned chapters are all concerned with the amplitude activity of individual neurophysiological areas.

The question of brain region interactions is then approached. A previous paper [157] indicated that the time-varying synchronisation between MEG and fMRI time series during resting state possessed power laws, suggesting that synchronisation in the brain showed evidence of criticality. However, in Chapter 5, the methods used in this latter paper are demonstrated to show significant weaknesses. This analysis suggests the need for a new method to be developed.

This is done in Chapter 6. The phase synchrony analysis method is developed, which assesses the presence of LRTCs in a different measure of human neural synchronisation data, and which relies on calculating the rate of change of phase difference between different time series. The method is validated by application to data with known presence of LRTCs (FARIMA time series), and to classical models of criticality such as the Ising model, [207] and the Kuramoto model of coupled oscillators [167].

In Chapter 7, the method is applied to the Cabral model [47], which is also based on the Kuramoto model, but includes additional features through which it can be used to produce time series that more closely approximate time series of the human brain at resting state. The method is used to investigate the role of clusters and network properties on LRTCs in time varying synchronisation of a model of the brain.

In Chapter 8 the phase synchrony analysis method is applied to neurophysiological data. It is used to assess the presence of LRTCs in the time-varying synchronisation between left and right motor cortex MEG data during rest, and data recorded during a movement task. The hypothesis in this thesis would suggest that resting state data would show characteristics of criticality. In Chapter 9 the potential to analyse data from subjects of different ages, including very young children, and to apply the method to time series from both central and peripheral nervous system recordings, is demonstrated.

## 1.3 Tests undertaken to explore the central hypothesis

- In [28] it was found that LRTCs existed in the amplitude envelope of EEG time series in the $\theta$, $\alpha$ and $\beta$ frequency bands. However, these results were not verified with the application of ML-DFA. The linearity of the log-log DFA fluctuation plots obtained from analysing this data is tested in Chapter 3 using the ML-DFA technique introduced in Chapter 2.

- The role of window sizes in applying DFA and ML-DFA are investigated in Chapter 4. Window sizes that do not include several oscillations of the oscillatory frequency of the data would not be expected to show linear DFA exponents. A maximum window size that extends to the full length of the time series would be more likely to show invalidity in the resulting DFA fluctuation plots due to noisy estimates for fluctuation magnitude at large window sizes. This is tested by applying DFA and ML-DFA to the amplitude envelope of EEG data using different window sizes.

- The ability of the phase synchrony analysis method to detect LRTCs in the rate of change of phase difference between two signals with known LRTCs in this time series is tested using surrogate data in Chapter 6.

- The phase synchrony analysis method is applied to the Ising model at a range of different parameter values, and the presence of LRTCs in the Ising model at critical parameter is tested in Chapter 6.

- The phase synchrony analysis method is also applied to the Kuramoto model at a range of different parameter values, and the presence of LRTCs in the Kuramoto model at its critical coupling parameter is also tested in Chapter 6.

- In Chapter 7, the phase synchrony analysis method is applied to the Cabral model of the brain in resting state [47], which is based on the Kuramoto model of coupled oscillators. The presence of LRTCs in the time-varying phase synchronisation between these model brain regions in the resting state is tested.

- The brain regions associated with these LRTCs are identified, and in particular, the regions that play a large role in the default mode network (the

network of regions activated during restful waking) are considered as the most likely locations for presence of LRTCs. This question is tested in Chapter 7.

- The role of the connectivity structure of the brain in contributing to LRTCs is also tested in Chapter 7. The hypothesis of this thesis would suggest is that disrupting clusters by network reorganisation may destroy LRTCs because it would destroy the pathways by which efficient information transfer may occur in the brain [135].

- The phase synchrony analysis method is applied to resting state human MEG data from the left and right motor cortices in Chapter 8. The central hypothesis is tested in human MEG data, and in particular, it is investigated whether LRTCs will be present in the time-varying synchronisation of these two regions during resting state. The phase synchrony analysis method is applied to human MEG data that is recorded during a finger tapping task. It is hypothesised that LRTCs will be disrupted during this task.

- EEG and EMG time series during a constant pincer grip is analysed in Chapter 9 with the phase synchrony analysis method to test whether this technique may also be applied to data collected from the peripheral and central nervous systems simultaneously and produce meaningful results. As the pincer grip in this task is not a task of active movement, the central hypothesis would lead to the expectation that LRTCs would still be present in the rate of change of phase difference between these two EEG and EMG time series.

## 1.4 Novel contributions in this thesis

A number of novel contributions have been made throughout this thesis:

- The phase synchrony analysis method is a novel method, which is developed and validated in this thesis in Chapter 6.

- ML-DFA is a technique that supports the phase synchrony analysis method, and is used as part of it throughout the thesis, however, as it is a stand-alone technique, it is introduced independently in Chapter 2.

- The presence of LRTCs in the rate of change of phase difference between the oscillators in the Kuramoto model has not previously been demonstrated. Similarly, the rate of change of phase difference between signals extracted from the Ising model and the Cabral model has not been previously shown to contain LRTCs.

- The ability of connectivity changes to disrupt LRTCs in the rate of change of the Cabral model is a novel addition to the analysis of this model.

- The tests applied to the method in [157] to demonstrate its weaknesses have not been performed previously.

- The demonstration of LRTCs in the rate of change of phase difference of MEG data during resting state has not previously been achieved and is a novel contribution, which leads to some additional insights into the understanding of brain activity. The disruption of LRTCs by a finger tapping task has also not been published previously.

## 1.5 Data sets used in this thesis

- Chapters 2, 3 and 9 : EEG and EMG data recorded simultaneously during constant pincer grip task from 48 healthy subjects aged 0-59 years. One record was taken per subject, $\approx$ 2 minutes in length. This data set was previously used in publications [140] and [28].

- Chapter 4 : EEG data recorded at rest, performed during music therapy from 20 healthy subjects aged 24-59 years. One record was taken per subject, $\approx$ 40-60 minutes in length. This data not previously published.

- Chapter 8 : MEG data recorded during resting state, and while subjects completed a total of 10 30 second trials of rest, tapping their left finger, their right finger, and both fingers simultaneously, in a random order. Data was recorded from 7 healthy subjects in total. This data has not previously been published.

- Chapter 11, Section 11.2.2 : EEG data recorded from 16 subjects during eyes closed and eyes open resting state conditions. One record was taken per subject, of length between 239 and 291 seconds. Data was downloaded from http://www.nbtwiki.net/

# Chapter 2

# A heuristic technique for DFA exponent validation

## 2.1 Introduction

In this chapter, the possibility of non-linearity in DFA log-log fluctuation plots, and the difficulty this presents for interpretations of scale free behaviour of data, is investigated. This observation has highlighted a potential problem in the application of DFA. At present there is no validated method which ascertains the linearity of a DFA plot (but see parabolicity index in [197]) and an important shortcoming of the typically used method (see below) is that unless there is gross violation of linearity that can be detected by visual inspection then DFA exponents can be used for data that are not self-similar. In fact, Maraun and colleagues went as far as suggesting that DFA results are sensitive but not specific concerning long-range correlations [188]. Further potential practical pitfalls of DFA application have been discussed in [43, 96, 268]. With exponent values often used to differentiate between clinical and healthy populations, for example, patients with cardiac disease [213, 214], Alzheimer's [1], epilepsy [253], balance problems [155, 289] and schizophrenia [203, 236], there is a need to prevent false positives from contaminating the interpretation of such differences.

Previous studies have described non-linear characteristics in DFA fluctuation plots for signals constructed by independent superposition of a number of processes with specific characteristics. When a noise time series contains a linear, sinusoidal, or a power law trend, the DFA plot will contain several linear segments, joined at crossover points [129]. Studies have also looked at noise time series with sections of silence, concatenations of noisy signals with different amplitude standard deviations, and of noisy signals with varying levels of temporal correlation [52, 53].

These fluctuation plots show different combinations of linear and quasi-linear fragments.

At present the standard approach used to characterise the fit of the linear regression in DFA is to calculate an $R^2$ value on a log-log plot (for example [107]). However, the $R^2$ value is a very insensitive measure and viewing a plot in the log-log space makes them more likely to appear linear [9]. An alternative technique may be to assume that the errors around a linear fit have a $\chi^2$ distribution, but this assumption cannot be made for a DFA fluctuation plot because the magnitude of detrended fluctuation is dependent on the window length so that the fluctuation plot suffers from heteroscedasticity [239]. Namely, this approach would not allow one to distinguish between a self-similar signal yielding non $\chi^2$-distributed regression errors and a non self-similar signal. Another approach may be to compute the probability of the fluctuation plot taking the form of a specific function for signals with different self-similarity properties, based on the probability distribution of the innovations. A paper by Bardet [18] formulates such a distribution for the scale-invariant process that would give rise to a perfectly linear plot in its DFA fluctuation plot, i.e., fractional Gaussian noise. However, this approach would restrict the technique to being able to identify only a limited set of signals, and furthermore, one would need to know *a priori* the nature of the signal in order to employ the appropriate distribution.

As an initial technique for discriminating between linear and non-linear DFA fluctuation plots here, the runs test [288] is first applied to the errors around the DFA fluctuation plot when a straight line is fitted. This test does not work well, the reasons behind which are discussed.

Subsequently, a technique to assess the validity of the assumption of linearity through a model selection approach is proposed.

The technique, referred to as ML-DFA henceforth, borrows ideas from maximum likelihood theory. A function similar to the log-likelihood function for both a linear model and a number of alternative models is demonstrated. This requires formulating the DFA fluctuation plot as a probability density, which is done by normalising the fluctuation magnitudes. This is used to compute the Akaike and Bayesian Information Criterion (AIC and BIC, respectively) [6, 251] which reveal the best-fitting model to the fluctuation plot, while compensating for over-fitting. If no model amongst the set of alternative models is a better fit than the linear model, then we accept (or more accurately, we do not reject) the hypothesis that the fluctuation plot is linear.

In this chapter, examples of non-linear DFA plots are first demonstrated. The runs test is used as an initial attempt to distinguish between linear and non-linear plots,

and shown not to perform well in this regard. We then introduce and validate the ML-DFA technique by applying it to simulated time series for which we can control the expected outcome.

Synthetic time series are generated by an Autoregressive Fractionally Integrated Moving Average (FARIMA) process [128] (also referred to as ARFIMA or AFRIMA). We use FARIMA because it provides an easily tunable algorithm for constructing time series with a combination of short-term and long-term correlations, which we will show influence the DFA fluctuation plot. A FARIMA process in its simplest form can be used to generate fractional Gaussian noise, which has been shown analytically to produce linear DFA fluctuation plots in their asymptotic limit [18, 268]. However, by gradually introducing short-term correlations through smoothing the data and enforcing autoregression, it is possible to destroy the self-similarity of the time series, and a statistically robust method should capture this. We note that a FARIMA process has also been used to model neurophysiological signals such as EEG, which have the properties of being stationary and whose amplitude fluctuations follow Gaussian statistics [191]. A FARIMA process therefore provides an efficient and malleable method of generating and manipulating time series. However, to produce time series that more closely capture the inevitably noisy nature of physiological recordings, we also consider noisy correlated FARIMA processes in which the signal-to-noise ratio is systematically varied. We further apply ML-DFA to a sinusoidal signal and a sinusoidal signal with independent additive noise, whose DFA fluctuation plots take known forms [129].

The following sections in large part correspond to the pre-print manuscript for the paper [35], in which this technique is presented.

## 2.2 EEG and EMG data set

Data was taken from the data set used in [28] in order to assess the presence of LRTCs in the amplitude envelope of bandpass filtered EEG and EMG signals. However, a final stage of cleaning the data using independent component analysis was not performed here. Eight subjects were excluded in the current analysis due to artefacts visibly evident in the data.

### 2.2.1 Subjects

Recordings were obtained, with local ethical approval (St Marys NHS Trust) that adhered to standards set out in the Declaration of Helsinki, from 48 adults and children (22 males and 26 females) aged from 0 to 59 years. Hand dominance was

recorded above the age of 2 years and all subjects were right-handed. Verbal and written consent was obtained from the subjects and, in the case of children, their parents.

For the purposes of further analysis the subjects were divided into four age ranges: $0-36$ months (n = 12, mean=0.8 $\pm$ 0.9 years); $4-10$ years (n = 13, mean = 7.15 $\pm$ 2.1 years); $12-17$ years (n = 10, mean = 15.42 $\pm$ 1.5 years); and $19-59$ years (n = 13, mean = 30.5 $\pm$ 10.5 years).

The subjects were recruited from the patient population and from a pool of volunteer subjects. The subjects taken from the patient population had been referred for clinical neurophysiological evaluation and their EEGs and EMGs were recorded simultaneously. The patient subjects whose data comprise this study were being investigated for brief episodes of loss or altered awareness. The ultimate diagnosis was either syncope or unexplained. None of the subjects whose data are included in the present study was suffering from significant neurological or neuro-developmental problems. Their EEG data had been passed as normal by a consultant clinical neurophysiologist.

### 2.2.2 EEG and EMG recording

Electroencephalograph and EMG were acquired (sampling rate 512 Hz) and stored digitally using a PC-based system built by Viasys Healthcare Oxford Instruments (Old Woking, UK). Common average EEGs were recorded (band pass filter: $4-256$ Hz). The head was measured and distances in millimetres between scalp electrodes were recorded in order to determine accurately the position of the electrodes relative to anatomical landmarks and to each other. EEG was obtained from 22 to 24 Ag/AgCl electrodes (Viasys Healthcare Oxford Medical Instruments, Old Woking, UK) positioned on the scalp in accordance with the modified Maudsley system of electrode placement (Pampiglione, 1956; Margerison et al., 1970). EMG from the dominant (right) forearm extensor muscle (FaExt) was recorded using pre-gelled bipolar electrodes (Ambu Neuroline, Cambridgeshire, UK). EMGs were bandpass filtered at $4-256$ Hz. The impedance of the scalp and EMG electrodes was maintained at $< 5$ kW. Subjects were asked to grip an object and extend the wrist. In subjects too young to comply with instructions EMG was obtained during grasping. EEG and EMG were recorded simultaneously during muscle contraction. Periods of constant EMG activity along with the corresponding EEG were selected for further analysis. In the case of young subjects (usually $< 3$ years) this involved selecting a number of non-contiguous sections that were free from artefacts and periods of EMG silence.

### 2.2.3 Filtering

The frequency band of interest was here set to 16-24 Hz because this range corresponds to the $\beta$ frequency band, which is prevalent during movement. As the EMG is studied in this chapter, which is activated during movement only, it was desirable to consider a frequency band in which neurophysiological activity relating to movement was present. Activity relating to the 16-24 Hz frequency band was extracted using bandpass finite impulse response (FIR) filtering and the Hilbert transform. The filter order of the FIR filter was set to include three cycles of the lower-frequency component of the band, namely 16 Hz.

## 2.3 Examples of DFA fluctuation plots obtained from EEG and EMG data analysis

In applying DFA to the amplitude envelope of EEG and EMG time series, some of the DFA fluctuation plots were clearly found not to show linearity. Two examples of the typical non-linearities that arise are shown in Figure 2.1 and 2.2. In Figure 2.1, the fluctuation plot has a periodic component, while in Figure 2.2, the fluctuation plot is concave rather than linear.

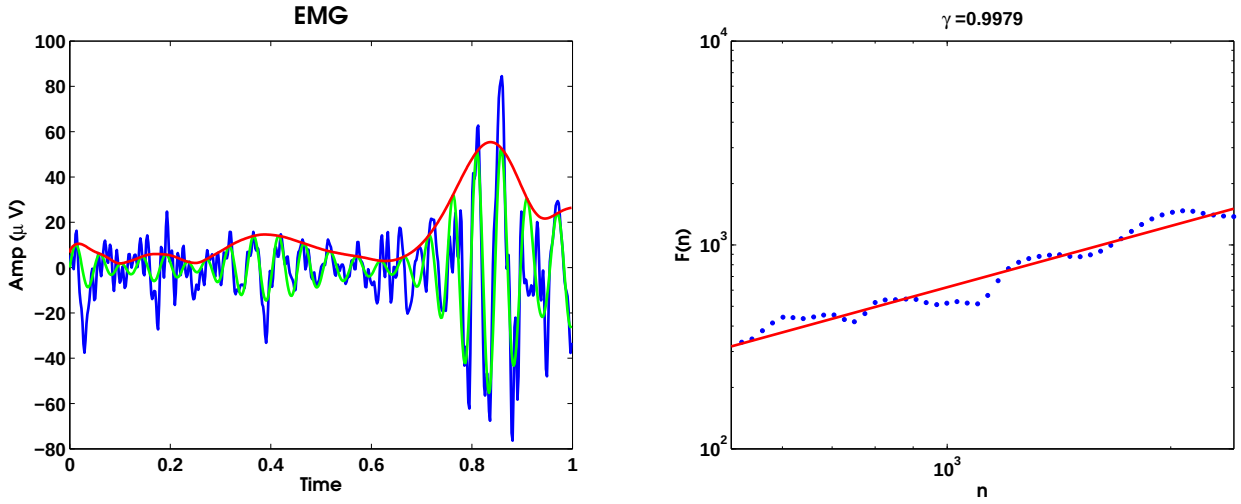


FIGURE 2.1: The EMG signal for subject 3 of Group 1, which seems to display concavity when a DFA is performed on it. The blue line in this figure is the raw signal, the green line is the same signal, bandpass filtered into the 16-24Hz range, and the red line is the amplitude envelope on the bandpass filtered signal. The EMG was not rectified in this case because this would modify the time series (amplitde envelope) to which DFA would be applied in a way that was not directly predictable and therefore not necessarily justifiable

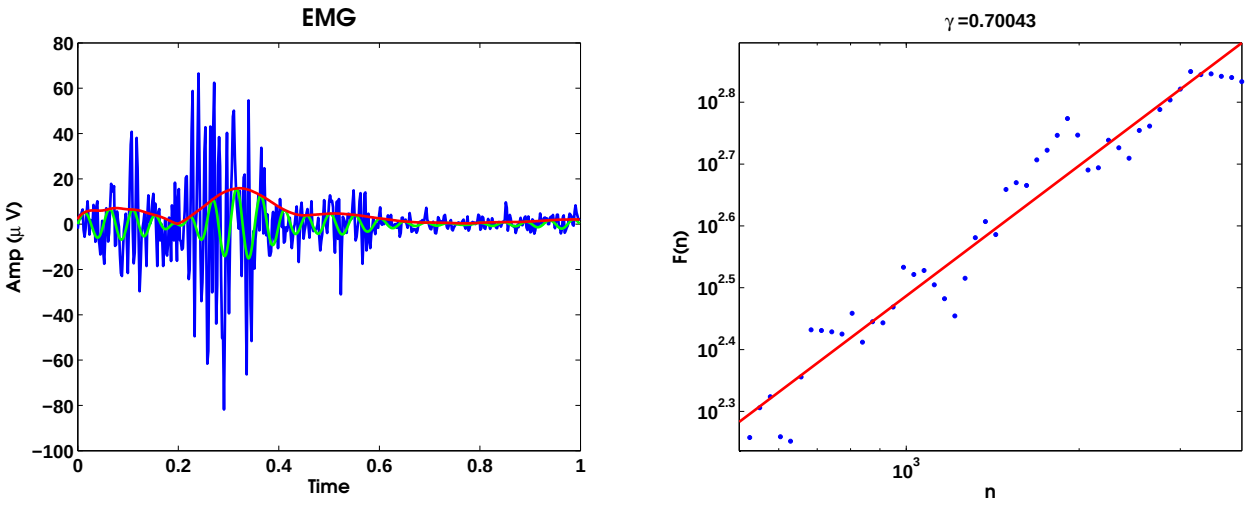


FIGURE 2.2: The EMG signal for subject 8 of Group 1, which seems to display periodic behaviour when a DFA is performed on it. The blue line in this figure is the raw signal, the green line is the same signal, bandpass filtered into the 16-24Hz range, and the red line is the amplitude envelope on the bandpass filtered signal. The EMG was not rectified in this case because this would modify the time series (amplitde envelope) to which DFA would be applied in a way that was not directly predictable and therefore not necessarily justifiable

This appears to be a particular concern for time series that are very short and do not offer enough data for the windows over which DFA is calculated to provide independent information. [1]

## 2.4 An initial attempt to judged linearity - the runs test

As an initial technique to determine whether a DFA fluctuation plot is linear or not the runs test was applied [288]. The 'runs' test is a non-parametric test that checks the hypothesis that the elements in a sequence are independent of each other. Runs are typically a set of numbers of data points for which the sequence is either above or below its mean value. In a DFA fluctuation plot, these were considered to be the instances where the fluctuation plot fell above or below a least squares linear fit.

The test determines the validity of a null hypothesis that runs of the observed length are possible in a sequence of independent data points. Such a test could be useful for determining the linearity of a DFA fluctuation plot because it would discriminate against heavily curved fluctuation plots such as that in Figure 2.1, which shows long runs of points below the linear fit, followed by long runs above.

[1] The recently developed technique of Adaptive Time-varying DFA (ATvDFA) provides a method for analysis of shorter time series [27].

In particular, the runs test is calculated by considering a random variable defined to be the number of runs in a sequence of length $n$ corresponding to that of the number of points in the DFA fluctuation plot. The conditional distribution of the number of runs given $n_+$ values above the average and $n_-$ values below the average is approximately normal with mean:

$$\text{mean} = \frac{2n_+n_-}{n} + 1$$

$$\text{variance} = \frac{2n_+n_-(2n_+n_- - n)}{n^2(n-1)}$$

There is no assumption of equality of number of instances of the $n_+$ and $n_-$ terms, but only that the sequence consists of independent, identically distributed elements. The null hypothesis is rejected if there are very many or very few runs observed.

Unfortunately, the runs test proved not to be helpful for analysing the linearity of a DFA fluctuation plot. Primarily it is not a test of linearity. For example, a DFA fluctuation plot which alternated between being below and above a least squares linear fit would not pass the runs test (see Figure 2.3 for a representative example), but it may be a fluctuation plot that we would like to consider to be linear if its deviations were not too great. Another important point is the fact that the points belonging to a DFA fluctuation plot cannot be considered to be independent from each other because they are extracted from the same single time series. The runs test cannot take this into account by its definition.

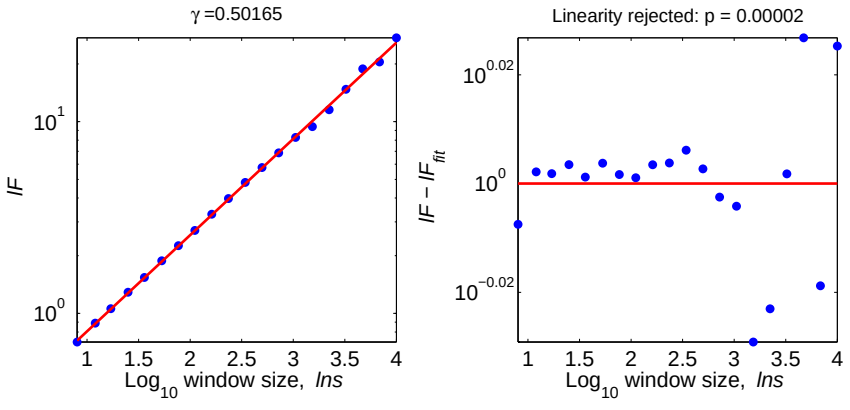


FIGURE 2.3: The runs test performed on a FARIMA time series with a Hurst exponent of 0.5. Linearity in this DFA fluctuation plot is rejected although it is known to be linear by construction.

This led to the development of a novel technique that is able to reject DFA fluctuation plots, on the basis of whether they are linear.

## 2.5 Methods and Materials

### 2.5.1 Scaling and Fit

To calculate the DFA exponent, the time series is first de-meaned and then cumulatively summed. After being divided into non-overlapping windows of a given size (i.e., a scale), it is detrended (linearly for 1-DFA, non-linearly for higher-order DFA) yielding a fluctuation calculated as the root-mean-square deviation over every window at that scale. The process is repeated for different window sizes.

For amplitude fluctuations of oscillatory signals, the smallest window size should be large enough to avoid errors in local root mean square fluctuations, and is typically taken to be three or four times the length of a cycle at the characteristic frequency in the time series. If the minimum window size is significantly smaller than this, then the fluctuation plot will typically contain a crossover at the window length of a single period [129]. In the case of non-oscillatory signals such as those from a FARIMA process, there is no characteristic time scale and a smaller window size may be used. The maximum window size should be small enough to provide a robust average for the fluctuation magnitude across the time series. It is typically taken to be $N/10$ where $N$ is the length of the data [196], however, a maximum window size of $N/4$ has previously also been used as an estimate of the average fluctuations [28, 178].

When developing the ML-DFA method, $ns$ is defined as the vector of window sizes and $F$ the vector of corresponding root mean square fluctuations. The number of distinct window sizes $n$, are taken as the maximum possible to allow each window to be non-overlapping. The base 10 logarithm of these two vectors are labelled $lns$ and $lF$ respectively.

However, since there is no *a priori* means of confirming that a signal is indeed self-similar, an exponent $\gamma$ can always be obtained even though the DFA fluctuation plot may not necessarily be linear – the only certainty being that it will be increasing (albeit not necessarily monotonously so) with window (box) sizes. The models used by ML-DFA are listed below, with the $a_i$ parameters to be found. The number of parameters ranges between 2 for the linear model, and 8 for the four-segment spline model.

Polynomial - $f(x) = \sum_{i=0}^{K} a_i x^i$ for $K = \{1, ..., 5\}$

Root - $f(x) = a_1(x + a_2)^{1/K} + a_3$ for $K = \{2, 3, 4\}$

Logarithmic - $f(x) = a_1 \log(x + a_2) + a_3$

Exponential - $f(x) = a_1 e^{a_2 x} + a_3$

Spline with 2, 3 and 4 linear sections.

The fluctuation magnitudes are first normalised with:

$$lF_{scaled} = 100 \times \frac{lF - lF_{min}}{lF_{max} - lF_{min}}$$

where $lF_{min}$ and $lF_{max}$ are the minimum and the maximum values of vector $lF$ respectively. A likelihood function is defined:

$$\mathcal{L} = \prod_{i=1}^{n} p(lns(i))^{lF_{scaled}(i)}$$

which is a product across all windows $i$, where $p(lns)$ represents the function:

$$p(lns) = \frac{|f(lns)|}{\sum_{i=1}^{n} |f(lns)|}$$

where $f(lns)$ is the fitted model. Absolute values are used in order to ensure that $p(lns)$ remains in the range $[0, 1]$, so that a likelihood function is rejected if it falls below 0.

The log-likelihood is then defined as:

$$\log\mathcal{L} = \sum_{i=1}^{n} lF_{scaled}(i) \log p(lns(i))$$

This function is maximised to find the parameters $a_i$ necessary for $f(lns)$. It is worth mentioning that the application of the logarithm to the likelihood function means that the values belonging to $lns$ are not equally weighted for all $i$. The larger window sizes have a lower weighting, which is beneficial because these estimates are also the least robust since they have fewer samples associated with them.

The largest log-likelihood is the model which best fits the data, however, no consideration of the number of parameters used is taken when comparing log-likelihoods. To address this, we compute both the AIC and BIC measures which are designed to prevent over-fitting, which should in general be avoided [182].

It should be noted that the scaling step implies that DFA exponents cannot be recovered from the parameters of the linear or spline models following ML-DFA. For this reason, if a spline model is found to be the best-fitting model and the user is interested in the value of the exponents at each scale – as is sometimes used in clinical studies of heart beat variability [269] – then the user should apply standard DFA to each segment separately to obtain the corresponding exponents.

### 2.5.2 Akaike's Information Criterion

Akaike's Information Criterion (AIC) is used to compare the goodness-of-fit of probability distributions [6]. For a model using $k$ parameters, with likelihood function $\log\mathcal{L}$, the Akaike Information Criterion is calculated using the following expression:

$$\mathrm{AIC} = 2k - 2\log\mathcal{L} + \frac{2k(k+1)}{n-k-1}$$

where $k$ is the number of parameters that the model uses. Note that the formula proposed by [134] is used, which accounts for small sample sizes with the final term $\frac{2k(k+1)}{n-k-1}$, as advocated by [39, 45, 183] amongst others. The model which provides the best fit to the data is that with the lowest value of AIC.

### 2.5.3 Bayesian Information Criterion

The Bayesian Information Criterion was developed by Akaike and Schwartz [251]. It puts harsher restrictions on the parameter number required for the model:

$$\mathrm{BIC} = -2\log\mathcal{L} + k\log(n).$$

As with the AIC, the model which provides the best fit to the data is that with the lowest value of BIC.

It is important to recall that both AIC and BIC can only be used to compare models. They do not give any information as to how good the models are at fitting the data, i.e., it is only their relative values, for different models, that are important; and it would not be possible, for instance, to compare AIC and BIC values obtained from different data sets to each other.

There is considerable discussion regarding which of the AIC or BIC measure is more effective at selecting the 'correct' model, and indeed it is possible to simulate situations in which one and the other is optimal [45]. In this analysis, the AIC and BIC measures will both be outputted, but ultimately conclusions will be based on the AIC when the two disagree. This is because the results will show that the AIC is more reliable in determining the best fit to fluctuation plots for signals whose functional form has previously been studied and is known, such as that of a sine function. This point will be returned to in the Discussion of this chapter.

### 2.5.4 Signal Simulation

In this section, FARIMA time series are generated (see Section 1.1.8.8). Because of the fact that FARIMA time series can be constructed to have variable levels of short and long-range temporal correlations, they can be used to generate a large range of different DFA fluctuation plots for which we understand the theoretical functional form. FARIMA time series therefore provide a good foundation of signals on which to test ML-DFA.

All simulations contain 100,000 innovations. This number of samples is of the same order of magnitude as the number of samples in many published DFA studies of EEG, e.g., $150,000$ samples for 4 minutes at 625 Hz sampling frequency [196] or $360,000$ samples for 20 minutes at 300 Hz sampling frequency [178]. Importantly, however, this number was chosen because it is comparable to, but shorter than, the number of samples in the EEG recordings analysed in this study. Note that the use of shorter synthetic time series reduces the risk of the results being biased by under-estimating any stochastic variation which may be more likely with much longer time series.

### 2.5.5 Signal-to-Noise Ratio

The signal-to-noise ratio (SNR) quantifies the level of noise with respect to that of the signal of interest, and is typically defined as the power ratio between the signal and the noise components of the recording. Since it could be argued that, as a noise-free signal, a FARIMA process does not exhibit the intrinsic noisiness of empirical data, we also generate times series in which a white noise is added to the data from a FARIMA process, and their relative amplitude systematically varied. The signal-to-noise-ratio is then calculated using the root mean square of their respective amplitudes. Specifically, letting the root mean square amplitude of the FARIMA signal be $A_F$ and the root mean square amplitude of the noise be $A_{noise}$, the SNR is determined as:

$$SNR = \frac{A_F}{A_{noise}}.$$

### 2.5.6 Matlab Code

The data from FARIMA processes were generated using Matlab code published by [264].

## 2.6 Results

In this section, ML-DFA is validated by application to signals with known characteristics in their DFA fluctuation plots.

### 2.6.1 Simulated Data

ML-DFA was applied to simulations of a FARIMA process. We first used FARIMA to generate self-similar fractional Gaussian noise with varying Hurst exponents (0.5-1), and then we altered its parameters to generate a more general non self-similar FARIMA signal. In order to assess the robustness of the approach to noise, such as may be encountered in recordings taken from natural phenomena, ML-DFA was also applied to time series in which data from a FARIMA process containing LRTCs were contaminated (additively) by white Gaussian noise, with varying level of signal-to-noise ratio. Finally, ML-DFA was also applied to sinusoidal signals with three different periods, and to sinusoidal signals with independently added noise.

1000 time-series of $100,000$ innovations were created. The DFA fluctuation plots of each of the generated time series were fitted with the set of alternative models listed in the Methods and Materials section. For each, the best model was determined using both the AIC and BIC measures. It is noted that, in addition to the models listed, all analyses included the quintic model as a candidate model. However, as no simulated signal was found to be best fit by a quintic model, this model is not included in any of the results shown.

In the Appendix for this chapter, and following a suggestion from a reviewer, synthetic data of length 8000 samples is also studied.

### 2.6.2 Fractional Gaussian Noise

Fractional Gaussian noise can be generated by a FARIMA(0,$d$,0) process with $0 < d < 0.5$. The case of $d = 0$ is called white Gaussian noise, however, we will here refer collectively to FARIMA(0,$d$,0) processes with $0 \leq d < 0.5$ as fractional Gaussian noise. Fractional Gaussian noise has been proved to be asymptotically scale-invariant, and therefore its associated DFA fluctuation plot should be linear with a slope $\gamma$ given by $d + 0.5$ [18, 268]. The value of $\gamma$ is an approximation to the Hurst exponent of the data, $H$, where $H = 0.5$ indicates Gaussian white noise and $H = 1$ indicates pink noise. ML-DFA is demonstrated on three simulations of fractional Gaussian noise, spanning the possible range of $d$ values.

DFA plots for three FARIMA time series with Hurst exponents of 0.5, 0.7 and 1.0 are shown in Figure 2.4A . The slopes of the DFA plots recover estimates of the Hurst exponents of 0.50, 0.71 and 1.01 respectively. Figure 2.4B-D shows that the results of ML-DFA confirm that a linear model is appropriate for each of the time series, thus validating the results of standard DFA.

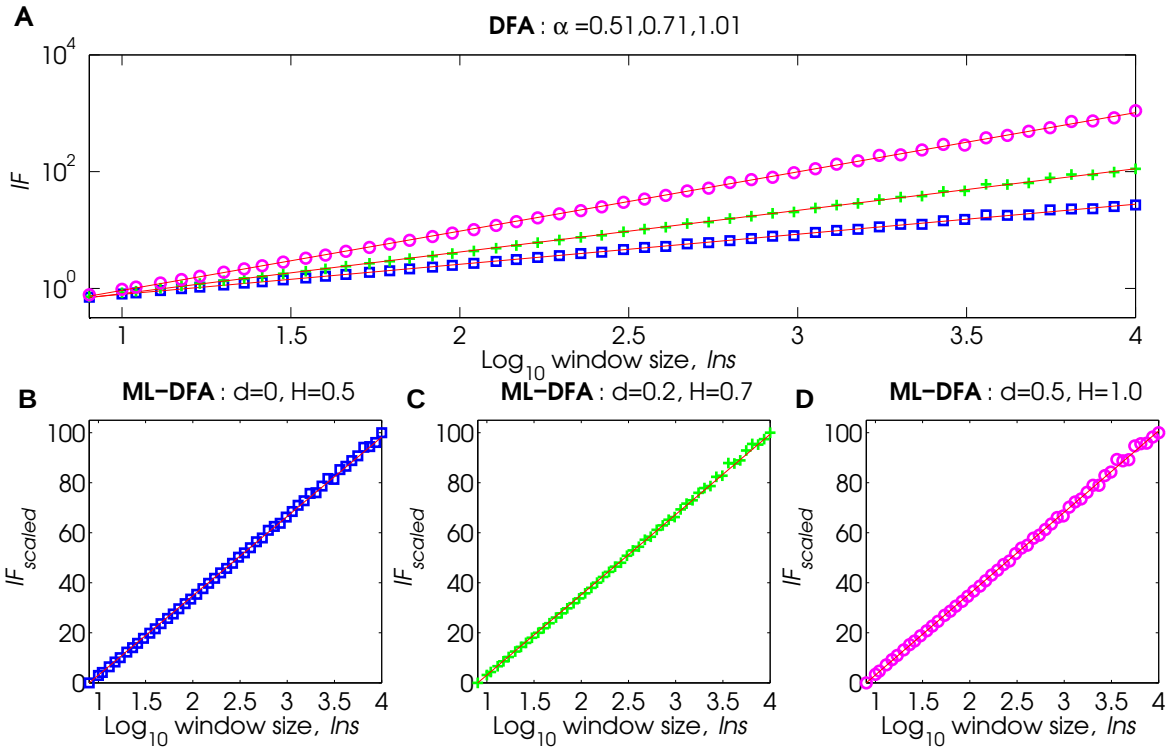


FIGURE 2.4: Time series and corresponding DFA fluctuation plots for signals obtained by FARIMA(0,$d$,0) processes with $\phi$ and $\theta$ set to 0 and with $d = 0$, and $d = 0.2$, and $d = 0.5$ to produce fractional Gaussian noise. Panel A shows the three DFA fluctuation plots fitted using standard DFA. Values $d = 0$, $d = 0.2$, and $d = 0.5$ will produce time series with Hurst exponents 0.5 (white noise, blue diamonds), 0.7 (correlated noise, green crosses) and 1 (pink noise, pink circles) respectively. The slopes estimated by application of standard DFA are stated at the top, and correspond closely to these theoretical values. Panels B-D show the best fit model according to the AIC measure in ML-DFA. The best-fit model is linear in all cases.

Tables 2.1 and 2.2 report the proportion of times out of 1000 simulations that each of the alternative models was found by ML-DFA to be the best fit, according to the AIC and BIC values respectively. We found that the AIC and BIC were both successful at identifying the linear model as the best fit in over 95% of the simulations. The mean slopes of those fluctuation plots that were not rejected were the same to 3 decimal places for both the AIC and BIC measures, and were 0.500, 0.696 and 0.995 respectively for expected Hurst parameters of 0.5, 0.7 and 1.0. The standard deviations for all slopes were 0.01.

### 2.6.3 FARIMA processes

The FARIMA(1,$d$,1) process is one which includes a single $\phi$ and a single $\theta$ coefficient, indicated by the parameter values of 1. It is possible to include a greater number of $\phi$ and $\theta$ coefficients, but only a single addition is considered for simplicity. Parameters $\phi$ and $\theta$ are varied in the range $0 < \phi < 1$, $0 < \theta < 1$, which satisfies the conditions $|\phi| < 1$, $|\theta| < 1$ for convergence [128]. Throughout this thesis, FARIMA($[\phi]$,$d$,$[\theta]$) will denote the FARIMA process with $\phi_1 = \phi$ and $\theta_1 = \theta$.

In the general case, a FARIMA(1,$d$,1) time series is not expected to be self-similar and therefore, the associated DFA fluctuation plots should not be linear. Variations in the $\phi$ and $\theta$ parameters contribute to a range of fluctuation plots, with examples in Figure 2.5 illustrating a number of cases in which different alternative models were found by ML-DFA to be the best fit.

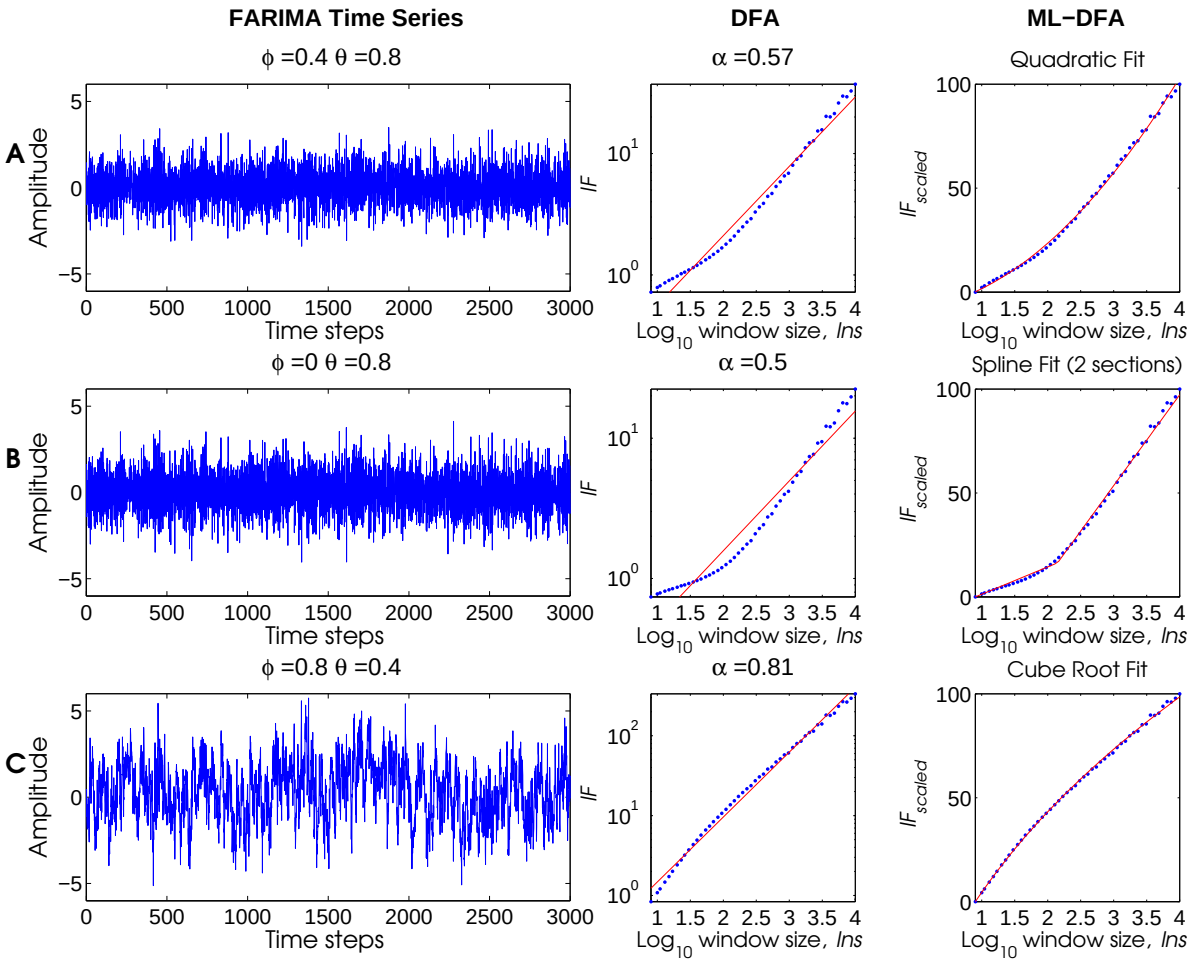


FIGURE 2.5: Time series and corresponding DFA fluctuation plots for signals obtained by FARIMA(1,0.2,1) processes with $d = 0.2$ taken as an representative value, and varying values of $\phi$ and $\theta$. Each row A-C corresponds to a different set of $\phi$ and $\theta$ coefficients, which alter the resulting DFA fluctuation plots. In each row, the left-hand side panel shows a representative 3000 innovations of the time series, the middle panel shows the fluctuation plot fitted using standard DFA with the resulting exponent $\gamma$ given above, and the right-hand side panel shows the best-fit model determined by ML-DFA using AIC.

In all cases, ML-DFA showed sensitivity to more or less subtle deviations from the linear model. Tables 2.2 and 2.1 provide the proportion of times out of 1000 simulations of FARIMA(1,$d$,1) time series that each of the alternative models were found by ML-DFA to be the best fit, using the AIC and BIC values respectively. In most cases (6/9 pure FARIMA scenarios), the results of AIC and BIC were compatible. Specifically, 4 of the 9 scenarios showed almost identical results (scenarios 1, 2, 6, 9) whilst 2 were qualitatively similar in that the same models were involved albeit with varying percentages (scenarios 3 and 8). Three scenarios showed substantial differences with different models being involved (scenarios 4, 5 and 7). However, on the most important point of whether the linear model hypothesis was to be rejected, there was strong agreement (8/9 pure FARIMA scenarios, 10/11 all scenarios) between AIC and BIC, the only exception being FARIMA([0.4],0.2,[0])

where BIC did not reject the linear model hypothesis in 31.1% of the runs (to be contrasted with 2.1% for AIC). This once again illustrates that because the BIC is less likely to select models with a greater number of parameters, it may show less sensitivity to very subtle deviations from the expected model, thus showing more false positives than AIC. To illustrate this point, the FARIMA([0.4],0.2,[0]) scenario is re-examined systematically varying the value of the $\phi$ parameter. Figure 2.6 shows that when $\phi = 0.4$ the DFA fluctuation plot could certainly be considered linear on visual inspection. However, closer examination (the reader may be assisted by a log-log plot of the autocorrelation function – it is helpful to remember that the DFA exponent is directly linked to the exponent of the power law in the autocorrelation function) reveals otherwise. Application of the runs test [288] on the residuals of the regression shows that the residuals are not independent ($p < 1e - 5$) which confirms that the BIC results are false positives. For comparison, the runs test for the fractional Gaussian noise returns $p > .2$. With increasing values of $\phi$, the distortion of the fluctuation plot (and associated autocorrelation function) becomes readily available to visual inspection and agreement between AIC and BIC is strong. Specifically, 100% of the simulations reject the linear model hypothesis and AIC and BIC return the same set of alternative models in more than 99% of the simulations for both $\phi = 0.6$ and $\phi = 0.8$.

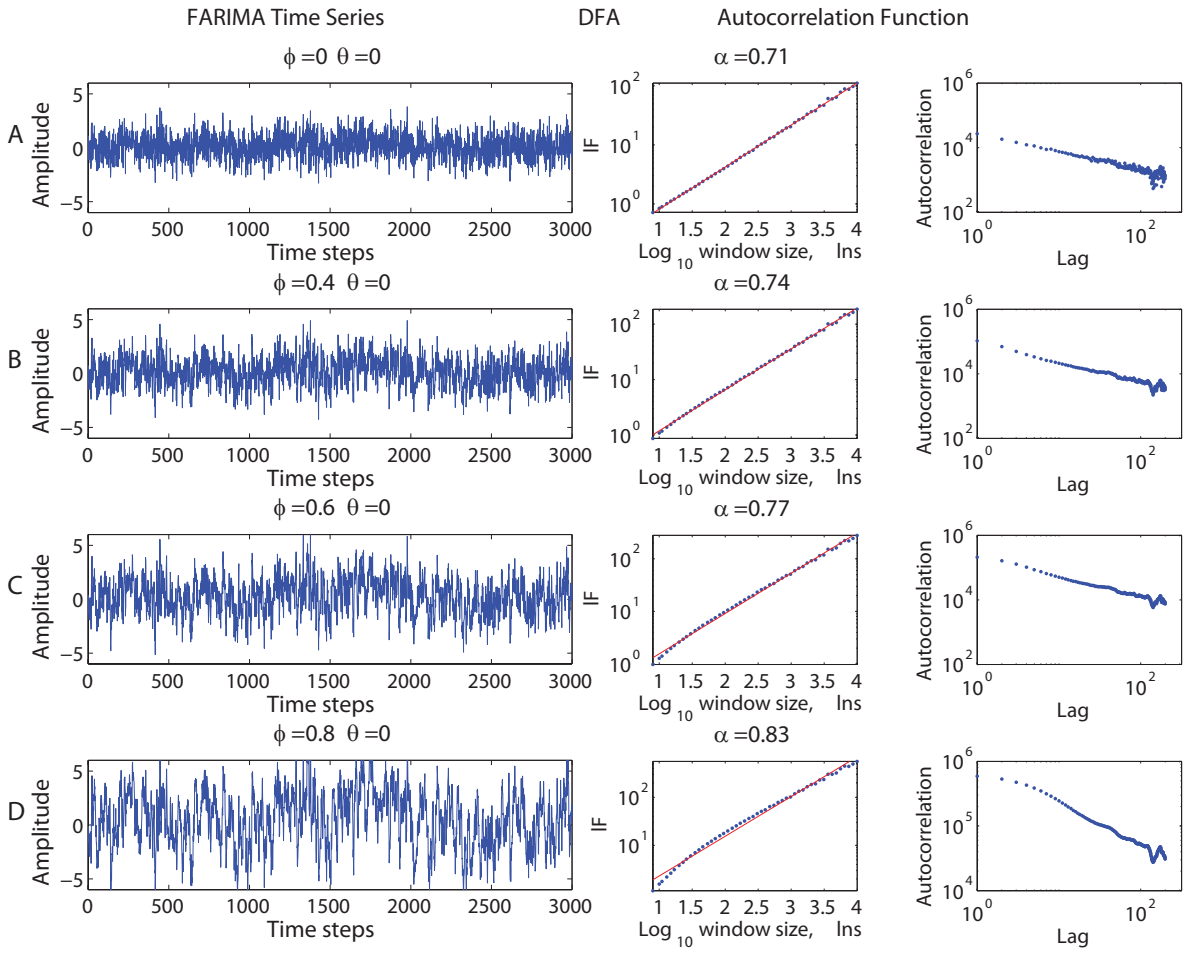


FIGURE 2.6: Time series, DFA fluctuation plots and autocorrelation functions for signals obtained by FARIMA([p],0.2,[0]) processes with varying values of $p$. Each row A-D corresponds to $\phi$ taking values from $0, 0.4, 0.6, 0.8$. In each row, the left-hand side panel shows a representative 3000 innovations of the time series, the middle panel shows the fluctuation plot fitted using standard DFA with the resulting exponent $\gamma$ given above, and the right-hand side panel shows the autocorrelation function of the (complete) signal in log-log coordinates.

### 2.6.4 FARIMA process with noise

As reported in [52], adding random spikes to a FARIMA time series with LRTCs and scaling exponent $\gamma > 0.5$ destroys the linearity of the DFA fluctuation plot obtained for the signal. The resulting fluctuation plot contains two segments of linear scaling – with exponents $\gamma > 0.5$ corresponding to the time series used, and $\gamma = 0.5$ corresponding to noise – connected by a smooth crossover. In this section, we report the application of ML-DFA to 1000 FARIMA(0,0.45,0) time series ($H = 0.95$) to which white Gaussian noises modelled by a FARIMA(0,0,0) are added, with signal-to-noise (SNR) values of $200, 100, 50, 20, 10, 5, 2$ and $1$ respectively. It should be noted that the stated SNR values are average values as

TABLE 2.1: ML-DFA results on synthetic data using AIC. From 1000 simulations of noise time series, the table gives the proportion of times that each of the alternative models was found to be the best fit, according to AIC values when ML-DFA was applied to fractional Gaussian noise, FARIMA(1,$d$,1) processes and noisy sinusoidal signals.

| | Linear | Non-linear | | | | | | | | |
|---|---|---|---|---|---|---|---|---|---|---|
| Model | $x$ | $x^2$ | $x^3$ | $x^4$ | $\sqrt[n]{x}$ | 4-$x$ | 3-$x$ | 2-$x$ | log | $e$ |
| FARIMA([0],0.5,[0]) | 96.6 | 3 | - | - | - | - | - | - | - | 0.4 |
| FARIMA([0],0.2,[0]) | 96.3 | 2.9 | - | - | - | - | - | - | - | 0.8 |
| FARIMA([0],0,[0]) | 95.9 | 2.8 | - | - | 0.1 | - | - | - | 0.1 | 1.1 |
| FARIMA([0.4],0.2,[0]) | 2.1 | 7.5 | - | - | 56.0 | - | - | - | 14.5 | 19.9 |
| FARIMA([0],0.2,[0.4]) | - | 77 | 19.3 | 0.1 | - | - | - | 1.2 | - | 2.4 |
| FARIMA([0.8],0.2,[0]) | - | - | 0.3 | - | 90.3 | - | - | - | 7.1 | 2.3 |
| FARIMA([0],0.2,[0.8]) | - | 47.7 | 2.8 | 2.8 | - | - | - | 45.5 | - | 1.2 |
| FARIMA([0.4],0.2,[0.8]) | - | 64.7 | - | - | - | - | - | 22.1 | - | 13.2 |
| FARIMA([0.8],0.2,[0.4]) | - | 0.4 | - | - | 76.5 | - | - | - | 13.5 | 9.6 |
| FARIMA([0],-0.2,[0])+sin($\frac{2\pi t}{200}$) | - | - | - | - | - | 7.4 | 92.6 | - | - | - |
| FARIMA([0],0,[0])+sin($\frac{2\pi t}{100}$) | - | - | - | 2 | - | 98 | - | - | - | - |

The fitted models are listed in the top row, alongside the proportion of best fits assigned to each one by the value of the AIC measure. The shorthand n-$x$ is used to denote a n-segment spline. The shorthand $\sqrt[n]{x}$ combines results for $n = 2, 3, 4$. The signals whose DFA fluctuation plots are analysed are described in the left-hand side column.

TABLE 2.2: ML-DFA results on synthetic data using BIC. From 1000 simulations, the table gives the proportion of times that each of the alternative models was found to be the best fit, according to BIC values when ML-DFA was applied to fractional Gaussian noise, FARIMA(1,$d$,1) processes and noisy sinusoidal signals.

| | Linear | Non-linear | | | | | | | | |
|---|---|---|---|---|---|---|---|---|---|---|
| Model | $x$ | $x^2$ | $x^3$ | $x^4$ | $\sqrt[n]{x}$ | 4-$x$ | 3-$x$ | 2-$x$ | log | $e$ |
| FARIMA([0],0.5,[0]) | 96.6 | 3 | - | - | - | - | - | - | - | 0.4 |
| FARIMA([0],0.2,[0]) | 96.3 | 2.9 | - | - | - | - | - | - | - | 0.8 |
| FARIMA([0],0,[0]) | 96.8 | 2.3 | - | - | 0.1 | - | - | - | 0.1 | 0.7 |
| FARIMA([0.4],0.2,[0]) | 31.1 | 4.6 | - | - | 40.6 | - | - | - | 11.4 | 12.3 |
| FARIMA([0],0.2,[0.4]) | 0.1 | 93.9 | 1.6 | - | - | - | - | 0.5 | - | 3.9 |
| FARIMA([0.8],0.2,[0]) | - | - | - | - | 90.4 | - | - | - | 7.1 | 2.5 |
| FARIMA([0],0.2,[0.8]) | - | 71.2 | 1.7 | - | - | - | - | 23.6 | - | 3.5 |
| FARIMA([0.4],0.2,[0.8]) | - | 86.3 | - | - | - | - | - | 0.4 | - | 13.3 |
| FARIMA([0.8],0.2,[0.4]) | - | 0.4 | - | - | 76.5 | - | - | - | 13.5 | 9.6 |
| FARIMA([0],-0.2,[0])+sin($\frac{2\pi t}{200}$) | - | - | - | - | - | 7.4 | 92.6 | - | - | - |
| FARIMA([0],0,[0])+sin($\frac{2\pi t}{100}$) | - | - | - | 15.1 | - | 84.9 | - | - | - | - |

The fitted models are listed in the top row, alongside the proportion of best fits assigned to each one by the value of the BIC measure. The shorthand n-$x$ is used to denote a n-segment spline. The shorthand $\sqrt[n]{x}$ combines results for $n = 2, 3, 4$. The signals whose DFA fluctuation plots are analysed are described in the left-hand side column.

the stochasticity involved in generating the FARIMA and noise time series means that the actual (measured) signal-to-noise ratios oscillate slightly around the stated/expected value. Figure 2.7 confirms that, as expected, increasing the level of noise in the signal, i.e., decreasing the SNR, leads to increased curvature of the DFA fluctuation plot. Tables 2.3 and 2.4 present the proportion of times (out of 1000) that each of the alternative models was found to be the best fit by the AIC and BIC respectively.

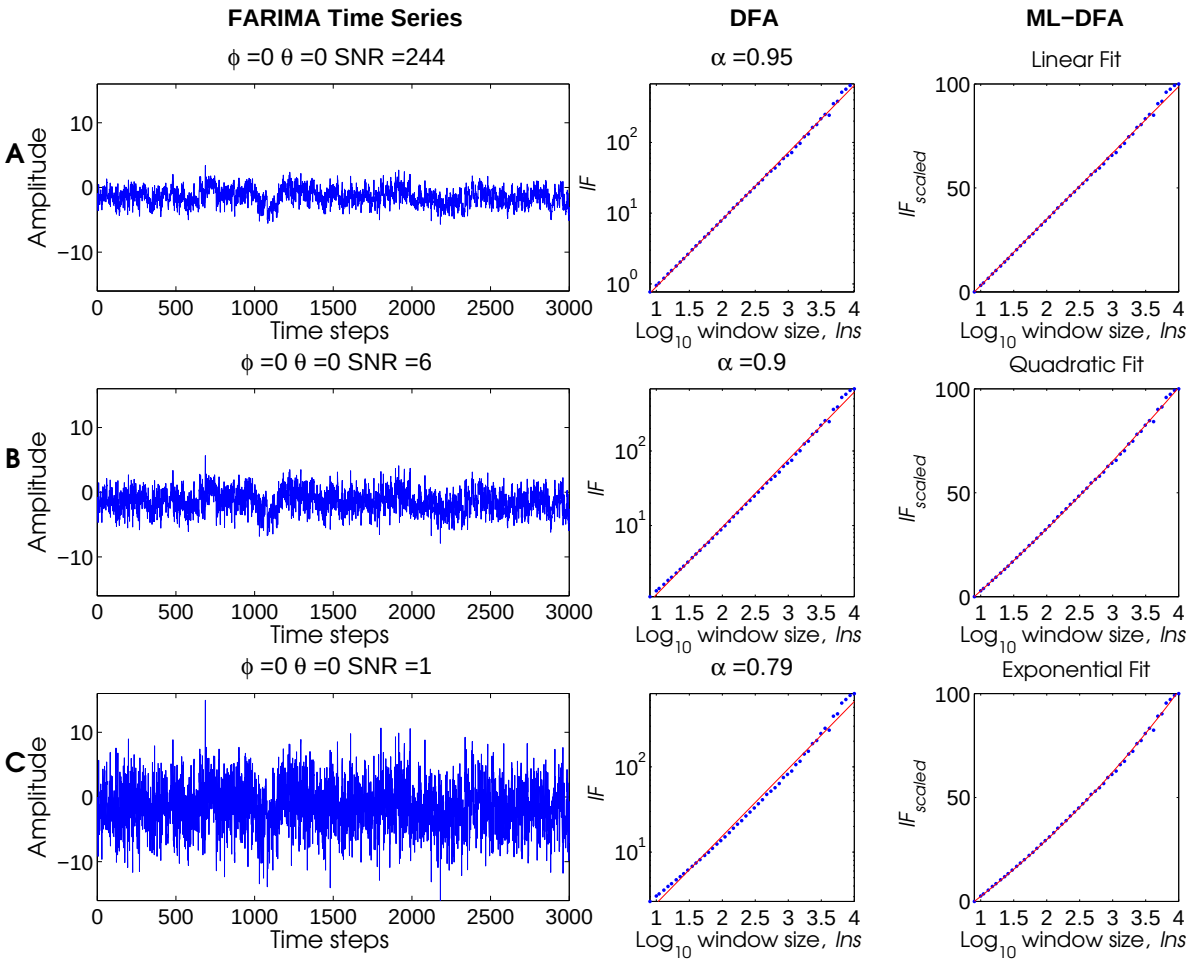


FIGURE 2.7: Time series and corresponding DFA fluctuation plots for signals obtained by FARIMA([0],0.45,[0]) processes with varying signal to noise ratio (SNR). Each row A-C corresponds to a different value of SNR, which alters the resulting DFA fluctuation plots. In each row, the left-hand side panel shows a representative 3000 innovations of the time series, the middle panel shows the fluctuation plot fitted using standard DFA with the resulting exponent $\gamma$ given above, and the right-hand side panel shows the best-fit model determined by ML-DFA using AIC.

When the SNR was 200, so that the time series was dominated almost completely by the FARIMA(0,0.45,0) process, it was found that the AIC and BIC measures gave identical results, with only 15 out of 1000 DFA fluctuation plots rejected because they were best fit by the quadratic or exponential models. For a SNR

value of 1, i.e., when signal and noise have equal power and fluctuation plots have a crossover [52], the AIC and BIC measures produced similar results whereby 100% (respectively 99.1%) of the fluctuation plots were rejected by the AIC and BIC measures. The propensity of the AIC measure to be stricter in rejecting noisy signals is clearly illustrated when the SNR is equal to 2 in particular. When the signal only has twice the power of the added noise, the AIC measure rejects 99.1% of the fluctuation plots whereas the BIC measure only rejects 80.5% of them.

TABLE 2.3: ML-DFA results on noisy synthetic data using AIC. From 1000 simulations, the table gives the proportion of times that each of the alternative models was found to be the best fit, according to AIC values when ML-DFA was applied to additive combinations of a FARIMA(0,0.45,0) and FARIMA(0,0,0) scaled by a constant value.

| | Linear | Non-linear | | | | | | | | |
|---|---|---|---|---|---|---|---|---|---|---|
| SNR | $x$ | $x^2$ | $x^3$ | $x^4$ | $\sqrt[n]{x}$ | 4-$x$ | 3-$x$ | 2-$x$ | log | $e$ |
| 200 | 98.5 | 1.3 | 0 | 0 | 0 | 0 | 0 | 0 | 0 | 0.2 |
| 100 | 97.9 | 1.8 | 0 | 0 | 0 | 0 | 0 | 0 | 0 | 0.3 |
| 50 | 96.6 | 2.9 | 0 | 0 | 0 | 0 | 0 | 0 | 0 | 0.5 |
| 20 | 82.4 | 16.1 | 0 | 0 | 0 | 0 | 0 | 0 | 0 | 1.5 |
| 10 | 79.7 | 16.8 | 0 | 0 | 0 | 0 | 0 | 0 | 0.001 | 3.4 |
| 5 | 49.1 | 37.5 | 0 | 0 | 0 | 0 | 0 | 0 | 0 | 13.4 |
| 2 | 0.9 | 82.3 | 0 | 0 | 0 | 0 | 0 | 0 | 0 | 16.8 |
| 1 | 0 | 87.9 | 0 | 0 | 0 | 0 | 0 | 0 | 0 | 12.1 |

The fitted models are listed in the top row, alongside the proportion of best fits assigned to each one by the value of the AIC measure. The shorthand n-$x$ is used to denote a n-segment spline. The shorthand $\sqrt[n]{x}$ combines results for $n = 2, 3, 4$. The signal-to-noise ratio (SNR) are given in the left-hand side column.

TABLE 2.4: ML-DFA results on noisy synthetic data using BIC. From 1000 simulations, the table gives the proportion of times that each of alternative models was found to be best fit, according to BIC values when ML-DFA was applied to additive combinations of a FARIMA(0,0.45,0) and FARIMA(0,0,0) scaled by a constant value.

| | Linear | Non-linear | | | | | | | | |
|---|---|---|---|---|---|---|---|---|---|---|
| SNR | $x$ | $x^2$ | $x^3$ | $x^4$ | $\sqrt[n]{x}$ | 4-$x$ | 3-$x$ | 2-$x$ | log | $e$ |
| 200 | 98.5 | 1.3 | 0 | 0 | 0 | 0 | 0 | 0 | 0 | 0.2 |
| 100 | 97.9 | 0.018 | 0 | 0 | 0 | 0 | 0 | 0 | 0 | 0.3 |
| 50 | 96.6 | 0.029 | 0 | 0 | 0 | 0 | 0 | 0 | 0 | 0.5 |
| 20 | 82.4 | 0.161 | 0 | 0 | 0 | 0 | 0 | 0 | 0 | 1.5 |
| 10 | 79.8 | 0.167 | 0 | 0 | 0 | 0 | 0 | 0 | 0.001 | 3.4 |
| 5 | 69.4 | 0.226 | 0 | 0 | 0 | 0 | 0 | 0 | 0 | 8 |
| 2 | 19.5 | 0.67 | 0 | 0 | 0 | 0 | 0 | 0 | 0 | 13.5 |
| 1 | 0.9 | 0.871 | 0 | 0 | 0 | 0 | 0 | 0 | 0 | 12 |

The fitted models are listed in the top row, alongside the proportion of best fits assigned to each one by the value of the BIC measure. The shorthand n-$x$ is used to denote a n-segment spline. The shorthand $\sqrt[n]{x}$ combines results for $n = 2, 3, 4$. The signal-to-noise ratio (SNR) are given in the left-hand side column.

### 2.6.5 Sinusoidal signals

From [129], the DFA fluctuation plot of a pure sine will have a crossover at a window size corresponding to the period of the oscillation, with a slope of 2 for small window sizes, and a slope of zero after the crossover point. These fluctuation plots are reproduced and demonstrate that they are best fit by a two-segment spline model, with crossovers as predicted by theory [129]. In Figure 2.8A-C, results for three pure sine curves with periods of 1000, 100 and 30 respectively are presented. It is observed that the crossover points in each plot are at 3, 2 and 1.48, which are the base-10 logarithms of 1000, 100 and 30, respectively. ML-DFA therefore recovers both the spline function and at its point of inflection the period of the original sine signal.

The addition of independent noise to sinusoidal signals has also been studied [129]. The DFA fluctuation plot of a sine signal with anti-correlated noise (Hurst exponent $H \in [0, 0.5)$) will have two crossover points, and therefore three segments. One will be located at the window size corresponding to the period of the oscillation, and one at a smaller window length. It is demonstrated in Figure 2.8D that ML-DFA identifies a three-segment spline as the best fitting model for such a fluctuation plot.

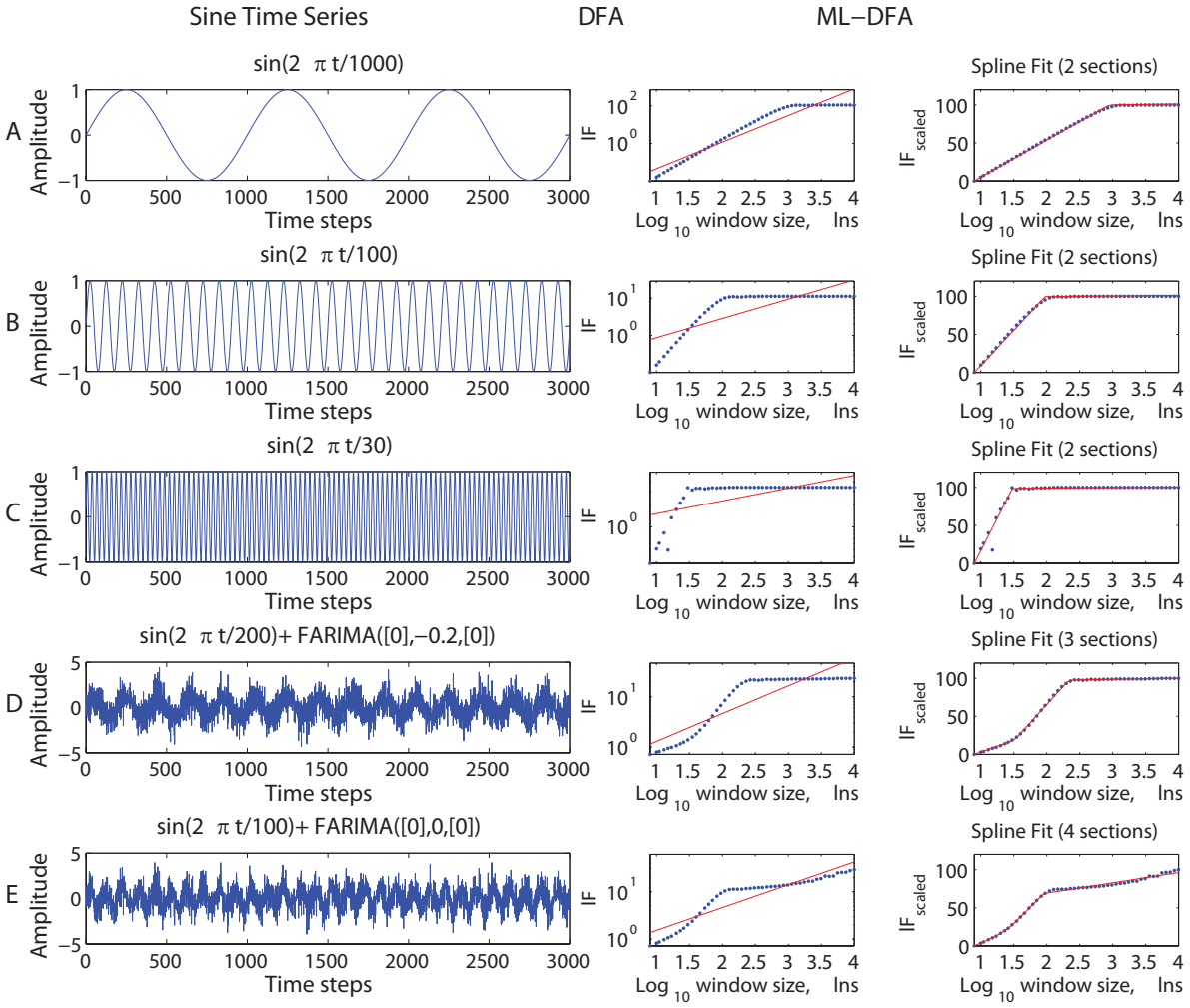


FIGURE 2.8: Time series and corresponding DFA fluctuation plots for 5 sinusoidal signals with varying levels of independent, additive noise. Each row A-E corresponds to a different sinusoidal function. In each row, the left-hand side panels show a representative 3000 innovations of the time series, the middle panel shows the fluctuation plots fitted using standard DFA, and the right-hand side panel shows the best-fit model as determined by ML-DFA using AIC.

A sine curve with independent, additive white or correlated noise will show three crossovers, or four segments in its DFA fluctuation plot. One crossover is again at the period of the sine curve. Figure 2.8E demonstrates ML-DFA alongside its resulting best-fit four-segment spline.

Tables 2.2 and 2.1 provide the proportion of times out 1000 simulations of two sets of sines with added noise that each of the alternative models was found to be the best fit by the AIC and BIC measures, respectively. No data are provided for repeated simulations of sines without added noise since these would produce rigorously identical fluctuation plots. Compared to the BIC measure, it was found that the AIC measure assigned a greater proportion of the DFA fluctuation plots

obtained from the sine with FARIMA([0],0,[0]) noise to the four-segment spline model (98% vs 84.9% for AIC and BIC, respectively), as predicted by theory [129]. The BIC measure returned a higher proportion of quartic model because of the reduced number of parameters. However, both AIC and BIC performed similarly in identifying the three-segment spline as the best fit for fluctuation plots of the sine with FARIMA([0],-0.2,[0]) noise, as expected.

Finally, it was found that all the results presented in this section are consistent when the FARIMA and sinusoidal time series used for application of ML-DFA is of length 8000 samples. The reader is referred to the Appendix for Chapter 2 for the presentation of these results.

## 2.7 Discussion

In this chapter a model selection approach for characterising DFA fluctuation plots (ML-DFA) has been presented with the aim of addressing a known shortcoming of DFA whereby there is no validated method for ascertaining the linearity of a fluctuation plot – a theoretically-derived asymptotic property of stationary, self-similar time-series. ML-DFA has been validated by applying it to DFA fluctuation plots obtained from FARIMA(0,$d$,0) time series, which have been shown to be asymptotically linear [18, 268]. ML-DFA has been systematically explored in relation to DFA plots obtained from time series generated by FARIMA(1,d,1) processes. These processes allow flexible combinations of long and short correlations in the time series thus inducing various types of loss of scaling. This, in turn, is expected to produce fluctuation plots that should be rejected as not being linear. The effect on ML-DFA of a varying signal-to-noise ratio using FARIMA(0,d,0) processes was also explored, i.e., pure self-similar time-series, that were contaminated with additive white noise. The piecewise linear form of the DFA fluctuation plot was recovered for sinusoidal signals, and sinusoidal signals with additive independent noise, as previously documented [129].

### 2.7.1 Stringency of the model selection approach

In a substantial number of cases, the application of ML-DFA to data with a controlled signal-to-noise ratio led to the rejection of the linear model hypothesis, contrary to what visual inspection and/or intuition may suggest. It is suggested that if the fluctuation plot of a particular experimental time series is rejected as not being linear, then this time series should not be included in the analysis. It has been suggested that such stringency makes ML-DFA too conservative to be of

practical value and that few studies in neuroscience could afford to discard such a number of samples. We believe that any assessment of the stringency of a model selection approach needs to be placed in the context of a decision (by the experimenter) as to what property of the data DFA is characterising. By construction, DFA seeks to quantify the presence of self-similarity in data, namely, the fact that the auto-covariance function of the signal has power-law decay. Although self-similarity implies the presence of long-lasting correlations in the data, it should be stressed that the mere presence of long-lasting correlations does not imply a power-law correlation structure. If it is the intention of the experimenter to test the presence of self-similarity in their empirical data, then we believe that a stringent approach is appropriate because not all non-random signals or signals with long-lasting correlations should be considered self-similar. As a model selection-based methodology, ML-DFA makes no assumption regarding the self-similar nature of the signal but will instead establish whether the linear model is the best model for the data available. It is only when that is the case that ML-DFA will consider a DFA exponent to be valid.

In the model selection approach, the best model is identified by the lowest value of the chosen information criterion (in this paper, AIC and BIC, see Section below). As demonstrated by the results, it is often the case that the information criterion for various models will be close in value. This should not be taken to mean that deviations from the expected model (here, the straight line) are subtle. Rather this is a result of the penalty assigned to the complexity of each of the models considered. Near identical BIC or AIC values for two models involving a significantly different number of parameters would actually reflect a large difference in the measure referred to here as the maximum likelihood of each model. In this regard, it is important to keep in mind that visual inspection of log-log data can be very misleading given the known tendency of log-log plots to 'flatten' distributions (i.e. flatter the linearity of distributions) [58].

If, on the other hand, the experimenter seeks to index the non-randomness of the data then it is indeed the case that ML-DFA may be too stringent. In the next section, a way by which this stringency could be mitigated is outlined. It is suggested, however, that the experimenter be clear about the interpretation of the exponents thus obtained, namely, that these are not strictly quantifying a power law decay of the correlations but rather that they index the presence of long-lasting correlations in the data (i.e., a decay slower than exponential but not necessarily power law). This may be particularly important given that non-trivial DFA exponents are often used to make statements about the fact that the underlying system may be operating at criticality.

### 2.7.2 AIC vs BIC

The outcomes of using both the AIC and BIC measures have been stated throughout. As mentioned previously, there is much discussion about which of these criteria is the best (see, e.g., [45, 144]). A key argument in favour of BIC is that it is, by construction, an approximation to the Bayes factor, which is considered by many to be the only possible approach to model selection (see Chapter 1 of [70], and [305] which tries to combine the two measures). In contrast, others argue that the strength of AIC comes from its foundation in Kullback-Leibler information theory [45]. In [144], it is stated that BIC is often preferred because of its tendency to select simpler models, i.e., those with fewer parameters [275]. In the context of the work in this thesis, such a preference would result in BIC showing a bias toward selecting the linear model as the most likely candidate. The results presented here show that this is indeed the case, with the result that AIC shows fewer false-positives for time series of known scaling – although see Section on signal-to-noise ratio below. This was demonstrated by the fact that a greater proportion of time series generated by FARIMA(1,$d$,1) processes were rejected as not being linear – a result that would be expected – and by the clearer distinction that the AIC drew between a pure correlated FARIMA process and one that has been additively contaminated with white noise. Furthermore, the AIC was more successful at correctly identifying the fluctuation plots that would be expected to be four-segment splines because they were obtained from a sinusoidal curve with independent, additive anti-correlated noise [129]. The BIC often selected a quartic model instead, because of its fewer parameters. For this reason, and based on a strict interpretation of the purpose of DFA, it is suggested that AIC should be used to determine the best-fitting model.

### 2.7.3 Signal-to-noise ratio

When investigating the robustness of the proposed methodology to varying levels of signal-to-noise ratio, it was found that the AIC and BIC rejected a high proportion of DFA fluctuation plots when SNR was low, which agreed with a previous result [52]. When the SNR was equal to 2, i.e., when it should be difficult to distinguish signal from noise, and therefore to develop reliable conclusions based on analysis, the AIC criterion rejected 99.1% of the fluctuation plots, which seems appropriate. Note that, in keeping with the observation that BIC favours the simpler model, the BIC measure only rejected 80.5% of the fluctuation plots. For all SNR greater than 10, there was good agreement between AIC and BIC with fewer than 20% of the 1000 fluctuation plots rejected at SNR of 10. The greatest discrepancy between AIC and BIC was observed at SNR of 5 where AIC rejected 50% of the

plots compared to 30% by the BIC. It has been suggested that rejecting half of the plots for a SNR of 5 was excessive. In this regard, we would like to refer the reader to the above discussion. If the aim is to assess the presence of self-similarity in the resulting time series (a true self-similar system contaminated by $\approx 20\%$ noise, then we believe that the results are appropriate in that they reflect that the signal is no longer self-similar. We do appreciate, however, that in scenarios in which a SNR of 5 is considered to be very good or, perhaps, when there is a strong prior that the underlying data may actually be self-similar, then the experimenter may prefer to use the BIC. For example, it is observed that significant additive noise yields DFA plots for which a quadratic or exponential model is best. Therefore, if an experimenter has good reason to expect that their data are contaminated by such noise, it may be that the finding of such plots by ML-DFA will still allow them to argue that their underlying signals are self-similar. Irrespective of the choice of criterion, however, these results demonstrate the sensitivity of ML-DFA to the presence of noise in time series, and suggest that ML-DFA may have considerable implications for practical research. It should be noted, however, that this analysis was limited to additive forms of noise. Where noise is multiplicative, the distinction between signal and noise becomes particularly challenging to make and is beyond the scope of this chapter.

### 2.7.4 Assessment of linearity of fluctuation plots

It is important to stress that ML-DFA does not verify or demonstrate the linearity of a plot. Merely, it concludes that a linear model is the best choice given the set of alternative models considered. For this reason, it is important to carefully select the set of alternative models. Since fluctuation plots should always be monotonic because the fluctuations of a time series will yield an error of at least equal size for windows of greater length, only models that (a) can capture the monotonicity of a DFA fluctuation plot and (b) are informed by experience and previous studies of non-linear DFA fluctuation plots have been considered. Note that the necessarily finite set of alternative models means that there is always a possibility that a different model could prove a better fit and therefore one should be very cautious of drawing conclusions about the nature of a time-series based on the best-fit model. Further, because the best fitting models are calculated from initial parameters that are set randomly; using a set of closely-related models with an equal number of parameters may result in different best-fit models for different runs of ML-DFA. To address this concern, initial parameters for the polynomial models were set to those that best fitted the fluctuation plots in a least square sense; however, this remains an open issue for arbitrary models. It is for these two above reasons that the focus has been primarily on whether the linear model

hypothesis is rejected and we do not focus on interpreting or explaining why a particular functional form was the best fitted model.

Several papers have discussed non-linear DFA fluctuation plots for specific time series. A DFA fluctuation plot which flattens out with increasing box size typically reflects a periodic signal, such as a sine [129]. Increasing fluctuations at large window sizes may be consistent with a noise process with segments removed, one with spikes added, one using concatenated segments of different standard deviations, or else with a power law trend [52, 53, 129]. Finite-size effects cause smaller windows to always have fluctuation magnitudes below the expected regression line [43].

Additionally, a fluctuation plot can be non-linear if the DFA scaling exponent is not a single value, but comes from a distribution. In this case, it may be relevant to apply multi-fractal DFA [149]. If the scaling behaviour of a time series is not constant across time, then a suitable technique is Adaptive Time-varying DFA [27], which uses optimal filtering to track changes in DFA exponent over the record. Any of these considerations may help elucidate a DFA fluctuation plot for which the linear model hypothesis is rejected.

### 2.7.5 Choice of window sizes

FARIMA signals do not have a characteristic time scale, so the minimum window size can be small, and 8 innovations were taken (a smaller window size of 1 or 2 innovations would have given an artefactual result because 1 or 2 samples can always be fitted perfectly by a line and the fluctuation magnitude will thus always be zero, a minimum window size of 4 samples can cause inaccuracies due to finite-size effects [43]). For the sinusoidal curves, 8 innovations were also used for the minimum window, which was smaller than the cycle period, precisely to allow us to demonstrate the crossovers in the fluctuation plot.

The maximum window size was set to a tenth of the length of the time series for all signals considered to allow a sufficient number of values for a robust estimate of an average fluctuation size [117]. In order to obtain a reliable fluctuation plot for larger time scales, a longer data series would typically be required [178]. In general, the use of these or similar guidelines is recommended for correct application of DFA and ML-DFA to biological data.

DFA exponents have previously been used to differentiate between clinical and healthy populations [1, 155, 203, 213, 236, 253, 289]. These studies applied rigorous statistical testing to identify differences between the DFA exponents obtained in each condition and/or population, however, the exponents themselves were not

subject to an equally thorough examination of whether the linear scaling hypothesis of the DFA fluctuation plot is supported. The ML-DFA technique provides the means to establish whether exponents from each of the recorded time series can be subject to further analysis. Its application would therefore have a two-fold benefit. First it would increase confidence in any reported differences. Second, it would make it possible to ask the valuable question of whether disorders that were previously characterised in terms of changes in the value of DFA exponents, could in fact be better characterised by loss of scaling. In fact, a loss of scaling in a previously scale-free system may be of much greater scientific interest. More research is therefore required to investigate whether stringent assessment criteria of the linearity in DFA plots will also discriminate between data from healthy controls, and subjects possessing a neurological or neuro-psychiatric disorder. More generally, we believe that this could lead to an interesting re-evaluation, whereby loss of scaling becomes a key marker in its own right, along with change in the strength of LRTCs.

The EEG and EMG time series introduced in the first section of this chapter are returned to in the next chapter, and DFA is applied to their amplitude envelopes, using ML-DFA to validate the results.

# Chapter 3

# Assessing the presence of LRTCs in the amplitude envelope of EEG and EMG

## 3.1 Introduction

Detrended Fluctuation Analysis (DFA) has previously been used to assess the presence of long-range temporal correlations (LRTCs) in the amplitude envelope of human EEG time series [28, 178]. In this chapter, the effects of the application of ML-DFA to human EMG as well as EEG data are investigated, and it will be demonstrated that ML-DFA lends insight to the question of whether LRTCs are present in the amplitude envelope. Specifically, it will be demonstrated that ML-DFA is a useful tool for being able to distinguish between data with power law scaling in its associated amplitude envelope DFA fluctuation plot, and data where this may not be the case.

Non-linearities in the DFA fluctuation plot may occur for a number of reasons, such as the fact that a time series may not be sufficiently long to obtain robust results from application of the technique. Another reason may be that the data recording contains artefacts which disrupt the power law scaling in the detrended fluctuation magnitude. It would be desirable to remove such data from any further analysis.

A data set analysed in the recent paper by Berthouze et al. [28] and previously used in James et al. [140] provides an informative basis for an investigation of the application of ML-DFA to neurophysiological time series. The data set contains EEG and EMG recordings from subjects with a range of different ages, who were asked to perform a steady pincer grip hold (see Section 2.2). Due to the nature

of a pincer grip, this task presented a different level of difficulty for individuals of different ages. Specifically, young children were not able to maintain a steady grip for long time periods, which sometimes caused artefacts in the data (see Section 2.2). This implies that in particular, data collected for the youngest age group of children younger than 36 months is more likely to contain artefacts and may not be as good in quality as that collected from the older subjects. Indeed, when this data was analysed in [28], a number of artefact removal procedures were necessary and were performed. In the analysis of the data here, the raw data was used. Artefacts were not removed prior to analysis and data containing artefacts was not rejected. This allowed a range of time series qualities for application of ML-DFA.

## 3.2 Data

The data analysed in this chapter is that described in Section 2.2.

## 3.3 Methods

The time series used in this chapter come specifically from the EEG recording at the C3 electrode and the EMG signal recording from the right first dorsal interosseous (R1DI) muscle of each subject. These time series were selected for analysis because the task involved the use of the R1DI muscle, so that the EMG was non-trivial. The C3 recording was used because activation of the R1DI muscle is modulated by the left motor cortex in healthy subjects. These time series were bandpass filtered in the 16-24 Hz $\beta$ frequency range prior to analysis. The $\beta$ band was selected because the EEG and EMG data was recorded during a pincer grip task during there was a spectral peak in these frequencies (Section 1.1.4.4). The amplitude envelope of the bandpass filtered time series was computed (Section 1.1.6.4). DFA and ML-DFA was applied to the amplitude envelope in order to compute the DFA exponent and to verify the validity of the obtained exponent.

### 3.3.1 Statistical tests of differences in exponent value

A one-sample t-test was used to compare the valid DFA exponents of subjects to a value of 0.5 in all the age groups.

### 3.3.2 Statistical tests for proportion of valid exponents

Equality of proportions of valid DFA exponents across different groups was tested using a $\chi^2$ test of homogeneity. The Pearson $\chi^2$ statistic was calculated:

$$\sum_{i=1}^{k} \frac{(o_i - e_i)^2}{e_i}$$

where index $i$ indicates the group number from the $k = 4$ groups. The value $o_i$ is the observed proportion of valid DFA exponents. Specifically:

$$o_i = \frac{x_i}{n_i}$$

where $x_i$ is the number of valid DFA exponents and $n_i$ is the number of subjects in group $i$. The value $e_i$ is the expected proportion of valid DFA exponents for group $i$ under the hypothesis that the proportion of valid exponents is identical for all groups. Specifically:

$$e_i = n_i \times \frac{\sum_{i=1}^{k} x_i}{\sum_{i=1}^{k} n_i}$$

Pearson's $\chi^2$ statistic was compared to a $\chi^2_2$ distribution with 2 degrees of freedom. The number of degrees of freedom is calculated by $k-1-p$ where $k$ is the number of groups $k = 3$ and $p = 1$ is the number of degrees of freedom in the null hypothesis.

### 3.3.3 Control Analysis

The steps of the method used to analyse the EEG and EMG data were also applied to time series of white Gaussian noise, which matched those of EEG and EMG data in length. One Gaussian white noise time series was generated for comparison to both the EEG and EMG because the length of the EEG and EMG time series are identical. The DFA exponents obtained from the analysis of white Gaussian noise signals were compared to those from the EEG and EMG time series individually using a one-tailed Student's t-test.

## 3.4 Results

ML-DFA was applied to EEG and EMG data, according to the method set out in Linkenkaer-Hansen et al. [178]. Specifically, the power spectrum of the EEG / EMG was taken, and the peak corresponding to the $\alpha$ rhythms and bandpass filtered the signal was used to isolate the corresponding range. Following this, the amplitude envelope was obtained by using the Hilbert transform, and applied standard DFA and ML-DFA. The amplitude envelope $A(t)$ was obtained using the steps described in Section 1.1.6.3.

### 3.4.1 Analysis of EEG

Figure 3.1 shows 1 second of the raw and bandpass filtered EEG signal and the corresponding amplitude envelope for a representative subject. The DFA fluctuation plot is also shown.

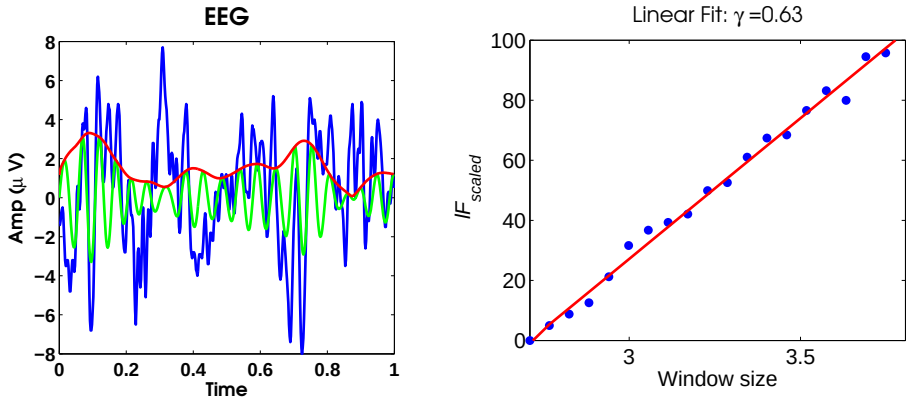


FIGURE 3.1: DFA and ML-DFA results on the amplitude envelope of EEG recorded at the C3 electrode and bandpass filtered to 16-24Hz range. This example corresponds to Subject 4 of Group 3. The data was recorded with a sampling rate of 512 Hz and filtered in a frequency band of 4-256 Hz prior to further analysis.

The DFA exponents calculated from the amplitude envelope of the bandpass filtered EEG signal are given in Table 3.1. Exponents found to be valid using ML-DFA are indicated by an asterisk. Only these exponents were used in any further analysis and calculation (e.g. of t-test statistics).

All valid DFA exponents are greater than 0.5, indicating that LRTCs are present in the amplitude envelope of EEG time series. The difference is significant at the 5% level. This is in agreement with the result of [28].

TABLE 3.1: DFA exponents for the amplitude envelope of beta band EEG for all subjects. The Groups represent different ages as previously detailed in Chapter 2, namely these are Group 1 (0-36 months), Group 2 (4-10 years), Group 3 (12-17 years) and Group 4 (19-59 years). Exponents from DFA fluctuation plots shown to be valid by ML-DFA are marked with an asterisk. The mean and standard deviation takes only these exponents into account. The proportion of valid subjects in each group and the $p$-value obtained by a t-test to assess the difference between the exponents and 0.5 are shown. All exponents are given to 2 d.p.

| Subject | Group 1 | Group 2 | Group 3 | Group 4 |
|---|---|---|---|---|
| 1 | 0.48 | 0.66 $*$ | 0.58 $*$ | 0.68 $*$ |
| 2 | 0.57 | 0.57 | 0.62 $*$ | 0.79 |
| 3 | 0.71 | 0.73 | 0.61 $*$ | 0.61 |
| 4 | 0.67 $*$ | 0.69 $*$ | 0.65 $*$ | 0.65 |
| 5 | 0.72 $*$ | 0.61 | 0.93 $*$ | 0.62 $*$ |
| 6 | 0.58 $*$ | 0.53 | 0.92 $*$ | 0.69 $*$ |
| 7 | 0.54 | 0.54 | 0.58 | 0.65 |
| 8 | 0.85 $*$ | 0.58 $*$ | 0.62 $*$ | 0.59 $*$ |
| 9 | 0.51 | 0.63 | 0.64 $*$ | 0.64 $*$ |
| 10 | 0.54 $*$ | 0.77 $*$ | 0.61 $*$ | 0.90 $*$ |
| 11 | 0.60 | 0.76 $*$ | 0.67 $*$ | 0.67 |
| 12 | 0.49 | 0.72 $*$ | 0.61 $*$ | 0.82 $*$ |
| 13 | | 0.60 $*$ | | 0.57 |
| Mean | 0.67 | 0.68 | 0.68 | 0.71 |
| Standard Deviation | 0.12 | 0.07 | 0.12 | 0.12 |
| Proportion valid subjects | 0.42 | 0.54 | 0.92 | 0.54 |
| $p$-value | 0.002 | 1.83E-05 | 1.99E-04 | 1.74E-04 |

Group 1, which contains data from children younger than 36 months has the lowest proportion of valid subjects. The significance of this difference was tested using the Pearson's $\chi^2$ statistic.

Pearson's $\chi^2$ statistic was calculated to be 2.84 to 2 significant figures. This corresponds to a cumulative $\chi^2$ $p$-value of 0.24, indicating that the null hypothesis of equal proportions of valid subjects in each group is not rejected at the 5% level. This difference in the number of valid subjects in each group is therefore not significant.

### 3.4.2 Analysis of EMG

Figure 3.2 shows 1 second of the raw and bandpass filtered EMG signal and the corresponding amplitude envelope for a representative subject. The DFA fluctuation plot is also shown.

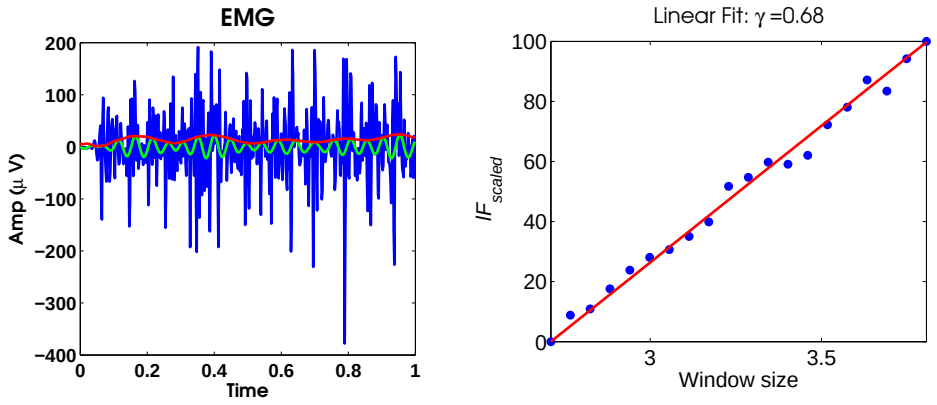


FIGURE 3.2: DFA and ML-DFA results on the amplitude envelope of EMG before rectification was perfromed, recorded at the R1DI muscle and bandpass filtered to 16-24Hz range. This figure corresponds to Subject 10 of Group 3. The data was recorded with a sampling rate of 512 Hz and filtered in a frequency band of 4-256 Hz prior to further analysis.

DFA exponents calculated from the amplitude envelope of the bandpass filtered EMG signal are given in Table 3.2. Exponents found to be valid using ML-DFA are indicated by an asterisk. Only these exponents were used in any further analysis and calculation.

TABLE 3.2: DFA exponents for the amplitude envelope of $\beta$ band EMG for all subjects. The Groups represent different ages as previously detailed in Chapter 2, namely these are Group 1 (0-36 months), Group 2 (4-10 years), Group 3 (12-17 years) and Group 4 (19-59 years). Exponents from DFA fluctuation plots shown to be valid by ML-DFA are marked with an asterisk. The mean and standard deviation takes only these exponents into account. The proportion of valid subjects in each group and the $p$-value obtained by a t-test to assess the difference between the exponents and 0.5 are shown. All exponents are given to 2 d.p.

| Subject | Group 1 | Group 2 | Group 3 | Group 4 |
|---|---|---|---|---|
| 1 | 0.75 | 0.89 * | 0.90 * | 0.72 |
| 2 | 0.68 | 0.78 * | 0.67 | 0.61 |
| 3 | 0.75 | 0.94 | 0.65 * | 0.72 * |
| 4 | 0.67 | 0.68 | 0.68 * | 0.72 |
| 5 | 1.13 | 1.18 | 0.88 | 0.68 * |
| 6 | 0.68 | 0.77 * | 0.75 * | 0.62 |
| 7 | 0.76 | 0.79 * | 0.82 * | 0.73 * |
| 8 | 0.74 | 0.78 | 0.72 | 0.96 |
| 9 | 0.80 * | 0.89 * | 0.89 * | 0.61 * |
| 10 | 0.94 | 0.83 * | 0.69 * | 0.83 * |
| 11 | 0.70 * | 0.83 * | 0.68 * | 0.65 * |
| 12 | 0.89 * | 0.87 * | 0.83 * | 0.79 * |
| 13 | | 0.72 | | 0.61 * |
| Mean | 0.80 | 0.83 | 0.76 | 0.70 |
| Standard Deviation | 0.09 | 0.05 | 0.10 | 0.08 |
| Proportion valid subjects | 0.25 | 0.62 | 0.75 | 0.62 |
| $p$-value | 0.001 | 3.91E-09 | 2.83E-06 | 8.90E-06 |

Group 1, containing the youngest subjects is again the age group that contains the lowest proportion of valid DFA exponents for its subjects.

Pearson's $\chi^2$ statistic was calculated to be 2.98 to 2 significant figures. This corresponds to a cumulative $\chi^2$ $p$-value of 0.23, indicating that the null hypothesis of equal proportions of valid subjects in each group is not rejected at the 5% level. This difference in the number of valid subjects in each group is therefore not significant.

### 3.4.3 Noise data

DFA exponents calculated from the amplitude envelope of a bandpass filtered time series of Gaussian white noise are given in Table 3.3. Exponents found to be valid using ML-DFA are indicated by an asterisk. Only these exponents were used in any further analysis and calculation.

TABLE 3.3: DFA exponents for the amplitude envelope of noise time series filtered in the $\beta$ band. The noise time series was matched in length to the EEG and EMG time series. Exponents from DFA fluctuation plots shown to be valid by ML-DFA are marked with an asterisk. The mean and standard deviation takes only these exponents into account. $p$-values for a one-sided Student's t-test between noise, EEG and EMG results, respectively, are given. All exponents are given to 2 d.p.

| Subject | Group 1 | Group 2 | Group 3 | Group 4 |
|---|---|---|---|---|
| 1 | 0.59 | 0.45 | 0.57 * | 0.62 * |
| 2 | 0.45 | 0.64 * | 0.62 * | 0.48 |
| 3 | 0.58 | 0.56 | 0.48 | 0.49 * |
| 4 | 0.60 | 0.51 | 0.50 * | 0.52 |
| 5 | 0.59 | 0.71 | 0.52 | 0.54 * |
| 6 | 0.49 | 0.62 | 0.55 * | 0.51 |
| 7 | 0.60 | 0.61 | 0.60 * | 0.54 |
| 8 | 0.59 | 0.51 | 0.57 * | 0.60 * |
| 9 | 0.58 * | 0.59 * | 0.60 * | 0.52 |
| 10 | 0.53 | 0.60 * | 0.51 | 0.51 * |
| 11 | 0.58 * | 0.51 | 0.48 | 0.55 * |
| 12 | 0.57 * | 0.49 | 0.53 * | 0.56 * |
| 13 | | 0.53 * | | 0.58 * |
| Mean | 0.58 | 0.59 | 0.57 | 0.56 |
| Standard Deviation | 0.01 | 0.05 | 0.04 | 0.04 |
| Proportion Valid Subjects | 0.25 | 0.31 | 0.67 | 0.62 |
| EEG $p$-value | 0.12 | 0.02 | 0.01 | 2E-03 |
| EMG $p$-value | 7E-03 | 5E-06 | 4E-05 | 2E-04 |

A comparison of DFA exponents obtained from EMG time series with those of noise time series shows a significant difference for all groups at the 5% level, however, for

EEG time series, there is no significant difference between DFA exponents between EEG time series and noise time series in Group 1.

The mean DFA exponent in this table is not equal to 0.5 because bandpass filtering of a pure noise signal will impose some structure on the signal, which is evident over the very short time scales of this data. The short time series are necessary in order to ensure that the noise data matches the recorded data in length.

## 3.5 Discussion

The amplitude envelope of both EEG and EMG signals showed a DFA exponent greater than 0.5 in all age groups indicating that LRTCs were present in these time series. Exponents in age groups 2, 3 and 4 were significantly different from those of white noise time series that were matched in length for the EEG and in all groups for EMG data. The lack of significant difference in DFA exponents for subjects of age group 1 may be a result of the difficulties of recording data during a steady pincer grip task in younger subjects.

The results in this chapter were additionally validated by the application of ML-DFA and agree with those of [28] regarding the $\beta$ band in particular.

The amplitude envelope of adult EMG has previously been shown to contain LRTCs in a previous conference paper [226], but not to my knowledge in a journal published paper. However, because EMG recorded from a muscle is closely connected to the force applied by that muscle, it is necessary to also mention a published paper, which recorded the presence of LRTCs in the force fluctuations during a finger movement task [10].

Group 1, which contained subjects aged 36 months or fewer contained the smallest number of valid subjects, which suggested that the potential artefacts caused by the inability of very young children to maintain a constant pincer grip may be responsible for non-linearities of the DFA fluctuation plots in this age group. However, the numbers of valid DFA exponents across the age groups were not significantly different from each other.

The study in this chapter provides a further justification for the application of ML-DFA to the analysis of neurophysiological time series, in which power law scaling of the detrended fluctuation magnitude may be disrupted by artefacts of recording. However, because the time series were not first cleared of potential noise and artefacts as in [28] it is necessary to add that the specific results that have been obtained in the course of in this chapter are provisional. In order to validate these results, it would be necessary to apply the methodology to a set of longer

time series, which contained fewer artefacts. In this case, it may be necessary to alter the task protocol slightly in order to allow the youngest subjects to perform the task for a long period of time, or to consider subjects only older than $\approx 3$ years old.

# Chapter 4

# The effect of window sizes on DFA

## 4.1 Introduction

In Chapter 2, a heuristic technique was introduced, which can be used to determine whether a DFA fluctuation plot may be considered to be linear. In Chapter 3, this technique is used in conjunction with classical DFA to analyse the amplitude envelope of a data set of EEG and EMG data from subjects of different ages. In this Chapter, DFA and ML-DFA are applied to a further data set. In particular, these techniques are applied to EEG data recorded from a group of twenty human subjects at rest. The analysis of Linkenkaer et al. is therefore replicated using the additional rigour of ML-DFA to test validity of fluctuation plots [178]. The effects of the choice of window lengths are studied over which DFA is calculated on the linearity or otherwise of the fluctuation plot.

The results presented in this chapter were also included in Chapter 2.

## 4.2 Data participants

### 4.2.1 Ethics Statement

Ethical approval was obtained from the ethics committee of the Royal Hospital for Neuro-disability, London UK, and informed consent was obtained from subjects. Consent was written and in accordance with local guidelines. Recording procedures were carried out in accordance with the declaration of Helsinki.

### 4.2.2 Neurophysiological Data

A total of twenty healthy subjects were recruited from the workforce at the Royal Hospital for Neuro-disability 6 males, age range 24-59 years, of mean age 39.94 years, $\pm 10.2$. None of the subjects had previous history of blackouts, faints, or psychiatric illness. None of the subjects were on any medication known to have centro-encephalic effects. All subjects were right handed.

The EEG recordings were conducted as part of a study exploring EEG changes occurring during music therapy. The subjects were seated in a comfortable chair with arm rests. A total of 23 Ag/AgCl electrodes (Unimed Electrodes, Surrey, UK) were applied individually to the scalp in accordance with the $10-20$ system of electrode placement [142]. Electrodes were fixed in place using Ten20 conductive paste (Weaver and Company, USA). Electrode impedances were maintained below $5K\Omega$. The EEG was acquired using an XLTEK Video-EEG monitoring system (Optima Medical, Putney, UK) which incorporated a 50 channel amplifier. The EEG signals were acquired using a sampling rate of 256Hz, and filter settings between $0.5-70$Hz without mains suppression. The montage regime used for on-line acquisition was common average reference [62]. Recordings were taken over a period of $40-60$ minutes. The initial 5 minutes of the recording was designated the baseline silence period (background noise 34dB) Here, the subjects were instructed to close their eyes on hearing a series of clicks. The initial 2.5 minutes of the baseline recording during the silence period were taken with the eyes open. Across the remainder of the session, subjects listened to different sounds/music the order of delivery having been randomly selected.

The recorded EEG signals were converted off-line to Laplacian derivation [124, 125]. Artefact rejection was performed through visual inspection of the EEG and Independent Component Analysis in EEGlab [71]. For this reason, the length of the continuous signals subjected to analysis varied from subject to subject but had a minimum length of approximately 20 minutes, and a maximum of 48 minutes. This corresponded to records of between 252,000 and 750,000 samples.

Mains artefacts (50Hz) were notch filtered using an infinite impulse response filter. The frequency band of interest (8-13 Hz) was extracted using bandpass finite impulse response (FIR) filtering and the Hilbert transform. The frequency band of 8-13 Hz was selected for the analysis of this data because in this chapter, the resting state is of interest to our analysis, and the recordings were performed specifically during resting state. The 8-13 Hz range is within the $\alpha$ frequency band, which is prevalent during the resting state (see Section 1.1.3.3). The filter order of the FIR filter was set to include three cycles of the lower-frequency component of the band, namely 8 Hz.

## 4.3 Results

### 4.3.1 Physiological Data

ML-DFA was applied to EEG data, according to the method set out in Linkenkaer-Hansen et al. [178]. Specifically, the power spectrum of the EEG was taken, and the peak corresponding to the $\alpha$ rhythms and bandpass filtered the signal was used to isolate the corresponding range. Following this, the amplitude envelope was obtained by using the Hilbert transform, and applied standard DFA and ML-DFA. The amplitude envelope $A(t)$ was obtained using the steps described in Section 1.1.6.3.

The steps of the method are demonstrated in Figure 4.1.

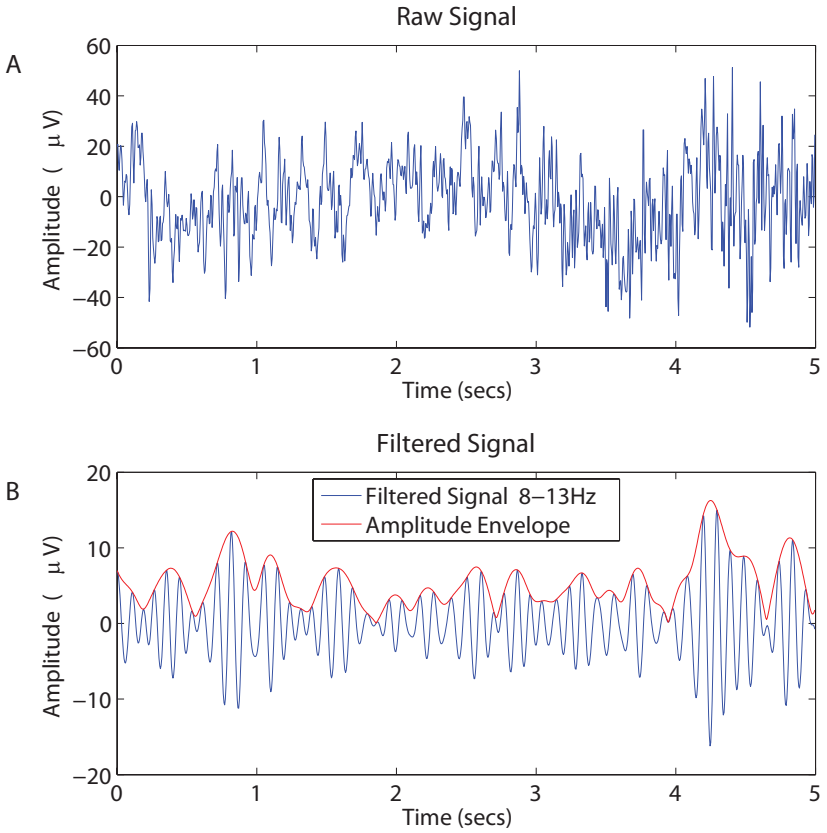


FIGURE 4.1: Preprocessing of the time series on an example EEG data set. Panel A shows the raw EEG signal. This is filtered between $8 - 13$ Hz for Panel B, and the amplitude envelope, derived from the real part of the Hilbert transform, is plotted above the filtered data.

DFA and ML-DFA were applied to $A(t)$, the amplitude envelope of an EEG time series filtered between 8 and 13 Hz. The minimum box size for applying DFA was 1 second of data, in order to include at least 8 oscillations at the minimum

frequency of the bandpass filter. The largest window size was set to one tenth of the full length of the data for each subject, as suggested by [196]. This allows a sufficient number of windows to provide a robust measure of the average fluctuation magnitude for a large window length, thus correcting for the variability of root mean square fluctuations from one window to the next. Note that, in [178] and [196], the window sizes are determined by inspecting a fluctuation plot that spans across all possible window sizes, and then the range of windows that adhere to a power law is selected for further analysis. This will be returned to in the Discussion of this chapter.

### 4.3.2 Human EEG Data

The best fit models are reported as determined by ML-DFA for the amplitude envelope of the EEG of 20 human subjects tested, which had previously been filtered between 8 and 13 Hz. For each subject, an EEG time series from the Cz electrode was used after artefact removal because of its central location on the scalp, leading to fewer potential artefacts caused by muscle movements or eye-blinks. If the best fit model, as assessed by the BIC value, is linear, then the DFA exponent is reported in Table 4.1.

Figure 4.2 shows 4 examples of each of the ML-DFA fit types obtained from the 20 subjects. These data were selected to illustrate both the linear fitting by standard DFA and a range of model fits that led to the rejection of the linear model hypothesis. In total, the linear model hypothesis was not rejected in 12/20 (AIC) and 16/20 (BIC) of the subjects (see Table 4.1).

In the appendix for this chapter, the DFA plots of the 4/20 subjects for which linear model was rejected by BIC are additionally presented.

Taken together, these results reveal that the assumption of scale invariance of the auto-correlation function of the data being tested is not always supported, and thus that some of the exponents returned by DFA do not necessarily provide an accurate description of the behaviour of the auto-correlation function. We suggest that if the fluctuation plot of a particular time series is rejected as not being linear, then this time series should not be included for further analysis.

### 4.3.3 Minimum and Maximum Window Sizes

In neurophysiological data, the choice of window sizes over which DFA is calculated is an important consideration. Using the data from one subject for which both the DFA fluctuation plot was best fit by a linear model according to both

AIC and BIC, the choice of how minimum and maximum window sizes affects the linearity of the DFA fluctuation plot is now explored. It can be demonstrated that using a minimum window length smaller than a minimum oscillatory period of the data examined gives rise to DFA fluctuation plots for which the linear model hypothesis is rejected. It is shown that taking a maximum window length larger than $\frac{N}{10}$ gives rise to DFA fluctuation plots for which the linear model hypothesis may be rejected.

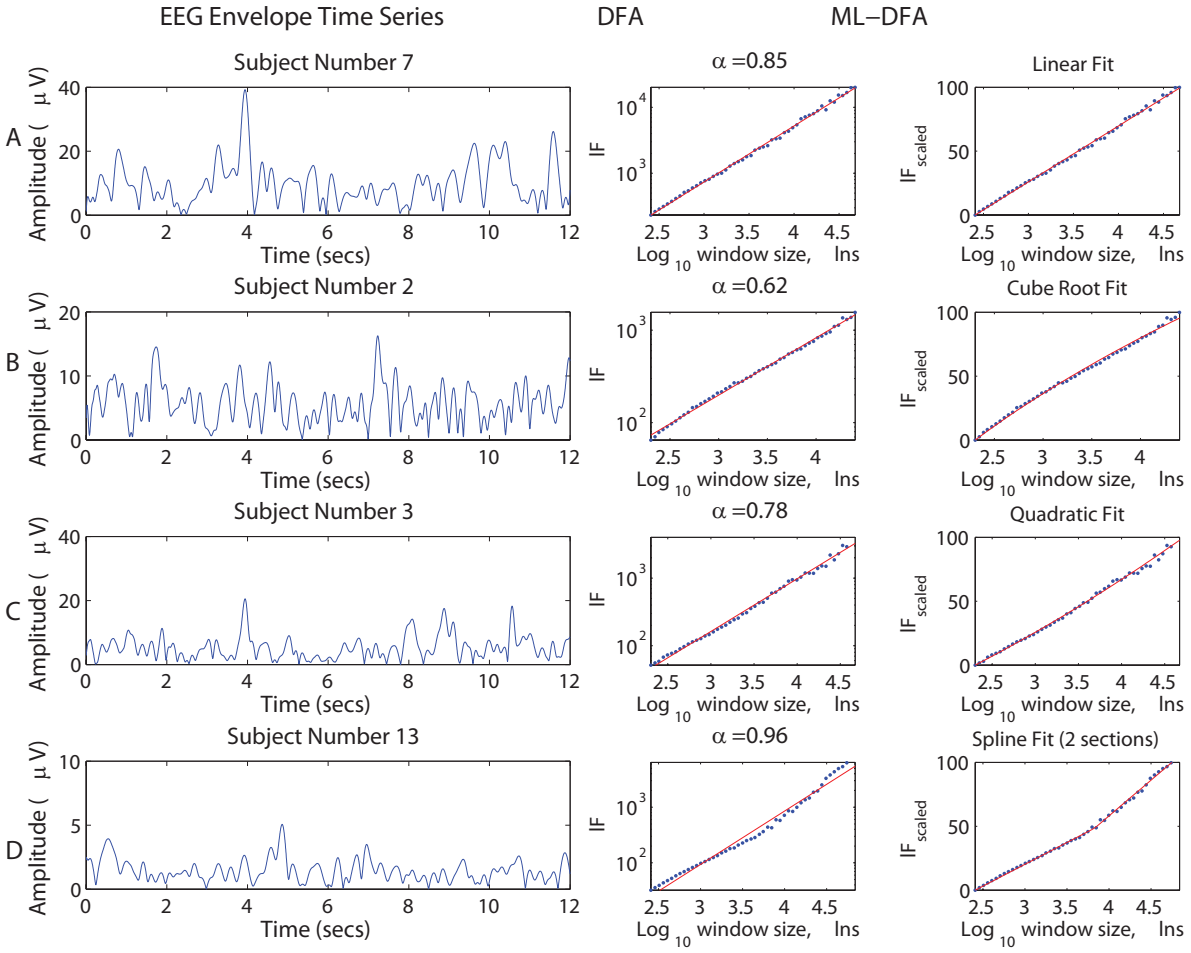


FIGURE 4.2: DFA fluctuation plots for 4 example signals from the Cz electrode of an EEG recording. Specifically, the 4 rows A-D correspond to subjects 2,3,7,13. In each row, the left-hand side panel shows a representative 12 seconds of the time series, the middle panel shows the fluctuation plot fitted using standard DFA with the DFA exponent $\gamma$ given above each plot, and the right-hand side panel shows the best fit model as determined by ML-DFA using AIC. Note that the x-axes of the fluctuation plots are given in seconds rather than samples, as in the corresponding figures for simulated data.

Figure 4.3 shows the application of standard DFA to the fluctuation plots of the EEG signal subject number 7, alongside the best-fitting model determined by ML-DFA using AIC. In Panel A, the minimum and maximum window sizes are set as

suggested by [196]. In Panel B, the minimum window length is set to 1 second of data as previously in Figure 4.2, while the maximum window length is $N$. The magnitude of detrended fluctuations grows more slowly for large window sizes due to the finite length of the data, and this gives rise to a two-segment spline as the best fit model. Such a model could be used to recover two exponents either side of the inflexion point, thus providing a more accurate description of the data. In Panel C of Figure 4.3, the minimum window size is set to 8 samples of the recording ($\approx$ 0.31 seconds), while the maximum window length is held constant at a tenth of the length of the time series, $\frac{N}{10}$ as before. The linear model hypothesis is rejected by the AIC method, because the best-fit model is logarithmic. This is consistent with the fact that, as the signal was filtered in the $\alpha$ range of 8-13 Hz, a minimum window length less than $\frac{fs}{8}$, is less than a single cycle of the slowest 8Hz frequency present, which will certainly produce a crossover, as shown in Figure 4.3. This crossover shows short time scales in the fluctuation plots of 0.03s, which is where the filter integration effect is evident. In order to select a suitable minimum window size for a signal, its characteristic frequency should be known. In this case, the characteristic frequency is not a single value, but a range between 8 and 13 Hz, so that the crossover in the fluctuation plot is not a single point (as with previously studied pure sine curves), but rather a range of points. It is for this reason that the best fit model is the smoother logarithmic model rather than a spline.

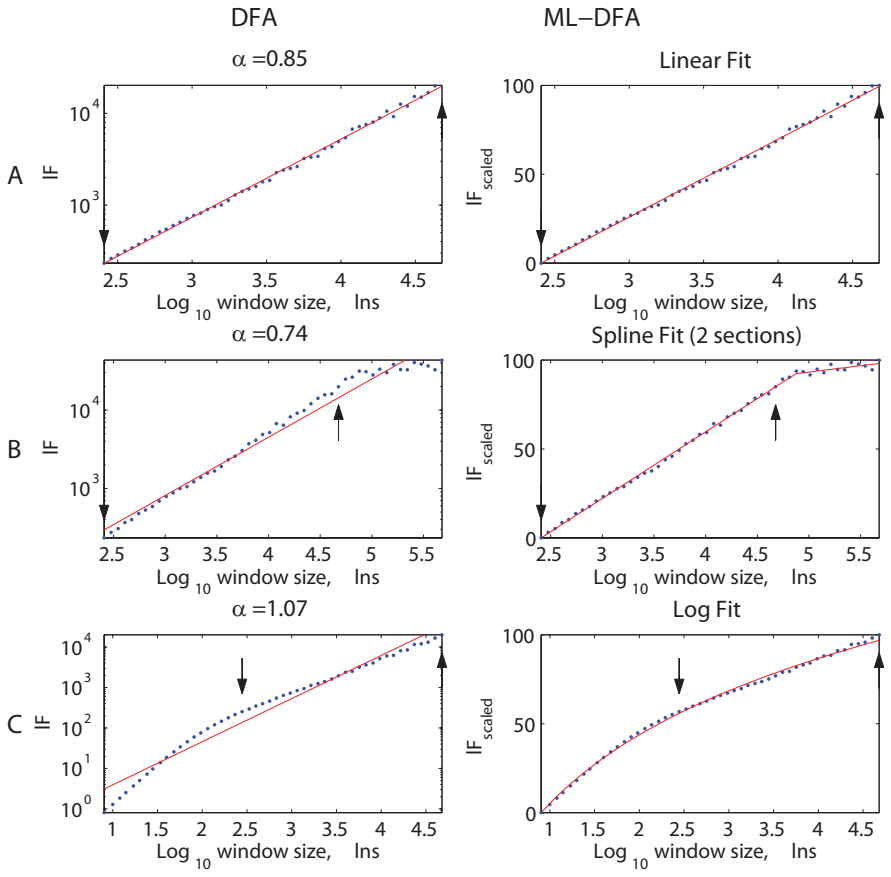


FIGURE 4.3: DFA fluctuation plots when different window lengths are used to analyse the Cz electrode signal of an EEG recording for subject number 7. Panel A shows the DFA and ML-DFA analysis performed for Subject 7 in Figure 4.2. The minimum window size is 1 second, and the maximum is $\frac{N}{10}$, or 187 seconds, both following [196]. The arrows in each plot indicate the range over which the fluctuation plot is calculated to obtain the DFA exponents in Tables 4.1, which is the full range of the fluctuation plot in Panel A. In Panel B, the minimum window length is also 1 second of data, and the maximum window length is $N$, which is the full length of the signal, or 1865 seconds (31 minutes) in this case. In Panel C, the minimum window length is 8 samples ($\frac{8}{256} \approx 0.031$ seconds) and the maximum window length is $\frac{N}{10}$, or 187 seconds. In each row, the left-hand side panel shows the fluctuation plots fitted using standard DFA with the DFA exponent $\gamma$ given above each plot, the right-hand side panel shows the best-fit model as determined by ML-DFA using AIC. Note that the x-axes of the fluctuation plots are given in seconds rather than samples, as in the corresponding figures for simulated data.

The ML-DFA analysis was applied to all 20 subjects. When the minimum window size was taken to be 8 samples (while keeping the maximum window size at $\frac{N}{10}$), the fluctuation plots of data for all 20 subjects were rejected as not being linear by both AIC and BIC. The DFA fluctuation plots for three additional subjects when a minimum window size of 8 samples is used are presented in the appendix for this chapter. This additionally demonstrates the filter integration effect, and shows that it is consistent across subjects.

When the maximum window size was set to $N$, and the minimum kept at 1 second,

application of ML-DFA resulted in 4/20 (BIC) and 10/20 (AIC) fluctuation plots for which the linear model hypothesis was rejected.

TABLE 4.1: Results of ML-DFA with the EEG signals obtained from the Cz electrode in 20 healthy subjects.

| Subject Number | Slope | AIC | BIC |
|---|---|---|---|
| 1 | 0.7861$^{\dagger}$ | Square Root | Linear |
| 2 | 0.6204$^{\dagger}$ | Cube Root | Cube Root |
| 3 | 0.7798$^{\dagger}$ | Quadratic | Linear |
| 4 | 0.7504 | Linear | Linear |
| 5 | 0.8593$^{\dagger}$ | Two-segment spline | Linear |
| 6 | 0.9231$^{\dagger}$ | Two-segment spline | Two-segment spline |
| 7 | 0.8496 | Linear | Linear |
| 8 | 0.8450 | Linear | Linear |
| 9 | 0.7654 | Linear | Linear |
| 10 | 0.7249 | Linear | Linear |
| 11 | 0.7795 | Linear | Linear |
| 12 | 0.6856 | Linear | Linear |
| 13 | 0.9595$^{\dagger}$ | Two-segment spline | Quadratic |
| 14 | 0.9093$^{\dagger}$ | Two-segment spline | Two-segment spline |
| 15 | 0.8762$^{\dagger}$ | Two-segment spline | Linear |
| 16 | 0.8578 | Linear | Linear |
| 17 | 0.7833 | Linear | Linear |
| 18 | 0.7631 | Linear | Linear |
| 19 | 0.7350 | Linear | Linear |
| 20 | 0.9120 | Linear | Linear |

Each subject is identified by number in the left-hand side column, alongside the best fit model determined by ML-DFA using AIC and BIC. The $^{\dagger}$ symbol indicates those subjects whose fluctuation plots were rejected as not being linear by at least one of the AIC or BIC measures. When the fluctuation plot is rejected by BIC, it is also rejected by AIC in all cases. The exponent provided in column 2 was obtained using standard DFA.

Finally, an additional EEG data set was analysed, and in particular, one that has been claimed to be free of artefacts and is publicly available. This analysis was performed to verify that our low rate of valid DFA fluctuation plots across subjects was not due to poor data quality in our EEG recordings. The results of analysing this data set are presented in the appendix for this chapter, and these are largely consistent with those presented in the body of this chapter.

## 4.4 Discussion

In this chapter, ML-DFA was applied to the amplitude envelopes of filtered EEG time series as in [178]. In some cases, it was observed that the application of ML-DFA to physiological time series led to the rejection of the linear model hypothesis,

contrary to what may have been concluded simply by visual inspection and/or intuition. The discussion in Chapter 2 gives a further consideration of this point.

Varying the minimum and maximum window sizes used in the course of DFA application highlighted the fact that an inappropriate window size may affect the validity of the DFA exponent. A preliminary inspection of the whole fluctuation plot (as done by [178, 196]) can be instructive for gaining a broad idea of the scales over which long-range correlations may be located. However, good practice should be to establish *a priori* the range of scales over which LRTCs are expected – taking into account the constraints of both the nature of the data (e.g., sampled oscillatory data) and a statistically appropriate number of maximum window sizes – and to accept the result returned by ML-DFA. It would be inappropriate to use this technique to identify the range of scales over which LRTCs exist. Indeed, it will always be possible to find a range of scales over which the linear model hypothesis will be accepted.

For neurophysiological data, the minimum window size should include several oscillations of the lowest frequency, and 1 second of the recording was taken to ensure this. The frequencies present are determined by the range of the bandpass filter used. The minimum window size to achieve the desired aim of several oscillations at the lowest frequency will therefore not be constant for different data sets (even those arising from the same source), and it would be implausible to prescribe a single optimal minimum window size.

Interestingly, ML-DFA makes it possible to approach the question of the maximum box size in a more systematic manner. The length of a neurophysiological time series will depend on numerous considerations, many of them experimental, and using a tenth of the data length as a maximum box size may lead to confusion when trying to infer meaning in time series of different length. Depending on the strictness of the model selection criteria used, the linear model hypothesis was not rejected for between 50 and 80% of the EEG time series even when the entire record length, i.e. $\sim$ 20 minutes, was considered. As this may easily lead to confusion, it is stressed that when linearity of the DFA fluctuation plot is not rejected when a larger maximum window size is considered, this merely indicates that the fluctuations recorded within the smaller number of windows are consistent with the magnitude of average detrended fluctuation expected under the scaling hypothesis considered. Although the fluctuation estimates at larger box sizes may show greater variance due to the smaller number of samples, this variance is compensated for by the lower weighting given to fluctuation estimates at larger window sizes resulting from taking the logarithm of the likelihood function. This has been often observed in experimental data, and a number of studies have used a maximum window size set to just a quarter of the full length of the time series,

e.g., [178]. Thus, when the linear model hypothesis was rejected at large window sizes, the window size above which loss of scaling occurred could be identified (see Figure 4.3). We therefore suggest that ML-DFA can be used to validate relaxing a conservative choice of maximum window size (i.e., to extend the length of analysable correlations) to help with heterogeneous lengths of time series.

In conclusion, the results of this chapter suggest that it is useful to apply ML-DFA alongside DFA in order to determine whether the DFA exponent obtained does indeed come from a plot that is best approximated by a line. ML-DFA will be applied alongside any further DFA analysis in this thesis.

# Chapter 5

# A critical look at a previous attempt to quantify criticality in neural synchrony

## 5.1 Introduction

Support for the concept of a brain characterised by critical dynamics has emerged from comparing brain dynamics at many different scales with the dynamics of physical systems at criticality (see Section 1.1.8). The literature in this field has primarily focused on the identification of power law distributions in the size of neuronal avalanches [23, 254]. Further literature has identified power laws in scaling functions of metrics derived from the activity of the brain [80, 88, 229, 240]. A further line of enquiry has identified the presence of a power law form in the autocorrelation function (LRTCs) in the amplitude envelope of EEG and MEG time series [178, 230]. In the previous two chapters, the presence of LRTCs in the amplitude envelope of EEG and EMG recordings from humans have been investigated.

Functionally, it has been difficult to attribute relevance to these findings other than by making observations of differences in the scaling exponent between different human subject populations or with the subject's age. In a critical state, the dynamics of an anatomically distributed critical system would be expected to contribute to optimising their capacity for information transfer and storage, and allow rapid reconfigurations (see Section 1.1.7.4 and [158]). It would therefore be of great interest to find evidence of criticality in the synchronisation of activity between different brain areas i.e. a parameter that has been directly linked with information processing, storage, and transmission [90, 256].

A first attempt to do this noted parallels between power laws detected in a thresholded measure of inter areal MEG and fMRI synchrony to those detected when the same measure was applied to two models of critical coupling: the Ising and Kuramoto models [158]. In this chapter, the methods presented by [158] are explored and critiqued in detail. To assess criticality of synchronisation, Kitzbichler et al. [158] proposed two measures characterising the pattern of synchronisation in a complex system. The first measure is the frequency density of phase locking intervals (PLI), which are defined as the periods of time for which two oscillators differ in their phase by less than a value of $\pi/4$ in modulus (see Section 1.1.6.3). The second measure is the frequency density of the change in number of phase locked pairs between successive time points (global lability of synchronisation or GLS). Both measures are derived from a thresholded wavelet-transformed instantaneous phase difference (further introduced in Sections 5.2.1.1 and 5.2.2).

Kitzbichler et al. validated the PLI and GLS results by showing that in two known models of critical interaction, namely, the Ising model [137, 207] and the Kuramoto Model [167–169] (these were introduced in Sections 1.1.7.3 and 1.1.3.4, respectively), these measures display power law distributions at the critical threshold but not in a decoupled system [158]. The presence of this power law in the PLI and GLS was determined using a model selection approach [57, 164] whereby both the power law and alternative models (log-normal and exponential) were fitted and the best model is decided on the basis of the Akaike Information Criterion (already introduced in Section 2.5.2).

There are a number of questions regarding this technique that have led me to question these methods. These are discussed in Section 5.3. Whilst it has been suggested that power law statistics of some observable of the system should be evident in a system at criticality [12, 14, 225, 258], the point has been made that power laws could result from the superposition of multiple processes each with their own characteristic time scale [286] or from the use of thresholds [274]. Specifically, the work of [274] suggests that power law distributions can be observed in the thresholded amplitudes of a shot noise time series. Given this, it is asked whether power law distributions in the PLI and GLS measures introduced in [158] are uniquely indicative of a system in a critical state. The approach adopted here is to pool the phase locking intervals (respectively, the number of phase locked pairs between successive time points) of a non-critically interacting system of Kuramoto oscillators and to compare the resulting distributions with those derived from a critically-coupled system. If this pooling produces distributions that, within the limits of a model selection approach, cannot be distinguished from those of a critically-coupled system then this approach to inferring criticality may be suspect.

To investigate this question, a system formed from a collection of independent

paired oscillators is studied, which is referred to as the Independent Pairs model. The two oscillators making up a pair are coupled, having phases evolving according to the Kuramoto differential equations (formally introduced in Section 1.1.3.4), but there is no connection between pairs. A schematic diagram of the two connectivity structures are shown in Figure 5.1. Each pair can snap into synchronisation at a coupling value unique to itself, however, there is no collective order parameter to unite their progressive synchronisation, i.e., this system can have no critical coupling value and has no mean field.

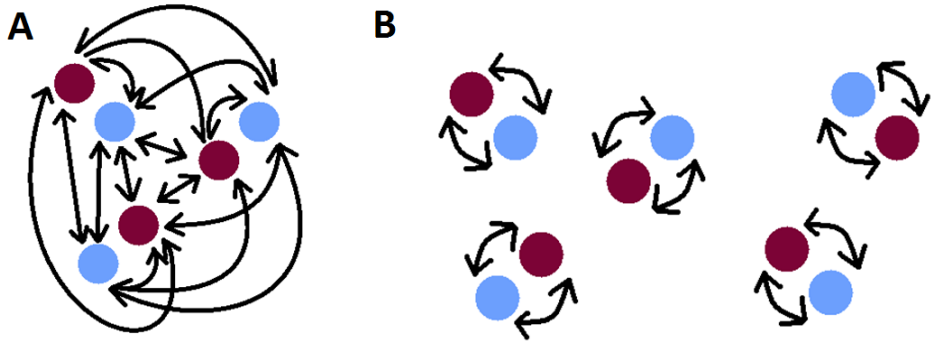


FIGURE 5.1: A schematic diagram to show A. the all-to-all connectivity in the Kuramoto model in contrast to B. the pairiwse connections in the Independent Pairs model.

The chapter is organised as follows. First, a summary of the paper by Kitzbichler et al [158] is presented, and the conclusions derived from this paper. Next, the weaknesses in the paper are discussed.

Following this, attention is turned to the Independent Pairs model. The phase difference between two sine-phase coupled oscillators is derived analytically, which makes it possible to generate a large number of Independent Pairs, with natural frequencies drawn from a normal distribution and pair-wise coupling a free parameter (Section 5.4.1). After summarising the methodology of Kitzbichler et al. (Sections 5.4.2-5.4.5), its application to both the Kuramoto model and the Independent Pairs model (Sections 5.4.7-5.4.8) is compared, revealing the coupling parameters under which PLIs and GLSs may give rise to power laws within a model selection approach.

The work presented in this chapter closely follows the manuscript for the paper, published in Physical Review E [34], in which the methods of Kitzbichler et al. are critically analysed.

## 5.2 A summary of the previous paper [158]

### 5.2.1 Introducing measures of neural synchronisation

The authors of [157] introduce two measures for the phase relationship of two time series - the phase-lock interval (PLI) and the global lability of synchronisation (GLS). They use these two measures to suggest that synchronisation in the human brain is in a state of broadband criticality, which follows from the observation that the frequency distributions of the two measures are of power law form in a broad range of frequency scales (which gives rise to the term 'broadband'). Before introducing the definitions of the PLI and GLS measures, some preliminary ground is covered by introducing the notation associated with the frequency scales used in the paper by Kitzbichler et al. [158].

#### 5.2.1.1 Frequency scales

An important feature of the findings in [158] is that the critical behaviour of neural activity extends across a number of frequency scales, so that criticality is referred to as being broadband. The decomposition of the phase difference data into several frequency scales is performed using a Hilbert wavelet transform, and it was implemented computationally here using the algorithms from [252, 298, 299]. Specifically, wavelet scales 3 - 11 were used, corresponding to frequencies of $125-62.5$Hz, $62.5-31$Hz, $31-15.5$Hz, $15.5-8$Hz, $8-4$Hz, $4-2$Hz, $2-1$Hz, $1-0.5$Hz, and $0.5-0.25$Hz.

First, Kitzbichler et al. [158] take two signals denoted here as $x_i$ and $x_j$ in this chapter. They then take the $k$-th scale wavelet transforms of $x_i$ and $x_j$ to obtain $\mathcal{W}_k(x_i)$ and $\mathcal{W}_k(x_j)$, which are time-varying complex vectors of wavelet coefficients. The wavelet transform can be used as an alternative means to the Hilbert transform to calculate the phase of a time series amongst other quantities (see Section 1.1.6.3).

Each set of wavelet coefficients quantifies the power of the signal in the corresponding frequency band. These two sets of wavelet coefficients are multiplied element-wise to form the vector $\mathcal{W}_k(x_i)^{\dagger}\mathcal{W}_k(x_j)$, where the symbol † indicates the complex conjugate. This vector is then normalised by dividing it (again, element-wise) by the element-wise product $\mid \mathcal{W}_k(x_i) \mid\mid \mathcal{W}_k(x_j) \mid$ where operator $\mid . \mid$ denotes the modulus. An instantaneous time-varying complex phase vector is found by this procedure:

$$C_{ij}^{k} = \frac{\mathcal{W}_k(x_i)^{\dagger}\mathcal{W}_k(x_j)}{\mid \mathcal{W}_k(x_i) \mid\mid \mathcal{W}_k(x_j) \mid} \tag{5.1}$$

To ensure a more robust and less noisy estimate of the phase relation, the instantaneous phase vector is smoothed by using a moving average of the numerator and the two vectors contributing to the denominator of $C_{ij}^{k}$, yielding a new vector $\bar{C}_{ij}^{k}$ given by:

$$\bar{C}_{ij}^{k} = \frac{\langle \mathcal{W}_k(x_i)^{\dagger}\mathcal{W}_k(x_j) \rangle}{\sqrt{\langle \mid \mathcal{W}_k(x_i) \mid^2 \rangle \langle \mid \mathcal{W}_k(x_j) \mid^2 \rangle}} \tag{5.2}$$

Here the operator $\langle . \rangle$ denotes that a moving average is taken. The length of the sliding window used for the moving average is set to the number of time steps spanning 8 oscillation cycles at the highest frequency in that wavelet scale [158].

The argument of $\bar{C}_{ij}^{k}$ is then taken as a measure of the phase relationship of the two oscillators $i$ and $j$ corresponding to wavelet scale $k$, so that $\triangle_{ij}^{k} = \arg(\bar{C}_{ij}^{k})$.

### 5.2.2 PLI and GLS

In this section, $\triangle_{ij}^{k}(t)$ will be used to denote the value of $\triangle_{ij}^{k}$ at time $t$. For phase difference $\triangle_{ij}^{k}$ between two oscillators $i$ and $j$, the PLIs are defined as the duration (in seconds) for which $-\alpha < \triangle_{ij}^{k}(t) < \alpha$, for some threshold $\alpha$. This definition was given by [158] for $\alpha = \pi/4$.

The GLS was also defined in [158] and characterises the evolution of the number of synchronised pairs, $\mathrm{N}_{SP}$, to describe the lability of synchronisation. The number of synchronised pairs at wavelet scale $k$ is formally defined as:

$$N_{SP}^{k}(t) = \sum_{i<j} \left\{ \mid \triangle_{ij}^{k}(t) \mid < \alpha \text{ and } {M_{ij}^{k}}^2(t) > \frac{1}{2} \right\} \tag{5.3}$$

where ${M_{ij}^{k}}^2 = \mid \bar{C}_{ij}^{k} \mid^2$ is proposed as a measure of the significance of the phase difference estimate $\bar{C}_{ij}^{k}$, and $\alpha = \pi/4$ as above. It should be noted here that the condition ${M_{ij}^{k}}^2(t) > \frac{1}{2}$ introduces an additional threshold. The use of thresholds on otherwise stochastic data has been shown by Touboul et al. [274] to occasionally give rise to spurious power laws.

The GLS at scale $k$ is then obtained by calculating the square of the difference in the number of phase-locked pairs between two successive points in time, $\mid N_{SP}^{k}(t+\delta t) - N_{SP}^{k}(t) \mid^2$, where $\delta t$ is an increment in time and $k$ denotes the wavelet scale. In the figures of this chapter, the GLS is labelled with the symbol $\Delta^2$.

### 5.2.3 The use of computational models in the Kitzbichler et al. paper

In order to demonstrate whether their measures are capturing phase synchrony, they apply them to time series obtained from the Ising model (Section 1.1.7.3) and to signals from the Kuramoto model (Section 1.1.3.4) before applying them to human fMRI and MEG data.

#### 5.2.3.1 The Ising model

The Ising model is studied at two temperature values - one critical and one at a disordered state, at a temperature above critical. Results for temperatures below the critical value are not presented in [158], although they are mentioned in passing.

The Ising lattice is taken to be $96 \times 96$ in size with 256 time series generated by averaging the spin values within $8 \times 8$ size sub-lattices. The lattice is allowed to evolve for 12,192 time steps, of which the first 4,000 are discarded to allow the system to settle into a steady state of activity. The results obtained are reproduced in Figure 5.2. The plots suggest that the PLI and GLS frequency distribution looks similar to a power law when $T = T_c$, but not when the temperature is very hot at $T = 10^5$. When the Ising model temperature parameter is set to be very low ($T = 0$), it is stated that PLIs have a Dirac delta distribution because the spins are identical, which means that their phases are identically phase-locked. This does not give interpretable results in the PLI or GLS distributions. Temperatures that are smaller than $T_c$ but greater than 0 are not discussed here. Importantly, power law distributions are seen only when $T = T_c$.

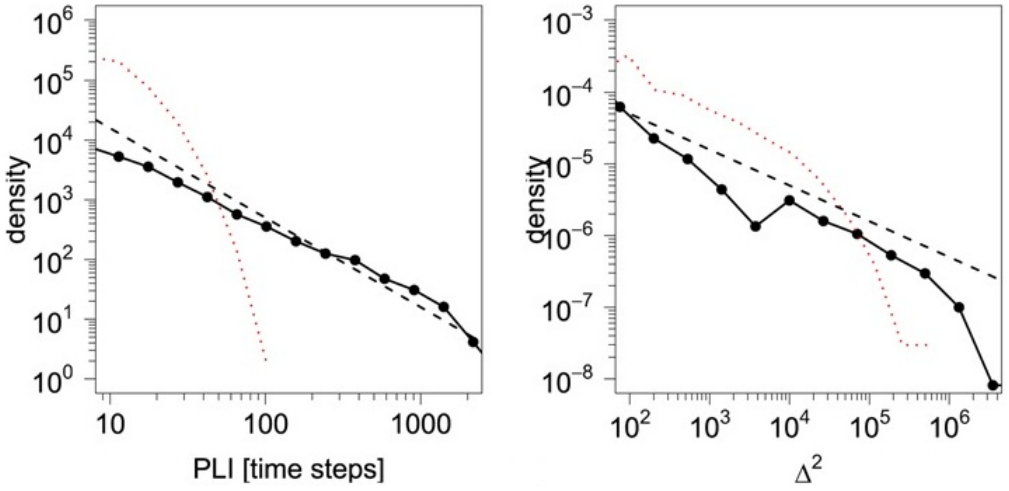


FIGURE 5.2: Ising model PLI distributions for critical and high temperatures. The left-hand panel is a log-log plot of the probability distribution of PLIs between pairs of time series at temperature $T_c$ (black line) and at $T = 10^5$ (red dotted line). The additional dashed line is a perfect power law with an exponent of $-1.5$ to guide the eye. The right-hand panel is a log-log plot of the probability distribution of GLS at $T = T_c$ (black line) and at $T = 10^5$ (red dotted line). Image taken from [158].

### 5.2.4 The Kuramoto model

The paper by Kitzbichler et al. (see their Figure 2, reproduced in Figure 5.3) states the coupling value at which criticality occurs by locating the coupling value $K$ of the greatest change in the order parameter or $\Delta(Kr)$ [193], and states that this measure changes in a similar way to the proportion of oscillators that have synchronised to the mean field, $\Delta N$. These measures are illustrated in Figure 5.3, replicated from Kitzbichler et al. [158].

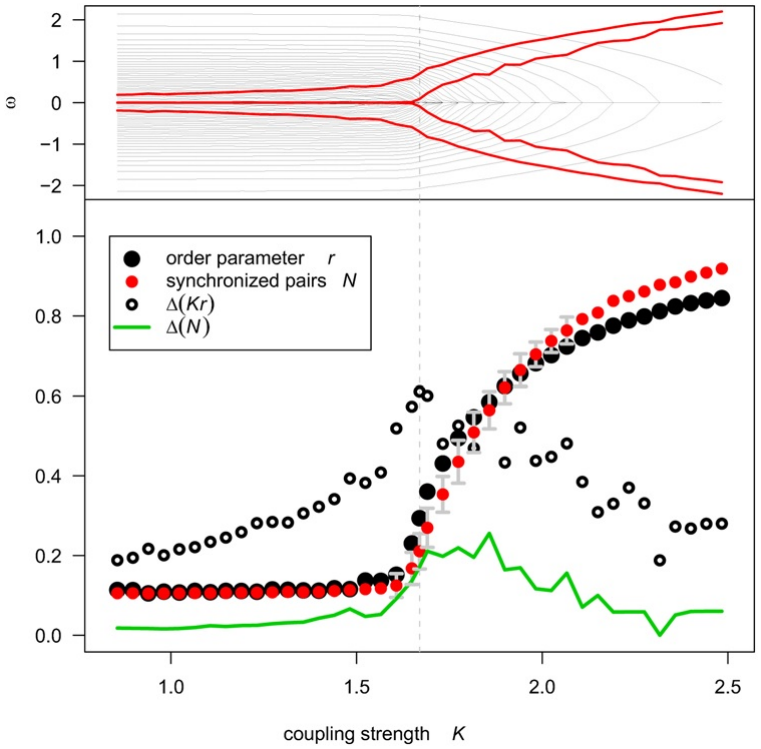


FIGURE 5.3: Simulations and metrics of the Kuramoto model. The $x$-axis in this figure represents the coupling value $K$. At critical coupling $K_c$, the mean field of the system and the number of synchronised oscillator pairs fluctuates In the top panel, the change in oscillator frequencies is shown as a function of the coupling $K$ with grey lines. When the coupling is 0 or low, these are the natural frequencies of the oscillators, but they converge to the mean field as oscillators synchronise and $K$ is increased. The red lines indicate the range of $Kr$, which is termed the effective mean field coupling strength. Oscillators with natural frequencies below this value in modulus synchronise to the mean field. There is a bifurcation point at $K_c$. In the bottom panel, the order parameter (black discs) is shown alongside $\Delta(Kr)$ (black circles) as well as the proportion of synchronised oscillators $N$ (red discs) and $\Delta(N)$ (green line) as a function of $K$. The peaks of these two measures occur at similar coupling values (slightly higher for $\Delta(N)$), which is higher than but similar to the theoretical $K_c = 1.596$. This is indicated approximately by the grey dashed line running vertically across the figure. Image taken from [158].

In the paper by Kitzbichler et al., 44 Kuramoto oscillators were simulated for a total of $10^5$ time steps. The power spectra, the frequency distributions of the PLI and the GLS measures are shown in Figure 5.4. The PLI is labelled in the $x$-axis of the data, and the GLS is represented by the symbol $\Delta^2$.

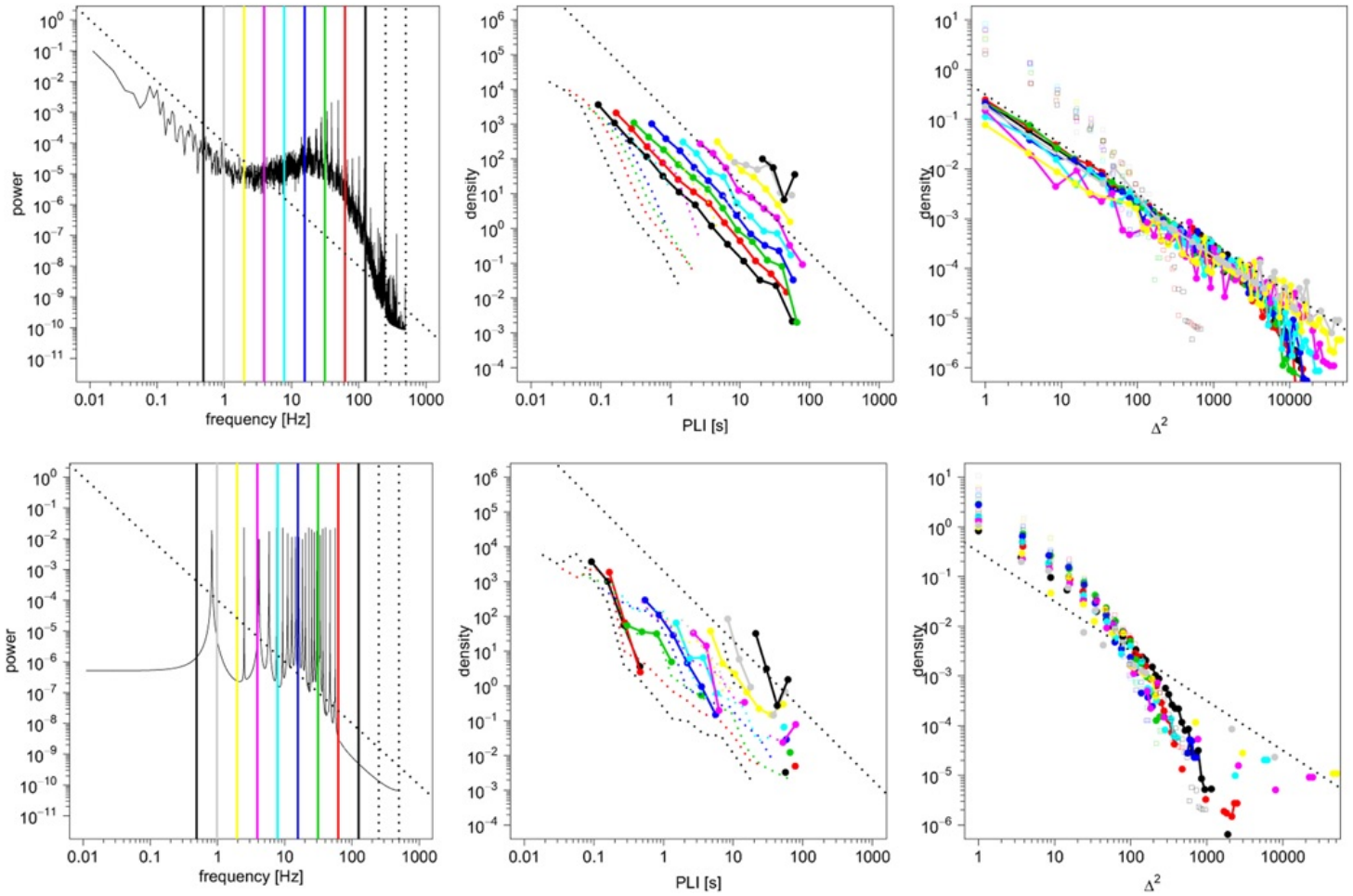


FIGURE 5.4: PLI and GLS for the Kuramoto model. The results of analysing time series of the Kuramoto model using the methods of [158]. In the top row, the coupling strength is $K_c$ and in the bottom row it is $K = 0$. Solid lines represent simulation data and dotted lines represent surrogate data. The colours indicate the wavelet scales used spanning from 3 to 11 (for details see [158] or Section 5.2.1.1 of this chapter). The left-hand column shows the logarithmic power spectra of time series from the Kuramoto model. At $K_c$ the spectrum follows a power law on its logarithmic scale with an additional large hump which is caused by synchronisation between many of the oscillators at this coupling value. In the power spectrum corresponding to $K = 0$, the individual natural frequencies if the oscillators are superimposed. Coloured lines represent the different wavelet scales. In the middle column, the log-log PLI distributions are shown for the two temperature values. The critical time series is suggested to produce a power law, while surrogate data and $K = 0$ give a steep drop-off. The dashed line is a perfect power law with exponent $-2$. The right-hand column shows the log-log distribution for the GLS. Again, the power law is suggested to only appear for critical coupling, and not in surrogate data or for $K = 0$. The dashed line represents a power law with exponent $-1.5$. Each of the coloured lines represents a different wavelet scale. Image taken from [158].

### 5.2.5 fMRI data

Finally, in [158] the method is demonstrated by application to functional Magnetic Resonance Imaging (fMRI) data and MEG data [158]. fMRI measures the change

in blood flow related to neural activity in the brain or spinal cord and magnetoencephalography (MEG) is a technique for mapping brain activity described in Section 1.1.2.3. Figure 5.5 shows an example time series of the phase synchronisation seen in fMRI data. An equivalent example for MEG is not given in the paper [158].

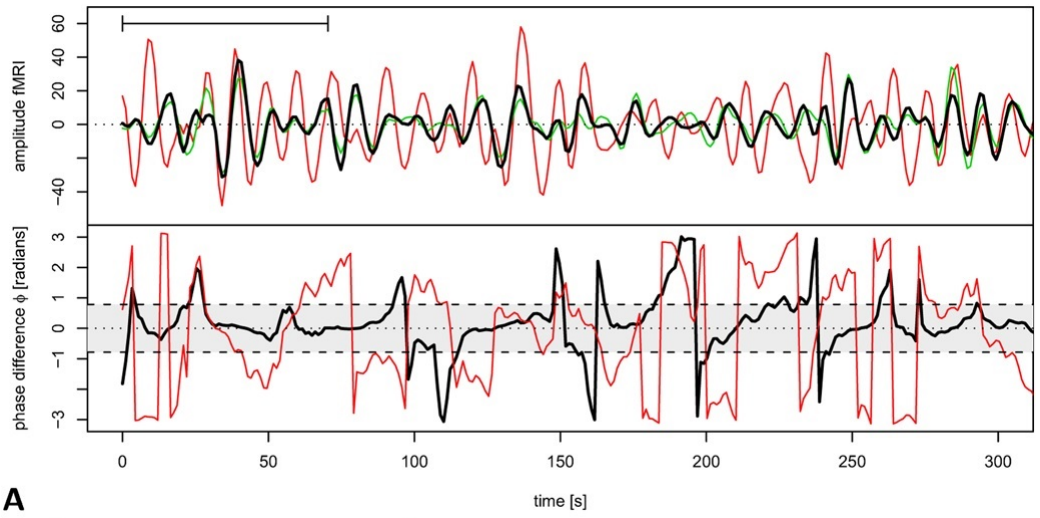


FIGURE 5.5: This figure displays the work done on fMRI only. The top panel displays the amplitude of fMRI signals in the frequency intervals $0.05 - 1$ Hz, for three brain regions in a single subject. These are the left precentral gyrus (black), right precentral gyrus (red) and left olfactory cortex (green). The left and right precentral gyrus regions are functionally similar. The phase difference between the time series recorded from these two regions is shown in black in the bottom panel, and displays a certain amount of phase-locking. The phase difference between the left precentral gyrus and olfactory cortex is also shown in red on the bottom panel, with far less phase locking observable. Image taken from [158].

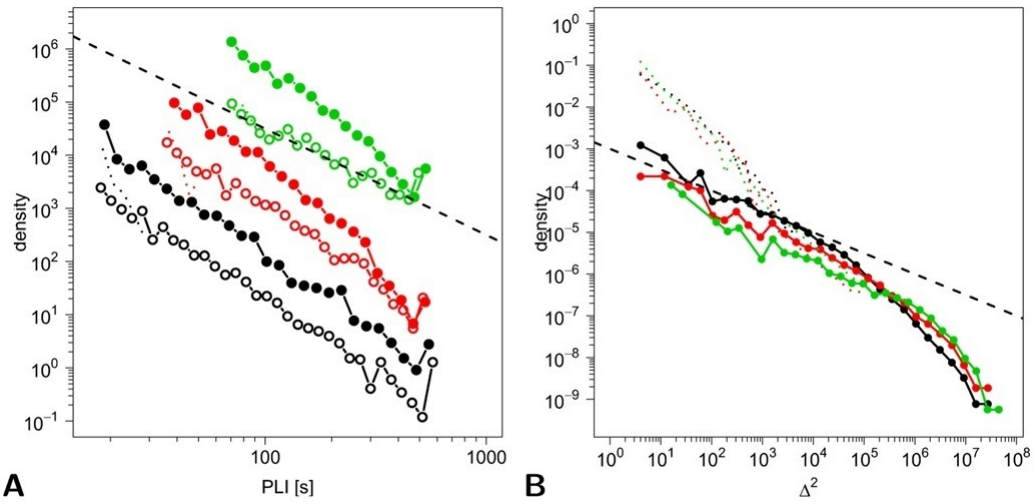


FIGURE 5.6: PLI and GLS distributions in an fMRI network. Different colours correspond to different wavelet scales - black is scale 1 (0.4520.22 Hz), red is scale 2 (0.2220.11 Hz) and green is scale 3 (0.1120.05 Hz). A. Log-log distributions of PLI for two regions performing distinct functions (filled circles), and two regions performing similar functions in the brain (empty circles). The dotted lines represent surrogate data and the straight dashed line indicates a power law with exponent $-2$. It may be supposed that the plot for similar region PLI distribution follows a power law with exponent $-2$ closely. On the other hand, the plot for different region PLI probability distribution also seems to follow a power law, but with a different, and more negative exponent. B. Corresponding log-log GLS distributions for fMRI data. The straight dashed line indicates a power law with exponent $-1/2$ to guide the eye. Image taken from [158].

The log-log plot of the frequency distributions of the PLI and GLS measures is shown in Figure 5.6). It is stated that both the PLI and GLS measures show power law frequency distributions.

### 5.2.6 MEG data

Corresponding results to those seen in the fMRI data are also presented for MEG data in Figure 7 of [158], and adapted in Figure 5.7. It is stated by [158] that the distributions of PLI approximated a power law reasonably well at all scales, whereas the surrogate data did not. It is also stated that the GLS showed only limited power law behaviour in the frequency distribution because of the limitations of a finite sized system.

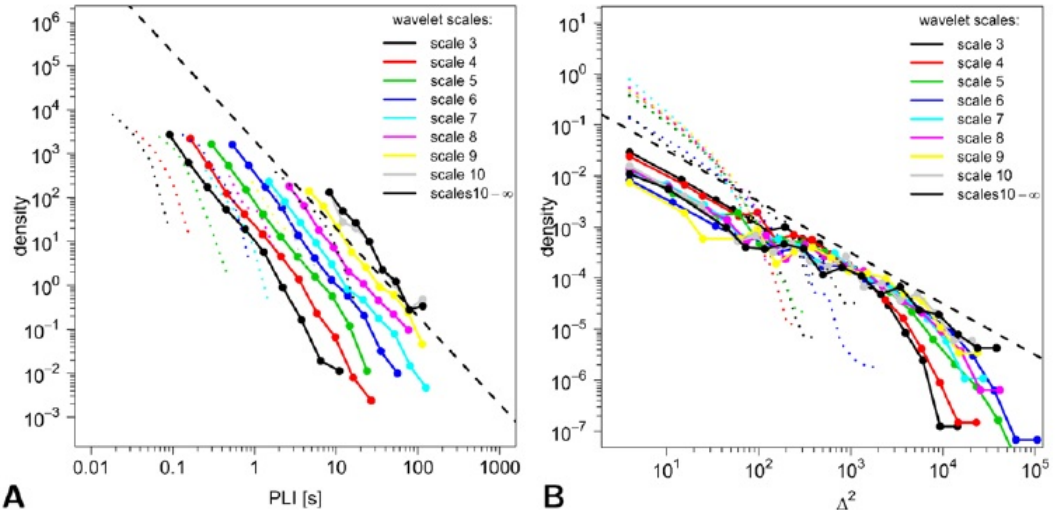


FIGURE 5.7: PLI and GLS distributions in an MEG network. Different colours correspond to different wavelet scales as follows: black = scale 3(125-62.5 Hz); red = 4 (62.5-31 Hz); green = 5 (31-15.5 Hz); blue = 6 (15.5-8 Hz); cyan = 7 (8-4 Hz); magenta = 8 (4-2 Hz); yellow = 9 (2-1 Hz); grey = 10 (1-0.5 Hz); black = 11 (0.5-0 Hz). Solid lines denote MEG data and dashed lines denote surrogate data. A. Log-log distributions of PLI for pairs of MEG sensors in each wavelet scale. The dotted lines represent surrogate data and the straight dashed line indicates a power law with exponent $-2$. It may be supposed that the plot for similar region PLI distribution follows a power law with exponent $-2$ closely. On the other hand, the plot for different region PLI probability distribution also seems to follow a power law, but with a different, and more negative exponent. B. Corresponding log-log GLS distributions for fMRI data. The straight dashed line indicates a power law with exponent $-1/2$. Image taken from [158].

## 5.3 Concerns and questions about the paper by Kitzbichler et al. [158]

In examining this paper, a number of weaknesses and aspects of concern were noted. Two of the general concerns were mentioned directly in the Introduction of this section, namely, the potential problems associated with drawing conclusions about power laws from a frequency distribution, which may be obtained by superposition of multiple individual processes, and that of generating non-stochastic processes by thresholding stochastic time series [274]. Both of these procedures are applied when calculating PLI and GLS. However, there were also some specific concerns regarding the details of the paper, which are listed below:

- The phase-lock intervals are defined by setting a lower and upper threshold of $[-\pi/4, \pi/4]$. It was unclear how these values were obtained. It is stated in the paper that these values are midway between full synchronisation (a phase difference of 0) and full independence at $[-\pi/2, \pi/2]$, but there is no

reason that this value should be of especial importance. Similarly a threshold of ${M_{ij}^k}^2(t) > \frac{1}{2}$ is used.

- It was stated in the paper that natural frequencies in the Kuramoto model came from a normal distribution $\mathcal{N}(0, 1)$. However, the corresponding power spectra were dispersed in a range from $\approx$ 1 to $\approx$ 60 Hz (Figure 5.4). It did not seem that the mean and standard deviation corresponding to these spectra were given in the paper. This made it difficult to replicate any results, although a visual judgement was made. This point is touched upon later in Section 5.4.7.

- It was very difficult to find 44 oscillators which showed the power law form in the power spectrum as seen in Figure 5.4 either at or near $K_c$. Indeed, there was only one simulation which could be identified to achieve this. This required an iterative exploration of the different random seeds used to generate the natural frequencies for the Kuramoto model.

- It is stated in [158] that the GLS frequency distribution of fMRI data is well-approximated by a power law. This would not appear to be the case from Figure 5.6 B.

- Similarly, in the MEG results, the GLS frequency distribution did not appear to resemble a power law. Indeed, this was stated by the authors [158]. The frequency distributions for MEG and fMRI data appeared similar, and it was unclear that a distinction should be drawn in describing them.

- Furthermore, the reason for the lack of a power law distribution in the MEG data is given as a limitation of a finite sized system. However, the MEG was recorded from 204 gradiometers and 102 magnetometers. This means that there are 306 sensors in total. However, the power law result was demonstrated with a Kuramoto system of only 44 oscillators.

These concerns led me to question the measures and conclusions of this paper in greater detail. They were first aired with the authors of [158], but not responded to entirely. Whether the power law distributions of PLI and GLS as obtained by the Kitzbichler et al. paper were specific to critical systems was investigated.A system that was known not to be critical, but one that was still based on the Kuramoto model was therefore constructed. This system is referred to as the Independent Pairs model here and in [34], which is introduced in the sections below. The results obtained from analysing it are presented.

The following sections of this chapter again closely follow the manuscript for the published paper [34].

## 5.4 Methods and Materials

### 5.4.1 Analytic Phase Difference for the Independent Pairs Model

An independent pair is defined as two coupled oscillators $i$ and $j$ whose phases $\phi_i$ and $\phi_j$ evolve according to Equation (1.1), namely:

$$\begin{aligned}\dot{\phi}_i - \dot{\phi}_j &= (\omega_i - \omega_j) + \frac{K}{2}\left(\sin(\phi_j - \phi_i) - \sin(\phi_i - \phi_j)\right) \\ &= (\omega_i - \omega_j) - K\left(\sin(\phi_i - \phi_j)\right)\end{aligned} \tag{5.4}$$

It is noted that the phases in this model and in the Kuramoto model can be transformed into signals $x_i$ and $x_j$ taking the cosine of phases $\phi_i$ and $\phi_j$ respectively.

Letting $\triangle_{ij} = \phi_i - \phi_j$ yields:

$$\dot{\triangle}_{ij} = (\omega_i - \omega_j) - K\sin(\triangle_{ij}) \tag{5.5}$$

This equation has two solutions depending on whether $K <\mid \omega_i - \omega_j \mid$ or $K >\mid \omega_i - \omega_j \mid$. If we let $C = \frac{K}{(\omega_i - \omega_j)}$, and $D$ is an integrating constant, then the solution for $K <\mid \omega_i - \omega_j \mid$ is:

$$\triangle_{ij} = 2\tan^{-1}\left[\left(\sqrt{1-C^2}\right)\tan\left(\frac{(t-D)\,(\omega_i - \omega_j)\sqrt{(1-C^2)}}{2}\right) + C\right] \tag{5.6}$$

The solution for $K >\mid \omega_i - \omega_j \mid$ is:

$$\triangle_{ij} = 2\tan^{-1}\left[\sqrt{C^2-1}\left(\frac{e^{-t(\omega_i-\omega_j)\sqrt{(C^2-1)}} - A}{A + e^{-t(\omega_i-\omega_j)\sqrt{(C^2-1)}}}\right) + C\right] \tag{5.7}$$

with $A$ an integrating constant. A full derivation is provided in the Appendix. After deriving this, the authors were made aware that the dynamics of a single pair from this model has previously been described in [4] in relation to the interaction between a pendulum suspended in a viscous fluid inside a rotating container, and used in [281] as a basis for constructing a Lyapunov function.

The time evolution of $\triangle_{ij}$ is dependent on two parameters: the coupling $K$, and the difference between the natural frequencies of rotation, $\omega_i - \omega_j$ of the two oscillators. The selection of these two quantities is crucial to further analysis and each is considered in turn.

In the Independent Pairs model, the phase differences within each pair are known analytically (see Section 5.4.1), however, they are not associated with particular wavelet

scales. To produce probability distributions comparable to those in [158], surrogate pairs of signals were created with the first signal evolving constantly at a frequency given by a base value drawn from the distribution of natural frequencies $g(\omega)$, and the second signal phase shifted from the first by $\triangle_{ij}^{k}$.

### 5.4.2 Natural Frequencies

The natural frequencies of oscillators in the Kuramoto system considered in [158] were drawn from a normal distribution $\mathcal{N}(0,1)$. As any normal distribution may be scaled and shifted such that it is equivalent to one with a mean of 0 and a standard deviation of 1, we consider that the natural frequencies are also distributed with $\omega_i \sim \mathcal{N}(0,1)$ without loss of generality. If both natural frequencies $\omega_i$ and $\omega_j$ are drawn in this way, then by laws of normal distributions, $\omega_i - \omega_j \sim \mathcal{N}(0,2)$. As the quantity $\omega_i - \omega_j$ only is of interest to us in order to calculate $\triangle_{ij}$ (Equations 5.6 and 5.7), we draw values from a distribution of $\mathcal{N}(0,2)$ for the Independent Pairs Model.

### 5.4.3 Coupling Parameter

It is appropriate to remind ourselves that the critical coupling parameter was calculated analytically by Kuramoto under a certain set of assumptions [167]. Namely, if the probability distribution of the natural frequencies $g(\omega)$ is unimodal and symmetric, and the number of oscillators is infinite ($N \to \infty$), then the analytic critical coupling parameter $K_c$ is:

$$K_c = \frac{2}{\pi g(0)} \tag{5.8}$$

And, in the case of $g(\omega) = \mathcal{N}(0,1)$:

$$K_c = \frac{2\sqrt{2}}{\sqrt{\pi}} \simeq 1.596 \tag{5.9}$$

In any feasible realisation of the Kuramoto model, the assumption $N \to \infty$ is not realistic. This means that the theoretical value of $K_c \simeq 1.596$ is not necessarily the precise coupling parameter at which the system reaches critical behaviour. Kitzbichler and colleagues [158] describe two practical measures characterising the onset of synchronisation with increasing coupling. The first is the change in the 'effective mean-field coupling strength', $\Delta(Kr)$. If the value of $Kr$ exceeds the difference between the natural frequency and the mean phase $\omega_i - \psi$ (in modulus) i.e. $|\omega_i - \psi| < Kr$, then oscillator $i$ will synchronise to the mean field [193]. Thus the value of $K$ at which $Kr$ increases maximally is the coupling value at which the greatest number of oscillators are drawn

into the mean field, i.e., a defining feature of the critical point in the system. The second measure is the change in the time-averaged number of synchronised pairs $N_{SP}$ as the coupling increases, $\Delta N_{SP}$. Again, this describes the point at which the greatest change in synchronisation occurs, i.e., the critical point. The two measures $\Delta(Kr)$ and $\Delta N_{SP}$ peak at the same point. The coupling value at this point is referred to as the effective critical coupling value for the system.

In contrast, in the Independent Pairs model, there is no longer a global critical coupling parameter $K_c$ since there can be no mean field. From the two distinct analytical solutions for $\triangle_{ij}$ (Equations 5.6 and 5.7) it can be seen that each pair of oscillators will synchronise independently when $K$ exceeds $\mid \omega_i - \omega_j \mid$ for that pair. Some insight can nevertheless be gained by calculating the measures derived from a standard Kuramoto model, namely, $r$, $N_{SP}$, $\Delta(Kr)$ and $\Delta N_{SP}$.

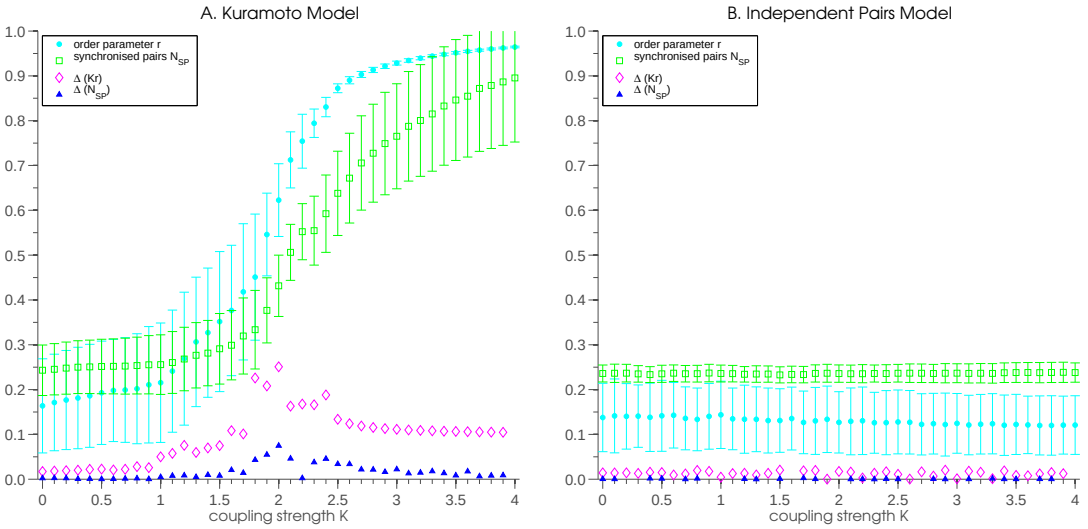


FIGURE 5.8: Kuramoto model. Plot A. shows the evolution of order parameter $r$ for the classical Kuramoto model with cyan solid circles (error bars show standard deviations). The coupling parameter $K$ increases along the $x$-axis. The hollow purple diamonds show $\Delta Kr$, the change in order parameter multiplied by coupling (error bars not shown for readability). The time-averaged number of synchronised pairs, $N_{SP}$ is shown with hollow green squares (error bars show standard deviations), and the difference in $N_{SP}$, $\Delta N_{SP}$, is indicated by solid blue triangles (error bars not shown for readability). The peaks in $\Delta Kr$ and $\Delta N_{SP}$ can be used to indicate the location of the critical point for a specific system, which for this selection of natural frequencies occurs at around $K = 2$. This effective coupling value of $K = 2$ will be used throughout the paper. Note that, for the Kuramoto model, the order increases with rising coupling. Plot B. displays the corresponding measures $r$, $\Delta Kr$, $N_{SP}$ and $\Delta N_{SP}$ for the Independent Pairs model. There is no change in order parameter with coupling, indicating that the oscillators are not critically coupled to a mean field.

As shown by Figure 5.8A, there is a clear growth in order in the Kuramoto model, with the parameter beginning near 0 for low coupling, and increasing to nearly 1 after the coupling value exceeds $K = 3$. The maximum rise in $Kr$ occurs at around $K = 2$, which is therefore the effective critical coupling for this system. A similar pattern

is traced by $N_{SP}$, with $\Delta N_{SP}$ peaking at around $K = 2$. In this chapter, results for the theoretical critical value $K_c \simeq 1.596$ are provided (occasionally referred to as $K_c \simeq 1.6$), as well as for the (above defined) effective critical coupling for the finite system, $K = 2$. This latter value is where one might expect power law statistics to be present in the Kuramoto model. It has been empirically confirmed here that as $N$ increases, the effective critical coupling $K$ converges to the theoretical critical coupling $K_c$ (results not shown, but the effective critical coupling is $K = 1.8$ for $N = 1000$ for example). It should be noted that although the number of oscillators considered here is limited, 44 oscillators as in [158], this system still gives rise to 946 pairwise interactions, which is more substantial. It has been shown that 44 interacting oscillators can model neural dynamics. For example, the use of a Kuramoto model of 66 phase oscillators by the authors of [47] led to the emergence of slow activity fluctuations consistent with empirically measured fMRI functional neural connectivity. Nevertheless, in order to verify the conclusions, the analysis is replicated with $N = 1000$ oscillators yielding similar results (not shown but available upon request).

With independent pairs, on the other hand, both the order parameter and the number of synchronised pairs remain unchanged across all coupling values, at the values observed for $K = 0$ in the Kuramoto model (compare Figures 5.8A and 5.8B). This is because, although the pairs individually synchronise with each other, the frequencies at which they synchronise are distributed across the whole range of possible frequencies.

### 5.4.4 PLI and GLS for individual Kuramoto oscillator pairs

From examination of the analytic equations for phase difference (Equations 5.6 and 5.7), it can be observed that the phase difference $\triangle_{ij}^{k}$ changed with time in a very structured way. For $K <\mid \omega_i - \omega_j \mid$, $\triangle_{ij}^{k}$ is a periodic function. For $K >\mid \omega_i - \omega_j \mid$, there is a short-lived transient before $\triangle_{ij}^{k}$ settles to a constant.

Before proceeding to pool the probability distributions across many pairs of oscillators, we first consider what might be expected from a single pair.

For $K <\mid \omega_i - \omega_j \mid$, the lengths of PLIs between two oscillators would be identical within any given oscillation cycle, and the probability distribution will only contain just one value. If a given simulation is cut off before a full cycle is complete, or more precisely, before a phase locked interval has come to an end, this may give rise to a second phase locked interval, and the probability distribution may have more than one value in this case. For $K >\mid \omega_i - \omega_j \mid$, the phase difference will be a single constant, either occurring during the transient, or at the permanent value to which the phase difference converges, depending on the starting phase difference, and the value of the final constant. Again, the probability distribution contains one value.

The GLS can either take the value 1 if the oscillators either go from being non-phase-locked to phase locked, or the value 0 if no change occurs. This allows two possible values in the probability distribution.

For a single oscillator pair, we would therefore not expect to find a valid probability distribution of either PLIs of GLS for any coupling $K$.

This is a trivial, but important point to make. If a single pair of oscillators could give rise to a probability distribution which appear linear on a log-log plot (as a power law does) for some pairwise coupling value that could be considered 'critical' over some small range of values, then the final, observed power law created by pooling many pairs may be the result of a simple superposition of these smaller linear components. We now demonstrate that the power law can indeed result from a process that does not involve 'critical' interactions for any reasonable definition of the term (even on a pairwise level), but through completely independent systems evolving with no connections between the elements that then combine to produce the power law.

### 5.4.5 Akaike Information Criterion

As in [158], the presence of power law statistics is assessed using a model selection approach whereby the Akaike's Information Criterion [6] is used to compare the goodness-of-fit of a power law distribution with that of two alternative distributions, namely, the exponential and log-normal distributions. The AIC was previously introduced to do this in Section 2.5.2.

The fact that the Akaike Information Criterion only provides a means of comparing models in relation to each other is especially relevant here because all three models were fitted to the binned histogram heights, rather than the full data set. Since the basis of the AIC is a log-likelihood function, it can be used with binned data in this way [63]. The number of bins used will affect the raw values of the $AIC$, but not the relative values obtained for the models used, so that the best-fitting model will pertain for the data analysed.

## Results

### 5.4.6 Independent Pair model simulation

Pairs of Kuramoto-coupled oscillators were simulated alongside the analytic solution. Both were calculated over 1000 seconds, with an integration time step of $\delta t = 2^{-11}$ for the simulated oscillators. This provided a total of $1000 \times 2^{11}$ time steps. Then the resulting time series was down-sampled by a factor of 2 to obtain a time series with

sampling frequency of $2^{10}$Hz. The analytic signal was also generated with a sampling frequency of $2^{10}$Hz. The coupling $K$ was incremented between 0 and 4, in intervals of 0.2, and the two curves were compared.

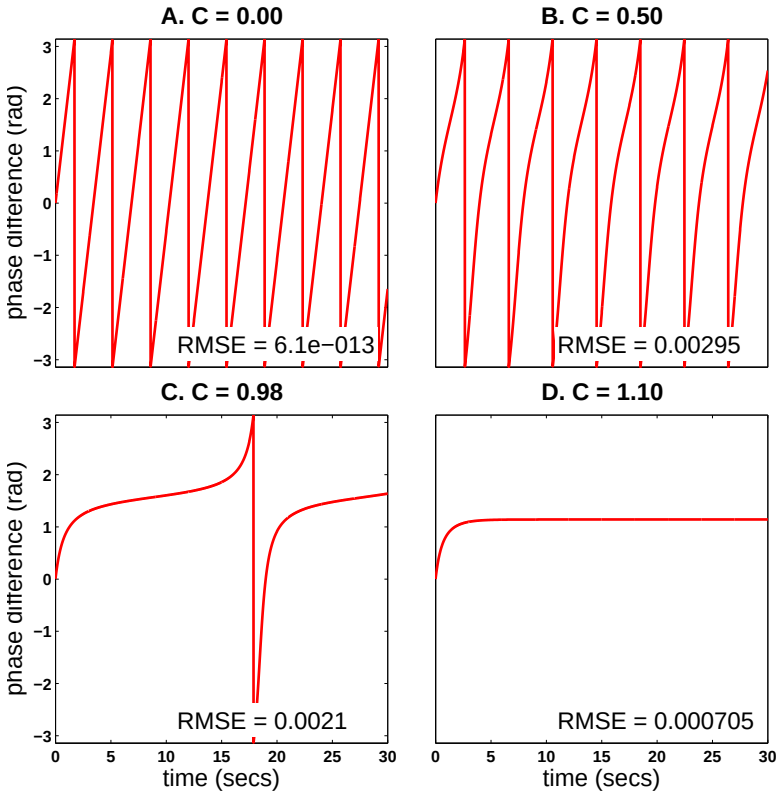


FIGURE 5.9: The evolution of phase difference between the oscillators in a two-oscillator Kuramoto system, plotted using the analytic expression (blue), and a simulation of the Kuramoto model by Euler's method (red). The two phase calculations are perfectly superimposed. The root mean square error (RMSE) is shown for different coupling values,for a single simulation. Panels A,B,C have $C < 1$ (where $C$ is defined in Section 5.4.1), but coupling is increased progressively. The phase evolves periodically. Panel D is the same pair of oscillators, but for $C > 1$. There is a brief transient before the oscillators fully synchronise with a constant level of phase difference. The initial phase separation has been set to $\triangle = 0$ without loss of generality.

The behaviour of the phase difference is qualitatively different in the cases $C = \frac{K}{(\omega_i - \omega_k)} < 1$ and $C > 1$. We demonstrate the phase difference between two oscillators in Figure 5.9 as obtained with the analytic expressions alongside a simulation of the Kuramoto model, using Euler's method to iteratively update the phase by Equation 1.1. The two phase calculations are perfectly superimposed.

Although the root mean square error (RMSE) varies for different coupling values, the normalised RMSE is less than 0.1% for the range of coupling values considered in this paper, demonstrating good agreement between simulated and analytic results.

It is evident that when the coupling exceeds the difference in natural frequencies ($C > 1$), the two oscillators synchronise in exponential time. When the coupling is small ($C < 1$),

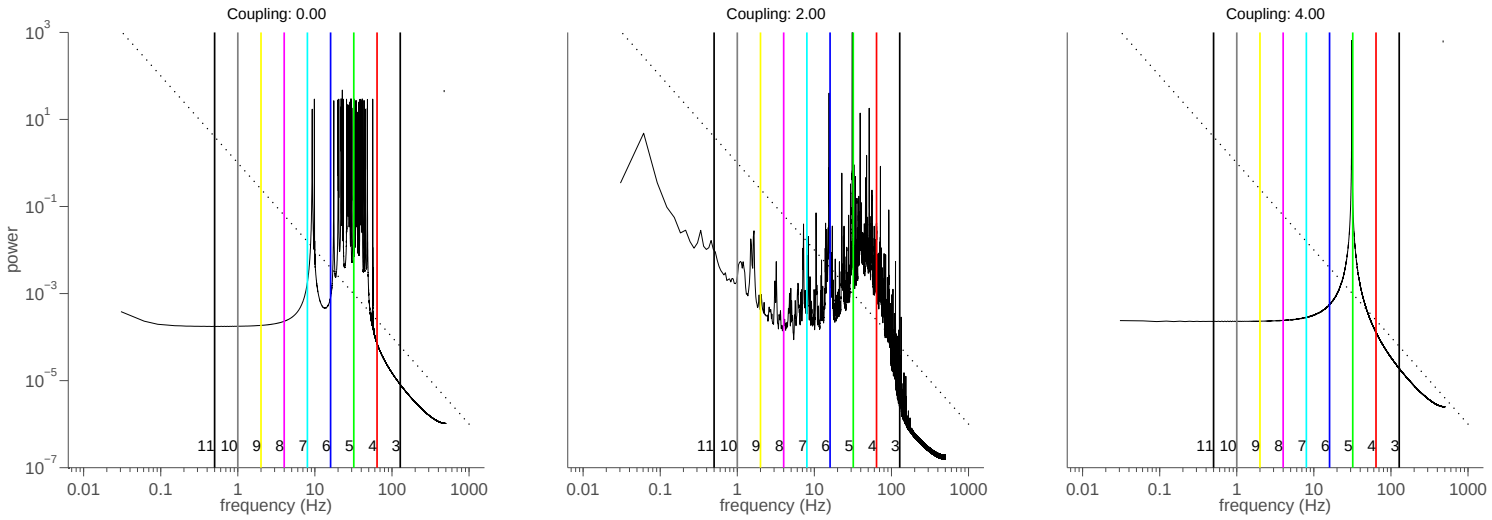


FIGURE 5.10: Power spectra for a system of 44 Kuramoto oscillators, with natural frequencies drawn from a $\mathcal{N}(60\pi, 20\pi)$ distribution and three distinct levels of coupling A) $K = 0$, B) $K = 2$, the effective critical coupling for this specific finite Kuramoto system, as seen from Figure 5.8A and C) $K = 4$. The vertical numbered lines represent wavelet scales $3 - 11$.

however, the phase difference grows (or falls) at a rate dictated by the frequency difference, but with increasingly lengthy periods of constant phase difference, or synchronisation.

### 5.4.7 PLI and GLS of Kuramoto model

As a baseline for comparison, the results of Kitzbichler et al. [158] on the Kuramoto model were replicated using our own code in the Matlab environment. A system of 44 Kuramoto oscillators, each with a natural frequency drawn from a normal distribution $\mathcal{N}(60\pi, 20\pi)$, was simulated using the same simulation parameters as in Section 5.4.6. Three different regimes (uncoupled, critically coupled, and super-critically coupled) are presented, which yield the power spectra shown in Figure 5.10.

Next, using 44 oscillators whose natural frequencies were drawn from a $\mathcal{N}(0, 1)$ distribution, the PLI and GLS probability distributions were calculated for the following coupling values - $K = 0$, $K = K_c = 1.596$, $K = 2$ and $K = 4$. At $t = 0$, all oscillators had a phase $\phi_i = 0$. The data presented in figures 5.10, 5.11 and 5.12 were obtained from a single run of the model, however, it was confirmed that the results were not sensitive to the exact values of the natural frequencies.

A histogram for the PLI data was constructed using 20 logarithmically spaced bins, with the first bin beginning at a single time step of $2^{-10}$ seconds, and the largest bin ending at the total length of the data, of 1000 seconds. The histogram was then scaled so that

each bin count was divided by the total number of PLIs, and then by the bin size that it represented.

For GLS, we took 1000 logarithmically spaced bins ranging from a value of 1 to $10^{4.5}$, as displayed on the plot. The GLS histogram was also scaled. Here each bin count was divided by the total number of counts (sum of all bin counts), and then by the bin size that it represented.

TABLE 5.1: Akaike Information Criterion values for various models applied to the PLI distributions of the classical Kuramoto model at $K = 2$, the effective critical coupling value for the system. Smaller values indicate a better fit, but comparisons are only meaningful across rows. The smallest value in each row is indicated with an asterisk.

| Wavelet Scale | Power-Law | | Exponential | Log-Normal | |
|---|---|---|---|---|---|
| 3 | 251.04 | | 288.75 | 116.26 | * |
| 4 | 253.87 | | 289.35 | 123.10 | * |
| 5 | 257.03 | | 316.55 | 157.24 | * |
| 6 | 258.62 | | 370.14 | 218.44 | * |
| 7 | 254.59 | | 396.20 | 252.47 | * |
| 8 | 245.74 | * | 359.41 | 250.97 | |
| 9 | 220.50 | * | 343.30 | 227.93 | |
| 10 | 224.56 | * | 318.80 | 229.26 | |
| 11 | 220.38 | * | 306.27 | 223.93 | |

TABLE 5.2: Akaike Information Criterion values for various models applied to the GLS distributions of the classical Kuramoto model at $K = 2$, the effective critical coupling value for the system. Smaller values indicate a better fit, but comparisons are only meaningful across rows. The smallest value in each row is indicated with an asterisk.

| Wavelet Scale | Power-Law | | Exponential | Log-Normal | |
|---|---|---|---|---|---|
| 3 | -2533.43 | * | -1019.49 | -2478.83 | |
| 4 | -2531.41 | * | -1296.02 | -2484.28 | |
| 5 | -2540.75 | * | -1351.52 | -2490.46 | |
| 6 | -2520.30 | * | -1304.60 | -2473.17 | |
| 7 | -2439.44 | | -1293.77 | -2465.53 | * |
| 8 | -2415.82 | | -1163.59 | -2426.63 | * |
| 9 | -2000.55 | * | -941.78 | -1985.62 | |
| 10 | -1536.79 | * | -686.48 | -1515.75 | |
| 11 | -546.67 | | -239.38 | -568.82 | * |

The Akaike Information Criterion ($AIC$) was calculated for both the PLI and GLS distributions for all studied coupling values. Only PLI intervals of length 0.1 seconds or more were used for model-fitting, and these only are shown in the plot. The power-law model was fitted using the procedure described by Clauset et al. [58], and implemented using their freely available code, and a minimum data value of 0.1 seconds. The log-normal and exponential distributions were both fitted using in-built Matlab functions.

The values obtained for the effective critical coupling $K = 2$ are shown in Table 5.1 for PLIs and Table 5.2 for GLS. As in [158], the power law distribution was only found to

be the best fit at certain wavelet scales (see Tables 5.1 and 5.2). The *AIC* values in Table 1 of Kitzbichler et al. [158], stated as being at critically coupled Kuramoto, favour a power law model of the PLI frequency distribution for 5 of 9 wavelet scales, although no value is reported for wavelet scale 11.

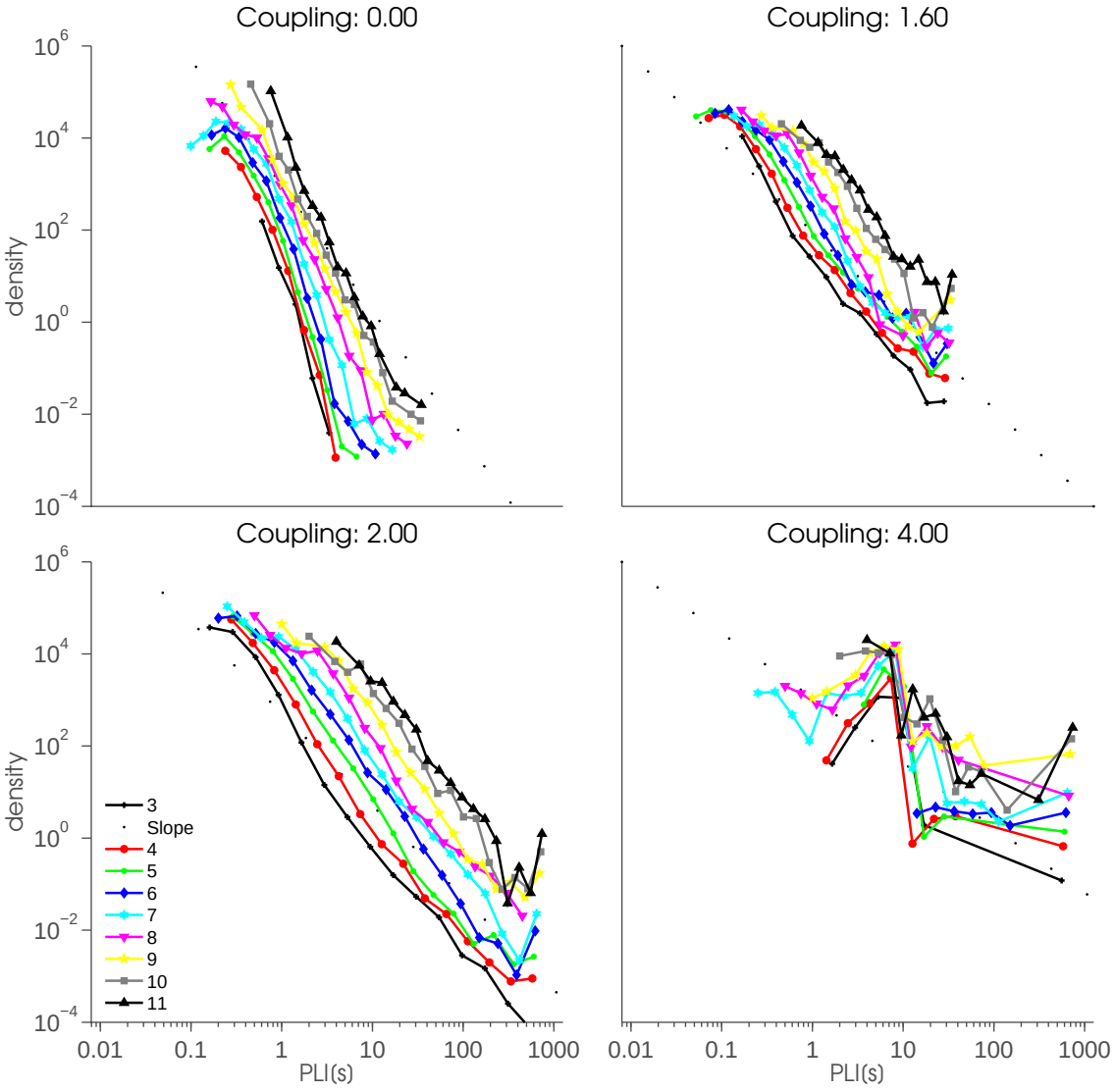


FIGURE 5.11: Distribution of PLIs in a system of 44 classical Kuramoto oscillators, with natural frequencies drawn from a $\mathcal{N}(0,1)$ distribution and four levels of coupling $K = 0$, $K = K_c \simeq 1.6$, $K = 2$ and $K = 4$ (from top-left, clock-wise). A power law of exponent -2 is shown by a dotted black line to guide the eye. The coloured lines represent wavelet scales $3 - 11$ (see key).

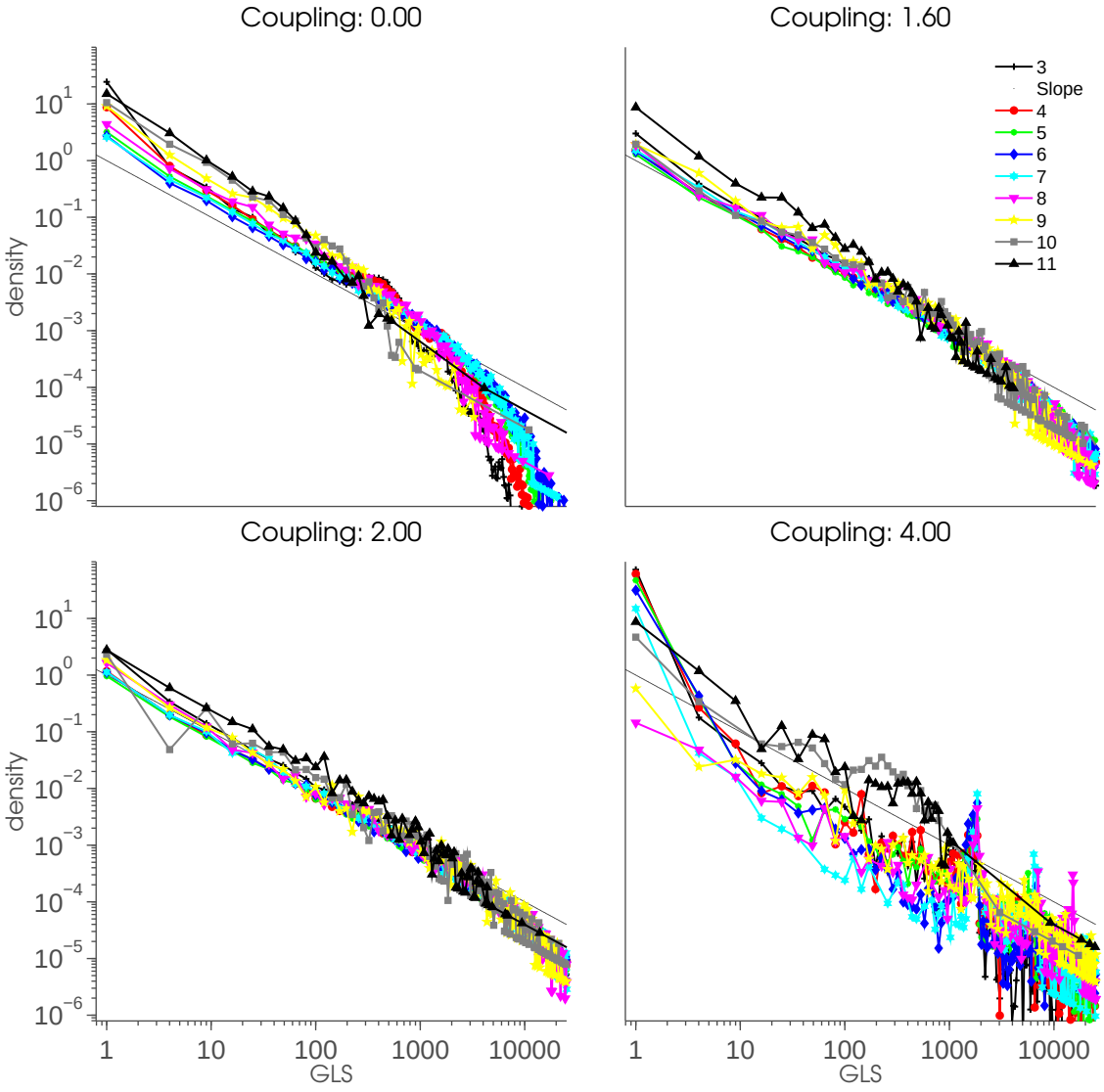


FIGURE 5.12: Distribution of GLS in a system of 44 classical Kuramoto oscillators, with natural frequencies drawn from a $\mathcal{N}(0,1)$ distribution and four levels of coupling $K = 0$, $K = K_c \simeq 1.6$, $K = 2$ and $K = 4$ (from top-left, clock-wise). A power law of exponent -1 is shown by a dotted black line to guide the eye. The coloured lines represent wavelet scales $3 - 11$ (see key).

In the system, at the effective critical coupling $K = 2$, the power law distribution was the best model for the data for 4 out of 9 wavelet scales for the PLI data. Note that the same number of wavelet scales were also best fitted by a power law distribution for coupling values $K = 1$, $K = 3$ and $K = 4$. At coupling $K = K_c = 1.596$, 3 wavelet scales were best fitted by a power law, and at no coupling, i.e., $K = 0$, only 2 wavelet scales. The log-normal distribution was otherwise the best fit at all coupling values and all other scales. The fact that less than half of the wavelet scales were best fitted by a power law distribution at the critical coupling, combined with the fact that non-critical coupling parameters ($K = 1, 3, 4$) resulted in the same proportion of scales being best fitted by a power law distribution, leads us to conclude that the distribution of PLIs is not a reliable

measure of criticality in a finite size Kuramoto system. Importantly, neither exponent value (-2 for PLI and -1 for GLS) matches the exponents of -1.5 expected for a critical diffusion process.

For the GLS probability distribution the coupling values giving greatest resemblance to power law distributions were $K = K_c \simeq 1.6$ and also $K = 3$, both with 8 of 9 wavelet scales best fitted by the power law model. (The *AIC* values for the GLS distribution were not included in [158]). In contrast, a power law model was best-fitting for only 2 wavelet scales at coupling value of $K = 0$. It was the best fit for 4 wavelet scales at coupling $K = 1$, for 6 wavelet scales at coupling $K = 2$ and for 3 wavelet scales at coupling $K = 4$. The remaining wavelet scales for all coupling values were again best fitted by a log-normal distribution. The prevalence of good power law fits in the GLS probability distribution across wavelet scales for coupling values $K = K_c$, 2 and 3, and the fact that power law distributions were not a good fit for the data resulting from coupling values $K = 0$ and $K = 4$, collectively suggest that the GLS measure may be an acceptable but not very sensitive indicator of the region of critical coupling for the finite size Kuramoto system.

The probability distributions of PLIs and GLS in Figures 5.11 and 5.12 are consistent with those shown in Figure 3 of [158] for the zero and critical coupling values. For $K = 0$, the probability distribution of the PLIs has a drop-off for PLI values above $10^0$. However, our plot at this value differs from that in Kitzbichler et al. [158], which shows that no intermediate length PLIs exist for many of the scales. We observe PLIs of all lengths from 0.1 to over 100 seconds with non-zero probability. We suspect that their data was truncated for display, but no detail is given in the paper. The distributions at all wavelet scales appear linear in the log-log space both at theoretical critical coupling of $K_c \simeq 1.6$, and at $K = 2$, the effective coupling parameter for this simulation of the Kuramoto system. The range in which this linearity holds is similar to that in [158], lying between $10^0$ and $10^2$. The results for coupling values beyond criticality show that the distributions remain power-law-like as the coupling is increased to $K = 3$, suggesting that linearity in the log-log space is not specific to $K = K_c$ for this system. This linearity in the log-log space vanishes for $K = 4$, where sufficiently many oscillators have synchronised at the mean field phase for the system, which induces a particular interval of phase-locking, indicated by the peak in the distribution. Qualitatively similar observations can be made regarding the GLS distributions.

### 5.4.8 PLI and GLS in the Independent Pairs model

PLI and GLS probability distributions were computed from the phase difference of 1000 pairs of oscillators with $\omega_i - \omega_k \sim \mathcal{N}(0, 2)$. The length of data, and time steps used were identical to those described in Section 5.4.6. The number of pairs was set to a value close to that of the total number (946) of pairings available in a system of 44 oscillators.

All PLIs across these pairings, and the measures of GLS for all consecutive time points were computed. Histograms of PLI and GLS, and $AIC$ values were computed exactly as in the previous Section (see Figures 5.13 and 5.14, and Tables 5.3 and 5.4).

#### 5.4.8.1 PLI probability distribution

As indicated by Figure 5.13, the structure of the probability distribution alters as the coupling increases. For $K = 0$, there is a drop-off below the power law of the distribution for values of the PLI above 1 second. At or around the theoretical and effective critical couplings, the log-log plot of the distribution approaches the same power law with slope $-2$ as indicated by [158]. For values up to $K = 3$, there is no significant difference between the evolution of PLI probability distributions with coupling in the Independent Pairs model and that of the Kuramoto model. The main dissimilarity arises from the continuing presence of an apparent power law distribution in the 'super-critical' range of $K = 4$. In the Independent Pairs model, the log-log plot of the distribution retains some of its linearity whereas there is synchronisation to the mean field in the classical Kuramoto model, as evidenced by a well-defined peak in Figure 5.11.

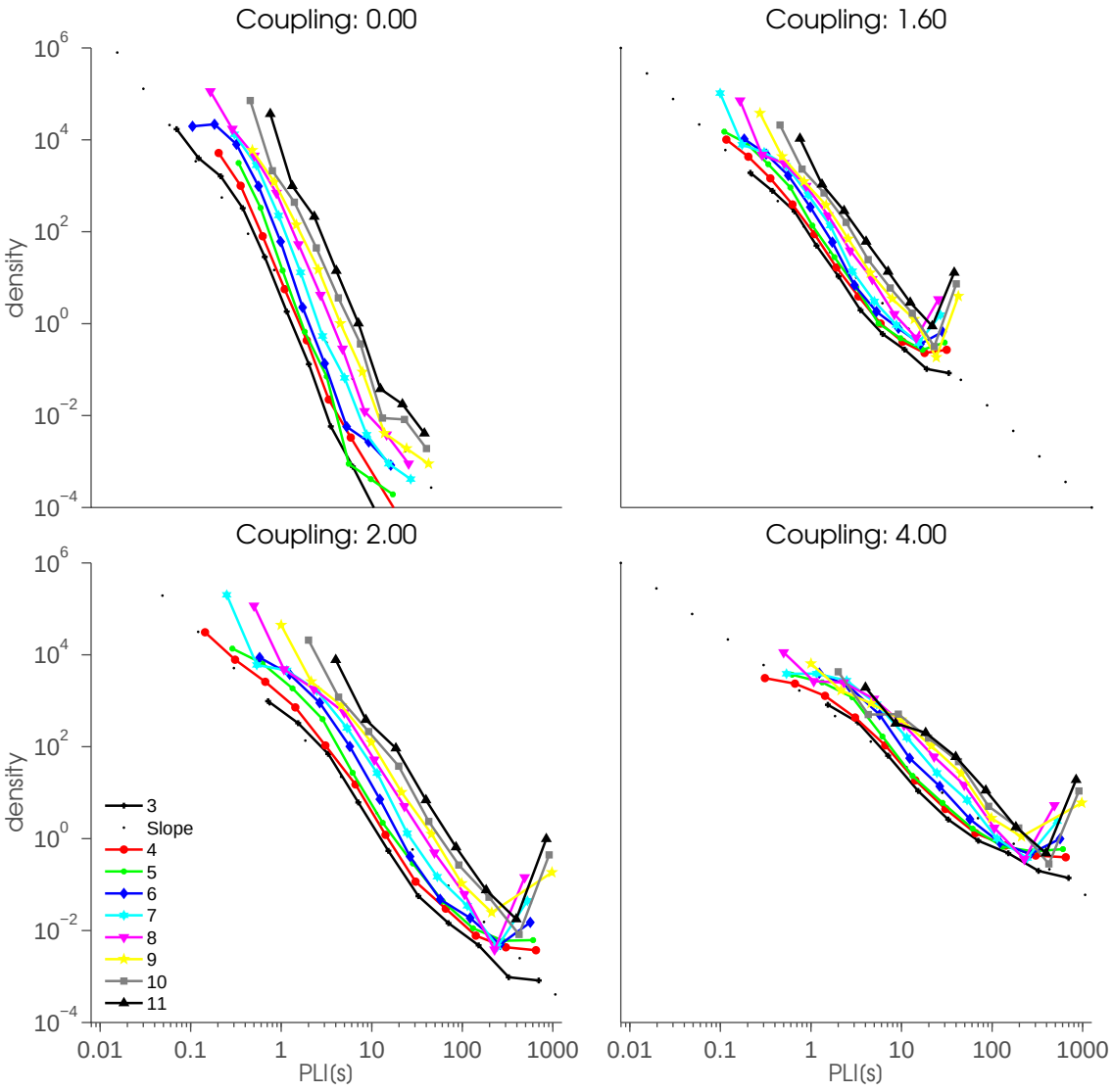


FIGURE 5.13: Distribution of PLIs in the Independent Pairs Model, with natural frequencies drawn from a $\mathcal{N}(0,1)$ distribution and four levels of coupling $K = 0$, $K = K_c \simeq 1.6$, $K = 2$ and $K = 4$ (from top-left, clock-wise). A power law of exponent -2 is shown by a dotted black line. The coloured lines represent wavelet scales $3 - 11$ (see key).

For the Independent Pairs Model, the *AIC* indicated that the power law distribution best fitted the PLI probability distribution for 4 of the 9 wavelet scales, at critical coupling value $K \simeq 1.6$, as well as for coupling values $K = 1$ and $K = 4$. Both the effective critical coupling value $K = 2$ (see Table 5.3) and $K = 3$ favoured the power distribution for 5 wavelet scales in contrast to only 1 wavelet scale for coupling $K = 0$. The remaining wavelet scales at all coupling values were best fitted by a log-normal distribution. As there is little difference between the numbers of wavelet scales best fitted by a power law distribution for corresponding coupling values of the classical Kuramoto and Independent Pairs models, we conclude that the PLI measure is therefore unable to distinguish between critically and non-critically coupled systems.

TABLE 5.3: Akaike Information Criterion values for various models applied to the PLI distributions of the Independent Pairs Model at $K = 2$, the effective critical coupling value for the system. Smaller values indicate a better fit, but comparisons are only meaningful across rows. The smallest value in each row is indicated with an asterisk.

| Wavelet Scale | Power-Law | | Exponential | Log-Normal | |
|---|---|---|---|---|---|
| 3 | 205.74 | | 121.02 | 49.49 | $*$ |
| 4 | 189.05 | | 222.37 | 120.70 | $*$ |
| 5 | 171.14 | | 192.08 | 107.80 | $*$ |
| 6 | 154.09 | | 166.67 | 93.89 | $*$ |
| 7 | 138.37 | $*$ | 241.74 | 139.03 | |
| 8 | 122.33 | $*$ | 210.90 | 124.66 | |
| 9 | 104.09 | $*$ | 174.94 | 109.51 | |
| 10 | 88.21 | $*$ | 161.30 | 93.26 | |
| 11 | 72.94 | $*$ | 129.74 | 80.59 | |

#### 5.4.8.2 GLS probability distribution

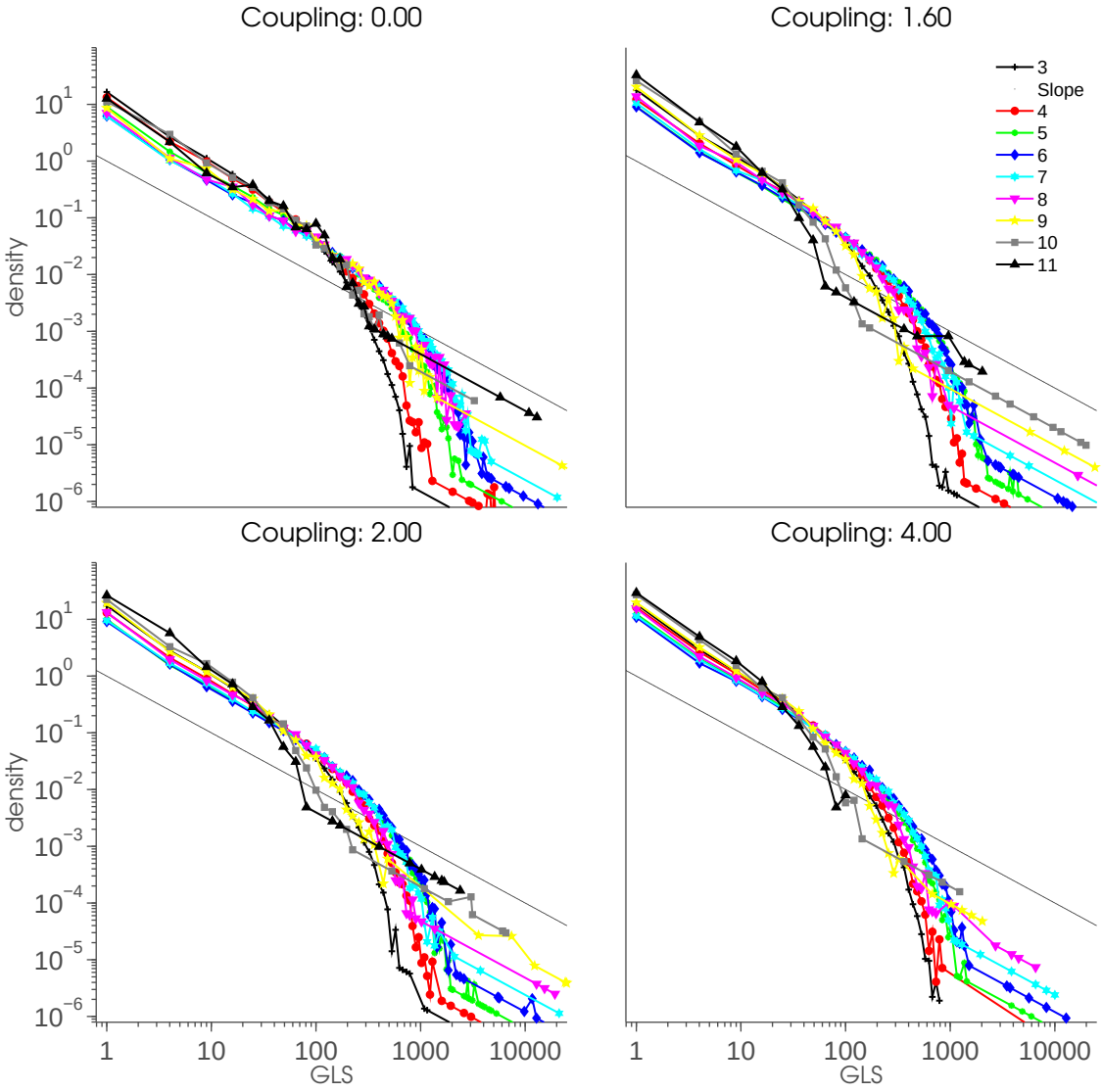


FIGURE 5.14: Distribution of GLS in the Independent Pairs Model, with natural frequencies drawn from a $\mathcal{N}(0,1)$ distribution and four levels of coupling $K = 0$, $K = K_c \simeq 1.6$, $K = 2$ and $K = 4$ (from top-left, clock-wise). A power law of exponent -1 is shown by a dotted black line. The coloured lines represent wavelet scales $3 - 11$ (see key).

In contrast to the PLI results, the probability distribution for the GLS of the Independent Pairs model remains largely unaltered as coupling increases, as shown in Figure 5.14. The GLS distributions do not resemble those of the classical Kuramoto model. The range in which the log-log plot of the distribution is linear is narrower with a drop-off in the distribution for values of GLS above 100s, suggesting that the Global Lability of Synchronisation measure may be more sensitive to the lack of critical interaction in the independent pairs system.

For GLS, only 2 wavelet scales were best modelled by the power law model at the effective critical coupling $K = 2$ (see Table 5.4 for $K = K_c$). 1 wavelet scale was best

fitted by a power law at coupling $K = 0$, 3 at $K = 1$, 2 at $K = K_c$, 4 at $K = 3$, and 3 at $K = 4$. The remaining wavelet scales at all coupling values were best fitted by a log-normal distribution. There is no evident pattern of increasing similarity to a power law of the GLS distribution, as the coupling increases.

TABLE 5.4: Akaike Information Criterion values for various models applied to the GLS distributions of the Independent Pairs model at $K = 2$, the effective critical coupling value for the system. Smaller values indicate a better fit, but comparisons are only meaningful across rows. The smallest value in each row is indicated with an asterisk.

| Wavelet Scale | Power-Law | | Exponential | Log-Normal | |
|---|---|---|---|---|---|
| 3 | -297.16 | | 42.78 | -301.51 | * |
| 4 | -379.92 | | 8.93 | -391.39 | * |
| 5 | -591.87 | | -54.62 | -596.56 | * |
| 6 | -409.53 | | -38.71 | -425.36 | * |
| 7 | -227.94 | | -6.39 | -251.63 | * |
| 8 | -193.42 | | 23.66 | -204.54 | * |
| 9 | -129.49 | | 51.58 | -132.82 | * |
| 10 | -84.46 | * | 57.75 | -78.53 | |
| 11 | -63.34 | * | 62.20 | -51.41 | |

## 5.5 Further concerns with PLI and GLS measures

Following the publication of the paper [34], a subsequent paper showed in that the results obtained by Kitzbichler et al. for MEG and fMRI data were indistinguishable from data recorded from an empty scanner [255]. We reproduce the figure from this paper in Figure 5.15.

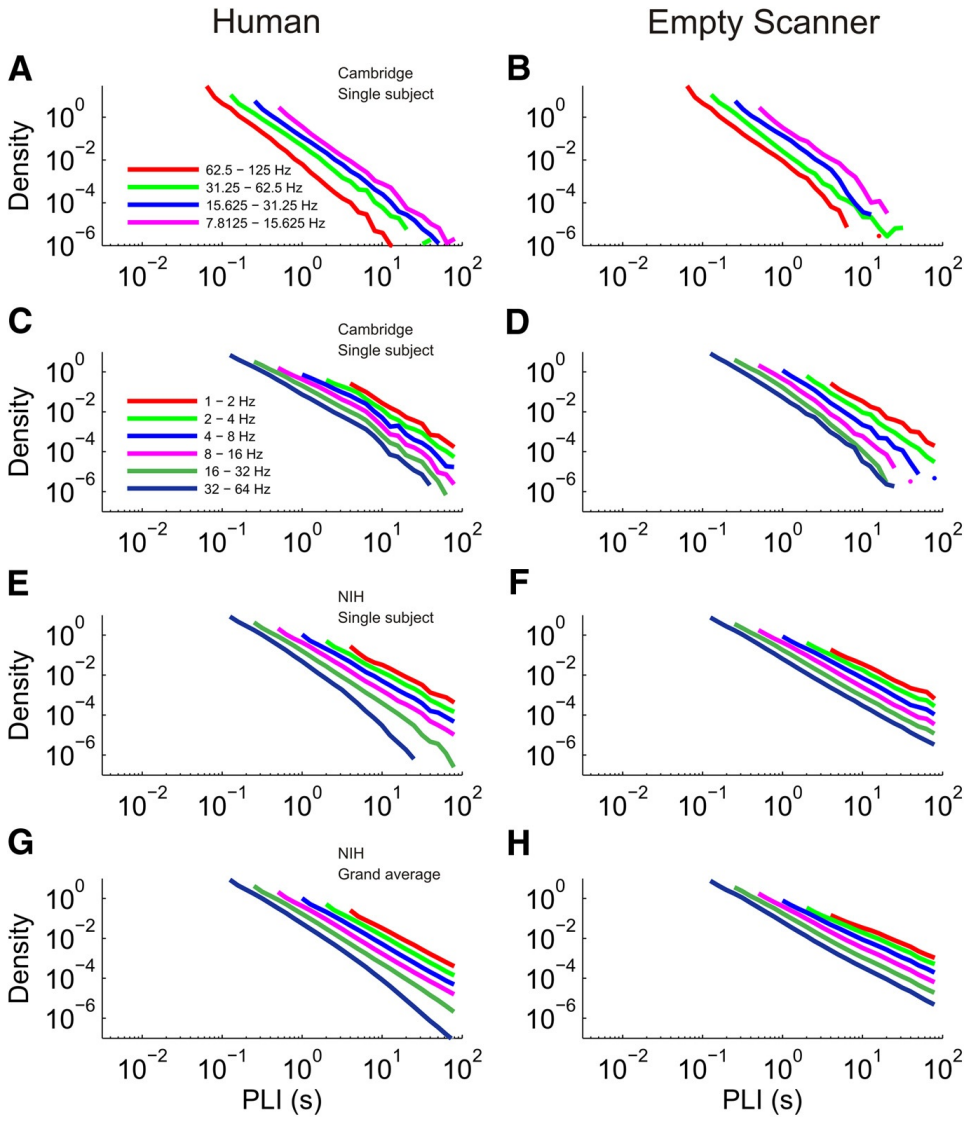


FIGURE 5.15: PLI analysis yields similar results from human data and empty scanner recordings. A,B: PLI distributions of a single human subject and a single empty scanner (B) both at the Cambridge MEG facility. The recordings were filtered using the Hilbert wavelet pairs at four wavelet scales with corresponding frequency bands included in the legend. C-H, PLI analysis using bandpass filtering and the Hilbert transform to acquire phase information. C,D Single human and empty scanner analysis (Cambridge) E,F. Single empty scanner and human recordings (NIH). G,H Average of 104 human NIH recordings (G) and 8 empty scanner recordings (H). Image reproduced from [255].

In this figure, recording facilities at Cambridge and NIH additionally suggest that PLI is not a measure to be trusted in drawing any conclusions of criticality about data.

## Conclusions

In this chapter, we began by mentioning the concept of criticality as an approach to understanding the human brain. Although there have been a number of studies demonstrating characteristics of critical systems in amplitude measures and avalanche sizes,

there has been relatively less exploration of such characteristics in measures of dynamic interaction in the nervous system. Synchronisation is such a measure of dynamic interaction, and a recent paper has approached the question of criticality in human brain network synchronisation. Here, this paper was summarised in full. The two measures, phase-locking intervals (PLI) and global lability of synchronisation (GLS), that were proposed by Kitzbichler and colleagues [158] as a means of characterising the presence of critical synchronisation in a critical model and which are applicable to human brain data were described.

The reasons of concern about these measures were discussed and critically examined in detail. This was done by presenting those measures with two very different models of synchronisation. In the first (Kuramoto Model) the oscillators are coupled with increasing $K$ to the mean field and undergo a critical transition. In the second (Independent Pairs Model) the oscillators are only allowed to couple in a pairwise manner. This latter model cannot be formulated as a system at criticality because there is no global coupling to associate the pairs with one another, and so no possibility of a mean field.

When calculating the phase locking intervals (PLI) following the methodology of Kitzbichler et al. [158], it was shown that power laws were the best fit for a similar number of wavelet scales when considering PLI distributions for the critical, Kuramoto, model and the non-critical, Independent Pairs, model. The power law distribution and the slope found for the PLIs of the non-critical system was closely similar to that shown by the critical model. Importantly, this slope is not -1.5. When further exploring the PLI probability distribution for coupling parameter values exceeding criticality, we found that the linearity of the log-log plot of the distribution at a number of wavelet scales still led to a best fit by a power law, suggesting that the observation of power laws within this framework can be present in a wide range of coupling values. We therefore conclude that the PLI measure should not be used to infer criticality (broadband or otherwise) in a system.

In simulations the GLS measure appeared better at discriminating between the critical, Kuramoto, system and the non-critical, Independent Pairs, model. We therefore conclude that GLS is a better measure than PLI for identifying critical systems, however, we believe that further work should be done to ascertain more precisely where its strengths lie, and compare it to other, non threshold-based methods such as proposed by Gong et al. [102]. In particular, we note that the GLS measure relies on counting the number of synchronised oscillators and that this depends crucially on how oscillators are defined, and distinguished. The GLS measure is not feasible in analysing MEG and fMRI data and indeed the authors of [158] have not used it again, citing concerns about finite size contamination of the power law. In the Kuramoto model, the number of oscillators is well defined, and each one is a discrete entity. With recorded neural activity, however, distinguishing multiple discrete oscillators is less straightforward. Kitzbichler et al., have applied the GLS measure to fMRI and MEG signals but its interpretation was limited

by finite size effects (see loss of log-log linearity in the GLS distribution of MEG data in their figures 5D and 7D). To my knowledge the GLS measure has not been applied again to human neural data. Recently Meisel et al. [192] have claimed to detect when compared to seizure-free electro-corticogram (ECoG) data a loss of adaptive self-organized criticality of the ECoG during epileptic seizures. This conclusion was arrived at through exploring power law scaling of ECoG phase locking using the PLI measure only. This is an exciting finding which received support from analysing the changes in PLI scaling seen in a computational model of self-organized criticality [33]. However, the work in this thesis indicates that interpreting the presence of a power law in the PLI probability distribution as a marker of criticality is problematic especially when a threshold has been applied to detect PLIs and when there has been pooling across many elements.

In the next chapter, a new method for the assessment of power laws in a measure of time-varying synchronisation is proposed, that can be applied to neurophysiological time series.

# Chapter 6

# Phase synchrony analysis method

## 6.1 Introduction

In the previous chapter, it was demonstrated that the PLI and GLS measures, which have been used to investigate the presence of power laws in human neuronal synchronisation, are affected by methodological difficulties [34]. A subsequent paper involving the authors of [158] demonstrated that the measure could not reliably distinguish between human MEG and an empty scanner [255]. Taken together, these results suggest that an alternative marker of criticality in time-varying neuronal synchronisation is required.

This question leads to two methodological issues. One is to determine a technique that may be used to measure time-varying synchronisation and the other is to identify a putative marker of critical behaviour.

Robust detection of time varying synchrony between two time series is a non trivial problem. Coherence-based methodologies have previously been used to quantify the oscillatory synchrony between different brain regions. However, coherence is a time-averaged measure, and does not provide information about the temporal evolution of neural synchrony. Alternative methods include windowed measures such as windowed coherence, wavelet coherence and OST (see Section 1.1.5). Additional insight may be gained by averaging a time-varying measure across trials to obtain a more robust estimate for a time-varying measure. Furthermore, as seen in Section 1.1.6, there are a number of instantaneous signal processing techniques that allow for an instantaneous estimation of synchronisation.

In response to the question of identifying a marker of criticality, we have the previously introduced DFA technique with a technique for validating the DFA exponent (ML-DFA). This can be used to detect LRTCs, which have been linked to critical behaviour [117, 178]. DFA is applicable to any time series including neurophysiological data.

In the following sections, a number of time-varying measures of the synchronisation between two time series are explored in detail before identifying one approach that may be used in conjunction with DFA to produce the phase synchrony analysis method. The method is validated by applying it to simulated time series for which there is an *a priori* expectation of critical synchronisation.

## 6.2 Data

The investigation of time-varying synchronisation measures are anchored by demonstrating their application to a specific data set. In particular, this is the data, which was described previously in 2.2.

## 6.3 Optimal Spectral Tracking (OST)

The optimal spectral tracking (OST) framework was introduced in Section 1.1.5.2.

Because DFA depends on calculating detrended fluctuation magnitude for a range of different window sizes, it is desirable to have as many data points as possible in the time series to which it is applied. In order to apply a framework such as OST, the time series must be segmented or windowed in the temporal and spectral domains. Increased segmentation in one of these domains requires coarser segmentation of the other. For the DFA to be effective, the coarsest division in the temporal scale could certainly be no more than 0.0625 seconds, which would mean that a 2 minute sample of a time series would yield 1920 innovations of data for the application of DFA. In contrast, the application of DFA to 2 minutes of EEG data sampled at 512 Hz would yield $120 \times 512$ innovations. This, by definition allows a spectral division of no finer than 16 Hz for every segment, creating six frequency bands for consideration of 0-15 Hz, 16-31 Hz, 32-47 Hz, 48-63 Hz, 64-79 Hz and 80-96 Hz. The band considered for exploration in this section is 16-31 Hz ($\beta$ band), because the data set includes EMG, which shows a spectral peak in this band.

### 6.3.1 Data results

The application and display functions of OST are demonstrated in Figure 6.1.

In Figure 6.1, a single frequency band was selected to observe its temporal dynamics. Namely, information corresponding to the frequency range 16-32 Hz ($\beta$-band) was chosen. DFA is now applied to the time-varying coherence measure (Figure 6.1 C.)

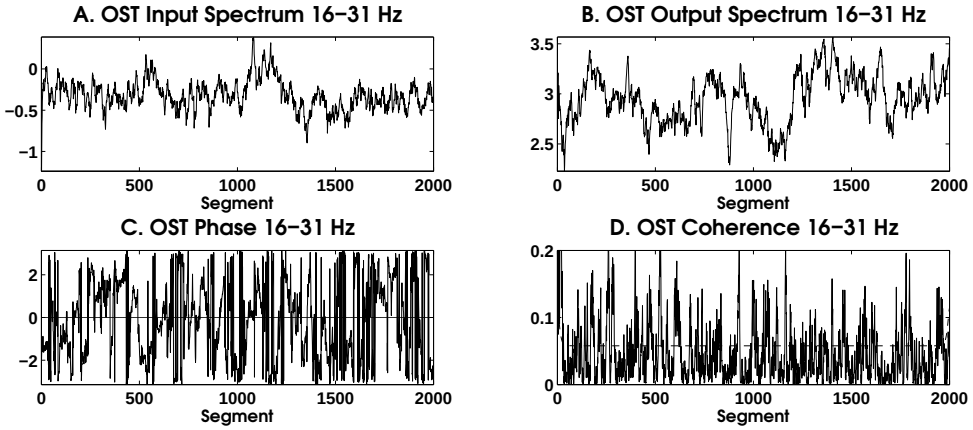


FIGURE 6.1: Panels A-D. show 1-dimensional analysis of left motor cortex EEG (input) and right-hand EMG (output) data for a representative subject using the OST method [37]. Time evolves along the $x$-axis and the frequency band considered is 16-31Hz. The temporal axis is divided into segments of 0.0625 seconds A. The spectrum for the EEG time series corresponding to the selected subject. B. The spectrum of the EMG time series corresponding to the same subject. C. The phase spectrum of EEG and EMG. The dashed line indicates the level of zero phase. D. The time-varying coherence of EEG and EMG. The dashed line indicates a 95% significance level.

The DFA fluctuation plot of the coherence between the left motor cortex EEG and the right-hand EMG is shown in Figure 6.2 for Subject 1 of Group 3 of the data.

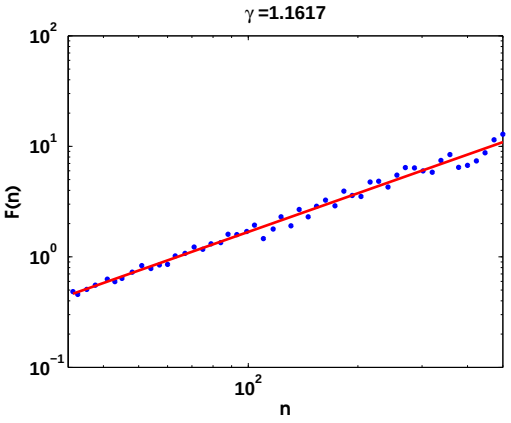


FIGURE 6.2: The DFA fluctuation plot of the coherence between the left motor cortex EEG and the right-hand EMG for a representative subject.

The exponent in Figure 6.2 is clearly greater than 0.5. In analysing several subjects in this way, it was found that many of them showed exponents that were also significantly greater than 0.5. However, in further exploring this approach, additional problematic aspects were noticed, and in particular these can be seen when white Gaussian noise was analysed.

### 6.3.2 OST on Gaussian Noise

In order to verify the plausibility of any potential findings, the OST method and DFA were applied to two time series of Gaussian white noise signal. As white noise time series are independent of each other, one would expect that the DFA of their time-varying coherence should be of the form of white noise, i.e. a DFA exponent of $\gamma = 0.5$ (Section 1.1.8.7). An example of the OST coherence time series obtained is shown in Figure 6.3 for the 16-32 Hz band. The result of applying DFA to this time series is presented in Figure 6.4.

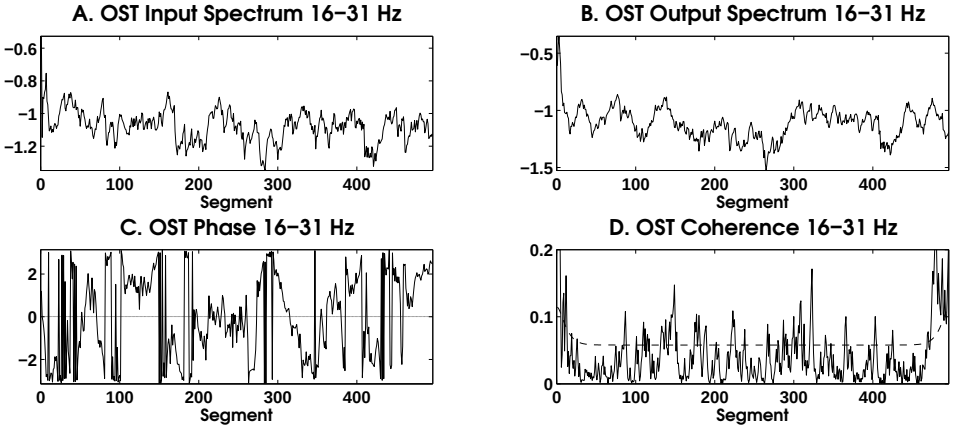


FIGURE 6.3: Panels A-D. show 1-dimensional analysis of two Gaussian white noise signals using the OST method [37]. Time evolves along the $x$-axis and the frequency band considered is 16-31Hz. The temporal axis is divided into segments of 0.0625 seconds A and B. The time-varying power spectra for the two signals, generated using OST analysis and considered in the frequency range of 16-31 Hz. C. The phase spectrum of EEG and EMG. The dashed line indicates the level of zero phase. D. The time-varying coherence of EEG and EMG. The dashed line indicates a 95% significance level. The time-varying power spectrum of a white noise signal, generated using OST analysis, and considered in the frequency range of 16-31 Hz.

The power spectrum for white noise should not show preference for any particular frequency band or time period. However, there is a reasonable variation in the power spectrum of Figure 6.3 at particular times, suggesting that particular time segments were much more inundated with 16-31 Hz frequencies than others. Indeed, the DFA exponent from this time series takes a value close to 0.75 (Figure 6.4). Repeated trials of this analysis yielded values of between 0.7 and 1.1. This result seriously called into question the potential interpretation attached to any findings from the real data analysis.

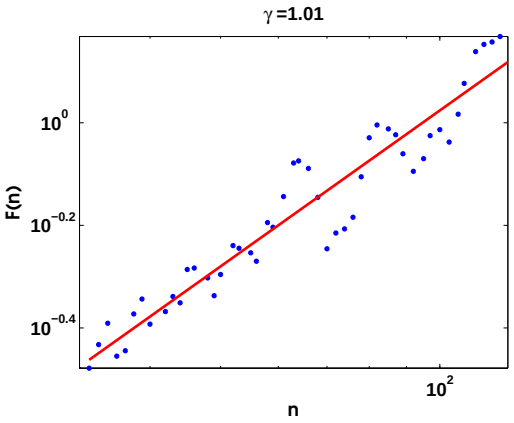


FIGURE 6.4: The DFA fluctuation plot generated by performing DFA on non-smoothed time-varying power spectrum of a white noise signal. OST analysis is used to generate the time-varying coherence from which the DFA is taken. The frequencies under consideration are in a band of 16-31 Hz.

The DFA exponent of OST coherence between two time series of Gaussian white noise takes a value of 1.01, which is above 0.5. This was not an isolated result, and it was found that depending on the length of the time series used for analysis, exponents ranged between 0.74 and 1.4. From this it was concluded that OST was unsuited to a DFA based approach.

One possible reason for an inflation of the DFA exponent is that OST requires a Kalman filtering process (Section 1.1.5.2). In order for Kalman filtering to be performed, two assumptions must be made - one is that the signal is noisy, and the second is that this noise is of a Gaussian nature. The Kalman filter thus reduces the input to a deterministic signal with additive independent and identically distributed noise. For the case of two purely Gaussian time series inputs, this is clearly a poor representation because in a time series of pure Gaussian noise, there is no underlying non-noise signal.

If a recorded EEG or EMG time series has a time-varying coherence that is similar to white noise, and OST is applied, this would be likely to yield artefactually high results in the DFA exponent. This may be the reason that the DFA exponent in Figure 6.2 was above 0.5.

It was also evident that shorter time series have higher DFA exponents of OST coherence. It is therefore possible that very long time series would be more suited for OST and DFA analysis. The data used for analysis in the section was described in Section 2.2, and is approximately 2 minutes in length. This may not be sufficient for OST and DFA analysis.

As the results of DFA yielded exponents that did not correspond to what we would expect when applied to Gaussian white noise, it was not considered necessary to apply ML-DFA to determine validity.

For these reasons, it was concluded that OST coherence was not a measure of time-varying synchronisation that was suited to DFA application. This led me to think about some potential alternative measures.

## 6.4 Further measures of time-varying synchronisation

An alternative method for calculating time-varying coherence is that of wavelet transforms [172, 210, 215, 247]. Wavelets are a technique for time-frequency analysis, which combine high temporal resolution with good frequency resolution [159]. A potential pitfall with these, however, in relation to EEG signals is that the signal to noise ratio is very low [159]. Wavelet transforms were not considered in this thesis because of the need to window in the temporal domain, which makes it likely that they would give rise to the same difficulties as the OST method. Windowed Fourier transform methods were not investigated for the same reasons [216].

## 6.5 Phase Difference

The next technique that was considered as a metric of time-varying synchronisation was that of phase difference [228, 270], which provides the advantage of being a well-defined technique to calculate an instantaneous value for the time-varying synchronisation, and thus a large number of innovations in a standard length time series. It has previously been argued that the Fourier, wavelet and Hilbert transforms are all essentially equivalent when their parameters are set appropriately [42]. However, the Hilbert transform phase difference measure allows a straightforward and computationally efficient means by which to avoid the use of a windowed measure. The phase difference can be calculated from the Hilbert transform as described in Section 1.1.6.3. In Section 1.1.6.3, we discuss the need to unwrap the phase time series in order to avoid artefacts at jumps in the phase after a cycle is completed. Using the formula given on page 368 of [228] avoids this problem altogether as stated in Section 1.1.6.6:

$$\phi_1(t) - \phi_2(t) = \tan^{-1}\left(\frac{\mathcal{H}(s_1(t))s_2(t) - s_1(t)\mathcal{H}(s_2(t))}{s_1(t)s_2(t) + \mathcal{H}(s_1(t))\mathcal{H}(s_2(t))}\right) \tag{6.1}$$

As discussed in Section 1.1.6.8, the Hilbert transform should be applied to signals that are narrow band. Additionally, neurophysiological questions are often related to specific frequency bands of interest. For these reasons, the time series are first filtered to a specific frequency band of interest as identified by peaks in the power spectrum of the time series (Section1.1.4.4) before the phase difference is calculated. DFA is then applied to this time-varying measure of synchronisation.

### 6.5.1 Results

Applying this method to subjects from the data set yielded exponents of between 1.2 and 1.8, which were even higher than those obtained from OST coherence.

In applying the method to Gaussian white noise, but without bandpass filtering, it was found that the DFA exponent returned was close to 1.5 (see Figure 6.5). This DFA exponent for the phase difference between Gaussian noise time series corresponds to one associated with Brownian noise instead (see Section 1.1.8.7).

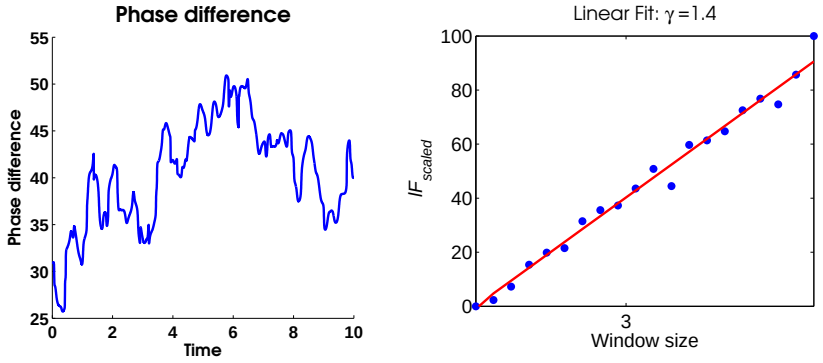


FIGURE 6.5: The result of DFA performed on the unwrapped phase difference of the Hilbert transform for a bandpass filtered noise signal. The DFA exponent takes a value of 1.37.

DFA assesses the degree of self-similarity in a time series, however, a time series that is self-similar cannot be bounded by definition. However, neurophysiological time series are very unlikely to be unbounded, indeed the amplitude of an EEG signal cannot be infinite. For this reason, the amplitude envelopes of neurophysiological time series are mapped onto unbounded time series before the application of DFA. This is done mathematically through integration, or can be done computationally, by cumulatively summing the time series. However, the phase and indeed the phase difference of a neurophysiological signal is already an unbounded time series because it always grows in time as the signal evolves. Therefore in applying DFA, the integration step is not required. Computationally, there are two ways in which the DFA algorithm can be modified to avoid this integration step. The first is to remove the cumulative summing and the second is to take the rate of change of the phase difference as input to the DFA algorithm. In this thesis, the latter of these steps is applied, but they are computationally equivalent. The latter step is used in particular because the full algorithm and any code used to calculate DFA can be inserted directly into the method, making it more straightforward to implement.

It is worth mentioning that in performing the latter step of applying DFA to the rate of change of the phase difference, we therefore apply it to the instantaneous *frequency* between the two time series. One way to intuitively understand this measure is as the correction that two signals exhibit in drawing closer to or further away from each other.

In the case of oscillatory signals, which are required for the Hilbert transform to be applied, we may imagine two pendulum clocks, which are oscillating. This analogy was first used by Christiaan Huygens in 1657 to describe synchronisation.

Huygens was the inventor of the pendulum clock. One of his particular concerns was to design a clock that could be used on ships, where the motion of the sea would disrupt the accuracy of his clocks [228]. On one occasion when he was ill and confined to his cabin for the day, he observed the activity of two specimens of his design suspended from the same beam (see Figure 6.6). He noticed that regardless of how quickly the two clocks were initially oscillating, they became synchronised and perfectly out of phase with each other after a time period. Such synchronisation occurred as a result of the weak coupling that existed between the two clocks due to the connection that they shared through the beam, which was itself induced to oscillate, almost imperceptibly. Synchronisation was not directly driven by either one or the other of the two clocks, and the speed at which they synchronised emerged as a combination of their two individual speeds.

This is the phenomenon of mutual synchronisation, whereby the clocks are coupled and therefore influence each other's speeds simultaneously. Huygens recorded his observation in a letter to his father in 1665 and called this phenomenon an 'odd kind of sympathy' [228]. Using the clocks analogy, the rate of change of phase difference will be the instantaneous *frequency* difference of the clocks oscillations, or in other words the difference in the oscillatory speed, at each time point, of the pendulums, as they synchronise with each other.

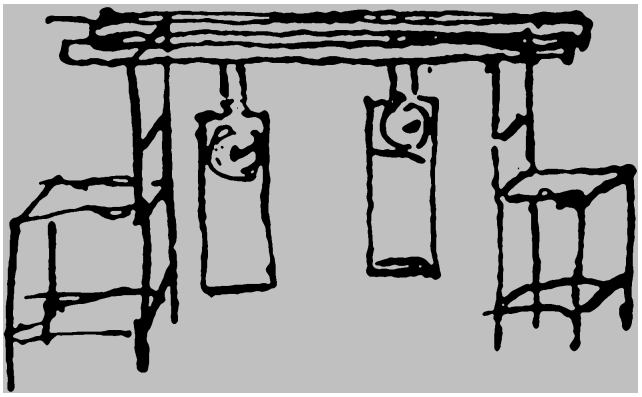

FIGURE 6.6: The original drawing by Christiaan Huygens to illustrate two of his pendulum clocks suspended from a single connecting bar. He noticed that these clocks became synchronised out of phase with each other. Image taken from [228].

## 6.6 Frequency Difference

As a preliminary check of the method, it is applied to a white noise signal in order to verify its appropriate treatment of such data. An example of a result obtained is

included in Figure 6.7. The exponents obtained from several iterations of this analysis gave values of between 0.40 and 0.63, with a mean values of 0.5. This is expected given the time series constructed.

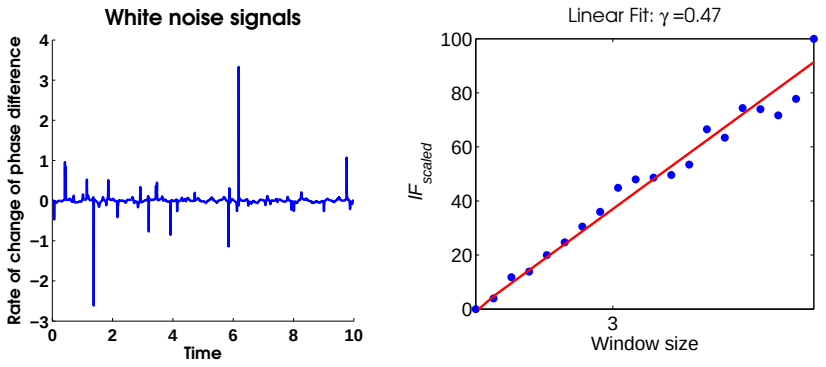


FIGURE 6.7: The result of DFA performed on the unwrapped frequency difference two bandpass filtered white noise signals.

One example of the output obtained from applying this method to a subject from the data set is also given in Figure 6.8.

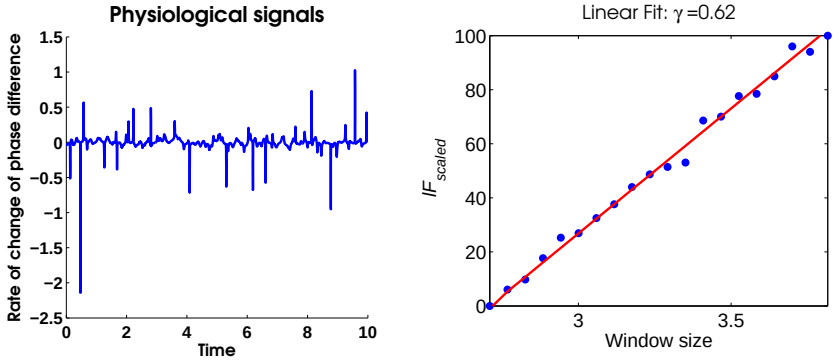


FIGURE 6.8: The result of DFA performed on the unwrapped phase difference of the Hilbert transform for a bandpass filtered signal.

## 6.7 Mid-chapter discussion

In the previous sections of this chapter, three measures of time-varying coherence were explored. It was found that the first and second of these contained methodological flaws when DFA was applied to them, leading to artefactual results. These were highlighted by inflated DFA exponents and invalid DFA fluctuation plots when ML-DFA was applied.

In the previous section, the frequency difference was identified as a measure that worked well and could be used as an input to DFA to create a putative method to assess criticality in time-varying synchronisation because it produced linear DFA fluctuation plots in

circumstances when linear scaling is to be expected and is straightforward to apply. This measure is straightforward to apply both to simulated and neurophsyiological data. This method is henceforth referred to as the phase synchrony analysis method.

In Figure 6.9, the steps of the phase synchrony analysis method are shown in full.

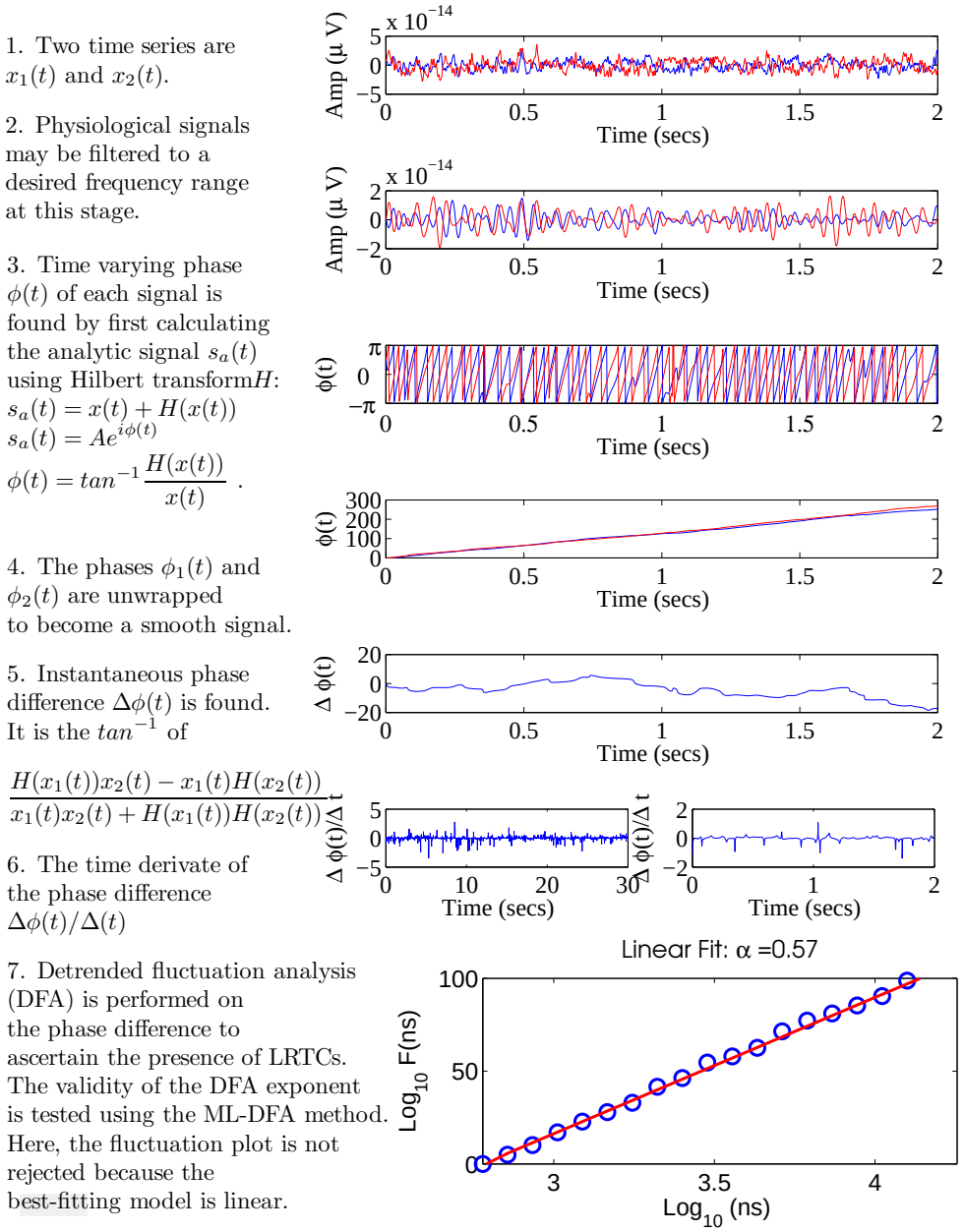


FIGURE 6.9: A schematic diagram of the steps of the method. The two time series in panel 1 can be taken from any source including data generated from model simulations, or biological recordings. In this figure two examples are shown of neurophysiological time series used to demonstrate the method: displayed in red and blue, respectively. The colour code and time segment of each signal is held constant in panels 1-4. Panel 2 describes a bandpass filtering step, which is necessary for neurophysiological time series, but does not typically need to be applied to other time series and is not used in this chapter. In panel 3 the time varying phases of the two time series are shown, as calculated using the Hilbert transform. In panel 4, the phases are displayed after being unwrapped, and in panel 5, the difference between their phases is taken. In panel 6, the rate of change of instantaneous phase difference is shown. We draw the reader's attention to the fact that panel 6 is illustrated using two plots, each of which shows a different time scale in the x-axis. The two time scales correspond to the minimum and maximum window sizes used when DFA analysis is applied to physiological time series. Panel 7 shows the DFA fluctuation plot obtained when the DFA technique is applied to the time series in panel 6. Following this, ML-DFA is applied to determine the validity of the fluctuation plot. In this case, it was accepted as being linear.

In the following sections, the phase synchrony analysis method is validated. It is first applied to surrogate data in which the rate of change of the phase difference is a time series with a known DFA exponent. Noise is added to this surrogate data in order to test the robustness of the method to noise.

The phase synchrony analysis method is next applied to data extracted from the Ising and Kuramoto models, in which critical behaviour of synchronisation is known at specific values of the model parameters. There is no published result to state certainly that LRTCs should be present in these models at their critical parameters. It is hypothesised that at or close to the critical value, depending on the direction from which it is approached, LRTCs will occur within the rate of change of phase difference.

These two models were used in the paper of Kitzbichler et al. [158], and power laws were identified in their phase-locked intervals (PLI) and global lability of synchronisation (GLS) frequency distributions in their respective critical regions. This result provided inspiration to explore the relationship between phase, phase difference and synchrony in their critical regions further.

The Kuramoto model is used in particular because it simulates the interaction between oscillators, each of which produces a time series that is coupled to the others, and it is thus comparable to a set of oscillatory signals of neurophysiological signals that mutually interact.

## 6.8 Surrogate Data

### 6.8.1 Methods

Two signals $x_1(t)$ and $x_2(t)$ can be constructed such that the rate of change of their phase difference is a time series $X(t)$ with a known DFA exponent [163]. To construct $x_1(t)$ and $x_2(t)$, we begin with the time series $X(t)$ to which DFA is applied. The phase difference of the two time series $\Delta(\phi(t))$ will be the cumulative sum of $X(t)$, which is discrete in this case:

$$\Delta(\phi(t)) = \sum_{s=1}^{t} X(s)$$

The two phases $\phi_i(t)$ and $\phi_2(t)$ of $x_1(t)$ and $x_2(t)$ respectively must be formulated so as to have a difference of $\Delta(\phi(t))$ or some multiple of $\Delta(\phi(t))$ (as DFA relates the size of detrended fluctuation amplitude at different windows to each other, its result is not affected by multiplying a time series by a constant). Therefore, $\phi_1(t)$ is set to $\phi_1(t) = \frac{\sum_{s=1}^{t} X(s)}{2f_s}$ and $\phi_2(t) = -\frac{\sum_{s=1}^{t} X(s)}{2f_s}$ where $f_s = 600$ and takes the role of a nominal sampling rate for the surrogate data. Such a nominal sampling rate is one typical value for neurophysiological recordings.

In order to recover the signals $x_1(t)$ and $x_2(t)$, the cosine of $\phi_1(t)$ and $\phi_2(t)$ should be taken. This is because the phase of a cosine signal is equal to its argument. The two signals are then defined to be:

$$x_1 = \cos\left(\omega + \frac{\sum_{s=1}^{t} X(s)}{2f_s}\right)$$

and

$$x_2 = \cos\left(\omega - \frac{\sum_{s=1}^{t} X(s)}{2f_s}\right)$$

where the factor $\omega$ is constant and here set to equal 1. The factors $\omega$ and $f_s$ modulate the time-varying $X(t)$. The reason that a constant factor of $\omega$ is required can be seen if we set $\omega = 0$. In this case, because of the symmetry of a cosine function we would have $x_1(t) = x_2(t)$, $\phi_i(t) = \phi_2(t)$ and $\Delta(\phi(t)) \equiv 0$. The value of $\omega = 1$ is taken without loss of generality for $\omega > 0$.

A hundred FARIMA time series $X(t)$ were generated using the algorithm described in [163] for each of the 11 DFA exponents $0.5, 0.55, 0.6, ..., 1$. Each simulation contains $N = 2^{22} = 4194304$ innovations, which corresponds to 6991 seconds of data with the nominal sampling frequency of $f_s = 600$ Hz. The value of the exponent of $X(t)$ is first computed, the two signals $x_1(t)$ and $x_2(t)$ are then constructed, and the method is applied. Window sizes used for application of DFA were logarithmically spaced with a minimum box size of 600 time steps, which corresponds to 1 second of the time series for the nominal sampling frequency $f_s$. The maximum window is $N/10$ where $N$ is the length of the time series, so that the maximum window is 699 seconds in this case.

A further control analysis was performed in which a Gaussian white noise time series $\eta_i(t)$ was added to one of the signals, in this case $x_1(t)$, before the method was applied to recover the DFA exponent of the phase difference $X(t)$. So that

$$x_1'(t) = \cos\left(\omega + \frac{\sum_{s=1}^{t} X(s)}{2}\right) + \sigma\eta_i(t)$$

where $\sigma$ is a value referred to as the 'noise level' throughout this chapter, and $x_2$ remains unchanged. This allowed the signal-to-noise ratio of $x_1(t)$ to be altered in an additive way. Because the noise is added outside the cosine function, it is added to the amplitude of the signal $x_1(t)$, which may occur in neurophysiological time series (for example see [108, 306]).

To construct $x_1'(t)$ and $x_2(t)$, $x_1(t)$ and $x_2(t)$ were first constructed as described above for each of the 11 DFA exponents $0.5, 0.55, 0.6, ..., 1$. The signal $x_1'(t)$ was then created by adding $\eta_i(t)$ with noise levels $\sigma \in [0, 1]$. It is noted that the noise level $\sigma$ is not the same as the signal-to-noise ratio [294]. The phase synchrony analysis method was

applied to $x_1'(t)$ and $x_2(t)$ and this was performed 100 times. For DFA exponents that were judged to be linear by ML-DFA, the average value for the 100 signal pairs was found.

By applying the method to signals with additive noise, it was possible to test the robustness of the method to noisy data. In this analysis, first the extent to which the DFA exponent altered when noise was added is estimated. Second, it is investigated whether ML-DFA rejects those DFA exponents that are known to contain noise, and if so, the level of noise at which exponents are no longer valid will be quantified.

### 6.8.2 Results

Surrogate data time series were analysed, and a scatter plot is presented in Figure 6.10A of expected DFA exponents against those recovered by applying the method. The scatter plot shows a strong linear relationship between the expected and recovered exponents with a slope of 0.998. The true slope of the plot is slightly below 1, indicating that the recovered exponent is slightly under-estimated by the method.

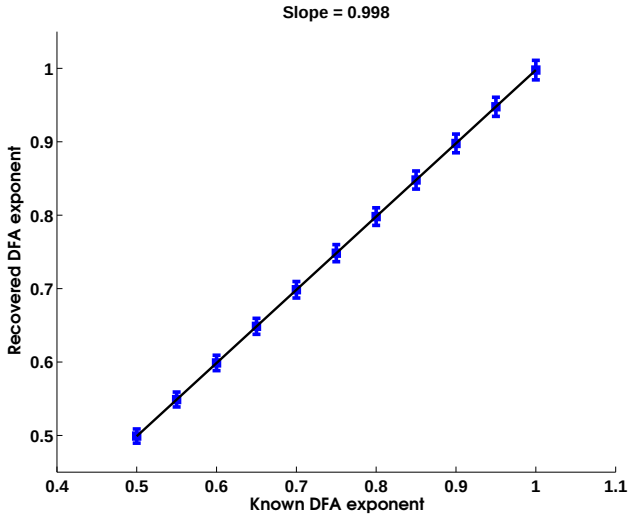


FIGURE 6.10: A plot of the recovered against the true DFA exponent for the time series. The relationship between recovered and true DFA values is well-approximated by a linear trend with a slope of 0.998 ($\approx 1$). The error bars increase very slightly with increasing DFA exponent. They represent a standard deviation around the mean.

When a small level of noise ($\sigma <\approx 0.1$ ) is added to signal $x_1$ with a known DFA exponent in its phase relationship with $x_2$, ML-DFA accepts the calculated DFA exponent because the DFA fluctuation plot does not deviate sufficiently from a linear plot. This is shown in Figure 6.11A. where noise levels of below $\approx 0.1$ still show valid DFA exponents. Figure 6.11A. shows that the level of noise for which valid DFA exponents are returned

is related to the value of the true DFA exponent of the phase. Where no data is shown, there are no valid DFA fluctuation plots found by ML-DFA.

When more noise is added to the system and the noise level $\sigma$ increases to above $\approx 0.3 - 0.4$, valid DFA exponents are again recovered with a value of 0.5 indicating that the phase relationship between the two signal has become white Gaussian noise. This occurs irrespective of the true DFA exponent of the rate of change of phase difference between $x_1$ and $x_2$.

In Figure 6.11B. the results of Figure 6.11A are presented in a slightly different way. Specifically, the *percentage difference* between the true DFA exponent and the recovered DFA exponent when noise has been added, is shown. These are presented for a range of true DFA exponent values as indicated by the legend. The plot demonstrates that the 'cut-off' point for the onset of invalidity is well approximated by a 5 % noise level of difference between recovered and true DFA exponent, although it is clear that this point varies slightly depending on the value of the true exponent. ML-DFA may therefore be a useful tool for identifying, and rejecting the results of those situations in which additive noise has disrupted the true DFA exponent of the rate of change of phase difference between two signals by more than 5%.

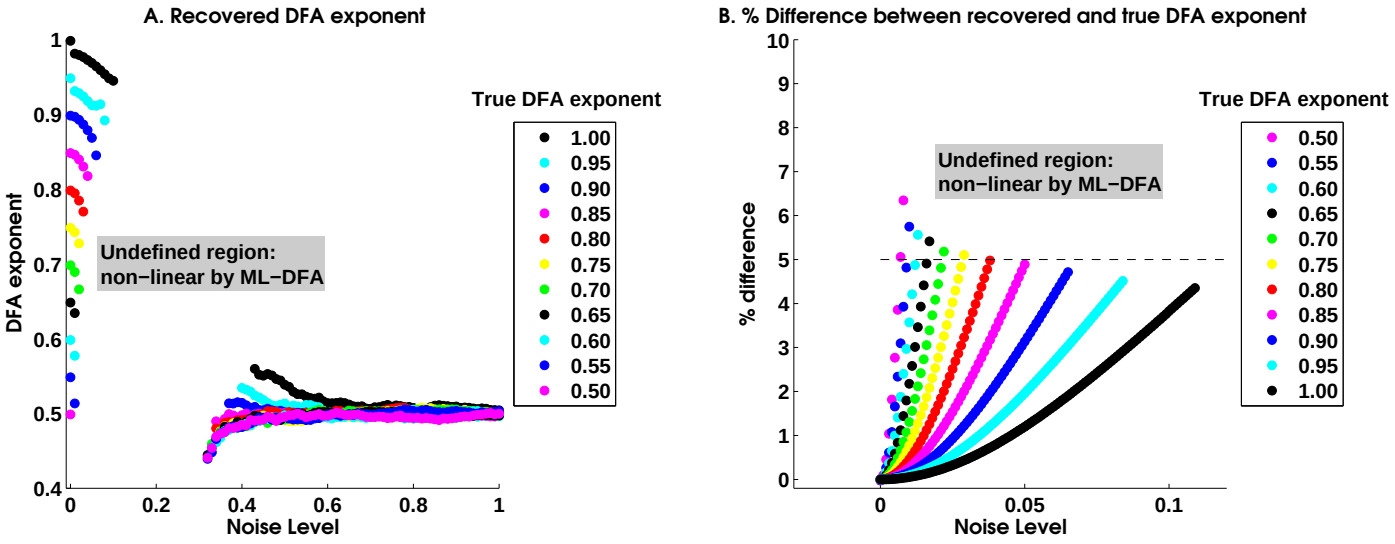


FIGURE 6.11: A. Recovered DFA exponent values as noise was progressively added. For each of the DFA exponents given in the legend (box insert), a signal $x'_1(t)$ was constructed with a noise level $\sigma \in [0, 1]$, shown on the $x$ axis. The phase synchrony analysis method was applied to $x'_1(t)$ and $x_2(t)$. This was performed 100 times. For DFA exponents that were judged to be linear by ML-DFA, the average value for the 100 signal pairs is shown. There are no data points corresponding to the intermediate noise level of $\approx 0.1$ to $\approx 0.3$ because all 100 DFA fluctuation plots for signals with this noise level were determined to be invalid by ML-DFA. B. The % difference between recovered and known DFA exponents as a function of the noise added to a signal with a known DFA exponent in its phase. The data shown in this plot is the same as that in panel A, but it is expressed in terms of the % difference between true and recovered DFA exponents rather than the raw recovered value. Only noise levels of $\sigma \in [0, 0.1]$ are shown. The colours represent different true DFA exponent values, as indicated by the legend within the inserted box. The dashed line indicates a 5% difference between known and recovered exponents. When the difference between the known and recovered exponent exceeded approximately 5% for any value of the true exponent, the recovered exponent is not accepted as being linear by ML-DFA and therefore not shown on the plots.

An alternative procedure for future research may be to consider multiplicative noise, or to add noise to the phase of a signal. Some published results exist for characteristics of the DFA fluctuation plots and exponents that may be expected from adding noise to a signal [129]. The addition of noise and other FARIMA time series at the level of the phase of a signal is explored further in the Appendix for this chapter.

## 6.9 The Ising Model

### 6.9.1 Methods

The Ising model on a lattice of elements is described in Section 1.1.7.3. In the implementation of the Ising model used here, the lattice consists of $96 \times 96$ elements. The constants $J$ and $k$ are set to $J = 1$ and $k = 1$ without loss of generality, which gives the critical temperature $T_c = \frac{2}{ln(1+\sqrt{2})} \approx 2.269$.

However, the phase synchrony analysis method is applied to time series rather than to a spatial structure. In order to obtain a time series from this spatial model, the procedure of [158] is followed. Namely, the lattice is divided into a number of smaller square lattices, which are referred to as sub-lattices, and a time series is created by taking an average spin value for the sub-lattice. A sub-lattice size of $8 \times 8$ was used as in [158]. Pairs of time series, for every possible pairing of sub-lattices belonging to the larger grid, were used as input signals for the method. For a sub-lattice of size $8 \times 8$, 144 time series could be created and these allowed for $10,296$ pairings. The average DFA exponent of the rate of change in phase difference between these time series is calculated.

Previous work by Priesemann et al. [233] suggests that the sub-sampling of a system may cause it to be misclassified as sub-critical or supercritical when it is in fact in a critical state. To verify that sub-sampling does not affect the result here, the phase synchrony analysis method is also applied to the Ising model in which the time series were obtained by sampling the lattice with a different sub-lattice size. Namely, results from the larger sub-lattice size of $16 \times 16$ are presented in the Appendix for this chapter.

### 6.9.2 Results

Figure 6.12 shows the average DFA exponent for the rate of change of phase difference between all pairs of time series generated by the 144 $8 \times 8$ sub-lattices in the Ising model. This average is calculated across the $10,296$ pairings of the 144 time series.

At a high temperature of $T = 10^5$, the spins of Ising model change rapidly (see Section 1.1.7.3). The DFA fluctuation plot is linear and therefore indicates that there is power law scaling in the detrended fluctuation magnitude. Indeed, ML-DFA shows that there is 100 % validity in the DFA exponents for all $T > 2.75$. The DFA exponent at $T = 10^5$ is below that at lower temperatures (see Figure 6.12), but above 0.5 and equal to $\approx 0.57$.

As temperature is decreased and $T_c$ is approached, clusters of identical spin appear in the Ising model lattice. An increasing number of time series pairs become synchronised so that the rate of change of their phase difference no longer fluctuates. DFA cannot be used to analyse a time series that contains no fluctuations, therefore there is a loss of linear scaling, as detected by ML-DFA. However, those pairs of time series that have not fully synchronised continue to show a valid DFA exponent, which increases with decreasing temperature. There is a range of temperatures above $T_c$ where LRTCs are present in the rate of change of the phase difference of these time series that are not dominated by identical spins, and these correspond to the Ising model being in a more disordered state than at criticality.

A peak in average DFA exponent is reached at a value close to but just above $T_c$. Specifically, the peak exponent has a value of 0.69 and occurs at a temperature of $T = 2.55$ with a high validity of 80 %.

As the temperature is decreased below $T_c$, which occurs between $T = 2.25$ and $T = 2.3$, validity is lost because many of the time series become synchronised due to a lack of fluctuations. The validity of DFA exponents across all pairwise time series falls from 56% to 34% in this interval. The DFA exponent changes from a value consistent with LRTCs (0.64) to a lower one between these temperatures. The standard deviation of exponents is large for $T < T_c$ because the lattice contains large clusters of elements with the same spin value, and the DFA exponent depends on whether the time series of averaged spins are taken from a single cluster, of from a region overlapping more than one cluster.

At temperatures below $T \approx 2.2$, the Ising system is magnetic and LRTCs are not possible between any pairs of time series because the rate of change of phase difference becomes approximately constant and equal to zero. The DFA exponent of a time cannot be interpreted because there is no power law scaling. This was detected by ML-DFA for all pairs of time series.

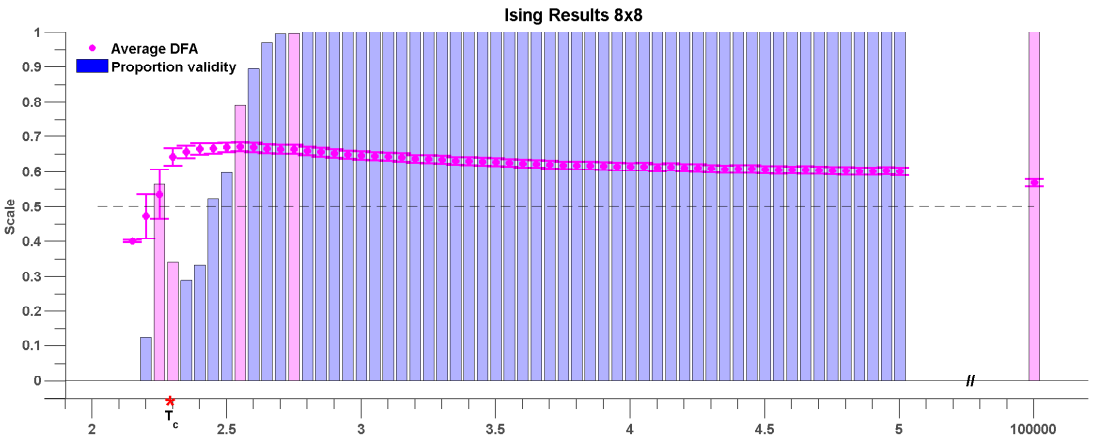


FIGURE 6.12: The average DFA exponents of rate of change of phase difference between pairs of time series generated by $8 \times 8$ sub-lattices of the $96 \times 96$ Ising model lattice. The temperature parameter, $T$, is varied on the $x$ axis. The average of the valid DFA exponents is shown in pink, and the error bars are a single standard deviation from the mean. The proportion of valid exponents, as calculated by the ML-DFA technique, is denoted by the vertical bars. The theoretical critical parameter $T_c$ is indicated by a red asterisk. The pink bars highlight some specific temperature parameter values that are discussed in greater detail in the text.

No results are shown for temperatures below $T = 2$ because at these temperatures the spins of the Ising model lattice change very little, and the time series produced by their average consist of a series of distinct 'steps', the Hilbert transform of which gives artefacts. The time series themselves are shown for a number of temperature values $T$ in Figure 6.13 and it is observed that the phase of these functions will only increase or decrease at points where a step occurs, and the phase will then change by a value of precisely $2\pi$ (see Figure 6.14). Finally, Figure 6.15 shows the rate of change of the phase for each of the time series. Here, it is possible to see that when $T = 1.5$, the rate of change of phase consists of a series of jagged lines at each time innovation,

which is a manifestation of the artefacts introduced by the application of the Hilbert transform. Such artefacts were discussed previously in Section 1.1.6.8 as edge artefacts, but they appear throughout a time series which contains discontinuities, such as that of the Ising time series at low temperatures. This point highlights the importance of visually assessing a representative sample of time series prior to any automated analysis.

In contrast to the above, we may observe the time series, the phase and the rate of change of phase extracted from the Ising model at higher temperatures. In these cases, there is a continuous structure to each of these quantities. It is noted that the phases in Figure 6.14 have not been unwrapped, which gives rise to its sawtooth properties. It has been presented in this way to allow the y-axis to be consistent throughout the figure, for ease of viewing. The phase is unwrapped prior to calculation of the rate of change of phase, which is a necessary step, as discussed previously.

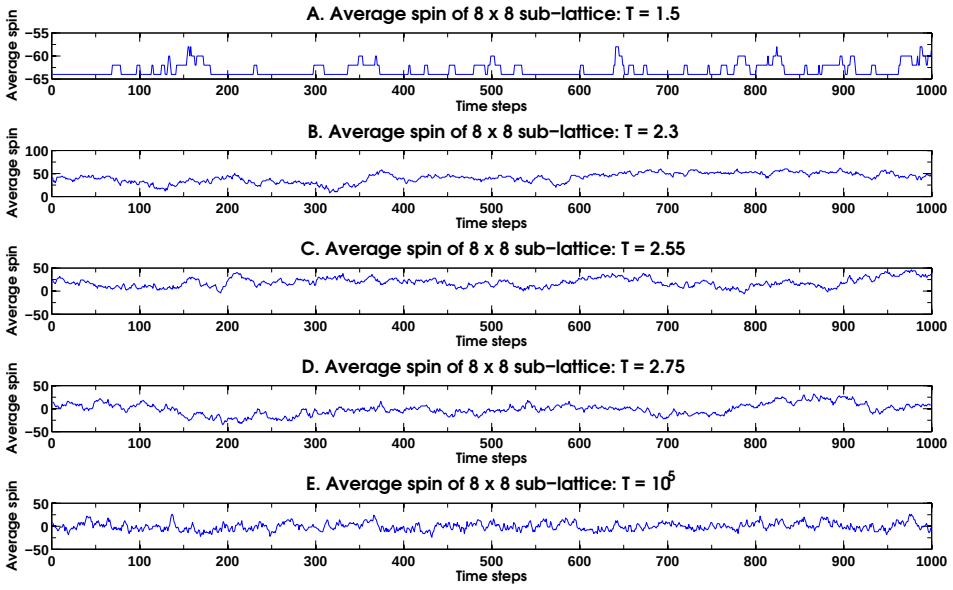


FIGURE 6.13: Time series generated by $8 \times 8$ sub-lattices of the $96 \times 96$ Ising model lattice. The temperature parameter, $T$, is set to $T = 1.5$, $T = 2.3$, $T = 2.55$, $T = 2.75$ and $T = 10^5$, which represent a low, critical and high temperature. The time series at $T = 1.5$ is not suitable for application of the Hilbert transform.

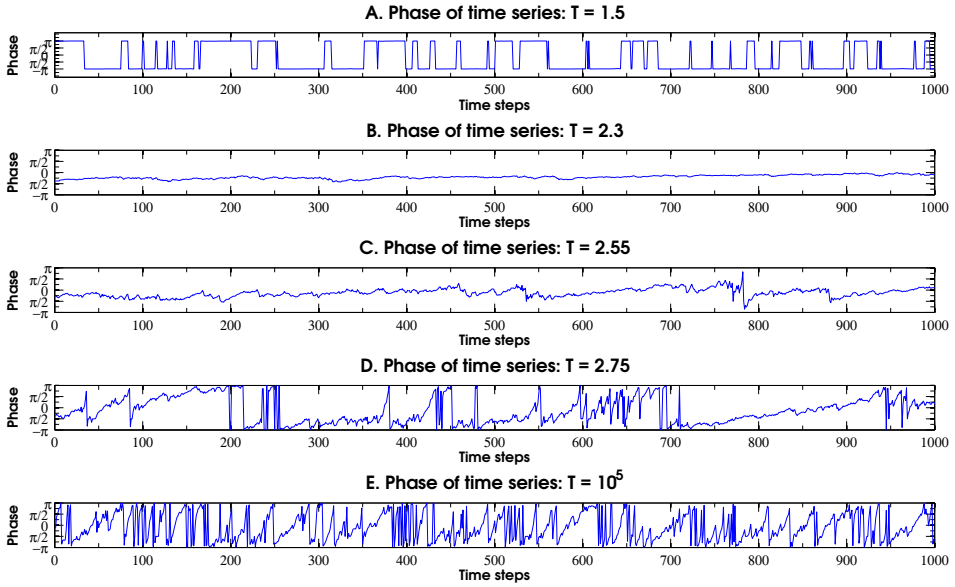


FIGURE 6.14: Phase of a single time series generated by $8 \times 8$ sub-lattices of the $96 \times 96$ Ising model lattice. The temperature parameter, $T$, is set to $T = 1.5$, $T = 2.3$, $T = 2.55$, $T = 2.75$ and $T = 10^5$, which represent a low, critical and high temperature. The time series at $T = 1.5$ has clear artefacts generated by application of the Hilbert transform. The reader's attention is drawn to the difference in the $y$-axis scale in panel A.

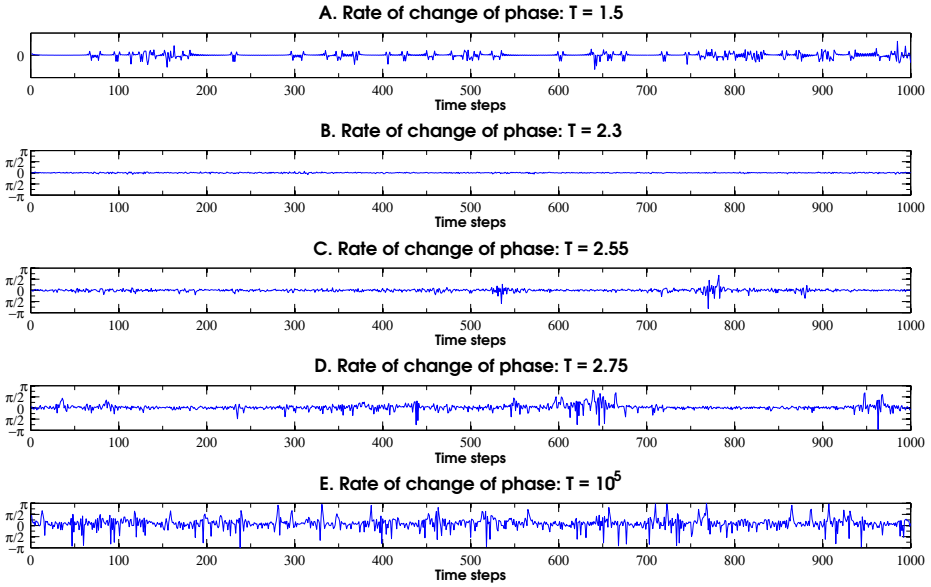


FIGURE 6.15: Rate of change of phase of a single time series generated by $8 \times 8$ sub-lattices of the $96 \times 96$ Ising model lattice. The temperature parameter, $T$, is set to $T = 1.5$, $T = 2.3$, $T = 2.55$, $T = 2.75$ and $T = 10^5$, which represent a low, critical and high temperature. The time series at $T = 1.5$ has clear artefacts generated by application of the Hilbert transform. The reader's attention is drawn to the difference in the $y$-axis scale in panel A.

## 6.10 The Kuramoto Model

The Kuramoto model is described in Section 1.1.3.4. As the Kuramoto model generates values for the phases of its oscillators, there is no need to apply a Hilbert transform to recover the phase of a signal in this case. For this reason, the method is applied from the point at which phase difference is calculated (see Figure 6.9).

The system generated in this section has the same properties as that used in Section 5. It is noted that the critical value is $K_c = \frac{2\sqrt{2}}{\sqrt{\pi}} \simeq 1.596$ in this model, but that the effective critical value, defined by the maximum rate of change of $Kr$ is at $K = 2$ [158]. As discussed in Section 1.1.3.4, this effective critical value occurs because we study a finite system, whereas theoretical results about the critical point in the Kuramoto model were derived by considering a system with an infinite number of oscillators.

The method was applied to the rate of change of the phase difference between all pairs of the 44 oscillators, which were simulated for 6100 time steps.

### 6.10.1 Observations

The first observation in analysing this model was that the DFA fluctuation plots were evidently non-linear. Application of ML-DFA showed that no DFA exponents could be recovered, but it is obvious without this technique that there cannot be linearity. Some examples of these plots are presented in Figure 6.16.

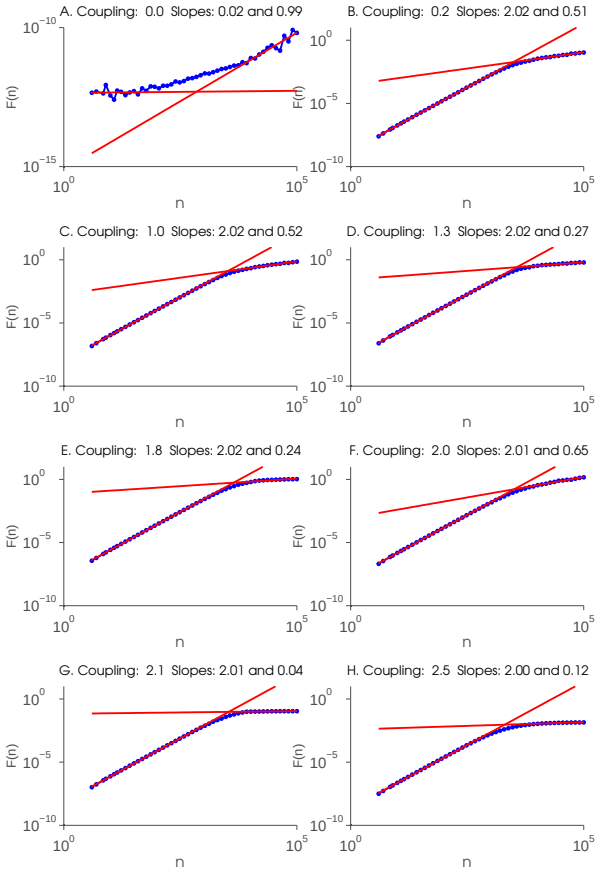


FIGURE 6.16: Application of the phase synchrony analysis method to oscillators of the classic Kuramoto model. The DFA fluctuation plots are shown for a range of coupling values $K$ (blue), and are fitted by two linear splines joined at a crossover point to demonstrate the non-linearity clearly (red). The coupling for each plot is written at the top. A. There is no coupling between the oscillators, and each evolves independently. The phase relationship between two oscillators is therefore a constant, which should yield an invalid DFA, however, computational inaccuracies give the signal some structure, which is recorded by the DFA. The reader's attention is drawn to the difference in y-axis for this plot. B.-H. For coupling between values 0.2 and 2.5, the DFA curve remains very similar in shape and invalid as indicated by ML-DFA. The DFA fluctuation plot remains similar in shape, with a slope of 2 for small time scales indicating an underlying sine function, and a slope ranging from 0.12 to 0.65 at large time scales. These slopes at large time scales represent the interactions between oscillators overlaying the sinusoidal phase evolution. The critical coupling $K_c = \frac{2\sqrt{2}}{\sqrt{\pi}} \simeq 1.596$ and the effective critical value, defined by the maximum rate of change of $Kr$ is at $K = 2$.

When coupling is $K = 0$, there is no interaction between oscillators, each evolves as an independent sine curve, and the differentiated phase relationship between any two oscillators is therefore a constant value. The DFA of a constant line is not defined. However, computational inaccuracies can sometimes lead to the existence of small fluctuations, and these are analysed by the DFA technique. The reader's attention is drawn to the difference in y-axis in Figure 6.16 A. in comparison to Figure 6.16 B.-H. These suggest that the slope at $K = 0$ is more likely caused by computational error than any genuine

structure to the data. For this reason, a further interpretation of the corresponding slope values was not attempted. Figures 6.16 B.-H. recover this with a slope of 2.

Figure 6.16 B.-H. can be explained using considerations from the paper by Hu et al., in which the DFA fluctuation plots of time series created by superimposing independent signals were studied [129]. The plot in Figures 6.16 B.-H. are similar to those created by the superposition of a sine curve with noise data (this point was discussed in detail in Section 2.6.5 when ML-DFA was developed). Since the phase interaction term between oscillators of the Kuramoto model is a sine function (Equation 1.1), one would indeed expect the phase relationship to behave like a sine curve.

The distinction between the DFA fluctuation plots in Figure 6.16 B.-H. is the slope of the curve for large window sizes. The slope of this segment may be supposed to contain some information of the interaction between oscillators above their respective natural frequencies that are reflected in the DFA exponents of value 2 at lower window sizes. As this slope occurs at large time scales in the system, it represents the interactions at long time-scales between the oscillators, whereas the short time-scale interactions are governed by a sinusoidal term. Indeed, it can be seen from Figure 6.16 that the slope of the DFA flucutation plot at large time-scales alters for different coupling values and looks as though it might show a peak value of the DFA exponent consistent with the presence of LRTCs at a coupling value of $K = 2$, which is at the effective critical value of the system.

However, three important points must be made to contradict this assumption. The first is that the crossover point seen in Figure 6.16 is by no means consistent for different oscillator pairs, or different coupling values, and it is difficult to distinguish a DFA fluctuation plot with a crossover from one which is simply a continuous curve such as Figure 6.16 H. The crossover point can be automatically detected by a spline fit, but because many fluctuation plots transition smoothly between one slope and the other, the location or presence of this crossover is hard to identify. The second point is that when the DFA fluctuation plots for all pairs of oscillators were divided as shown in Figure 6.16 using a spline curve, and the crossover point was estimated, the average slope of the large time-scale segment did not exceed 0.5. This suggests that although individual curves may show LRTCs if their DFA fluctuation plots are artificially manipulated in this way, the system globally does not. It is difficult to distinguish whether this is because the system does not contain LRTCs, or because the method for identifying crossovers in these cases is poor. This becomes especially difficult in a large Kuramoto system with many oscillator pairings. The third point is that when we need to manipulate the DFA fluctuation plot to look at a small range of window sizes, we can no longer suppose that the system is displaying the scale-free behaviour that we are aiming to assess using DFA. By its definition, many scales of window sizes are required to draw such a conclusion.

The conclusion of this section is that the classic Kuramoto model does not create a sufficiently rich structure of time-varying phase synchrony to show LRTCs in an interpretable

form. [1]

In order to obtain a model with a richer structure in oscillator dynamics, the Kuramoto model is studied with additive noise.

## 6.11 The Kuramoto model with noise

In this section the Kuramoto model with an added noise term is introduced. Equation 1.1 is developed to be:

$$\dot{\phi}_i(t) = \omega_i(t) + \frac{K}{N}\sum_{j=1}^{N}\sin(\phi_j(t) - \phi_i(t)) + \eta_i(t) \tag{6.2}$$

where $\eta_i$ is a noise input taken to be uncorrelated Gaussian noise with zero mean ($\langle\eta_i\rangle = 0$) and covariance $\sigma_i^2/T$ ($\langle\eta_i(t)\rangle\langle\eta_j(s)\rangle = \delta_{ij}\delta(t-s)\sigma_i^2/T$) where $\delta_{ij}$ is the Kronecker delta, $\delta(t-s)$ is the Dirac delta function, $\sigma_i$ is in radians and $T = 1$ second here.

In the Kuramoto model, coupling is global, meaning that each oscillator is connected to each other oscillator with a constant $K$.

In an essay by Daniels [67], the critical coupling for the infinite Kuramoto model with added noise $K_{c,noise}$ is calculated to be:

$$K_{c,noise} = 2\left[\int_{-\infty}^{\infty}\frac{\sigma_\omega}{\sigma_\omega^2+\omega^2}g(\omega)d\omega\right]^{-1}$$

where the parameter $\sigma_\omega$ is the standard deviation of the natural frequencies of the oscillators int he system, and the term $g(\omega)$ is the distribution of the natural frequencies.

As the number of oscillators in the model is finite, this value is only an approximation to the true critical coupling in the system, but is a useful approximation nevertheless. The value of $\Delta(Kr)$, which was introduced in the classical Kuramoto model, also provides a helpful marker of the effective critical coupling when noise levels are not too large [193].

In this chapter, time series were generated for 200 oscillators of the Kuramoto model described by Equation 6.2. Each time series was $T = 6100$ time steps. The standard deviation $\sigma_i$ was set to equal 0.32, however, the effects of changing the noise level are also presented in the Appendix for this chapter. The value of 0.32 was selected because it was sufficiently small for noise not to dominate the phase relationship, but sufficiently large

[1] This point has the potential to call into further question the finding of power laws in the time-varying synchronisation measures presented in the paper by Kitzbichler et al. [158], but this is not explored further in this thesis.

for noise affect the interactions between oscillators. For simulations of the Kuramoto model implemented here, the distribution of natural frequencies was $g(\omega) \sim \mathcal{N}(44\pi, \sigma_\omega)$, with $\sigma_\omega = 15$ as the standard deviation. This corresponds to a normal distribution centred around 22 Hz. The normal distribution is a unimodal distribution and as mentioned in Section 1.1.3.4, this ensures the presence of a critical coupling parameter. In order to get an idea of the spread of the distribution, the minimum natural frequency selected from this distribution was 16.3 Hz and the maximum was 27.8 Hz. This frequency range was selected because it spans the $\beta$ frequency band of EEG and MEG oscillations.

For these parameter values, the critical coupling $K_c$ is equal to:

$$K_c = \frac{2\sqrt{2}}{\sqrt{\pi}}\sigma_\omega = \frac{2\sqrt{2}}{\sqrt{\pi}}15 \sim 23.93$$

The integral for $K_{c,noise}$ is not analytically calculable for a normal distribution $g(\omega) \sim \mathcal{N}$, but empirical calculation yields:

$$K_{c,noise} \sim 23.85$$

Average DFA exponents of the rate of change in the phase difference are calculated for the 19900 pairwise combinations of the 200 oscillators in this Kuramoto model.

### 6.11.1 Results

Figure 6.17 shows the average DFA exponents obtained for the 19900 pairwise combinations of the 200 oscillators in the Kuramoto model when the method is applied.

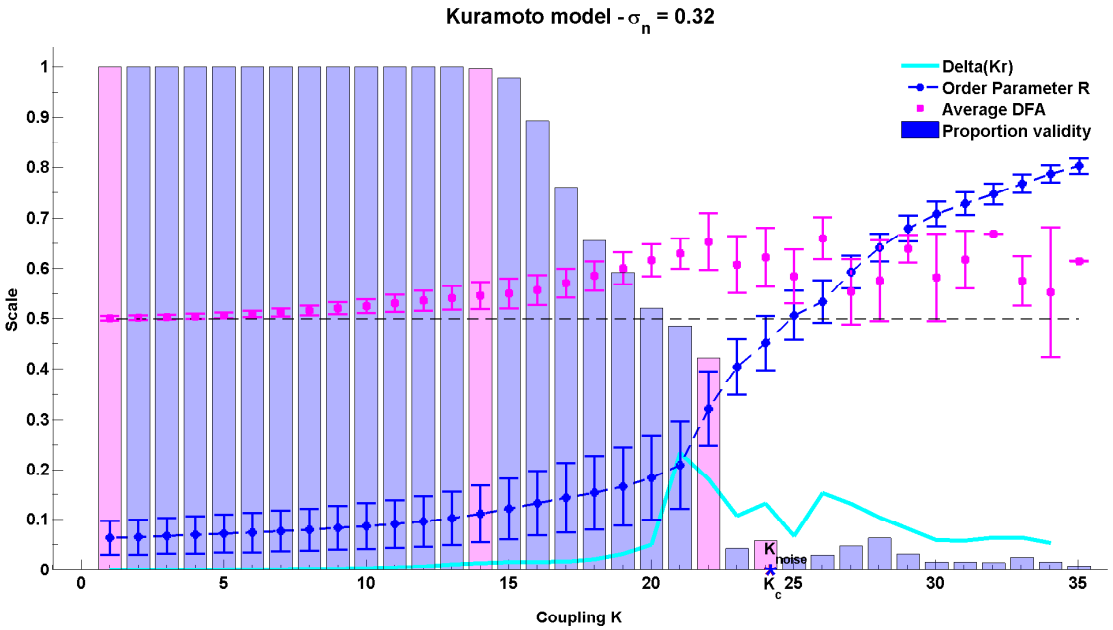


FIGURE 6.17: Results of the phase synchrony analysis method when applied to the Kuramoto model. There are 200 oscillators, with a mean natural frequency of 22 Hz, and a standard deviation of natural frequencies that is set to 15. The theoretical critical coupling $K_c$ (24) is marked on the plot with a red asterisk. The theoretical critical coupling $K_{noise}$ when noise is added is marked with a blue asterisk. The order parameter $r$, its difference $\Delta(Kr)$ and the proportion of valid DFA fluctuation plots from the full set of 199000 oscillator pairs are shown by bars. Validity bars that are referred to in the text are highlighted in magenta.

At low coupling $K$, the oscillators do not interact with each other, or do so very weakly, and each evolves at or near its own natural frequency. The order in the system is low, and the order parameter across all oscillators reflects this. The phase difference between pairs is a constant with an overriding noise term that comes from the dynamic equation of the Kuramoto model (Equation 6.2). DFA exponents of 0.5 are therefore observed in the pairwise phase differences as this is the exponent associated with white noise. This value of 0.5 DFA is also evident in the average DFA (Figure 6.17). There is almost 100% validity across all pairs for $K > 1$ and $K < 14$ because white noise time series are scale free and therefore the DFA fluctuation plots obtained from analysing them are expected to be linear (Figure 6.17). After $K = 14$, the validity drops to below 100 %.

The peak average DFA exponent occurs on average at $K \approx 22$ (Figure 6.17). The value of the average DFA exponent at this coupling value is 0.65 with standard deviation 0.06, which is indicative of the presence of LRTCs in the rate of change of phase difference. This peak is also close to and just below the theoretical critical coupling of the infinite Kuramoto system with noise $K_c \approx 23.85$. The peak in this average also occurs approximately at the location of the peak at $K \approx 21$ in $\Delta(Kr)$, which represents the coupling value at which the order parameter $r$ increases most, and the point of greatest flux in the system [158, 193]. It is noted that the location of the peak in average DFA is closer to the critical coupling than the peak in $\Delta(Kr)$ is.

The proportion of valid pairs at $K = 22$ is 42%. DFA exponents become invalid once the oscillators fully synchronise. At full synchronisation their phase difference no longer fluctuates, so that DFA cannot produce interpretable results. ML-DFA shows this by returning a non-linear model as the best fitting model for the DFA fluctuation plot.

After the peak average DFA exponent, a further increase in $K$ eventually causes full synchronisation between all the individual oscillator pairs. Across the whole system, fewer than 10% of the oscillator pairs yield a valid DFA after the theoretical critical coupling is exceeded.

Together, the results of analysing the noisy Kuramoto model suggest the peak in the DFA exponent of the rate of change of phase difference between oscillator pairs can be used to recover the peak in $\Delta(Kr)$. For coupling at and close to this value the rate of change of phase difference shows the presence of LRTCs. On the other hand, a noise phase difference indicates a DFA exponent of $\approx 0.5$ and a state when there is little or no coupling between the oscillators. Full synchronisation is characterised by loss of validity in the DFA fluctuation plots and non-linear DFA fluctuation plots.

#### 6.11.1.1 Individual oscillators pairs

In this section, the change in the DFA exponents for individual pairs of oscillators in the Kuramoto model is investigated as coupling is increased.

As the coupling parameter $K$ is increased, the DFA exponents of each of the oscillator pairs rise until the maximum is reached. The individual locations of these maxima, and the DFA exponent reached are related to the difference in natural frequencies of the two oscillators as well as to their interactions with the noise and mean field. Representative examples for separate oscillators are given in Figure 6.18 to illustrate this dependence.

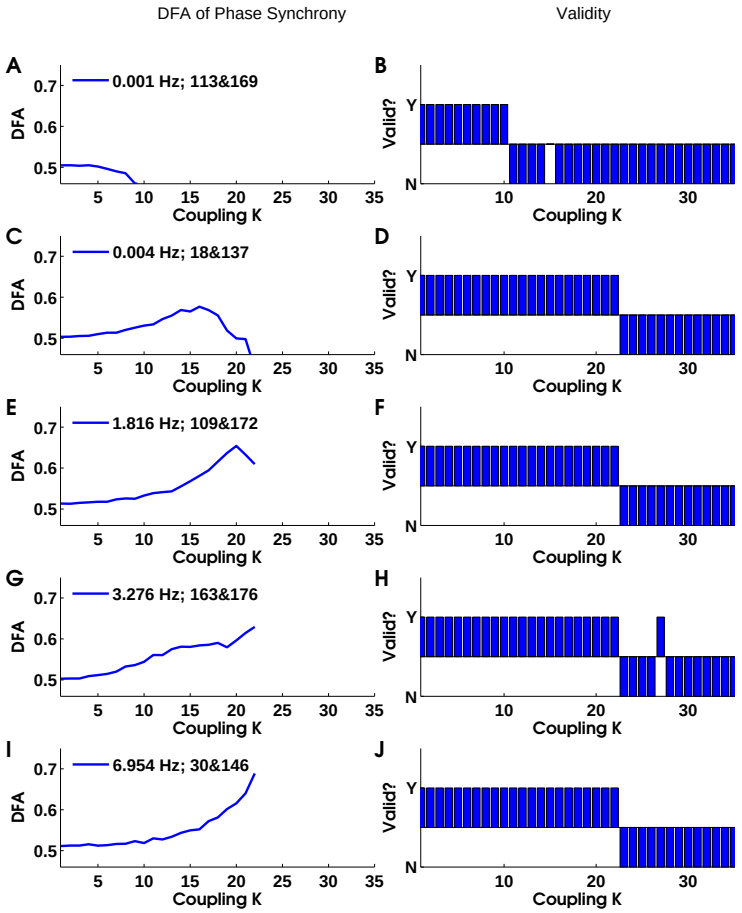


FIGURE 6.18: Representative relationship of DFA exponents for selected oscillator pairs in the Kuramoto system to the coupling parameter $K$. At low coupling, the DFA exponent of the phase difference between all oscillator pairs is at 0.5, indicating a fluctuation relationship that is white Gaussian noise. As the coupling increases, the phase difference shows LRTCs before full synchronisation. When the coupling $K$ is high and the oscillators synchronise fully, the DFA exponent is no longer valid because the phase difference is a constant time series and the results of DFA is no longer interpretable. A DFA exponent was determined to be valid if it was best fitted by the linear model when the ML-DFA technique was applied. Panels A,C,E,G,I and K show the value of valid DFA exponents, while panels B,D,F,H,J and L indicate whether the exponent is rejected as invalid by the ML-DFA technique (N) or not (Y). The oscillator numbers and the differences between their natural frequencies are recorded in the legend of panels A,C,E,G,I and K. The first number is the difference in natural frequency (in Hz), and the subsequent pair of numbers identifies which oscillators are observed. Note that when the initial frequency of the oscillators is very close, such as in panel A, the oscillators synchronise without showing LRTCs as $K$ increases. However, LRTCs are observed in panels C-I.

Figure 6.18 shows that oscillators with natural frequencies that are not close to each other (Figures 6.18 E, G and I) will show LRTCs in the rate of change of their phase difference at a coupling value which is on average $K \approx 22$. Oscillator pairs with natural frequencies that are very similar (such as those shown in Figure 6.18A.) will synchronise at a low value of the coupling value $K$ before the rate of change in their phase difference develop LRTCs.

The more separated the oscillators are in the difference of their natural frequencies, the

more potential there is for the DFA of the rate of change of their phase difference to be meaningful. If we consider again the analogy of Huygens' clocks, then the difference in natural frequencies will correspond to the difference in the initial oscillation frequencies between the two clock pendulums. As two such clocks synchronise with each other, there is a lot of fluctuation in the rate of change of their phase difference, or in the speeds with which they adjust towards each other. Clocks with pendulums that are very close in oscillating speed synchronise very quickly and need only a small amount of coupling to do so. Once they are synchronised, there will be no more fluctuation, and DFA will not give interpretable results. In contrast, clocks with a larger difference in initial frequency will show more fluctuations as they approach each other. It is important to note that whilst the Huygens example and the results presented in Figure 6.18 relate to oscillator pairs in the Kuramoto model, the mean field itself also affects the fluctuations of the rate of change of phase difference.

In the Kuramoto model, rather than just two clocks, there would be as many clocks as there are oscillators, which all try to synchronise with each other. Those clocks that are already close in natural frequency synchronise quickly as can be seen in Figure 6.18.

## 6.12 Discussion

### 6.12.1 Summary

The aim of this chapter was to develop a putative marker of criticality in neuronal synchronisation. Due to its relationship to power laws, which have previously been linked to criticality, DFA presented itself as a technique that could be used as a marker of critical behaviour. However, a measure of neural synchrony that could be used in conjunction with DFA remained an open question.

In the course of this chapter, a number of different techniques for calculating neural synchrony were considered, which included OST, wavelet and Fourier transforms and phase difference. However, none of these could be used alongside DFA. Finally, it was shown that the rate of change of the phase difference provided an instantaneous time series, which could be used both with DFA and ML-DFA.

Thus, the method used to calculate a marker of criticality in neural synchronisation is termed the phase synchrony analysis method and consists of a calculation of the rate of change of phase difference between two time series, followed by application of DFA and ML-DFA. The phase synchrony analysis method returns an exponent, which if equal to 0.5 indicates a phase relationship of noise, and if greater than 0.5, indicates the presence of LRTCs. In application of the method to model and simulated time series, conclusions are drawn based only on those exponents that are judged to be valid by ML-DFA.

It was found that the method recovers a known DFA exponent value in the phase difference of surrogate data well. When the structure in this phase difference value is perturbed with an additive noise time series, it was found that when the percentage difference between the true and recovered DFA exponents was more than approximately 5%, the DFA exponents were judged as invalid by ML-DFA. In this chapter, the noise level was additive, and included at the amplitude stage of the surrogate time series. Because the noise was added simply after multiplication by a scaling factor, the range of noise values added can be described by this factor, which may take any value greater than zero. At a value of 1, the level of the noise added would be approximately equal in magnitude to the level of the signal. As the value of the scaling factor is increased, the magnitude of the noise grows greater than that of the signal. The method will still work in this case, but the rate of change of phase difference of the signals will be dominated by noise, and the DFA exponent returned will be 0.5.

Analysis of the phase difference of pairs of time series extracted from the Ising model of ferromagnetism and the Kuramoto model of coupled oscillators shows that LRTCs exist globally in these models as they approach their respective, theoretically determined critical states. In both the Ising and Kuramoto models, the average DFA exponents take a value indicative of the presence of LRTCs when the parameter governing synchronisation results in a state that is slightly more disordered than at that of the critical point.

Furthermore, in the Kuramoto model with added noise, LRTCs were evident at coupling values corresponding to peaks in the rate of change of the order parameter with coupling. These occur when the system progresses most rapidly from a state of lesser to greater synchrony, and is therefore in its state of greatest transition from a disordered to an ordered state.

Neither the point of critical behaviour, not the point of greatest transition from disorder to order (the peak in $\Delta(Kr)$) are available for the human brain. Due to the ability of the phase synchrony analysis method to identify the presence of LRTCs in the rate of change of phase difference between time series of the Ising and noisy Kuramoto models at the critical parameter and at the parameter of greatest peak in $\Delta(Kr)$, it is suggested that application of the method to neurophysiological time series may provide an estimate of these parameter values for the human nervous system, based on the global identification or otherwise of LRTCs. It is important to note that the coupling value at which the maximum DFA exponent occurs in pairwise data is close to both the effective and the theoretical critical coupling values, so that the phase synchrony analysis method may provide a putative marker of both a finite and an infinite system.

On a local level, it was also found that individual noisy Kuramoto oscillator pairs showed a consistent increase in the DFA exponent of their rate of change of phase difference indicating LRTCs at a coupling value $K$, which was on average equal to that of the effective critical coupling parameter. This result suggests that the phase synchrony analysis method may be used individually as well as globally to identify the presence of

LRTCs in the rate of change of phase difference between neurophysiological time series and therefore to deduce whether the human nervous system may be in a critical state, and at a stage of greatest peak in $\Delta(Kr)$. It is important to note that the maximum average DFA exponent across all pairwise combinations of oscillators tends to take values that are lower than those of the pairwise oscillators, which is a result of the averaging procedure, and also that the peak DFA exponent of individual oscillator pairs can belong to a range of values from below 0.6 to above 0.7. This may also be the case for individual pairs of neurophysiological time series recorded at different EEG, EMG or MEG sensors.

Following a peak in this DFA exponent, oscillator pairs became synchronised, yielding a phase difference measure with no temporal fluctuation structure, such that the DFA exponent of the rate of change of phase difference was invalid. The phase synchrony analysis method may therefore also be used to provide some insight into the question of when more synchrony is too much synchrony [273], or in other words, whether the neurophysiological time series produced by two regions of the nervous system have synchronised too closely. At the critical parameter value, the phase synchrony analysis method indicates that across all pairs of oscillators, 34% of pairs in the Ising model and 41% of pairs in the Kuramoto model show a valid DFA exponent. Both of these values are below 50% indicating that criticality implies that most oscillators have fully synchronised. One potential route for future research may be to compute a similar statistic for the pairs of EEG or MEG sensors or channels in the human brain during different conditions or tasks. If found to be similar in value to those of the Ising and Kuramoto models, this may provide further evidence for the putative critical state of the human nervous system. Such a study is, however, beyond the scope of this thesis.

### 6.12.2 Methodological considerations

#### 6.12.2.1 Surrogate Data

In applying the method to surrogate data, a 'sanity check' could be performed. By creating surrogate data which was the cosine of the cumulative sum of a time series with LRTCs, it was possible to test whether the Hilbert transform worked well in being able to undo these functions, which is its theoretical purpose. The ability of the method to do so was indeed verified, but a potential pitfall was also encountered. It was noted that the Hilbert transform will give artefacts in the phase calculation of a time series when it is applied to the cosine of a time series which changes rapidly at each innovation. The signal to which the Hilbert transform is applied should be smooth enough to have a dominant frequency, or in other words, be narrowband [146]. This is an observation already made in Section 1.1.6.8.

In order to investigate the effects of applying the phase synchrony analysis method to possibly noisy neurophysiological time series, surrogate time series with added noise were

studied. It is also noted that only the 'level' of noise added is quoted, which is a multiple applied to a Gaussian white noise time series. This is not the same as a signal-to-noise ratio, which may be calculated using a number of procedures such as those discussed in [294].

The results for noisy surrogate data suggest that the technique of ML-DFA may have applications in identifying signals with self-similar that may have a self-similar phase, and which have been corrupted by more than 5% by noise. However, it is noted that in neurophysiological recordings, there are multiple levels in which noise can enter the system, and a possible route for future investigation may be to add multiplicative noise, or to add noise directly to the phase of the surrogate signal.

#### 6.12.2.2 The Ising model

The change in DFA exponent with difference in temperature for the Ising model shares some characteristics with a recently published measure of information flow in the same model [20]. In particular, the sharp rise in DFA exponent as temperature is increased towards the critical $T = T_c$ and the gradual descent towards an exponent of 0.57 as the temperature rises significantly was also seen in this measure. This gives further support to the method as a metric of information flow in a system.

It was initially expected that LRTCs would be seen in the Ising model exactly at the critical parameter, and a DFA exponents of 0.5 when the energy in the system was large. However, in applying the method to the Ising model, both of these hypotheses were not fully realised. It was found that when the temperature was increased to a very high level of $T = 10^5$, the DFA exponent of the time derivative of the phase difference does not fall to 0.5, but remained at $\approx 0.57$. This did not change when the temperature was set to an even higher value of $10^{12}$, and it was not a finite size effect of the system, as the same result was obtained from larger lattice sizes of $1000 \times 1000$ (results not shown). The expectation of a drop to 0.5 at high $T$ was not, however, based on a published statement, but rather an intuition about the operation of the system. As all elements in the Ising lattice interact with their neighbours by the nature of the model, some temporal correlation in the rate of change of phase difference may persist regardless of temperature value, and this may be the cause of a DFA exponent of above 0.5.

Although it was found that the rate of change of phase difference showed LRTCs at critical temperature $T = T_c$, the peak average DFA exponent occurred at a higher temperature than $T_c$ when the system was slightly more disordered than at $T_c$. This suggests that the peak in DFA exponent for the phase synchrony analysis method occurs at the *onset* of criticality rather than precisely at criticality.

#### 6.12.2.3 The Kuramoto model

In the Kuramoto model there was no amplitude attached to any oscillator, and therefore there could be no entanglement of phase and amplitude [2]. This is distinct from other models that are available, and indeed, distinct from neurophysiological data. The Kuramoto model is therefore of particular relevance to the investigation of a method designed to assess the presence of LRTCs specifically in a metric of phase such as the rate of change of phase difference.

In the Kuramoto model, the critical transition is typically characterised in terms of a global order parameter which reflects the overall organisation of the system, however, through the phase synchrony analysis method, it was also possible to make observations at a pair-wise level. As individual Kuramoto oscillator pairs become fully synchronised, their rate of change of phase difference no longer contained moment-to-moment fluctuations and thus power law scaling in the DFA measure was lost. This occurred at and above the critical coupling parameter. When coupling was just below this level, power law scaling existed, and the Hurst exponent of oscillator pairs with different initial frequencies indicated the presence of LRTCs.

As coupling decreased further, the DFA exponent of these pairwise rates of change of phase differences decreased towards 0.5 and yet scaling remained. This evolution in the DFA exponent was also evident on the global level in the average DFA value for different coupling values.

In these characteristics, the effect of $T$ in the Ising model and $K$ in the Kuramoto model played a similar role in controlling the *order* in the systems, and the results obtained from these models using the method also mirrored each other. In the Kuramoto model, there was a transition from an uncoupled to a synchronised state with increasing $K$. Similarly in the Ising model, there was a mirror transition from a very ordered to a disordered system with increasing $T$. In the human brain, we are not able to characterise the system by incrementally tuning a parameter and observing the result and we are only privy to snapshots of the working system. However, we can begin to understand the behaviour of the brain within this range of behaviours by comparing the DFA of the rate of change of phase difference of pairs of neurophysiological signals to the outcomes of these models of criticality.

It is important to note that the Kuramoto model for which results are analysed here included an additive noise input, but that the classical Kuramoto model did not allow for valid DFA exponents to be obtained at any coupling value. This finding may suggest that noise is an essential component of a system which produces LRTCs in the rate of change of phase difference. This may also be the case for the human nervous system.

In the next chapter, a further model of coupled oscillators is considered, called the Cabral model. There is no theoretical critical value for this model, which is based

on the Kuramoto model, but includes variable coupling, a distance matrix and noise terms which correspond to empirical values measured from the human nervous system. The order parameter, and the values of $\Delta(Kr)$ may, however, be calculated as for the Kuramoto model. The Cabral model allows a greater exploration of the connectivity structure of the nervous system, and its effects on the presence of LRTCs at the peak of $\Delta(Kr)$.

# Chapter 7

# Phase synchrony analysis of the Cabral Model

## 7.1 Introduction

In the last chapter, the phase synchrony analysis method for assessing the presence of LRTCs in the rate of change of the phase difference of two time series was introduced and validated for the Ising and Kuramoto models. The Kuramoto model of coupled oscillators, which was used in the previous chapter has been used as a model of oscillatory neurophysiological time series, however, it lacks some features that may be considered essential for an investigation of the emergence of neuronal synchronisation. In the Kuramoto model, all oscillators are connected to each other with a single global coupling value, and no spatial properties of the oscillators are considered. However, network properties of the human brain are considered to play an important role in neural synchronisation [259].

In this chapter the phase synchrony analysis method is applied to a model that was developed by Joana Cabral and colleagues, which is based on the Kuramoto model, but also incorporates the network properties observed in the human brain as well as noise [47]. This model will be referred to hereafter as the Cabral model. The phase synchrony analysis method is applied to time series generated by this model, which more closely represents a human brain network than a noisy Kuramoto model with global connectivity.

First, it is verified that the Cabral model time series pairs can show LRTCs in the rate of change of their phase difference. Next, the emergence of clusters in the Cabral model is investigated, and it is shown that the relationships within clusters are important for driving the LRTC phase relationships between oscillators. It is demonstrated that oscillators belonging to a central cluster are responsible for generating LRTCs in their phase relationship with other oscillators. In particular, this role is taken by two oscillators,

which correspond to two specific brain regions in this model, and which have previously been shown to be neuronal hubs, that are important in the resting state network [84].

Finally, it is shown that disruption of the connectivity network by severing connections between hemispheres and by assigning random connectivity to the oscillators, either disrupts the scaling relationship of the phase difference time series, and yields invalid DFA exponents, or produces 0.5 DFA exponents of similar value to those produced by uncorrelated noise time series. It is therefore suggested that the connectivity network of the human brain is essential to the organisational principles of neural synchronisation and the emergence of dynamic hubs showing LRTCs.

## 7.2 Methods

In a recent paper, the Kuramoto model is used as the basis for a model of gamma-band neuronal activity [47]. The authors show that when used in conjunction with the Balloon/Windkessel model [92] and filtering, the simulated neural activity can be used to reproduce human resting state data well (see Figure 7.1). Neuronal activity in the gamma-band is indeed thought to contribute fundamentally to the BOLD signal [161].

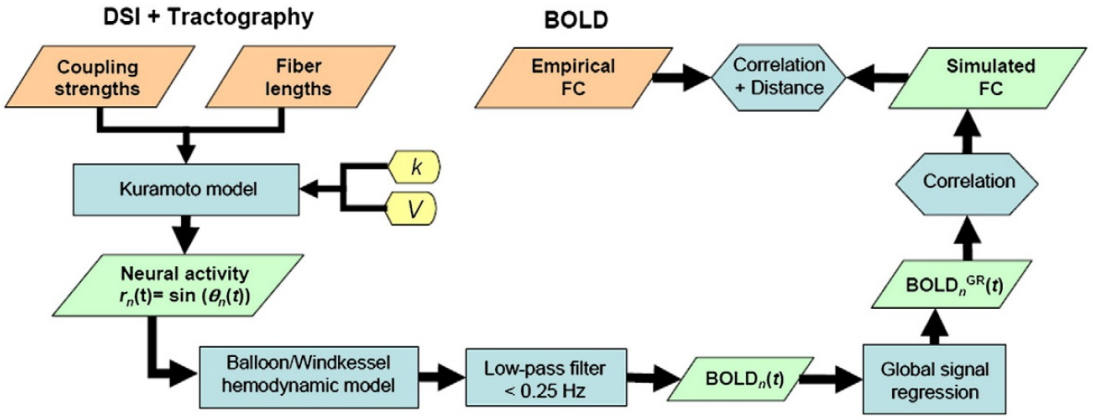


FIGURE 7.1: A schematic diagram describing the steps of the recreation of blood oxygen level dependent (BOLD) data using the model from Cabral et al [47]. The Kuramoto model is used to create time series to represent neural activity, which is then used as input to the Balloon/Windkessel model and ultimately used to create BOLD time series. The resting state BOLD activity of the human brain shows slow spatio-temporal correlations that fluctuate across time and space. The orange labels indicate experimental inputs, the green indicate simulated data, the blue are processes and the yellow are free parameters.

### 7.2.1 Phase evolution

The Cabral model uses 66 oscillators, which represent 66 brain regions. The regions were down-sampled from empirical measurements taken from 998 brain regions [126]. The full list of the 66 brain regions is given in the appendix for this chapter.

In the Cabral model, Equation 1.1 for the Kuramoto model is modified as follows:

$$\dot{\phi}_i(t) = \omega_i(t) + \frac{K}{N}\Sigma_{j=1}^{N} C_{ij}\sin(\phi_j(t - D_{ij}) - \phi_i(t)) + \eta_i(t) \tag{7.1}$$

where $\eta_i$ is a noise input taken to be uncorrelated Gaussian noise with zero mean ($\langle \eta_i \rangle = 0$) and variance $\sigma_i^2/T$ ($\langle \eta_i(t) \rangle \langle \eta_j(s) \rangle = \delta_{ij}\delta(t-s)\sigma_i^2/T$) where $\delta_{ij}$ is the Kronecker delta, $\delta(t-s)$ is the Dirac delta function, $\sigma_i$ is in radians and $T = 1$ second here. Element $C_{ij}$ of connectivity matrix $C$ is a weight assigned to the connectivity between oscillators $i$ and $j$ [126]. Element $D_{ij}$ of time delay matrix $D$ is the time taken a change in oscillator $i$ to reach oscillator $j$ [126]. The time delay matrix was calculated using

$$D_{ij} = \frac{\langle D \rangle L_{ij}}{\langle L \rangle}$$

Where $L_{ij}$ are the empirical distances between brain regions represented by oscillators $i$ and $j$. The values of the $66 \times 66$ matrices $C$ and $L$ are shown in Figure 7.2.

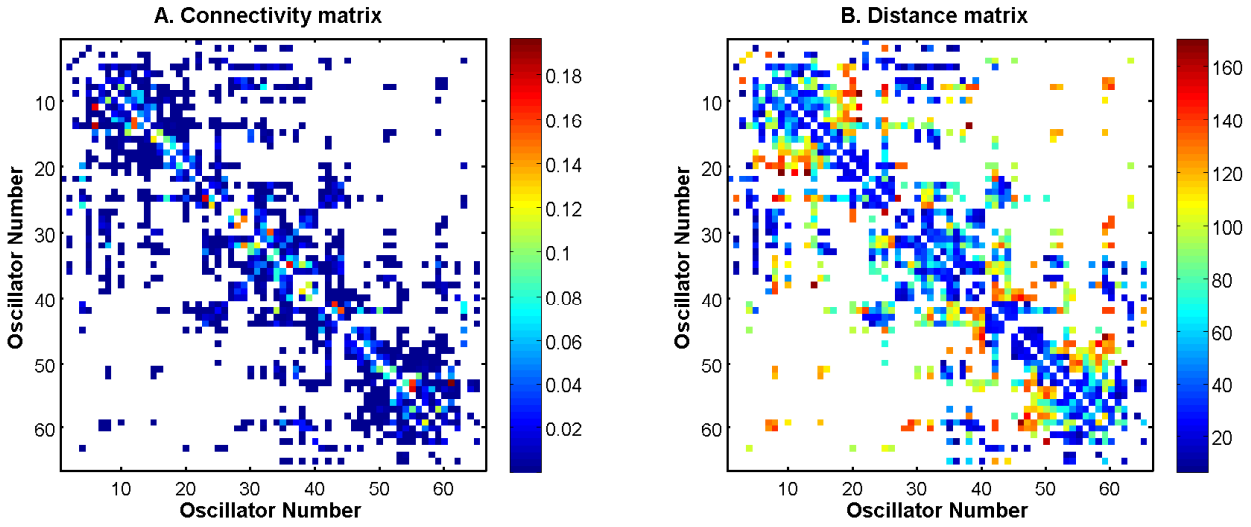


FIGURE 7.2: The connectivity and distance matrices for the Cabral model. Each oscillator number represents a brain region, which is defined in Table 11.4 in the Appendix. An empty (white) element means that the two regions are not connected. Regions are not connected to themselves so that the diagonals are white. The values associated with the colours of the plots are defined by the colour bars. They represent A. the pairwise connection weights $C$ between the 66 oscillators and B. the pairwise distances $L$ between the brain regions that are represented by the 66 oscillators. Matrix $L$ is symmetric, however, matrix $C$ is not because the connection weights are normlaised by row. Red colours in panel A represent higher weights and blue colours represent low weights. Red colours in panel B represent longer distance connections, and blue colours represent shorter distance connections. The units of length in this matrix are mm.

The embedded oscillators of the Cabral model can further be visualised by a schematic plot of brain region locations and their connection weights as shown in Figure 7.3.

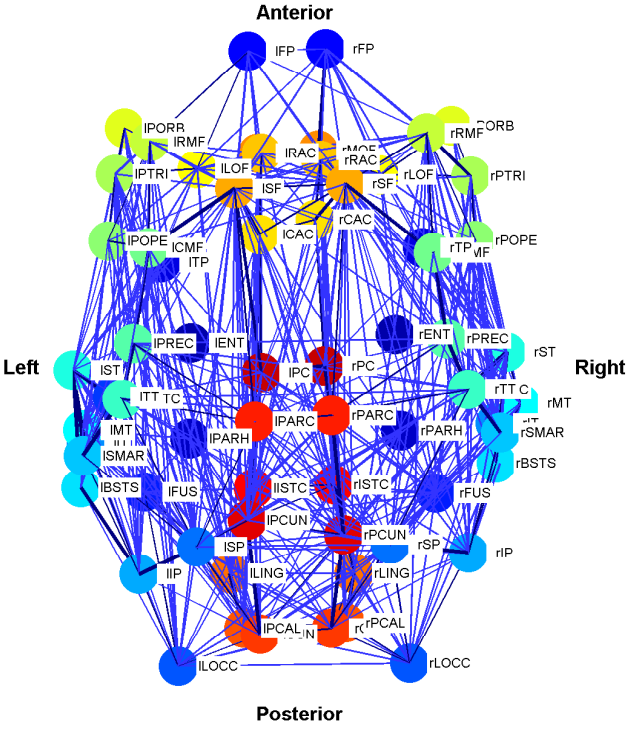


FIGURE 7.3: A schematic plot of a top view of the brain showing the connection weights between oscillators belonging to the Cabral model. The weight of the connection lines represent the strength of connectivity between the oscillators. The darkest blue lines are the strongest 1% of connections. The node colours represent oscillators, which model different brain regions as detailed in Table 11.4 in the Appendix. Colours are consistent for regions in the left and right hemispheres, for which the labels are preceded by an 'l' or 'r' respectively. These are also given in Table 11.4.

The method presented in this paper is applied to the Cabral model for coupling parameters $K$ ranging from 1 to 20. Each time series was generated for 1000 time steps. This is slightly below the 1200 steps used in [47] for computational speed, however, the results of the model are not affected by this, which is demonstrated by the ability to accurately reproduce the correlation matrix of simulated neural activity shown in Figure 6B of [47] and in Figure 7.4 in this thesis.

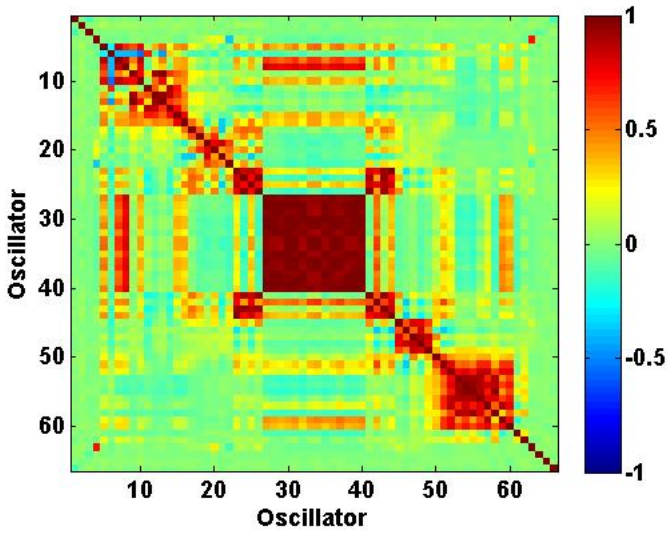


FIGURE 7.4: Correlation matrix for all pairs of time series generated by the Cabral model at $K = 18$. This plot is a replication of the oscillator correlation matrix in [47] and is reproduced here to demonstrate the correct implementation of the model in this thesis. This indicates the value of the Pearson correlation coefficient between all pairwise combinations of the 66 oscillators used in the model. Correlation values range form 0 to 1.

Natural frequencies were drawn from a normal distribution with $g(\omega) \sim \mathcal{N}(120\pi, \sigma_\omega)$ with $\sigma_\omega = 5$ as the standard deviation, which corresponds to a normal distribution centred around 60 Hz. These frequencies were used in order to accurately reproduce the Cabral model, which aimed to generate time series to represent in the $\gamma$ frequency band.

The noise standard deviation $\sigma_i$ is set to 1.25 here. It was found that values of $\sigma_i$ less than 3 did not significantly alter the resulting parameter values of $K$ and $\langle D \rangle$. The value $\langle D \rangle = 11$ is taken as in [47].

In this model, there is no theoretical critical coupling and the rate of change of the order parameter $\Delta(Kr)$ is the only empirical indicator of order in the system. An increase in coupling parameter $K$ will give rise to greater order in the system.

### 7.2.2 Clusters in the Cabral model

The division of the oscillators of the Kuramoto model into separate synchronous or almost synchronous clusters is a known phenomenon described in [228]. The role of clusters in the Cabral model is investigated here. Following the definitions given in [47], there are 6 clusters in the network, and a final set of 12 oscillators, which are not part of any cluster. Specifically, the clusters are defined by oscillator numbers listed in Table 7.1. These definitions are used to identify the clusters that are most dominant in driving LRTC structure in the rate of change of phase difference.

TABLE 7.1: The 66 oscillators of the Cabral model can be separated into 6 clusters, based on their connectivity and distance matrix patterns, and a final set of 12 oscillators, which are not considered to belong to a cluster, but are grouped together here for convenience. The table also states the average sum of weights per node belonging to each cluster and the average number of connections per node (both to 2 d.p.).

| Clusters | Oscillators | Average weight per node | Average degree distribution |
|---|---|---|---|
| Cluster 1 | 7-17 | 0.29 | 19.09 |
| Cluster 2 | 18-22 | 0.16 | 15.80 |
| Cluster 3 | 23-26,41-44 | 0.30 | 21 |
| Cluster 4 | 27-40 | 0.34 | 21.71 |
| Cluster 5 | 45-49 | 0.15 | 15.60 |
| Cluster 6 | 50-60 | 0.27 | 18.73 |
| Individual Oscillators | 1-6,61-66 | 0.03 | 8.583 |

It is observed that cluster 4 contains oscillators that are located primarily in the central region of the brain (see Figure 7.3), and that this is the cluster which shows the largest weights and numbers of connections on average. The hypothesis of this chapter is that this cluster behaves as a hub within the Cabral model network. This cluster may therefore play a dominant role in driving LRTC behaviour in the rate of change of phase difference with other oscillators in the network.

### 7.2.3 Disruptions to the connectivity structure

In order to disrupt the network structure in the Cabral model, the connectivity matrix will be modified in two ways.

First, any connection that extended from one hemisphere into the other is deleted. All the other elements of the model are preserved, including the weights between oscillators belonging to the same hemisphere, and the distance matrix and noise input. It was hypothesised that there would be no LRTCs in the rate of change of the phase difference between nodes located in opposite, disconnected hemispheres. As a consequence of disconnecting the hemispheres, cluster 4 of the Cabral model is also disconnected. It is therefore possible that there will be fewer oscillators pairs showing LRTCs in the rate of change of phase difference even *within* the same hemisphere. It has been suggested that the disruption of specific clusters is correlated to the severity of disease in patients where neurological illness is connected with disruption of neural connectivity [114]. This modification provides a straightforward example of a known clinical scenario (callosotomy) [98].

In the second disruption of the connectivity matrix, the connectivity matrix is reconnected in a random arrangement, while preserving the degree distribution and weight distribution of each oscillator by an algorithm adapted from that described in [100, 115]. Specifically, a list of the non-zero weights from oscillator $i$ to all of its neighbours was

made for each oscillator in the system. Two weights were selected from this list. If they did not begin at the same oscillator, then the weights were used to connect the two oscillators at which the weights did begin to each other with the chosen connection weights. These two weights were then deleted from the list. To continue the algorithm, two further weights were selected. It was then necessary to check at each iteration that the oscillators were not already connected. It is hypothesised that disruption of the connectivity matrix by randomisation will result in disruption of LRTCs in the rate of change of phase difference.

The two modifications of the Cabral connectivity matrix are shown schematically in Figure 7.5. It is noted that the random connectivity matrix appears to be denser than the empirical human brain matrix in Figure 7.3, however, this is a visual illusion. The reason for this illusion is that empirical connectivity used in the Cabral model tends to have many local connections and fewer long-range connections. This can be seen, by noticing the darkest links in Figure 7.3, which are visually very obvious. In the random brain, connections often extend over greater distances as there is no restriction on the weights of long-range connections.

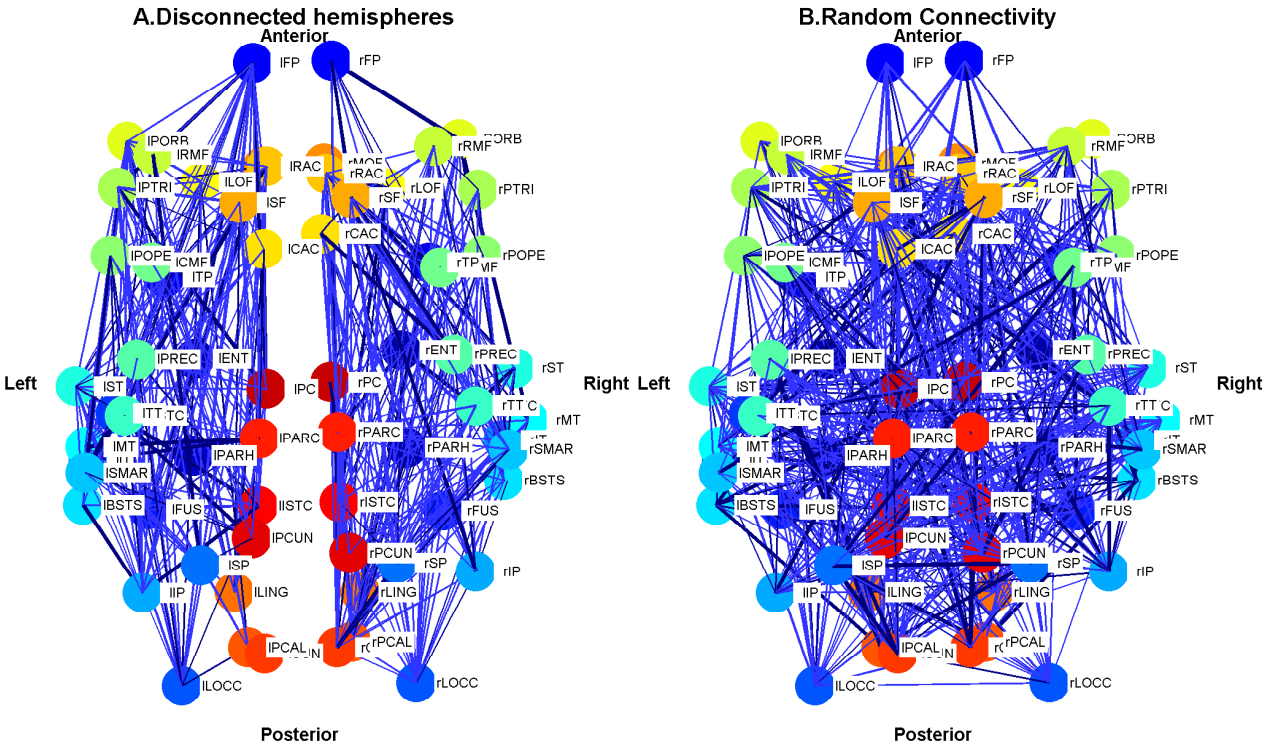


FIGURE 7.5: A schematic plot of a top view of the brain showing the connection weights between oscillators belonging to two modifications to the connectivity of the Cabral model. In panel A, the left and right hemispheres of the brain have been disconnected, but connections within each hemisphere are kept constant. In panel B, the connections and weights of each node are assigned randomly, but the degree distribution and weight distribution at each node is kept constant. The weight of the connection lines represent the strength of connectivity between the oscillators. The darkest blue lines are the strongest 1% of connections. The node colours represent oscillators, which model different brain regions as detailed in [47]. Colours are consistent for regions in the left and right hemispheres, for which the labels are preceded by an 'l' or 'r' respectively.

The dynamics of the disconnected hemisphere model and the randomised connection model were investigated in order to determine the extent to which connections and clusters play a role in emergence of LRTCs in the rate of change of phase difference between oscillators. The results are interpreted with the consideration that these oscillators correspond to specific brain regions in the model.

## 7.3 Results

The model introduced by Cabral et al. [47] provides a rich interplay between connectivity, time delays, noise and natural frequency elements. Figure 7.6 shows the average DFA exponent of the rate of change in the phase difference between all 2145 pairwise combinations of the 66 oscillators in the Cabral model as coupling is increased in the system. This average value indicates the global presence of LRTCs at coupling values close to the peak in the change in order parameter $\Delta(Kr)$. The number of pairings that yield valid DFA exponents in their phase difference is equal to 100 % when there is no

coupling $K$ in the system, but falls as coupling is introduced. At $K = 1$, the coupling falls to 72 %. At the coupling value of the greatest peak in $\Delta(Kr)$, $K = 6$, validity is at 20%, which is higher than the neighbouring coupling values.

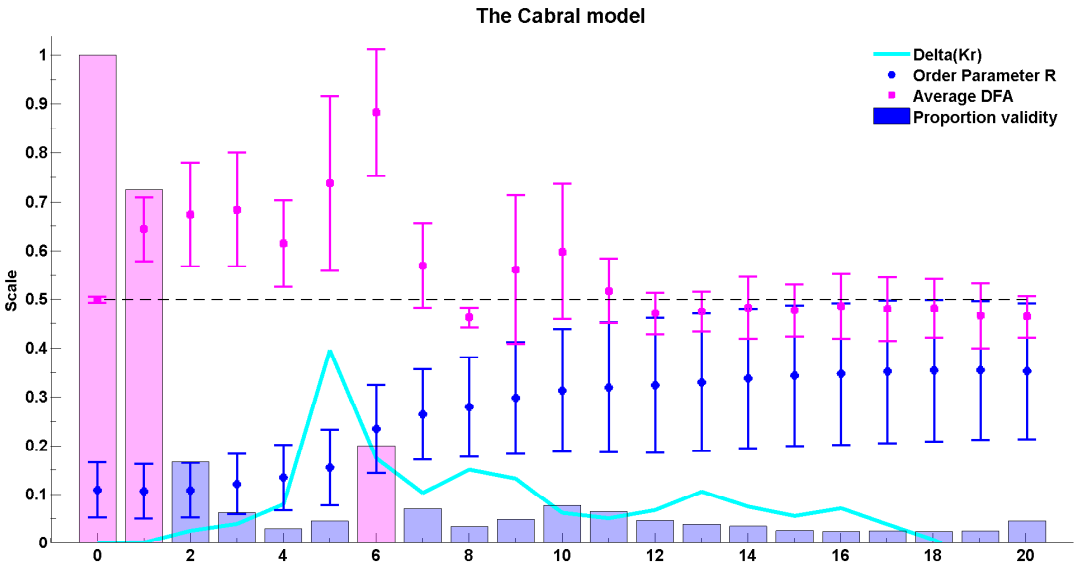


FIGURE 7.6: The average DFA exponents of phase synchrony, as a function of the coupling parameter, $K$ in the Cabral model [47]. The model includes 66 oscillators at normally distributed natural frequencies with mean 60 Hz and standard deviation $\sigma_w = 1.25$. The connectivity matrix and time delays used between oscillators correspond to empirical values. The average of the valid DFA exponents are shown in magenta and the proportion of valid exponents, as calculated by the ML-DFA technique, are indicated by bars. The Kuramoto model order parameter $r$ is in blue, and the quantity $\Delta(Kr)$ is in cyan. A horizontal line at DFA exponent 0.5 is plotted to guide the eye.

As the peak in $\Delta(Kr)$ occurs at $K = 6$, the correlation coefficient matrix of all oscillators in the system is considered at this coupling value. In Figure 7.7, the correlation coefficient between time series generated by each of the oscillators is shown at coupling $K = 6$. It may be observed that oscillators belonging to the central cluster (numbers 27-40) show highly correlated behaviour with other oscillators in this cluster. Correlations between other oscillators in the system are lower by comparison.

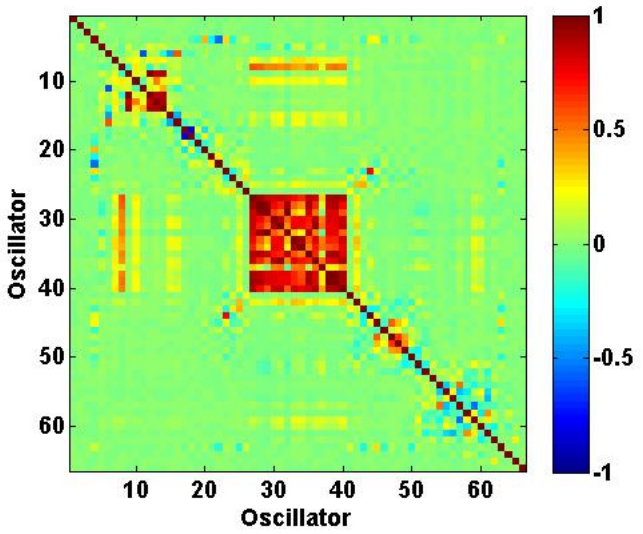


FIGURE 7.7: Correlation matrix for all pairs of time series generated by the Cabral model at $K = 6$. This indicates the value of the Pearson correlation coefficient between all pairwise combinations of the 66 oscillators used in the model. Correlation values range form 0 to 1.

For this reason, the DFA exponents of the rate of change of phase difference between all intra-cluster oscillators are considered individually for differing coupling values $K$. We expect that at $K = 6$, the oscillators in the central cluster will either be fully synchronised, and show invalid DFA exponents in the rate of change of their phase difference, or will show the presence of LRTCs if they have not fully synchronised. Other oscillators in the system show a low correlation value with all other oscillators in the system, suggesting that their rate of change of phase difference will yield DFA exponents that may be invalid, or may yield values of close to 0.5, suggesting a noise-like phase relationship.

### 7.3.1 Results for individual clusters

In Figure 7.8 the average DFA exponent calculated only for pairs of oscillators in the Cabral model that belong to the same cluster are shown, so that inter-cluster pairings of oscillators are not considered (see Table 7.1).

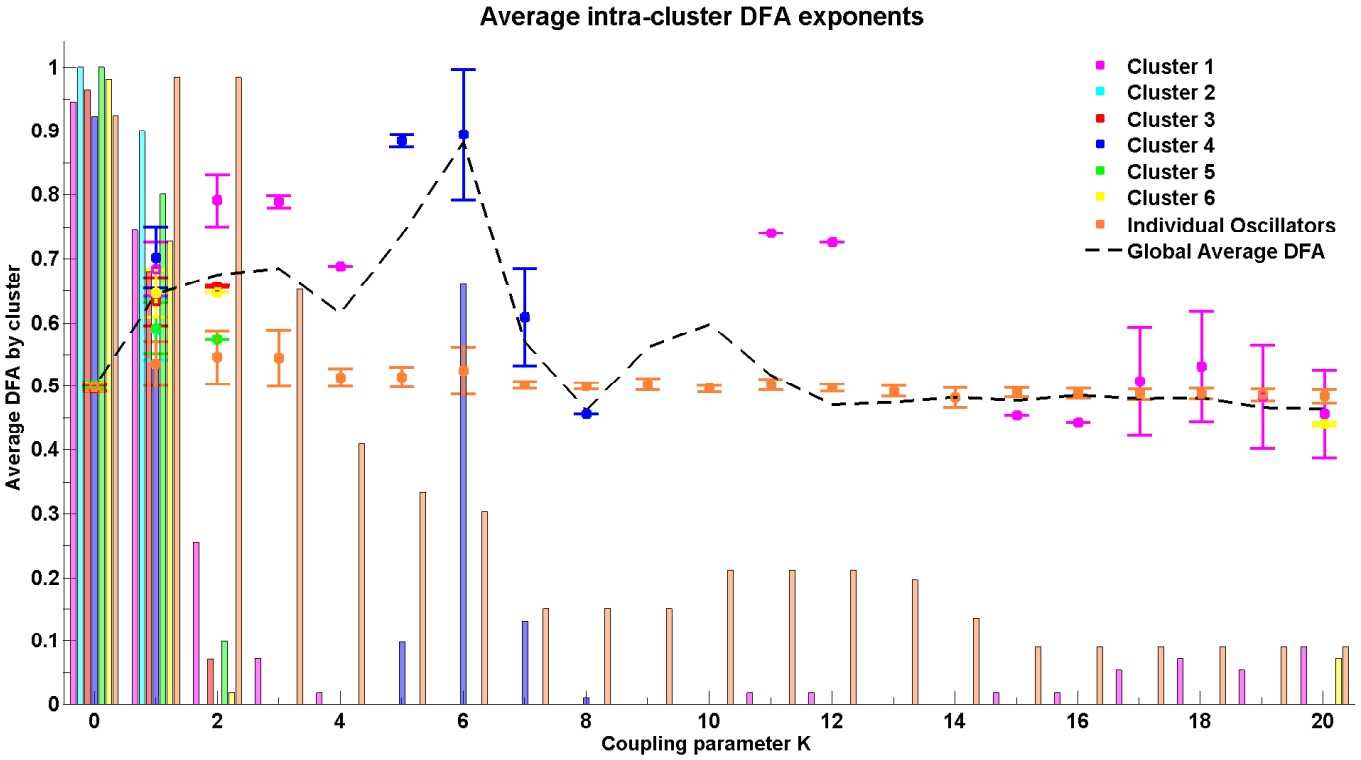


FIGURE 7.8: The average DFA exponent for intra-cluster pairwise phase differences with increasing coupling parameter $K$. Where no value appears for a particular cluster, this indicates that there are no valid DFA exponents for the pairwise phase difference within that cluster. The final cluster, which is labelled individual oscillators consists of a set of nodes which do not fit into any one of the clusters as determined by the connectivity and distance matrices [47], but are grouped together to demonstrate their relationship with each other.

At coupling value $K = 6$, the intra-cluster results indicate that only cluster 4 shows valid DFA exponents. These exponents are indicative of the presence of LRTCs. This suggests that cluster 4 acts as a driving force in the system when $K = 6$ and thus when the system is in its greatest state of flux, demonstrated by an increased rate of change of $\Delta(Kr)$. In particular, these oscillators correspond to brain regions listed in Table 11.4 in the Appendix.

This cluster has the greatest sum of weights per oscillator and the greatest number of connections per oscillator (see Table 7.1), which suggests that it may be play the role of a hub in the cortical network.

### 7.3.2 Results for disrupted connectivity matrices

The DFA exponents are shown for the rate of change of phase difference between all pairwise combinations of oscillators in the Cabral model with different connectivity structure at $K = 6$, which corresponds to the the peak in $\Delta(Kr)$.

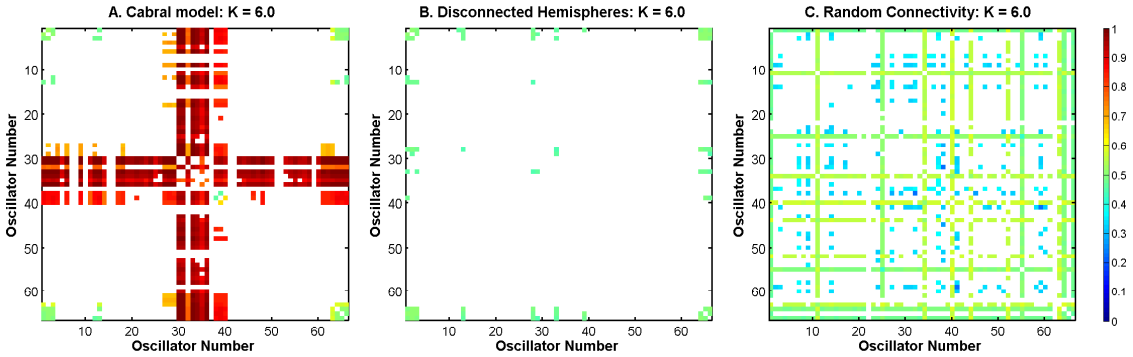


FIGURE 7.9: The DFA exponents of the rate of change of phase difference between all pairs of oscillators in the Cabral model at coupling $K = 6$ A. for the empirically observed connectivity matrix of the Cabral model, B. for a connectivity matrix representing disconnected hemispheres, and C. for random connectivity.

When the connectivity matrix used is the empirically observed matrix, $C$, the pairwise rate of change of phase difference shows DFA exponents that indicate the presence of LRTCs. Specifically, LRTCs occur in pairings that involve a central cluster of oscillators that corresponds to cluster 4 (see Table 7.1). These oscillators have a high number of connections and large weights associated with these connections (see Table 7.1). The result suggests that this cluster is a driving force behind LRTC behaviour in the system.

When the two hemispheres are disconnected, there are no LRTCs in the DFA exponents of the phase difference at this coupling value. The greatest valid value of a DFA exponent is equal to 0.51 in this case. This may be compared to a maximum valid value of 1.04 when the connectivity matrix is that containing empirically derived values.

The empirical connectivity matrix showed large DFA exponents indicating the presence of LRTCs at this coupling value for a small number of hub oscillators belonging to cluster 4 (see above).

When random connectivity is used, there are no clusters of high DFA exponent values.

## 7.4 Discussion

### 7.4.1 Interpretations of the method

In this chapter, the phase synchrony analysis method was applied to time series simulated by the Cabral model. It was demonstrated that for this model, which more closely resembles a neurophysiological system of brain regions than the Ising and Kuramoto models of the previous Chapter, LRTCs exist in the rate of change of phase difference between oscillator pairs at parameter values close to those at which the peak change in the order parameter.

Together, results obtained from the Kuramoto model and the Cabral model suggests that applying the phase synchrony analysis method to time series from an interacting system will show the presence of LRTCs when the order in that system is at or close to a point of maximal change in order.

It is noted that $Kr$ in the Cabral model does not reach a level of 1 in the range of coupling values studied in this chapter, but rather approaches a level of $\approx 0.4$ as $K$ approaches 20. In the Cabral model, $Kr$ will reach a value closer to 1 as $K$ increases above a value of 60 [47].

### 7.4.2 The role of clusters

Examination of oscillator pairs belonging to a single cluster, as defined by the original paper by Cabral, indicate that the emergence of LRTCs is driven primarily by oscillators belonging to a cluster which has a large number connections and a large sum of connection weights. The oscillators belonging to this cluster have a high degree of correlation with each other at the coupling value of peak change in order parameter $K = 6$.

Intuitively, the oscillators that are connected to many other oscillators will influence the phases of a large number of other clusters within the system. When oscillators try to synchronise, those that are well connected may have a lot of conflicting phase inputs from their neighbours and thus increased variation in their phase fluctuations, yielding a larger DFA exponent. It is suggested that these variations in fluctuations will in turn feed into the neighbouring oscillators and cause them to also have large fluctuation variations as they attempt to synchronise with their well-connected neighbour. On the other hand, an oscillator that is poorly connected, or connected to just one other oscillator may have a more straightforward task of synchronising with just this (albeit changing) oscillator speed.

Specifically, cluster 4 is located centrally, and contains four brain regions of particular importance to the resting state network [84]. These are oscillators 33 and 34, which correspond to the left and right posterior cingulate cortices, and oscillators 32 and 35 which represent the precuneus. These brain regions are associated with engagement in self-referential thoughts, and have a higher metabolic activity than other regions during rest. They were also shown to be be diminished at the onset of Alzheimer's disease [84]. A route for future investigation may be to consider modifications to specific alternative clusters or oscillators before application of the phase synchrony analysis method.

### 7.4.3 Connectivity

When the phase synchrony analysis method was applied to the Cabral model with an empirically driven connectivity matrix, it was found that LRTCs existed on average at

the peak in $\Delta(Kr)$. This may be suggestive of the fact that the resting state brain connectivity used in the Cabral model can give rise to behaviour associated with a critical system. This behaviour can be disrupted by random connectivity and by the disruption of clusters or hubs in the data [110, 259].

Within the region of coupling values showing LRTCs, the coupling value which showed the highest average DFA exponent was considered, specifically this was $K = 6$. The method was applied to time series generated by the Cabral model where the empirically determined connectivity matrix was disrupted. The findings were: 1) when the right and left hemispheres are disconnected, scaling of fluctuations in the rate of change of phase difference between oscillators is disrupted and 2) when a random connectivity is assigned, no clusters exist and the DFA exponents are reduced, although LRTCs are still seen to exist between some oscillator pairs.

Rather than finding a specific single coupling value $K$ at which LRTCs exist, it was found that LRTCs exist for a broad range of coupling values $K$. This finding agrees with a recent study by Moretti et al. in which the authors demonstrated that a complex connectivity network, containing clusters, such as that of the Cabral model and indeed that of the brain, causes the critical point to becomes a broader critical 'region' [200]. A systematic study of the effects of connectivity on critical behaviour is one potential route for future research, which may allow a deeper understanding of the implications of modifying the coupling value in the Cabral model. This may, furthermore, provide insight into the modifications made within the human nervous system in order to implement a change in the parameter that we model as the coupling value. This may also yield further insight into the distinction between the coupling value $K = 6$ at which the peak in $\Delta(Kr)$ is seen to occur and the value $K = 18$ at which the authors of Cabral et al. [47] find the strongest correlation between the output of the Cabral model and human BOLD data. Indeed, at this latter coupling value of $K = 18$, the Cabral model shows strong synchronisation, and no valid LRTCs in the rate of change of phase difference between the generated time series.

The results obtained from the phase synchrony analysis method here therefore pave the way for potential future use of the Cabral model in investigating specific pathological modifications of connectivity and their effects on the time-varying synchronisation patterns between different brain regions. The model also has the potential to be used to trace some types of pathological synchronisation, which may arise in epileptic or Parkinsonian conditions, to any roots that they may have either in the connectivity, clustering or noise input elements of the Cabral model and therefore potentially also of the nervous system.

# Chapter 8

# Phase synchrony analysis of MEG Data

## 8.1 Introduction

In Chapter 6, the phase synchrony analysis method was introduced, which provides a putative marker of criticality in systems approaching synchronisation. In this chapter, the phase synchrony analysis method was used to study neural synchronisation in particular in human MEG data. The approach is agnostic with respect to the level of synchronisation (as determined by measures such as coherence) between brain regions and asks only whether or not the variability of phase difference between two signals is scale-invariant and if so, what exponent value can be associated with it. If scaling can be detected through a strict validation of linearity in the DFA fluctuation plot then this will provide an important connection between the critical brain and the neural synchrony paradigms. If, through estimation of the Hurst exponent, there is evidence for LRTCs i.e. increased temporal order in the phase relationship between two signals, then the communication between regions may possess some of the advantageous properties of a critical system. In contrast, if the Hurst exponent of phase difference yields values similar to 0.5, then the instantaneous phase interaction between underlying neural regions would be considered to be random and uncorrelated in time.

Previous evidence for the breakdown of LRTCs in a force amplitude time series during finger-tapping was seen when visual feedback was introduced to a sustained muscle contraction task [10]. A decrease in DFA exponent was also found in the amplitude envelope of the EEG and MEG during electrical stimulation of the median nerve [179]. These results indicate that the LRTCs of amplitude may be susceptible to disruption due to efferent and afferent activation.

In this chapter, the question of whether finger movements will disrupt LRTCs in the rate of change of phase difference fluctuations that are established in the resting state,

is approached. Using resting state human MEG data, we estimate the Hurst exponent of the moment to moment variation in phase difference between signals recorded from left and right primary motor cortices. The effects of unilateral and bilateral muscle activation (finger tapping) on the phase difference scaling and the Hurst exponent are next explored. We show that in the resting state the phase difference between the left and right motor cortex MEG time series has both linear scaling and an estimated Hurst exponent $> 0.5$ in the $\mu$ and $\beta$ frequency bands, indicative of long-range temporal correlations within moment to moment changes of phase difference. The effects on this of finger movement are then examined. The results are validated by comparison with exponents obtained through the application of the phase synchrony analysis method to the following control conditions: analysis of synthetic noise, analysis of empty MEG scanner noise and permutation shuffling of MEG. All of these control conditions produce a Hurst exponent lower than those obtained from resting state data in the $\mu$ and $\beta$ frequency bands.

Finally, we interpret the analysis of time-varying MEG phase difference as reflecting a resting state brain that is sub-critical but with LRTCs in the phase difference that occur in the region just prior to the type of full synchronisation observed in the Ising and Kuramoto models, a state which is then disrupted through muscle activation.

The text of this chapter corresponds closely to a manuscript of which I am first author, written for submission to NeuroImage.

## 8.2 Material and methods

The phase synchrony analysis method was described in Chapter 6. Some additional procedures have been used that are specific to the analysis of this set of MEG data and these are described in Section 8.2.1.

In Section 8.2.2 we give details of the subjects and data recordings used to collect the data. In Section 8.2.3 we describe the control time series used to validate the results. Finally, in Section 8.2.4 we present previously existing measures of synchronisation, which we then use to demonstrate that the method brings new insight to the characterisation of the synchronisation relationship between time series.

In order to summarise the method with the specifics of application to this MEG data and to make it clear to the reader how the data is preprocessed, we include a step-by-step scheme in Figure 8.1.

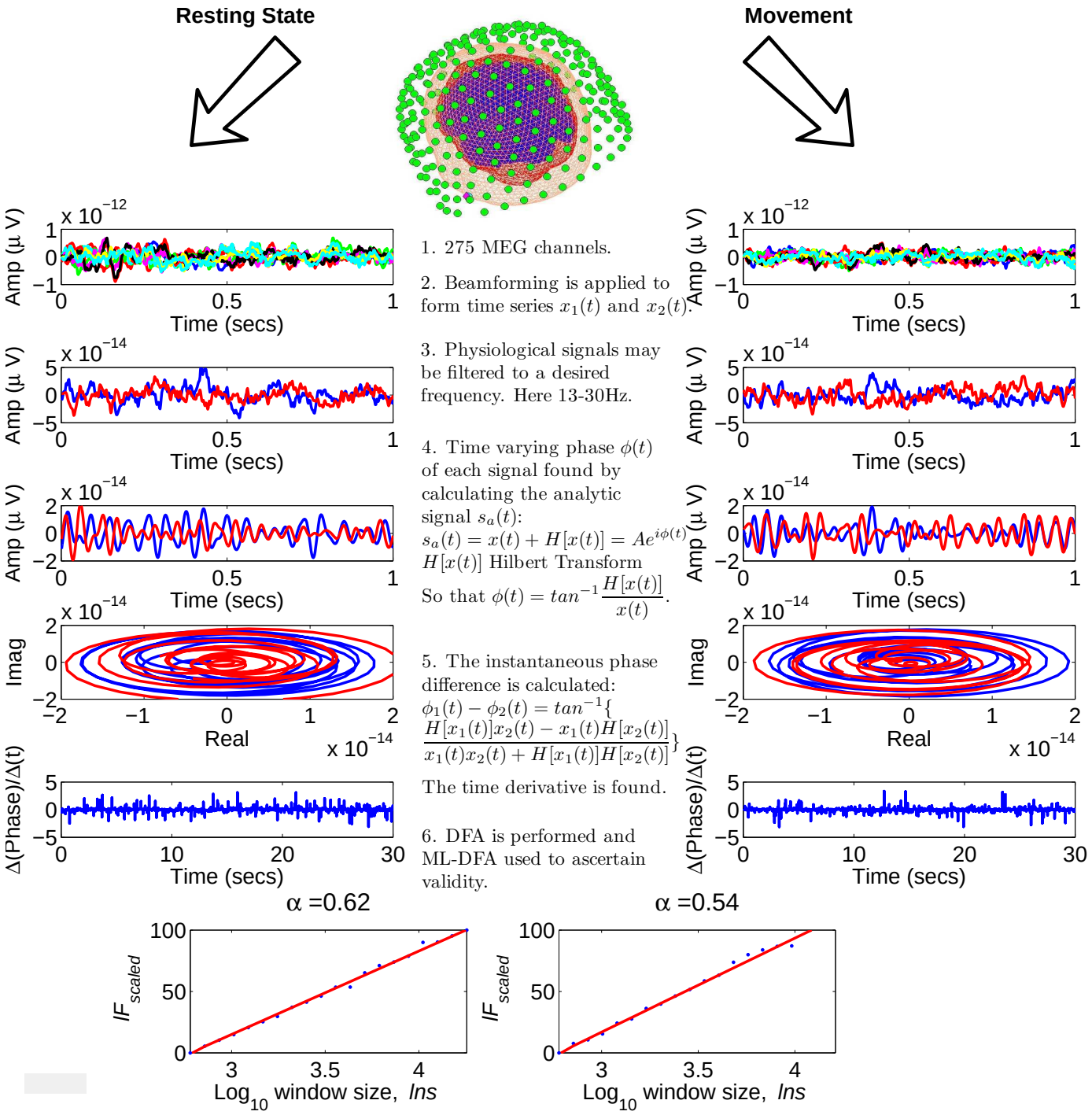


FIGURE 8.1: A schematic diagram describing the steps required for the phase synchony analysis method. The top middle panel is a schematic diagram of the location of MEG channels across the surface of the scalp. Each numbered step corresponds to a pair of plots in the diagram for resting state and movement data. The MEG time series in the panels on the left are taken from resting state MEG data, and those in the panels on the right are from human MEG data recorded while the subject was tapping both index fingers simultaneously. The red and blue colours in steps 2-4 correspond respectively to MEG time series for the left and the right motor cortices. The time segment of each time series remains consistent from one step to the next. Step 1) Data from the full set of 275 MEG channels is considered. Step 2) The data is beamformed to obtain two time series corresponding to the left and right motor cortices respectively. Step 3) Each time series is bandpass filtered to a frequency of choice as described later in the text. Step 4) The analytic signal $x_a(t)$ for each time series is found and plotted on a phase space diagram on axes representing the real and imaginary parts of $x_a(t)$. Step 5) The phase difference between the two time series is found by taking an arctan function as described. The rate of change of this phase difference is then taken to produce the time series plotted. Step 6) DFA is applied to obtain an exponent and ML-DFA is used to ascertain whether this exponent may be considered valid. In the case of this figure, both DFA plots are judged to be linear by ML-DFA. The brain image was generated using SPM8 [180].

### 8.2.1 Preprocessing

#### 8.2.1.1 Beamforming

MEG data were initially processed using a scalar linearly constrained minimum variance beamformer in order to estimate timecourses of source strength at locations of interest in the left and right motor cortices [282]. The forward models, covariance matrices and calculation of beamformer weights is described in [40]. Weights for left and right motor cortex were based on those contralateral voxels showing the largest change in beta band power for right and left hand movement respectively. This was done individually for each of the 7 subjects.

#### 8.2.1.2 Bandpass Filtering

The use of the Hilbert transform (see Section 1.1.6.3) requires a narrowband signal for the phase and amplitude components of the signal to be straightforward to separate [29, 132, 208, 243, 276]. The data is filtered with a finite impulse response (FIR) filtering. The filter order of the FIR filter was set to include three cycles of the lower-frequency component of the band. A similar approach has been used in many recent studies [117, 178, 179].

The frequency bands are selected as 2 Hz intervals spanning the full range of frequencies from 4 to 39 Hz following a technique used in Klimesch et al. [160]. In this paper, the authors identify the peak of a power spectrum and proceed to take frequency bands in intervals of 2 Hz in either direction from this peak. The peak is then used to define frequency ranges $...f-2$ to $f$, $f$ to $f+2$, $f+2$ to $f+4...$ for the full set of frequency bands. Here, the power spectra have two peaks in two frequency bands. One is at 10.5 Hz in the $\alpha$ band and another is at 21.5 Hz in the $\beta$ band (see Section 8.3.1.1). For this reason the time series are filtered in ranges $4.5-6.5$ Hz, $6.5-8.5$ Hz...$14.5-16.5$ Hz in the $\alpha$ and $\mu$ bands, in in ranges $15.5-17.5$ Hz...$25.5-27.5$ in the $\beta$, and $27.5-29.5$ Hz...$37.5-39.5$ Hz in the $\gamma$ band.

In the Appendix to this chapter, the results of bandpass filtering the data into frequency bands other than those used for this study are considered. It is shown that the results are consistent within a range of bandpass frequencies and widths close to those used in the results of this chapter.

#### 8.2.1.3 Data Stitching

One important consideration when applying the phase synchrony analysis method to MEG data is that meaningful results are obtained from DFA. The length of the time series is important because longer time series provide more estimates of the magnitude

of fluctuations for each given window size investigated [178, 212, 214]. In order to ensure the time series is sufficiently long, for each subject we stitch together all the trials that were recorded while the subject was performing the same task. This is done for data recorded from the left and right motor cortices after the filtering step.

Stitching is a commonly used step and does not affect the numerical results obtained by DFA if the window sizes are set appropriately [52, 97, 117, 156]. It would not be permissible to use a window size longer than any continuous segment of data. Thus, the maximum size used in DFA is set to the length of a single trial for all subjects, i.e., 30 seconds. As the windows are sized on a logarithmic scale, there will be some windows, which overlap distinct trials of data. These are justified for longer data sets (as are formed by stitching here), because at least half of the windows will always be contained within a continuously recorded segment of data.

When stitching is applied to time series, it is performed between steps 5 and 6 of the method (Figure 8.1). Namely, the dividing and stitching together of trials is performed after beamforming, filtering and calculating the phase difference. This minimises the chance of edge artefacts from the Hilbert transform [165, 300]. Further discussion of the stitching step will be given in the Discussion (Section 8.4.2.3).

#### 8.2.1.4 Statistical Tests

The DFA exponents of the 7 subjects corresponding to each task were tested for normality using a one-sample Kolmogorov-Smirnov test, for each frequency band individually. These tests showed that a null hypothesis of normally distributed DFA exponents could not be rejected for any task or frequency band where more than one DFA exponent was judged to be valid by ML-DFA. The $p$-values are given in full in Table 11.5. This was confirmed using the Jaque-Bera test for normality [141], but these $p$-values are not presented. As normal distributions could not be rejected, DFA exponents corresponding to the different movement tasks were tested for statistical difference with resting state data using a paired Student's t-test where pairings were maintained across the 7 subjects.

### 8.2.2 Participants

Seven healthy right handed subjects took part in the MEG experiments. The study was approved by the University of Nottingham Medical School ethics committee. Details of the experimental procedure are described in Brookes et al. [40]. In brief, MEG data were recorded using the third order gradiometer configuration of a 275-channel CTF MEG system at a sampling rate of 600Hz. The scanner is housed inside a magnetically shielded room (MSR) and a 150Hz low pass anti-aliasing hardware filter was applied. All subjects underwent a single experiment which comprised two contiguous phases, a resting state phase and a finger activation task. The localizer task comprised a total

of 10 trials. A single trial comprised 30s of left index finger movement, 30s of right index finger movement, 30s during which both left and right index fingers were moved together, and 30s of rest. The movement itself comprised abductions and extensions of the index finger. The motor task was cued visually via projection through a waveguide in the MSR onto a back projection screen located 40cm in front of the subject.

During data acquisition the location of the subject's head within the scanner was measured by energizing coils placed at 3 fiducial points on the head (nasion, left preauricular and right preauricular). If any subject moved more than 5 mm during the experiment, data from that subject was discarded. Following data acquisition, the positions of the coils were measured relative to the subject's head shape using a 3D digitizer (Polhemus isotrack). An MPRAGE structural MR image was acquired using a Philips Achieva 3T MRI system (1 $mm^3$ isotropic resolution, 256×256×160 matrix size, TR=8.3 ms, TR=3.9 ms, TI=960 ms, shot interval=3 s, FA=8° and SENSE factor=3). The locations of the fiducial markers and MEG sensors with respect to the brain anatomy were determined by matching the digitized head surface to the head surface extracted from the 3T anatomical MRI.

### 8.2.3 Control Data

The phase synchrony analysis method was applied to three different classes of both synthetic and experimental control time series.

First, pairs of time series with a time-varying phase difference of white Gaussian noise were constructed and analysed. This time series should give a DFA exponent of 0.5 if no artefacts are introduced by bandpass filtering or by the Hilbert transform in the method. This control data is therefore used to quantify any possible artefactual effects of these steps. Indeed, filtering has been known to potentially induce long-range correlations when DFA was applied to sequences of coherent activation interval lengths in EEG [284].

Next, time series recorded from an empty scanner were analysed. This control verifies the fact that the method can discriminate between meaningful recordings and noise, and also that the scanner introduces no artefactual LRTCs in the phase difference measure. This problem was recently highlighted when looking for power laws in the phase lock interval of MEG and fMRI data sets [255].

In the third control analysis, the phases of the MEG time series were shuffled before applying the phase synchrony analysis method. By this step it was verified that the results obtained from the data are not a generic feature of a random sequence or of MEG power spectra. We aim to show that the phase difference structure is disrupted by the loss of the specific temporal order of the sequence and that this is detected by the phase synchrony analysis method generating a DFA exponent of 0.5.

#### 8.2.3.1 Synthetic data with noise phase difference

Two time series $x_1(t)$ and $x_2(t)$ can be constructed such that their phase difference is set to equal white Gaussian noise $X(t)$ with a known DFA exponent of 0.5 [128]. The signals were calculated by $x_1 = \cos((\omega + \frac{X(t)}{2})t)$ and $x_2 = \cos((\omega - \frac{X(t)}{2})t)$. The factor $\omega$ is constant and here set to equal 1. It is necessary to include $\omega$ because white noise time series $X(t)$ are not smooth signals by definition, but alter sharply at subsequent innovations and the Hilbert transform produces artefacts when applied to such data. The factor $\omega$ modulates the time-varying $X(t)$. This situation will not arise in physiological data, because the sampling frequency with which physiological data is recorded produces a smooth signal once it is filtered.

Seven pairs of time series were created to correspond to the 7 subjects. Each time series consisted of 10 segments of $X(t)$ of length 30 seconds each were stitched together before constructing the two signals $x_1(t)$ and $x_2(t)$ (see Section 8.2.1.3 for more detail). This corresponded to the format of human MEG data set, and ensured that the filtering and Hilbert transform steps of the method were applied to continuous signals, which is important for preventing edge effect artefacts. The time series $x_1(t)$ and $x_2(t)$ were not beamformed because in this situation there is no additional noise or crosstalk present.

The difference between the phases of the two signals $x_1$ and $x_2$ are precisely $tX(t)$ and the rate of change of this is $X(t)$. When DFA is applied, one expects that the prescribed exponent will be recovered if no bandpass filter is applied. By constructing such time series we investigate whether the step of filtering and processing the data adds structure to the underlying phase synchrony, causing the presence of LRTCs to be evident. Window sizes used for application of DFA were the same as those for physiological data, namely logarithmically spaced windows with minimum 1 second and maximum 30 seconds. Although there is no sampling frequency associated with noise simulations, the minimum window was set to 600 time samples for consistency.

The DFA exponents of the synthetic pairs of time series were tested for normality using a one-sample Kolmogorov-Smirnov test, for each frequency band individually as for MEG data. These tests showed that a null hypothesis of normally distributed DFA exponents could not be rejected for any synthetic time series pair or frequency band where more than one DFA exponent was judged to be valid by ML-DFA. The $p$-values are given in full in Table 11.5. This was confirmed using the Jaque-Bera test for normality [141], but $p$-values are not presented here. As normal distributions could not be rejected, DFA exponents obtained from analysis of synthetic time series with a noise phase difference were tested for statistical difference with those of resting state human MEG data using a Student's t-test with no pairings because there was no pairwise connection between the noise time series and the human MEG.

#### 8.2.3.2 Scanner Noise

Seven data sets recorded from an empty MEG scanner were analysed. Time series obtained from sensors corresponding to the locations of the right and left motor cortices were recorded with sampling frequency 600Hz. These continuous time series of length 300seconds were divided into 10 segments of length 30seconds each, and reordered randomly to replicate the stitching procedure applied to MEG data. This reordering was performed after step 5 of applying the method (see Figure 8.1 and Section 8.2.1.3 for more detail), which ensured consistency with analysis of human MEG data. DFA exponents were then obtained for the 7 time series pairs, and checked for validity using ML-DFA. Window sizes used for DFA were the same as those for physiological MEG data.

The DFA exponents were again tested for normality using a one-sample Kolmogorov-Smirnov test, for each frequency band individually as for MEG data. These tests showed that a null hypothesis of normally distributed DFA exponents could not be rejected for any synthetic time series pair or frequency band where more than one DFA exponent was judged to be valid by ML-DFA. The $p$-values are given in full in Table 11.5. This was confirmed using the Jaque-Bera test for normality, but $p$-values are not presented here. As normal distributions could not be rejected, DFA exponents obtained from analysis of scanner noise recordings were tested for statistical difference with resting state human MEG data using a Student's t-test with no pairings because there was no pairwise connection between the noise time series and the human MEG.

#### 8.2.3.3 Phase Shuffling

A permutation of the rate of change of the phase difference time series (the time series in step 5 of the phase synchrony analysis method in Figure 8.1) was performed 100 times yielding 100 DFA exponents. These 100 exponents were tested for significant differences with the 7 human MEG data using the technique presented in [227]. The $p$-value is approximated using

$$p = \frac{b+1}{m+1}$$

where $b$ is the number of DFA exponents obtained from the permuted time series that are greater in size than that of the correctly ordered human MEG data, and $m$ is the number of permutations used $m = 100$. This is an approximation to the $p$-value when the number of possible permutations of the time series is very large. Here this is considered to be the case (the number of possible permutations is $180,000!$ where the symbol ! represents the factorial function).

### 8.2.4 Previous measures of phase interaction

Two commonly used metrics of the pairwise phase relationship between time series are defined here. We consider the application of these metrics to the MEG data in the light of earlier results obtained by applying these methods. It is shown that LRTCs in phase difference illuminates a characteristic of two time series that cannot already be accounted for by a strong coherent phase relationships between them.

#### 8.2.4.1 Mean Phase Coherence

The mean phase coherence (PC) was introduced by [201], as a practical method for quantifying the synchronisation between two neurophysiological signals. The mean PC is typically used as a statistical measure for phase synchronization. It was later incorporated into a framework for the analysis of frequency-specific synchronisation [171]. The mean PC is calculated using the following:

$$PC = \left| \frac{1}{T} \sum_{t_k=0}^{T-1} e^{i(\phi_n(t_k) - \phi_m(t_k))} \right|$$

where $m$ and $n$ represent two oscillators, $\phi_m(t_k)$ and $\phi_n(t_k)$ are their phases at time $t_k$ which runs between 0 and $T$, and $i$ is the imaginary unit $i = \sqrt{-1}$.

The phase coherence is not dependent on amplitude, in contrast to standard coherence analysis [262].

#### 8.2.4.2 Phase Lag index

The phase lag index [262] is an alternative measure of phase synchronisation. It was devised as a means of avoiding artefactual synchronisation that emerges because different MEG channels include components that originate at a common source. This is done by eliminating those phase differences that are precisely zero. PLI reflects the strength of the coupling, but is much less sensitive to artefacts resulting from the fact that different sensors can receive input from a common source [262].

The PLI is calculated using the following:

$$PLI = \left| \frac{1}{T} \sum_{t_k=0}^{T-1} \text{sign} \left[ \phi_n(t_k) - \phi_m(t_k) \right] \right|$$

where $m$ and $n$ represent two oscillators, $\phi_m(t_k)$ and $\phi_n(t_k)$ are their phases at time $t_k$ which runs between 0 and $T$, sign represents the signum function.

#### 8.2.4.3 Statistical Tests

For mean PC and PLI data, the difference between resting state time series and those recorded during tapping of both fingers was tested for significance using a one-tailed paired Student's $t$-test with pairings corresponding to the 7 subjects because a null hypothesis of normally distributed values could not be rejected (see Section 8.3.3).

## 8.3 Results

### 8.3.1 Physiological Data

#### 8.3.1.1 Power spectra

The pooled power spectra of time series for all the 7 subjects are shown in Figure 8.2. The technique used to create these pooled spectra is detailed in [113]. Power spectra for the right and left motor cortices are displayed. The pooled power spectra are considered rather than individual data for each subject because the average population behaviour is of interest here.

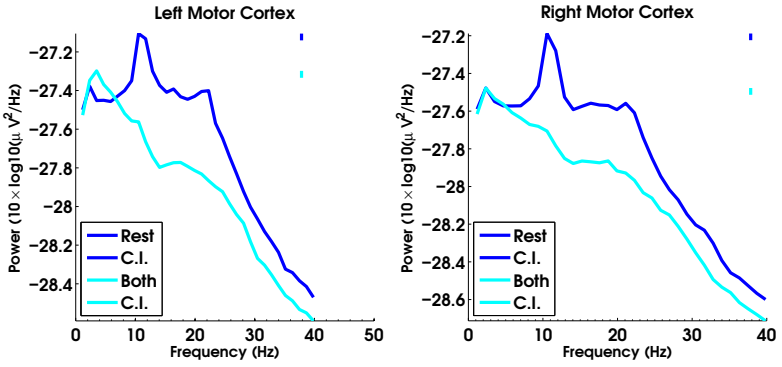


FIGURE 8.2: Pooled power spectra for all time series from 7 subjects. The power spectra of the right and left motor cortices during the resting state ('Rest') and during tapping of both fingers ('Both') are displayed on the same axes in the left and right plots, respectively. Prominent peaks in power during rest occur at 10.5 Hz and at 21.5 Hz. The short coloured lines at the top of the plots indicate the magnitude of the 95% confidence interval of the power level for each of the tasks. The dark blue line is associated with the rest condition, and the cyan line indicates the task of tapping both fingers.

All pooled power spectra show a prominent peak at low frequencies of 2-3 Hz, which is commonly observed in neurophysiological power spectra [72]. Resting state power spectra also have a $1/f^{\delta}$ form with peaks at $\sim 10.5$ Hz and $\sim 21.5$ Hz. These peaks were used to determine frequency bands for bandpass filtering the data (see below and [160]). For data recorded during the task of tapping both fingers, the power spectra also has this functional form, but the spectral peaks are diminished.

#### 8.3.1.2 Average DFA exponents for resting state and both fingers tapping

Differences between average DFA exponents obtained from analysing the rate of change of the phase difference between the left and right motor cortices of 7 human MEG signals are presented in Figure 8.3 for the resting state condition and for the task of tapping of both fingers. The time series were bandpass filtered in regular 2 Hz bands prior to analysis (see Section 8.2.1.2). As recommended by [223], we state the boundary values of each frequency band rather than expressing it in the form of a central frequency and bandwidth for ease of interpretation. All frequency bands are presented here, but a distinction is drawn between the $\alpha$ and $\mu$, $\beta$ and $\gamma$ frequency bands in plotting, and these bands are therefore shown separately.

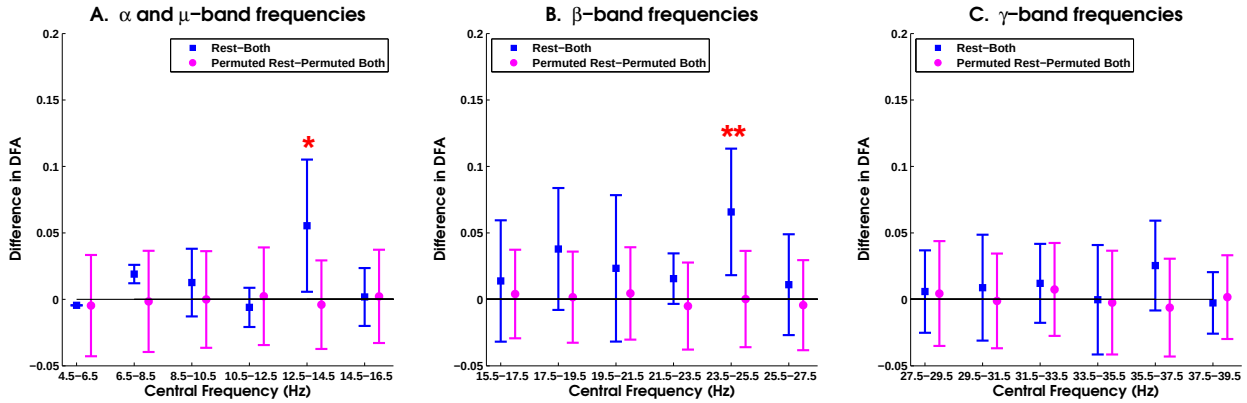


FIGURE 8.3: The differences between average DFA exponents obtained from analysing the rate of change of phase difference between left and right motor cortex MEG data from 7 subjects. Differences between resting state and the task of tapping both index fingers (blue squares) and differences between the corresponding phase-shuffled data (magenta circles) are shown. The $\alpha$ and $\mu$, $\beta$ and $\gamma$ frequency bands are distinguished and shown in separate plots. Each time series was bandpass filtered into 2 Hz bands ranging from 4.5 to 39.5 Hz as indicated by the $x$-axis. When ML-DFA determines that a DFA exponent is invalid the value is excluded from the average. The asterisk symbols indicate that the difference is significantly above 0. One asterisk indicates a $p$-value of $p < 0.05$, and two asterisks indicate $p < 0.01$. Significant differences are seen in frequency bands 12.5-14.5 Hz and 23.5-25.5 Hz for human MEG data that has not been phase-shuffled, but not for phase-shuffled data in any frequency band.

TABLE 8.1: The DFA exponents obtained from analysing human MEG recorded during all conditions analysed at each frequency band. Only DFA exponents determined to be valid by ML-DFA are included in the calculation.

| | Frequency Band (Hz) | | | | | | | | | | | | | | | | | |
|---|---|---|---|---|---|---|---|---|---|---|---|---|---|---|---|---|---|---|
| Data | 4-6 | 6-8 | 8-10 | 10-12 | 12-14 | 14-16 | 15-17 | 17-19 | 19-21 | 21-23 | 23-25 | 25-27 | 27-29 | 29-31 | 31-33 | 33-35 | 35-37 | 37-39 |
| Rest | 0.62 | 0.60 | 0.60 | 0.57 | 0.60 | 0.56 | 0.56 | 0.56 | 0.55 | 0.56 | 0.58 | 0.56 | 0.53 | 0.54 | 0.53 | 0.51 | 0.50 | 0.53 |
| Both | 0.64 | 0.58 | 0.60 | 0.57 | 0.55 | 0.56 | 0.54 | 0.54 | 0.53 | 0.54 | 0.52 | 0.55 | 0.53 | 0.55 | 0.54 | 0.51 | 0.52 | 0.52 |
| ShuffledR | 0.496 | 0.501 | 0.501 | 0.502 | 0.500 | 0.499 | 0.497 | 0.501 | 0.504 | 0.499 | 0.498 | 0.499 | 0.495 | 0.500 | 0.498 | 0.504 | 0.498 | 0.500 |
| ShuffledB | 0.500 | 0.497 | 0.495 | 0.502 | 0.499 | 0.500 | 0.497 | 0.497 | 0.497 | 0.497 | 0.505 | 0.501 | 0.499 | 0.500 | 0.504 | 0.501 | 0.502 | 0.499 |

The type of data analysed are listed in the left-hand column. The top row indicates the frequency band of the filter applied to data before it is analysed. Here the frequency bands are listed as integers to save space. Where the band is for example 4-6 Hz, this indicates that the bandpass filter was implemented from 4.5-6.5 Hz. The row labelled ShuffleR indicates phase shuffled time series from recordings of resting state data. ShuffleB denotes the phase shuffled time series from the task of tapping both fingers.

Average DFA exponents for the resting state task were higher than or comparable to those obtained from MEG data recorded during the task of tapping both fingers (see Table 8.1 for the full list of average DFA exponents). The difference between these average DFA exponents is significant in the $12.5 - 14.5$ Hz ($p < 0.05$) and $23.5 - 25.5$ Hz ($p < 0.01$) bands. These frequency ranges correspond to the $\mu$ and $\beta$ frequency bands. The full set of $p$-values for all bandwidths are given in Table 11.6 for all tasks as a comparison to resting state MEG data.

Since exponents associated with those fluctuation plots that are judged not to be valid by ML-DFA are not included in the average, the number of subjects contributing to the calculation of each average DFA exponent are listed for all data sets in Table 11.7. The issue of varying validity will be revisited in the Discussion (Section 8.4.2.5). In the frequency bands where significance is seen, there are 6/7 and 7/7 valid recordings from the 7 values for subjects in the non-shuffled data during the two tasks, respectively, in the $12.5 - 14.5$ Hz ($\mu$) and $23.5 - 25.5$ Hz ($\beta$) bands.

It is noted that peaks in average DFA exponent are in higher frequency bands than those for which the spectra show peaks in power. Furthermore, the power spectra suggest that the greatest distinction between the resting state and finger tapping task lies in the $\mu$ frequency band, in contrast to the most significant difference in average DFA is found in the $\beta$ band.

The power spectrum shows the power as the mean squared amplitude at each frequency but includes no phase information, so that the phase difference results identified are not caused by decreased signal-to-noise ratio of the recordings during finger tapping. Further to this, there is no difference in the DFA exponents of phase difference between

phase-shuffled time series for any frequency band, which has the same power spectra as the non-phase-shuffled data (spectra not shown).

#### 8.3.1.3 Phase Shuffling

Figure 8.4 shows the differences between the average DFA exponents from 100 phase shuffles of time series for resting state data and the task of tapping both fingers, for the left and right motor cortices of a representative subject DL. These differences are compared to differences between corresponding human MEG data that has not been shuffled. Table 8.1 gives a full list of average DFA exponents for phase shuffled time series.

The $p$-values for differences between human MEG data and the corresponding phase-shuffled data are given in Table 11.6. In the 12.5-14.5 Hz ($\mu$) band there is a significant difference between MEG data and corresponding phase-shuffled MEG data in both the resting state task and during tapping of both fingers. In the 23.5-25.5 Hz ($\beta$) band, there is only a significant different in the resting state task, and in the 33.5-35.5 Hz ($\gamma$) band there is no significant difference where all exponents are comparable to 0.5 on average (Table 8.1).

The numbers of valid DFA exponents in accordance with ML-DFA are given in Table 11.7, which are in excess of 93% across all frequency bands. The distributions of the 100 phase shuffled DFA exponents alongside results for human MEG data are shown in Figure 8.4. The power spectrum of a phase shuffled time series is the same as that of the original time series [195, 202, 272].

All 100 DFA exponents from phase-shuffled time series are shown in Figure 8.4 in the form of separate histograms of DFA values for frequency bands 12.5-14.5 Hz ($\mu$), 23.5-25.5 Hz ($\beta$) and 33.5-35.5 Hz ($\gamma$). Histograms are created in each case using 10 equally spaced bins spanning between the minimum and maximum DFA exponents obtained.

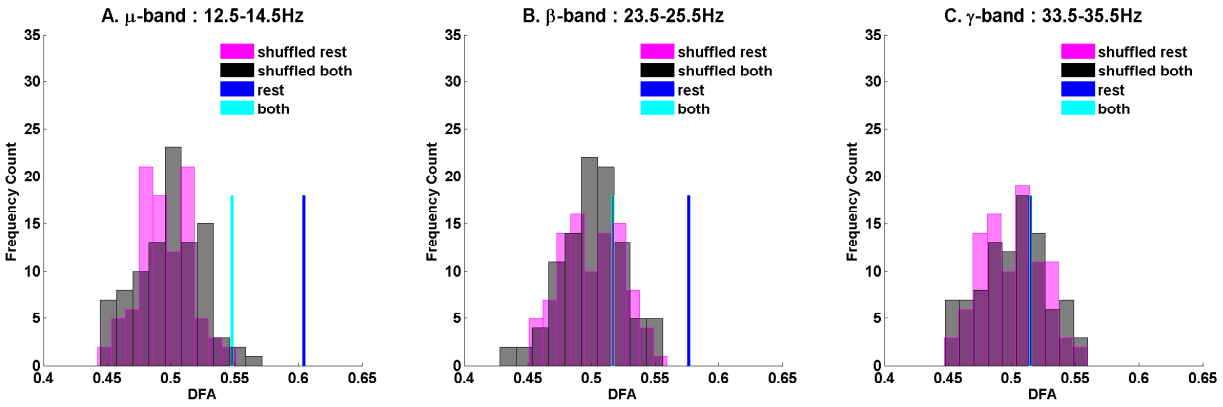


FIGURE 8.4: Distributions of DFA exponents obtained from analysis of phase-shuffled MEG time series alongside corresponding average DFA exponents for human MEG data for frequency bands 12.5-14.5 Hz ($\mu$), 23.5-25.5 Hz ($\beta$) and 33.5-35.5 Hz ($\gamma$) bands. Exponents from human data are in dark blue for resting state and cyan for the task of tapping both fingers. The distribution of phase-shuffled resting state exponents are in magenta, and that obtained during the task of tapping both fingers is in black. The DFA exponents are on the $x$-axis with the frequency count on the y-axis. In panel C, the exponents for resting state and task data are almost identical and are visually undistinguishable.

#### 8.3.1.4 Average DFA exponents for all finger-tapping tasks

The difference of average DFA exponents for the $\mu$, $\beta$ and $\gamma$ frequency bands are shown in Figure 8.5 for all tasks. The results for the task of tapping both fingers are repeated from Figure 8.3 for those frequency bands in which significance was seen and an additional band from the $\gamma$ band.

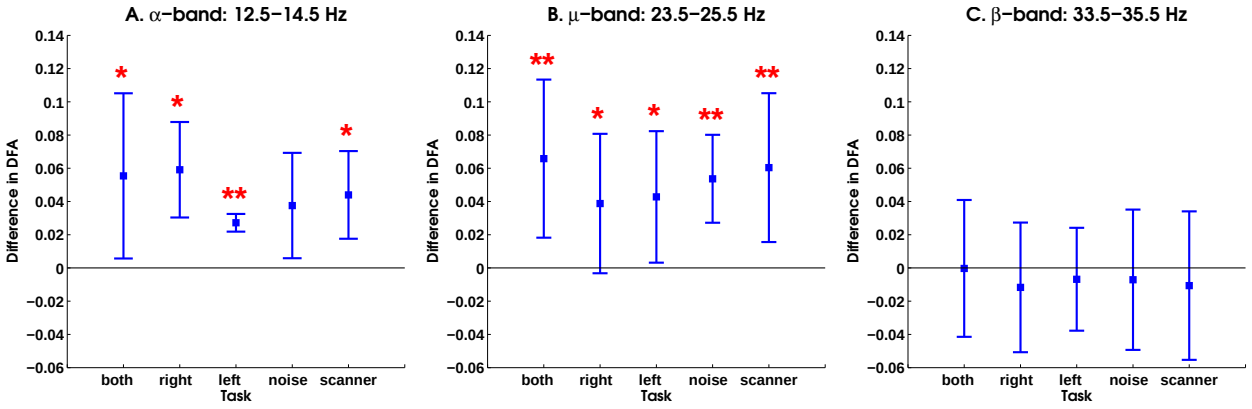


FIGURE 8.5: Differences between average DFA exponents for human MEG data recorded during rest and 1)the 3 finger-tapping tasks ('both', 'left', 'right' indicate the fingers being tapped) 2) time series with a noise phase synchrony ('noise') 3) recordings from an empty scanner ('scanner'), for frequency bands 12.5-14.5 Hz ($\mu$), 23.5-25.5 Hz ($\beta$) and 33.5-35.5 Hz ($\gamma$) bands. The results for the task of tapping both fingers are repeated from Figure 8.3 above for those frequency bands in which significance was seen and an additional band from the $\gamma$ range. The different data points correspond to different tasks and the y-axis shows the value of difference in DFA exponents. Only those values that are determined to be valid by ML-DFA are included in calculating the average value. Error bars represent a single standard deviation from the mean. The asterisk symbols indicate a significant difference between the exponents of resting state data and those recorded during the other tasks, so that the bar corresponding to the resting state will never have an asterisk. One asterisk indicates a $p$-value of $p < 0.05$, and two asterisks indicate $p < 0.01$.

The left and right finger tapping tasks yield DFA exponents that are significantly different from those of resting state in the $\mu$ and $\beta$ ranges (Table 11.6). The number of valid exponents are both 5 for the $\mu$ band and both 7 in the $\beta$ band in these two tasks (Table 11.7). In the $\beta$ frequency band it appears that movement is increasingly disruptive to the structure of the phase synchrony time series giving rise to progressively lower yet valid DFA exponents. In the $\gamma$ band there is no significant difference between any of the tasks (Table 11.6), but validity is high with $6-7$ subjects for each task (Table 11.7).

### 8.3.2 Control Data

Three sets of control data are used, which are described in Section 8.2.3. Results are summarised in Figures 8.3, 8.5 and 8.4, as well as tables 11.6 and 11.7.

#### 8.3.2.1 Synthetic data with noise phase difference

The numbers of valid DFA exponents obtained from analysing data with a white Gaussian noise phase difference are comparable to those of human MEG data in each frequency band (Table 11.7).

There is a significant difference between DFA exponents for this control data and those for resting state data in the $\beta$ band ($p = 0.0025$). However, there is no significant

difference in the $\mu$ or $\gamma$ bands ($p = 0.13$ and $p = 0.66$ respectively). These results show that the DFA exponents for resting state data are above those that may be expected from analysing noise data in the $\beta$, but not in the $\mu$ or $\gamma$ frequency bands. In other words, we can reject the possibility of noise data producing the DFA exponents seen in resting state data in the $\beta$ band. For the full set of results, see Table 11.6.

#### 8.3.2.2 Scanner noise

The numbers of valid DFA exponents obtained from analysing scanner noise are comparable to those of human MEG data in each frequency band (Table 11.7).

There is a significant difference between DFA exponents for this control data and those for resting state data in the $\mu$ band ($p = 0.03$) and in the $\beta$ band ($p = 0.02$), but not in the $\gamma$-band ($p = 0.76$) (see Table 11.6). These results show that the DFA exponents for resting state data are above those that would be expected from an analysis of scanner noise in the $\mu$ and $\beta$ bands, but not in the $\gamma$ band.

By viewing these results in conjunction with those from data with a noise phase difference, we suggest that in the $\beta$ frequency band DFA exponents of resting state data cannot be explained by artefacts introduced by the processing steps required by the phase synchrony analysis method.

### 8.3.3 Previous measures of phase interaction

#### 8.3.3.1 Mean Phase Coherence

Table 8.2 provides the values of the mean phase coherence obtained for each subject in all conditions. These data are tabulated according to the four frequency ranges previously identified and used in Figure 8.5, namely 12.5-14.5 Hz ($\mu$), 23.5-25.5 Hz ($\beta$) and 33.5-35.5 Hz ($\gamma$) bands.

The $p$-values obtained from a comparison of the resting state and finger tapping PC values are $p = 0.15$, $p = 0.48$, $p = 0.001$ respectively in the $\mu$, $\beta$ and $\gamma$ bands respectively). The only difference of significance is in the $\gamma$ range.

This indicates that the distinction made through finding the DFA exponent of the phase synchrony is not already well-described by the PC. Indeed, DFA of PC takes high values in the $\gamma$ band during the resting state compared with muscle activation. In contrast, no significant differences are seen between the DFA exponents of the rate of change of phase difference between the tasks in this frequency band and DFA exponents are $\approx 0.5$. In contrast, the $\mu$ and $\beta$ ranges show no difference in PC but show a significant difference in DFA.

TABLE 8.2: Mean Phase Coherence (PC) for time series from the left and right motor cortex during the task of tapping both, just the left and just the right index fingers, and during resting state, after filtering in the 12.5-14.5 Hz ($\mu$), 23.5-25.5 Hz ($\beta$) and 33.5-35.5 Hz ($\gamma$) bands. The left hand column gives a number corresponding to each subject in the study.

| | 12.5-14.5 Hz | | | | 23.5-25.5 Hz | | | | 33.5-35.5 Hz | | | |
|---|---|---|---|---|---|---|---|---|---|---|---|---|
| | Rest | Both | Right | Left | Rest | Both | Right | Left | Rest | Both | Right | Left |
| 1 | 0.21 | 0.16 | 0.15 | 0.19 | 0.26 | 0.24 | 0.26 | 0.25 | 0.25 | 0.21 | 0.22 | 0.23 |
| 2 | 0.17 | 0.18 | 0.16 | 0.19 | 0.24 | 0.27 | 0.22 | 0.26 | 0.22 | 0.22 | 0.21 | 0.24 |
| 3 | 0.16 | 0.17 | 0.19 | 0.21 | 0.23 | 0.24 | 0.26 | 0.28 | 0.22 | 0.19 | 0.24 | 0.27 |
| 4 | 0.21 | 0.15 | 0.16 | 0.20 | 0.27 | 0.25 | 0.23 | 0.24 | 0.25 | 0.22 | 0.21 | 0.22 |
| 5 | 0.17 | 0.18 | 0.19 | 0.19 | 0.25 | 0.25 | 0.28 | 0.22 | 0.23 | 0.22 | 0.24 | 0.23 |
| 6 | 0.19 | 0.19 | 0.19 | 0.15 | 0.26 | 0.25 | 0.24 | 0.25 | 0.25 | 0.22 | 0.24 | 0.21 |
| 7 | 0.20 | 0.18 | 0.15 | 0.17 | 0.25 | 0.26 | 0.24 | 0.24 | 0.24 | 0.22 | 0.23 | 0.21 |

The mean PC is given separately for each subject.

#### 8.3.3.2 Phase Lag Index

Table 8.3 provides the values of the phase lag index obtained for each subject in all conditions. These data are tabulated according to the four frequency ranges previously identified and used in Figure 8.5, namely 12.5-14.5 Hz ($\mu$), 23.5-25.5 Hz ($\beta$) and 33.5-35.5 Hz ($\gamma$) bands.

TABLE 8.3: Phase Lag Index for time series from the left and right motor cortex during the task of tapping both, just the left and just the right index fingers, and during resting state, after filtering 12.5-14.5 Hz ($\mu$), 23.5-25.5 Hz ($\beta$) and 33.5-35.5 Hz ($\gamma$) bands. All values are PLI multiplied by 10 here for readability. The left hand column gives a number corresponding to each subject in the study.

| | 12.5-14.5 Hz | | | | 23.5-25.5 Hz | | | | 33.5-35.5 Hz | | | |
|---|---|---|---|---|---|---|---|---|---|---|---|---|
| | Rest | Both | Right | Left | Rest | Both | Right | Left | Rest | Both | Right | Left |
| 1 | 0.14 | 0.16 | 0.31 | 0.01 | 0.10 | 0.29 | 0.03 | 0.08 | 0.23 | 0.08 | 0.17 | 0.11 |
| 2 | 0.06 | 0.11 | 0.00 | 0.25 | 0.06 | 0.10 | 0.02 | 0.07 | 0.05 | 0.05 | 0.08 | 0.28 |
| 3 | 0.02 | 0.16 | 0.02 | 0.46 | 0.12 | 0.11 | 0.06 | 0.11 | 0.05 | 0.04 | 0.04 | 0.32 |
| 4 | 0.49 | 0.12 | 0.38 | 0.30 | 0.06 | 0.31 | 0.06 | 0.31 | 0.18 | 0.03 | 0.04 | 0.06 |
| 5 | 0.40 | 0.30 | 0.20 | 0.14 | 0.11 | 0.28 | 0.47 | 0.06 | 0.09 | 0.06 | 0.26 | 0.20 |
| 6 | 0.30 | 0.09 | 0.04 | 0.04 | 0.10 | 0.09 | 0.10 | 0.11 | 0.06 | 0.12 | 0.03 | 0.07 |
| 7 | 0.07 | 0.30 | 0.08 | 0.07 | 0.05 | 0.01 | 0.17 | 0.06 | 0.11 | 0.16 | 0.06 | 0.14 |

The PLI is given separately for each subject. Note that all values are multiplied by 10 here for readability.

In the case of PLI, the resting state task did not exhibit significant difference (at the 5% level) when compared to the task of tapping both fingers or individual left/right finger tapping in any frequency band ($p = 0.33$, $p = 0.05$, $p = 0.17$ respectively in the $\mu$, $\beta$ and $\gamma$ bands respectively).

This indicates that the distinction detected through finding the DFA exponent of the phase synchrony is not already well-described by the PLI.

## 8.4 Discussion

### 8.4.1 Summary

In this chapter, it has been shown in the resting state that power law scaling can be detected in the time-varying phase difference between MEG recorded from the left and right motor cortices. The exponent of this scaling was greater than 0.5, which was indicative of long-range correlations in the rate of change of phase difference between the bandpass filtered MEG of left and right motor cortices. Furthermore, it was shown that these long-range correlations were disrupted by finger movement in the $12.5 - 14.5$ Hz and $23.5 - 25.5$ Hz frequency ranges. These ranges are in the $\mu$ and $\beta$ bands, which are known to play an important role in the human and primate motor system although they are not identical to peak spectral power in these ranges. They also contain spectral peaks in resting state data, although the maximal power of these $\mu$ and $\beta$ peaks is not in exactly the same frequency band [64, 81, 111, 140, 218, 223]. The most significant change was caused by tapping both index fingers simultaneously, however, unilaterally tapping the left or the right index finger was also associated with a lowering of the DFA exponents.

The results of this chapter are related to a previous result in which the DFA exponents of a measure referred to as the synchronisation likelihood between all possible pairs of *EEG* time series recorded from 19 channels [261]. The synchronisation likelihood gives a value for the likelihood that if a single time series takes similar values at two time points, another time series also takes similar or almost similar values, which is an alternative measure of time-varying synchronisation, but not the same as the phase difference. The DFA exponents in this earlier paper were found to be approximately 1.5 in time series bandpass filtered to the $\delta$, $\theta$ and $\alpha$ bands and approximately 1 in time series bandpass filtered in the $\beta$ and $\gamma$ bands. These exponents suggest that the synchronisation likelihood is a more ordered time series than the rate of change of phase difference, so that it is likely to be encoding a different property of the relationship between neurophysiological time series. The exponents of the $\alpha$ and $\beta$ bands in particular were shown to decrease when the subjects opened their eyes, but remained in a range close to 1.5 and 1 respectively. The validity of the DFA exponents in this earlier paper was not verified by any assessment of the linearity of the associated DFA fluctuation plots.

To validate the results of this chapter on control data, the phase synchrony analysis method was first applied to synthetically generated time series with a noise phase difference. This was used to verify that no step in the method would give rise to DFA

exponents that were comparable to those yielded on average by the rate of change of phase difference of resting state data in the $\beta$ band, and in particular, the bandpass filtering step was tested here because without it, the prescribed DFA exponent of the rate of change of phase difference of noise time series is known to be 0.5 on average.

Second, the results were compared to those obtained by applying the phase synchrony analysis method to noise recorded from an empty MEG scanner. It was shown that in the $\mu$ and $\beta$ frequency bands, exponents from analysis of resting state MEG were significantly greater than those of scanner noise. This verified that the obtained DFA exponents for resting state data were not produced by an effect of scanner noise on the phases of the signals.

Third, it was shown that the DFA exponents of the phase difference from both resting state and synchronous finger tapping in the $\mu$ and $\beta$ bands were significantly greater than the corresponding exponents after phase shuffling. This indicates that the phase difference structure is disrupted by the loss of the specific temporal order of the time series while the spectral amplitude of the data is maintained.

Furthermore, a comparison to previously published metrics of phase relationship, namely values of the mean phase coherence (PC) and the phase lag index (PLI) showed that the distinctions found here between resting state and movement tasks are not identified by these measures. Further to these measures, which specifically relate to phase synchrony, we present here a novel method that assesses the temporal structure of the phase relationship.

### 8.4.2 Methodological considerations

Prior to analysis, data is beamformed, and time series from trials corresponding to the same task for the same subject are stitched together. This data is then bandpass filtered. Since each of these steps introduce complexities and possible artefacts in the analysis, we discuss them in turn below.

#### 8.4.2.1 MEG recording

Cross-talk and noise is a potential problem for MEG recordings [78, 118, 147]. The surface locations of the sensors are not guaranteed to exactly detect activity corresponding to specific brain regions that show the most interesting activity. The effects of these shortcomings are minimised by identifying the motor cortices individually for each subject using a beamforming technique. It is now widely used in the literature and facilitates the study of brain regions that are not closely stimulus time and phase-locked [40, 122, 123]. The effects of beamforming on the results were not investigated in this chapter.

#### 8.4.2.2 Filtering

We chose to bandpass filter the data in bands of 2 Hz using a technique from [160]. In doing so, it was ensured that the frequency bands are small, and avoid difficulties inherent in separating amplitude and phase components of a time series [29], while at the same time being wide enough to avoid artefactual coupling [243]. Alternative techniques for selecting suitable bandpass limits exist (for example in [223]), however, we also analysed bands in the vicinity of those presented and thus ensured that the frequency bands used were representative of the data.

#### 8.4.2.3 Data stitching

It was necessary to stitch together data for robust application of DFA.

A DFA exponent calculated from a time series stitched from shorter segments with comparable exponents of their own will retain validity [35] and still give a good estimate of the Hurst exponent if this exponent is in the LRTC range ($> 0.5$) [52]. It has been demonstrated that that removing 50% of a correlated signal (one for which the DFA exponent $0.5 < \alpha < 1.5$) and stitching together the remaining parts does not affect the scaling behaviour of the signal [52]. The authors of [52] find that if a non-stationary correlated signal of comprised of two stitched segments, each with a different standard deviation value, and that there is no difference in their scaling behaviour, when compared to stationary signals with a constant standard deviation [52]. For signals comprised of segments with different levels of correlation, the resulting scaling behaviour of the stitched signal is a combined version of the distinct scaling behaviours of the two segments [52].

There are a number of publications in which the stitching of time series has been previously used. In a DFA analysis of a time series of minimum and maximum daily temperatures parts of the data are removed and the remaining segments stitched together [156]. Nucleotide blocks are stitched in order to obtain a bacterial coding genome before applying DFA to the data in [97]. A tutorial on DFA by [117] proposes stitching together time series after cutting artefact segments away.

Furthermore, any periodic, artefactual effects of stitching these trials would occur at a frequency of 1/30 Hz because each trial is 30 seconds in length. This frequency is below any bands that are used for analysis in this chapter, so is necessarily filtered out.

Furthermore, because the DFA technique is used to analyse the rate of increase of detrended fluctuation magnitude, the DFA exponent is independent of the signal amplitude, the original mean, or any linear trend present in a time series [129].

Finally, the increased length of the time series analysed, will in general produce a greater number of valid DFA fluctuation plots because a greater number of estimates of detrended fluctuation size will lead to a more accurate average, which supports stitching as a necessary and justifiable technique.

#### 8.4.2.4 Scanner Noise

It is further noted that although recordings of noise from an empty scanner were obtained from the same scanner as the human MEG, they were not recorded on the same occasion as the human data. This does not significantly affect the outcome, which was verified by analysing 7 noise recordings at a time from a selection of 10. Any selection of 7 gave the same result. MEG scanner noise should have a characteristic day to day temporal structure that reflects a specific scanner's characteristics and therefore we would expect that from one day to another, recordings would be different realisations of a similar underlying process.

#### 8.4.2.5 Frequency band dependence

It is observed that the number of DFA exponents found to be valid by ML-DFA increased with the frequency band. Indeed, it would be surprising is all signals considered showed power law scaling of phase difference regardless of the frequency band in which they were filtered. It is also observed that the value of the DFA exponent falls with increasing frequency band. Together, these two points suggest the existence of a critical regime of the human motor cortex MEG activity corresponding to the presence of LRTCs (widespread linearity in fluctuation plot and a Hurst exponent of $> 0.5$), and specifically, that this regime of the motor cortex occurs in the $\mu$ and $\beta$ frequency bands.

The value of the DFA exponent is observed to typically be higher at lower frequency bands. This observation is to be expected because when time series are filtered at lower frequencies they will have correlations extending over greater temporal periods because a typical oscillation will take longer. To eliminate this effect from the interpretation of the results, the DFA exponents were analysed as the difference between the DFA exponent observed at rest and during a task or control condition in the same frequency band. This means that any artefactual increase in DFA exponent as a result of the frequency band in which it was measured is controlled for. The difference between DFA exponents in resting state and finger-tapping tasks therefore persists above any frequency related dependency of DFA.

### 8.4.3 Wider interpretation of results

We draw an analogy between the results obtained from the MEG data of the $\mu$ and $\beta$ bands of the two motor cortices at rest and the Kuramoto oscillators in a state prior to full synchronisation, at the onset of criticality (see Section 6.11). The rate of change of their MEG phase difference show long range correlations in resting state. Movement tasks disrupt the phase relationship between the motor cortices into a less correlated state, and further away from a system that possesses long range temporal correlations (LRTCs). The finding of physiological LRTCs breaking down with activity and stimulation has previously been observed [10].

The presence of LRTCs may be indicative of the fact that the brain is in a state of readiness while in resting state. LRTCs are indicative of some properties of a critical system. They have been are associated with an ability to learn well, memory formation, rapid information transfer and efficient network reorganisation, all of which is indicative of a readiness to respond to change [24, 54, 178, 179, 192, 254, 258, 261, 295]. The phase relationship of oscillatory neurophysiological signals is a measure of communication between neuronal pools [7, 46, 74, 90, 228, 250, 256]. Therefore, we suggest that LRTCs in the phase relationship of motor cortices show that their interaction with each other at rest is in a state of readiness. During movement, the interaction is disrupted because the cortices become engaged in activity. In this state, we suggest that the cortices have a lower predisposition to synchrony.

Although these findings are related to previous studies of event related synchronisation and desynchronisation (ERS and ERD), [174, 206, 218–224, 238], the results here are distinct in a number of ways. First, we remain agnostic about the synchronisation level both in amplitude and phase domains within any specific neural region, but instead study the phase relationship between two regions, which is a property orthogonal to these earlier amplitude considerations [29]. Second, the analysis is applied to time series that last several minutes, during continuous segments of finger tapping rather than addressing the more transient effects of movement previously studied [218, 223]. Third, we relate properties of the phase relationship directly to those of a system in a critical state [54, 157, 158, 192, 254, 296].

It is important to note that DFA is dependent on finding power law scaling in the detrended fluctuation magnitude and that power law scaling in itself is not a sufficient condition for criticality [12, 34, 58, 119, 158, 255, 263, 271]. We conclude that the interactions between motor brain regions at rest are indicative of a system in a regime that provides a suitable environment for the brain to react readily to external stimuli. Since we do not have access to the full spectrum of brain activity, we cannot say precisely how close the brain is to the point of transition. We suggest that the ability of the phase synchrony analysis method to identify a system with the potential to change may

therefore have important implications in the future for assessing the sensitivity of a human subject in responding to drugs or other treatments.

# Chapter 9

# Phase synchrony analysis of EEG and EMG Data

## 9.1 Introduction

In this chapter, it is demonstrated that the phase synchrony analysis method may be applied to neurophysiological time series recorded from different locations in the nervous system, and in particular to EEG and EMG signals. The question of whether power law scaling may, in principle, be detected in the detrended fluctuation magnitude of the rate of change of phase difference between these time series is investigated, and whether the exponent of this scaling can indicate the presence of LRTCs.

Specifically, in order to approach this question, the data set of simultaneously recorded EEG and EMG time series studied by Berthouze et al. [28] is revisited.

The EMG time series allows a demonstration of the fact that the phase synchrony analysis method can be used to explore neuronal activity from the peripheral nervous system, which the data in Chapter 8 does not.

## 9.2 Data

The data analysed in this chapter is that described in Section 2.2.

## 9.3 Methods

The specific time series and data preprocessing steps for this data are as in Section 3.3. However, the amplitude envelope is not calculated here. Instead, the phase synchrony analysis method is applied.

The statistical tests used to compare the values of the DFA exponents and the proportions of valid exponents in different age groups are the same as those described in Section 3.3 for this data.

### 9.3.1 Control Analysis

the phase synchrony analysis method was also applied to two signals with a rate of change of phase difference equal to a time series of white Gaussian noise, which were matched in length to the EEG and EMG data. These signals were constructed by the same procedure as that described in Section 8.3.2.1.

## 9.4 Results

### 9.4.1 Physiological Data

Figure 9.1 shows 10 seconds of the rate of change of phase difference between a simultaneously recorded EEG and EMG signal for a representative subject. The DFA fluctuation plot is also shown.

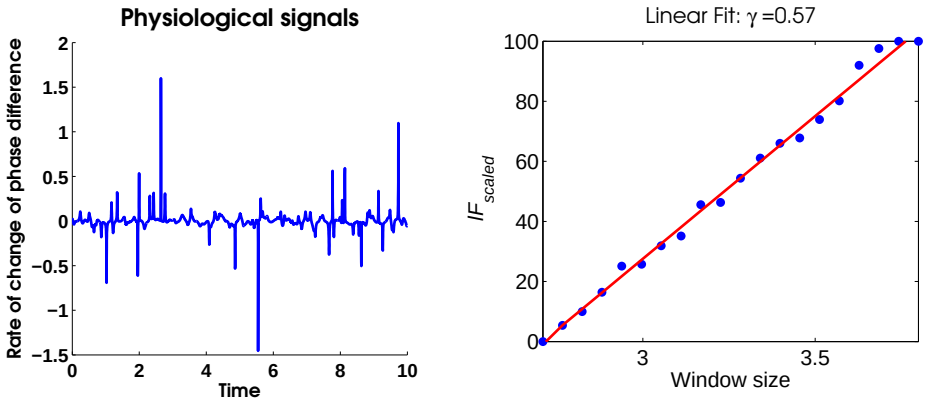


FIGURE 9.1: DFA and ML-DFA results for the rate of change of phase difference between the EEG signal recorded at the C3 electrode and the EMG signal recorded at the R1DI muscles and bandpass filtered to the 16-24 Hz range.

DFA exponents calculated from the rate of change of the phase difference of the bandpass filtered EEG signal are given in Table 9.1. Exponents found to be valid using ML-DFA are indicated by an asterisk. Only these exponents were used in any further analysis and calculation.

All age groups show a significant difference from 0.5 in their mean DFA exponent at the 5% level. Group 1, which contains subjects of ages less than 36 months show the least number of valid subjects.

TABLE 9.1: DFA exponents for unwrapped phase differences between EEG and EMG signals for all subjects. Only the exponents with an asterisk are valid by ML-DFA. The mean and standard deviation takes only these exponents into account. The proportion of valid subjects is given and the $p$-value obtained by a one-sampled Student's t-test to compare the DFA exponents in each group to 0.5. All exponents are given to 2 d.p.

| Subject | Group 1 | Group 2 | Group 3 | Group 4 |
|---|---|---|---|---|
| 1 | 0.60 | 0.52 $*$ | 0.53 $*$ | 0.57 $*$ |
| 2 | 0.46 | 0.64 $*$ | 0.57 $*$ | 0.49 $*$ |
| 3 | 0.56 | 0.59 | 0.45 | 0.53 $*$ |
| 4 | 0.48 | 0.53 $*$ | 0.58 $*$ | 0.51 |
| 5 | 0.61 $*$ | 0.61 | 0.59 $*$ | 0.52 $*$ |
| 6 | 0.50 $*$ | 0.55 $*$ | 0.52 $*$ | 0.54 $*$ |
| 7 | 0.52 | 0.54 $*$ | 0.57 $*$ | 0.54 $*$ |
| 8 | 0.44 | 0.52 $*$ | 0.54 $*$ | 0.57 $*$ |
| 9 | 0.58 $*$ | 0.58 $*$ | 0.58 $*$ | 0.51 $*$ |
| 10 | 0.57 | 0.59 $*$ | 0.59 $*$ | 0.58 $*$ |
| 11 | 0.43 | 0.50 | 0.58 $*$ | 0.62 $*$ |
| 12 | 0.51 | 0.59 $*$ | 0.52 $*$ | 0.54 $*$ |
| 13 | | 0.50 | | 0.60 $*$ |
| Mean | 0.56 | 0.56 | 0.56 | 0.55 |
| Standard Deviation | 0.06 | 0.04 | 0.03 | 0.04 |
| Proportion valid subjects | 0.25 | 0.69 | 0.92 | 0.92 |
| $p$-value | 0.017 | 1.69E-04 | 4.34E-06 | 1.58E-04 |

Pearson's $\chi^2$ statistic was calculated to be 5.20 to 2 significant figures. This corresponds to a cumulative $\chi^2$ $p$-value of 0.07, indicating that the null hypothesis of equal proportions of valid subjects in each group is not rejected at the 5% level.

### 9.4.2 Analysis of noise data

DFA exponents calculated from the rate of change of phase difference of a bandpass filtered time series of Gaussian white noise are given in Table 9.2. Exponents found to be valid using ML-DFA are indicated by an asterisk. Only these exponents were used in any further analysis and calculation.

Comparison of DFA exponents obtained from the time-varying synchronisation between EEG and EMG signals show a significant difference for age groups 2, 3 and 4. The decreased proportion of valid subjects in Group 1 for noise data as well as for neurophysiological data suggests that the reason for this decrease in proportion is the length of the time series, which is matched in noise and human data.

TABLE 9.2: DFA exponents for the rate of change of phase difference between two Gaussian white noise signals filtered in the $\beta$ band. The noise time series was matched in length to the EEG and EMG time series. Exponents from DFA fluctuation plots shown to be valid by ML-DFA are marked with an asterisk. The mean and standard deviation takes only these exponents into account. $p$-values for a one-sided Student's t-test between noise, EEG and EMG results are given. All exponents are given to 2 d.p.

| Subject | Group 1 | Group 2 | Group 3 | Group 4 |
|---|---|---|---|---|
| 1 | 0.48 | 0.53 $*$ | 0.53 $*$ | 0.53 $*$ |
| 2 | 0.59 | 0.51 | 0.53 $*$ | 0.53 $*$ |
| 3 | 0.76 | 0.45 $*$ | 0.51 $*$ | 0.49 $*$ |
| 4 | 0.68 | 0.43 | 0.49 $*$ | 0.58 |
| 5 | 0.38 | 0.37 | 0.58 | 0.51 $*$ |
| 6 | 0.51 | 0.53 | 0.55 $*$ | 0.47 $*$ |
| 7 | 0.54 | 0.39 | 0.59 | 0.62 $*$ |
| 8 | 0.43 | 0.47 $*$ | 0.70 | 0.45 $*$ |
| 9 | 0.61 $*$ | 0.56 $*$ | 0.53 $*$ | 0.59 |
| 10 | 0.63 | 0.45 $*$ | 0.60 $*$ | 0.49 $*$ |
| 11 | 0.51 $*$ | 0.60 $*$ | 0.52 $*$ | 0.57 |
| 12 | 0.46 | 0.46 $*$ | 0.48 $*$ | 0.50 |
| 13 | | 0.52 $*$ | | 0.48 $*$ |
| Mean | 0.56 | 0.51 | 0.53 | 0.51 |
| Standard Deviation | 0.07 | 0.06 | 0.03 | 0.05 |
| Proportion Valid Subjects | 0.17 | 0.67 | 0.75 | 0.75 |
| $p$-value | 0.47 | 0.01 | 0.01 | 0.02 |

## 9.5 Discussion

The results of this chapter suggest that the time-varying synchronisation between neurophysiological signals recorded at the cortex (EEG) and at the peripheral nervous system (EMG) may be analysed using the phase synchrony analysis method. It has been shown in this chapter that it is possible to detect LRTCs between these regions in principle.

The rate of change of phase difference between EEG and EMG signals in the $\beta$ (16-24 Hz) band collected simultaneously during a pincer grip task shows the presence of LRTCs in subjects of all age groups. However, there is a significant difference between DFA exponents of human data and those from noise time series in age groups 2, 3 and 4 only. This may be due to the fact that the time series in Group 1 were shorter, and matched in length to noise data. Time series were shorter because of difficulties with maintaining a steady pincer grip in younger subjects.

These results, if confirmed in longer time series, may suggest that LRTCs in the rate of change of phase difference between left and right motor cortices during resting state as seen in Chapter 8 are due to a lack of active movement, which is a property both of the resting state and of the steady pincer grip in this chapter. This in turn suggests that LRTCs are not destroyed by the contraction of a muscle, but rather by ongoing motor

activity. However, it is important to note that the time series analysed in this chapter did not undergo artefact removal as in [28], and that for this reason, the results here are provisional. In order to validate these results, it would be necessary to apply the methodology to a set of longer time series, which contained fewer artefacts. In this case, it may be necessary to alter the task protocol slightly in order to allow the youngest subjects to perform the task for a long period of time, or to consider subjects only older than $\approx 3$ years old.

# Chapter 10

# General Discussion

## 10.1 Summary of main results

- The heuristic ML-DFA technique for assessing the linearity of a DFA fluctuation plot was developed. ML-DFA was validated by application to time series with known characteristics in their DFA fluctuation plots and found to recover their exponents and these known characteristics.
- Human EEG and EMG signals recorded during a constant pincer grip were shown to have LRTCs in their amplitude envelope for all subjects who were greater than 36 months in age. These results demonstrate that ML-DFA is a useful tool in validating DFA analysis of neurophysiological data.
- DFA linearity was shown to be sensitive to the choice of window sizes for its analysis. The use of ML-DFA to determine the linearity of the fluctuation plot was therefore additionally justified.
- A previous method for assessing the presence of a power law distribution in a measure of time-varying synchronisation (PLI and GLS) between signals was found not to distinguish between critical and non-critical systems. The conclusion of criticality in human brain network synchronisation that was drawn from the application of this method to MEG and fMRI data was therefore called into question. It was concluded that care should be taken when interpreting power law frequency distributions that have been obtained from a set of variables with a characteristic time scale, or from a time series to which a threshold was applied.
- The alternative phase synchrony analysis method for assessing the presence of LRTCs using DFA and ML-DFA, in the rate of change of phase difference between two signals was introduced and validated.
- Through application to surrogate data, the phase synchrony analysis method was shown to recover known DFA exponents.

- Time series with a known DFA exponent in their phase difference were contaminated by additive noise. When additive noise caused the DFA exponent of the rate of change of phase difference between two signals to be altered by more than 5%, the DFA fluctuation plot that produced the DFA exponent was rejected by ML-DFA.

- The phase synchrony analysis method was applied to time series generated by the Ising model. The results indicated that the peak in average DFA exponent occurred at a temperature parameter associated with a state that is near but more disordered than the critical state. At the critical temperature parameter, LRTCs were present, on average, in the rate of change of phase difference between time series but validity of the DFA plots falls steeply as magnetisation occurs within the model.

- Application of the phase synchrony analysis method to time series generated by the Kuramoto model indicated the presence of LRTCs on average in the rate of change of phase difference at the critical coupling parameter. Again, the peak in DFA exponent occurred at a coupling parameter associated with a state that is very close to but slightly more disordered than the critical state. Taken together, the results of applying the phase synchrony analysis method to the Ising and the Kuramoto models suggest that the presence of LRTCs in the rate of change of phase difference may be a putative marker of a system close to its critical regime, but that the peak in DFA exponent occurs in a state more disordered than at criticality.

- In the Kuramoto model LRTCs in the rate of change of phase difference between oscillator time series occurred near the peak in the change of order parameter with increasing coupling value. The order parameter is another measure associated with the critical regime. As full synchrony developed, DFA validity was lost.

- In the Cabral model of the resting state brain, LRTCs were also seen to be present in the rate of change of phase difference between oscillators at the largest peak in the change of order parameter with coupling value.

- In the Cabral model, the oscillators that showed the greatest number of LRTCs in their interactions with other oscillators, belonged to clusters with a large number of connections and strong connectivity weights. These oscillators are modelled to represent brain regions including the precuneus and posterior cingulate cortex, which have both been implicated as important contributors to the resting state default mode network.

- In the Cabral model, disruption of the connectivity structure of clusters by disconnecting the cortical hemispheres and randomising connectivity was shown to disrupt LRTCs in the rate of change of phase difference between oscillators.

- In human MEG data, LRTCs were shown to be present in the rate of change of phase difference in the $\mu$ and $\beta$ frequency band between the left and right motor cortex during resting state. LRTCs were disrupted during a finger-tapping task. These results were validated with control data that included phase shuffling, simulated time series with a rate of change in their phase difference of white Gaussian noise, and recordings of scanner noise.
- LRTCs in time-varying synchronisation were seen to be present in the 16-24 Hz ($\beta$) frequency band between EEG and EMG time series during a pincer grip task for subjects older than 36 months in age. These results demonstrate that the phase synchrony analysis method may in principle be used to detect the presence of LRTCs in the phase difference between neurophysiological time series from cortical and peripheral regions of the nervous system.

## 10.2 Discussion and future directions

This thesis describes two methodological advances. The first is the development of ML-DFA, and the second is the introduction of the phase synchrony analysis method. Some methodological considerations for both of these techniques will be discussed in this section. An interpretation and discussion of the results obtained in this thesis will also be given, and potential new avenues for research will be suggested.

### 10.2.1 ML-DFA

It was demonstrated in Chapter 2 that ML-DFA is effective in classifying linear and non-linear DFA fluctuation plots in time series with known properties. It has also been stated that ML-DFA is a heuristic technique, but one that is nevertheless useful and informative[1]. ML-DFA was used throughout this thesis because it has provided a straightforward and automatic technique that can be used to distinguish between linear and non-linear DFA fluctuation plots. Ultimately, publication of the technique will enable the community using DFA to assume validity of scaling and the scaling exponents derived for their data.

With a number of other collaborators, a more mathematically rigorous method is being developed, with the same aim as ML-DFA. Specifically, as with ML-DFA, we have constructed the maximum likelihood estimates for a number of models fitted to the DFA fluctuation plot, which are based on the assumption that the errors around a fit of the DFA fluctuation plot will be log-normal. This would mean that the errors are normal

[1]Indeed, the frequently used method of empirical mode decomposition, which provides a method for the decomposition of a signal into a number of narrowband components was initially developed and published as a heuristic technique by Norden E. Huang in 1998 [132, 303].

in log-log space, where DFA fluctuation plots are typically visualised, and the squared errors would be distributed with a $\chi^2$ distribution. This assumption is not trivially satisfied, and further work will need to be done to verify that it indeed holds. Some preliminary empirical work was done on this data, without verifying this latter assumption, and evidence has suggested that the parameters of the models proposed here would have a 'peaky' distribution, so that a maximum likelihood may be calculated for these parameter values because the likelihood function maximum should be straightforward to locate at one of these peaks. The Bayes information criterion may then be calculated as in Chapter 2.

A preliminary application of this method to FARIMA time series with a DFA fluctuation plot that is known to be linear has indicated that $\approx 50$ % of such DFA fluctuation plots have been rejected. This may be an indication of the fact that DFA is a very poor technique for estimating the underlying Hurst exponent of time series, but we believe this is more likely a result of unsatisfied assumptions, or code implementation. Further work and exploration will be undertaken in this direction.

The conclusion regarding ML-DFA, notwithstanding the discussion here, is that it has proved useful in its present form and it is recommended that it be applied to validate the linear scaling of DFA fluctuation plots.

### 10.2.2 Amplitude and phase and synchronisation

In this thesis, DFA and ML-DFA have been applied to the amplitude envelope of individual neurophysiological time series, and to the rate of change of phase difference between two such time series. The provisional results for a small set of subjects in Chapters 3 suggested that LRTCs may be present in the amplitude envelope of EMG time series, and confirmed previous results for bandpass filtered EEG [28, 178]. The results of Chapter 8 additionally suggest that LRTCs are present at $\beta$ frequencies of MEG time series in the rate of change of phase difference between the motor cortices, at resting state.

Mathematically, the amplitude and phase are orthogonal properties of a complex number and the information that they provide about a time series does not overlap. Thus the amplitude of a neurophysiological time series provides an indication of the strength of its individual activity, and the phase indicates its speed and progress through time. The presence of LRTCs in an amplitude envelope would therefore suggest that the size of bandpass filtered neuronal activity is ordered, while LRTCs in the rate of change of phase difference between two time series suggests that the speed with which they adjust to each others rhythms is also a process ordered across time.

Computationally, however, phase and amplitude are known to become entangled in time series with a structure that is not a pure sinusoid [29, 243]. In analysis of neurophysiological time series, a bandpass filter was used to ensure that power in the signal existed

only in a narrow band, which meant that phase and amplitude were able to be separated. However, bandpass filtering may not always work well (see Section 1.1.6.8). Alternative methods for the separation of phase and amplitude components have been suggested, such as empirical mode decomposition and probabilistic amplitude and frequency demodulation [276, 277]. Furture analysis may lie in an exploration of these techniques and their application to the data used in this thesis.

Furthermore, the importance of both amplitude power [279] and phase [189] in modulating human responses to stimuli and ability to perform a task have been studied. In a recent study, a model in which phase information is supplemented by amplitude patterns is investigated and it is suggested that brain dynamics depend crucially on both the phase and the amplitude components of the neurophysiological signal [65]. This suggests that a future direction for modelling the presence of LRTCs in the time-varying interactions between brain regions might use a model that included both amplitude and phase components.

### 10.2.3 Limitation of DFA in relation to characterising interaction from phase difference

In the appendix to Chapter 6, the relationship between the DFA exponent of the rate of change of phase difference and the DFA exponents of the rate of change of the two individual phases was investigated. In order to investigate this question, the DFA exponents of two FARIMA time series with known true DFA exponents, were calculated and the difference of the FARIMA time series was taken. Each of the FARIMA time series provided a surrogate signal for the rate of change of phase. A surrogate for the rate of change of phase difference was then equivalent to the difference of the two FARIMA time series, by linearity. The 'new' DFA exponent of this time series was also determined. The DFA exponents of the original FARIMA time series and the 'new' exponent were compared.

It was shown that the 'new' DFA exponent was correlated with the larger of the two DFA exponents of the individual FARIMA time series, and was also judged to be valid by ML-DFA. A previous result by Hu et al. [129] suggests that the superposition of two FARIMA time series with different DFA exponents should lead to a DFA fluctuation plot with a crossover. However, the lack of a crossover may be a result of using the FARIMA time series to construct two surrogate signals following Section 8.3.2.1 rather than analysing the raw time series. The difference arises because the FARIMA time series is modulated by a cosine function and a nominal sampling rate is used, which smooth the crossover and shift it to a range outside that of the window range for which DFA is applied. The fact that no such crossover was detected by ML-DFA may suggest a limitation in its application.

A further investigation of the FARIMA time series suggested that the correlation between the maximum and the 'new' DFA exponents may become weaker when the amplitudes of the two time series are normalised prior to investigation. This suggested that the result was at least in part caused by the fact that a time series with a larger DFA exponent will have a larger magnitude of cumulative deviations from its mean, so that when the DFA exponent of the difference between two time series with different DFA exponents is calculated, then this difference will be dominated by the amplitude of the time series with the larger DFA.

In terms of physiology, a FARIMA time series is used as a model of the rate of change of phase difference between two neurophysiological signals. The latter result may therefore suggest that the presence of LRTCs in the rate of change of phase difference between two brain regions is strongly determined by the brain regions with the greatest DFA exponents in its individual rate of change of *phase*. Indeed, physiologically, it may be supposed that the interactions between two brain regions are dominated by the activity of the brain region with greater 'order' (larger DFA exponent) in the rate of change of its phase. This may be a mechanism by which one region of the human brain partially drives or imposes a structure on another region. A neurophysiological time series emerging from a brain region that has a rate of change of phase similar to white noise may in turn be more susceptible to being influenced by other brain regions and may not impose its own structure because it has no specific structure of its own to impose.

A different interpretation of these results is that, because of the very strong dominance of the maximum DFA exponent, a limitation is highlighted in the phase synchrony analysis method as a means of quantifying 'communication' between brain regions as opposed to an identification of the maximum DFA. If this is considered to be the case, then one potential avenue to explore in improving the method may be to consider applying DFA to the rate of change of a weighted difference between the phases of two neurophysiological time series. The use of a larger weight for the phase of a signal which had a lower DFA exponent of its rate of change may modify the amplitude deviations of the signal in such a way as to balance the influence of the two signals in our measure of time-varying synchronisation.

One possible question in this regard is how this weighting should be assigned. Would it be the case that a weighting should be purely related to the size of the DFA exponent of the rate of change of the individual phase? However, this may take a different value over time (see below) or be weighted by amplitude. On the other hand, an assignment of weights as a function of the 'true interaction' between brain regions would not be possible as this is precisely the information that we are trying to gain access to. These questions may provide fertile ground for future exploration.

### 10.2.4 Neurological noise

Investigation of the Kuramoto model using the phase synchrony analysis method indicated that its results could not be interpreted without a noise input to the process. Indeed, all other models studied in this thesis have had noise input at some level of the system. In the Cabral model, a white Gaussian noise term was added to the phase value at each stage of the evolution, and in the Ising model, the spin value taken by each element of the lattice was determined by a random process. The FARIMA time series used to generate surrogate time series are based on Gaussian white noise by construction. All of the above models or processes give rise to time series that yield valid DFA fluctuation plots for some parameter. Together, these points suggest that noise may play an important role in the emergence of LRTCs in the human brain.

The existence of noise in neurological processes has been documented extensively. It is well-known that the neuronal activity contains some noise fluctuations that do not necessarily give rise to neuronal firing or serve an obvious purpose to further information transfer [138]. It has also been observed that a particular neuron might respond differently to the same stimulus at different time points, which is in itself a form of noise. It has been suggested that neuronal noise is beneficial to the functioning of the nervous system, although it is not fully understood why this is the case [8, 181, 211, 287]

In this thesis, we have seen that the effects of noise can be different depending on where it is encountered in the system. For example, the results of Hu et al. [129] suggest that the sum of two FARIMA time series with different DFA exponents show a crossover in the fluctuation plot. We have also seen in Section 6.8 that noise added to the amplitude of a signal gave rise to an invalid DFA exponent with a low noise level. There is scope for further and systematic investigation of the variable locations of noise input and their relationship to the presence or absence of LRTCs both in the amplitude envelopes of time series and in the rate of change of phase difference.

### 10.2.5 Criticality in the brain

The critical brain hypothesis has recently attracted a great deal of attention [23, 54, 77, 158, 254, 261, 284]. The literature in favour of the critical brain hypothesis is dominated by the following results: the identification of power law distributions in neuronal avalanche sizes [23, 254], power law scaling functions [240] and power law decay of the autocorrelation function, measured using DFA, due to the presence of LRTCs [178, 230]. However, it is important to remember that power law distributions and power law statistics are not in themselves sufficient, or indeed necessary for criticality to be present [24, 233].

However, the work presented in this thesis may be viewed as additional evidence that LRTCs are indeed signatures of the critical state of a system, and as has been mentioned

throughout this thesis, the critical state of a system has been linked to a state of readiness to respond efficiently to incoming external stimuli.

In this regard, LRTCs, validated by ML-DFA, were found to be present in the rate of change of phase difference between time series derived from the Ising and Kuramoto models at and close to their critical parameters. They were also found to be present at the point of greatest change in $\Delta(Kr)$ in the Kuramoto and Cabral models, where the greatest change in order occurred in these systems as a function of the change in coupling parameter. Neither a theoretical critical parameter value nor a point of greatest transition in order is known for the human brain, so that the phase synchrony analysis method may have a role as a mathematical surrogate for criticality and change in order in the human nervous system.

### 10.2.6 Possible future directions for investigation

It is noted that the *peak* DFA exponent in the rate of change of phase difference of the Ising and Kuramoto models was not seen at the critical parameter, but at a parameter that indicated a transition towards a more disordered state such as that seen during finger tapping in MEG data. This may be evidence for the fact that although the resting state brain is in a state of readiness, it has not yet reached a point of 'greatest' readiness. A question may naturally arise as to where this point of 'greatest' readiness may occur physiologically.

One answer to the question of where the peak in DFA exponent lies may require a separation of the notions of 'readiness' and 'optimal information transfer' in criticality. The resting state may indeed be one in which the brain is ready to respond, but the point at which information transfer is optimal may be a slightly later one, specifically, precisely that one at which the neural network reorganises itself to allow the onset of a response or movement. This means that the greatest information transfer may occur in a short temporal window at the moment just before the response to a task is in fact actioned.

This answer may be an explanation for the relatively low value of DFA exponent seen in the rate of change of phase difference between the MEG motor cortex data during rest - namely, the DFA exponent in the resting state indicates that the system is ready to respond, but the DFA exponent will increase as the response occurs, or in practical terms at the point just before the actual onset of movement. As DFA requires a long time series in order to obtain a result, it may not be sensitive to such a short-lived change.

A recently developed technique (ATvDFA) allows for the DFA exponent to be calculated for time periods as short as ≈20 seconds [27]. ATvDFA was applied to the amplitude envelope of an EMG signal during a voluntary muscle contraction with steady and ramp

force conditions, which were directed by a visual cue. The results of this paper suggest that there is an increase in the DFA exponent of the amplitude envelope while the ramp force condition is being applied, and a decrease when a steady force condition is used.

In this light, it may be informative to apply ATvDFA in conjunction with ML-DFA to the rate of change of phase difference between two neurophysiological time series. However, it may also be the case that ≈20 seconds would be too long a period to characterise movement, in which case an alternative measure of order may be required. This may provide ground for future investigation.

My hypothesis with regard to such a study would be that the DFA exponent should show an increase at a point just before the onset of movement, followed by a decrease to 0.5 if the movement is ongoing such as a finger tapping action, or a decrease back to a DFA exponent indicating resting state if the movement is followed by a resting state. A task which involved a prolonged period of continuous, and unexpected response to stimuli may provide a framework that suited to testing this hypothesis more fully.

Furthermore, the provisional results indicating the presence of LRTCs in the rate of change of phase difference between EEG and EMG time series may suggest that a continuous muscle contraction would give rise to similar DFA exponents to those of resting state.

### 10.2.7 Connectivity and the critical range

In a recent paper by Moretti and Muñoz, it was suggested that brain network connectivity may give rise to a 'stretching' of the critical range whereby a range of parameters is considered to be critical [200]. The result of [200] was found for C. elegans and human connectivity structure. There are similarities between this result and the results of this thesis for the Cabral model. Specifically, the DFA exponent of the rate of change of phase difference shows several peaks. It was shown in the Appendix that this is also the case for the Cabral model with disconnected hemispheres at coupling values different to that of the peak change in order parameter for classical Cabral. It may be the case that the existence of a range of coupling values at which LRTCs can be attained reflects the fact that a brain with a disrupted connectivity may still be able to enter a state in which it may display readiness to respond [98].

It is therefore suggested that an adjustment of the 'coupling parameter' in the brain is a mechanism by which it can modify its state in the case of pathological disruption. It has been seen in this thesis that noise plays an important role in the emergence of LRTCs in systems, both in potentiating scale-free interactions (see Section 6.11) and in disrupting LRTCs when its level is increased (see Appendix for Chapter 6). It is possible that the 'coupling parameter' in itself is noisy, allowing for the nervous system to change or adjust this state [5]. The manifestation of such a coupling parameter in physiological

terms may arise from a number of sources including the interaction strength and relative timing of neuronal activity from different regions of the brain.

### 10.2.8 Pairwise and global measures of synchronisation

In Chapter 5, frequency distributions of phase-locked interval (PLI) and of the global lability of synchronisation (GLS) measures were examined as markers of criticality. It was found that while the PLI measure produced comparable frequency distributions in a critical and a non-critical model, the GLS measure was able to distinguish between these two systems. The results suggested that the GLS is a more informative measure in assessing criticality.

One important difference between these two measures is that the PLI may be calculated from pairs of time series, while the GLS is necessarily a global measure because it relies on counting the number of synchronised time series at at any time point.

While the GLS is straightforward to define in the Kuramoto model or the Cabral model of discrete oscillators, it is less clear how this should be done for neurophysiological signals. It is true that EEG, EMG and MEG signals are typically recorded from a discrete number of sensors, but it is not clear that the positions of these sensors are necessarily optimally located to record neuronal activity specific to particular brain regions or neuronal pools. It is likely that any recordings contain activity from a broad cortical area, the boundaries of which we are currently unable to define precisely. Furthermore, it is also not clear how sensors should be spaced on the cortical surface. If the sensors are too far away, then they may not provide a truly global measure. However, if sensors are too close, then they are likely to overlap in the neuronal activity that they record. Indeed, the beamforming technique was applied to MEG data precisely in order to minimise effects of cross-talk and isolate the electrical activity originating specifically from, in the present case, the motor cortex.

This also addresses a more general consideration of the difference between pairwise and global measures of synchronisation for the brain or the nervous system as a whole. Due to the moment-to-moment variations in neuronal firing and the dynamic interactions between neuronal pools, we would not expect synchronisation in the brain to be well-approximated by a single global metric. We might expect that a global synchronisation measure would be a blunter instrument in comparison to a pairwise measure.

One benefit of the phase synchrony analysis method in this regard is that it is a pairwise measure that does not make use of pooling or thresholds. However, a pertinent suggestion may be that neuronal pools do not only interact in a pairwise manner. A recently accepted paper reviews a range of bivariate and multivariate measures of synchronisation for EEG [139]. It would be an intriguing next step to the analysis presented in this thesis to assess the presence of LRTCs in multivariate synchronisation.

It may be noted that in the investigation of MEG data in Chapter 8, the presence of LRTCs was assessed in the rate of change of phase difference between only the left and right motor cortices. These brain regions were identified because we had aimed to investigate the effect of finger tapping on the resting state. The motor cortex was therefore a natural region on which to focus our investigation. However, it may be expected that movement is by far not the only activity that would disrupt LRTCs in the rate of change of phase difference between brain regions. It is therefore suggested that the motor cortices are not the only locations that are prone to such disruptions.

### 10.2.9 Possible future applications for the phase synchrony analysis method

The phase synchrony analysis method is straightforward to apply to neurophysiological time series such as EEG, MEG and EMG. Each of these recording techniques have different advantages over each other, and used collectively, they may be able to help us further understand the dynamics of the brain.

Although network disruptions have been investigated in the Cabral model, the effects of pathological modifications to empirical neurophysiological recordings have not been considered in this thesis. There is scope to make such an investigation in the future and the use of the phase synchrony analysis method in such an investigation would be of interest.

One non-invasive method that can be used to selectively alter the activity of specific brain regions is transcranial magnetic stimulation (TMS). The successful use of TMS was first recorded in 1985 [19]. It would be interesting to how disrupting or inducing activity in specific brain regions would affect the presence or absence of LRTCs in the rate of change of their phase difference with other regions. Relatively recently, it has become possible to perform TMS while recording EEG in such a way as to minimally disrupt the EEG signal [136]. The combination of these two techniques may have the potential to provide time series that can be analysed by the phase synchrony analysis method.

It has been argued that the results of this thesis suggest that the phase synchrony analysis method indicates the presence of LRTCs in the rate of change of phase difference between neurophysiological signals when the brain regions underlying these signals are in a state whereby they are ready to respond to each other. The phase synchrony analysis method thus provides a measure of the *potential* for change. Such a measure has the potential for future applications in assessing the extent to which a patient would be expected to respond to a drug or treatment. It may thus lay the ground for new and intriguing diagnostic approaches, with potential application in the medical field.

# Chapter 11

# Appendices

## 11.1 Chapter 2

In this section the results of analysis of FARIMA and sinusoidal time series that are 8000 samples in length are presented rather than the $100,000$ presented in the main chapter.

### 11.1.1 Simulations of shorter time series

Figures 11.1-11.3 show the results of ML-DFA applied to synthetic data of length 8000 samples. These figures can be compared to the equivalent figures included in the main chapter for the longer simulations. Here, the window sizes used to perform DFA are in the range of 8 to 800 samples. Tables 11.1 and 11.2 report the proportion of simulations, out of 1000, in which each of the models was found to be best fit, for FARIMA (1,$d$,1) processes and noisy sinusoidal signals.

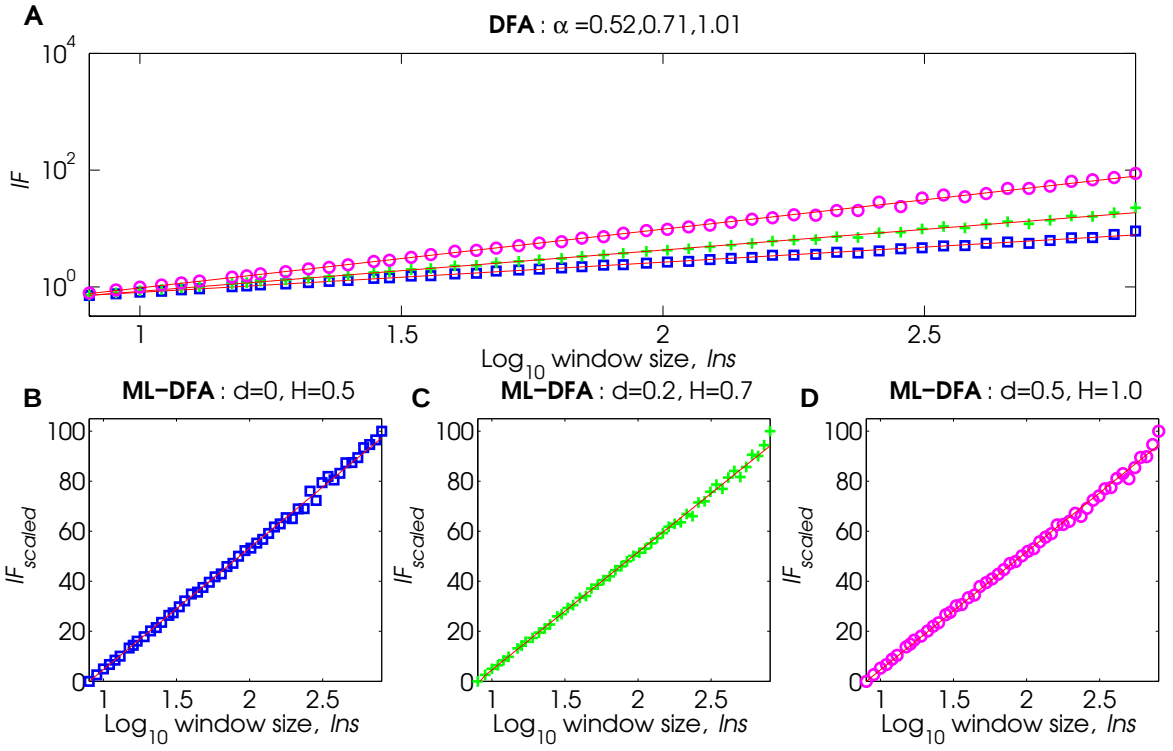


FIGURE 11.1: Simulated time series, containing 8000 innovations, and corresponding DFA fluctuation plots for signals obtained by FARIMA(0,$d$,0) processes with $\phi$ and $\theta$ set to 0 and with $d = 0$, and $d = 0.2$, and $d = 0.5$ to produce fractional Gaussian noise. Panel A shows the three DFA fluctuation plots fitted using standard DFA. Values $d = 0$, $d = 0.2$, and $d = 0.5$ will produce time series with Hurst exponents 0.5 (white noise, blue diamonds), 0.7 (correlated noise, green crosses) and 1 (pink noise, pink circles) respectively. The slopes estimated by application of standard DFA are stated at the top, and correspond closely to these theoretical values. Panels B-D show the best fit model according to the AIC measure in the ML-DFA technique. The best fit is linear in all cases. It is noted that, because the fluctuation plots have been scaled during application of the ML-DFA technique, the slopes of panels B-D are almost identical, and that this is the case for all ML-DFA plots.

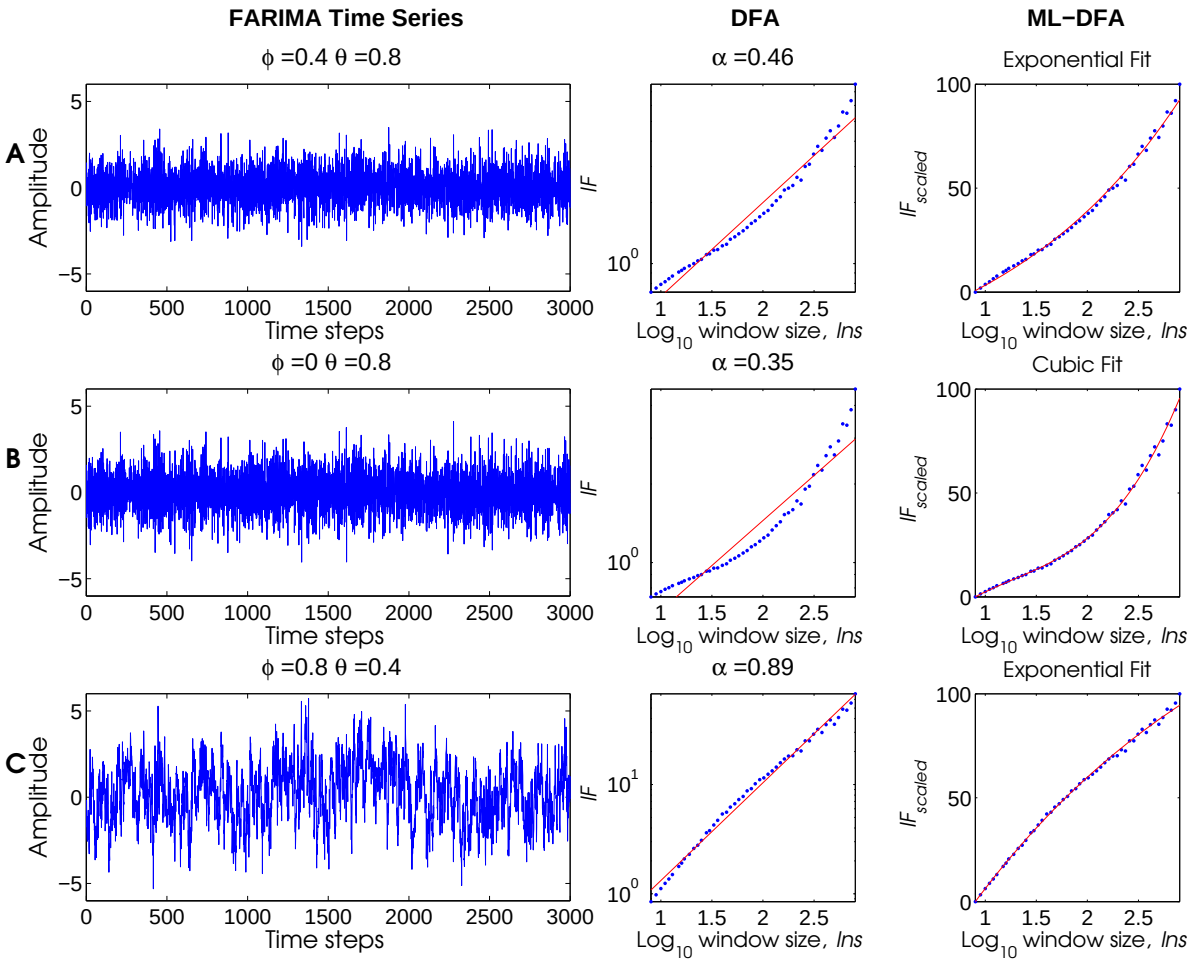


FIGURE 11.2: Simulated time series, containing 8000 innovations, and corresponding DFA fluctuation plots for signals obtained by FARIMA(1,0.2,1) processes with $d = 0.2$ taken as an representative value, and varying values of $\phi$ and $\theta$. Each row A-C corresponds to a different set of $\phi$ and $\theta$ coefficients, which alter the resulting DFA fluctuation plots. In each row, the left-hand panels show a representative 3000 innovations of the time series. The middle panels show the fluctuation plots fitted using the standard DFA technique, with a linear function, with the DFA exponent $\alpha$ given above. The right-hand panels show the application of the ML-DFA technique to the same fluctuation plots, with best fit function determined by the AIC measure.

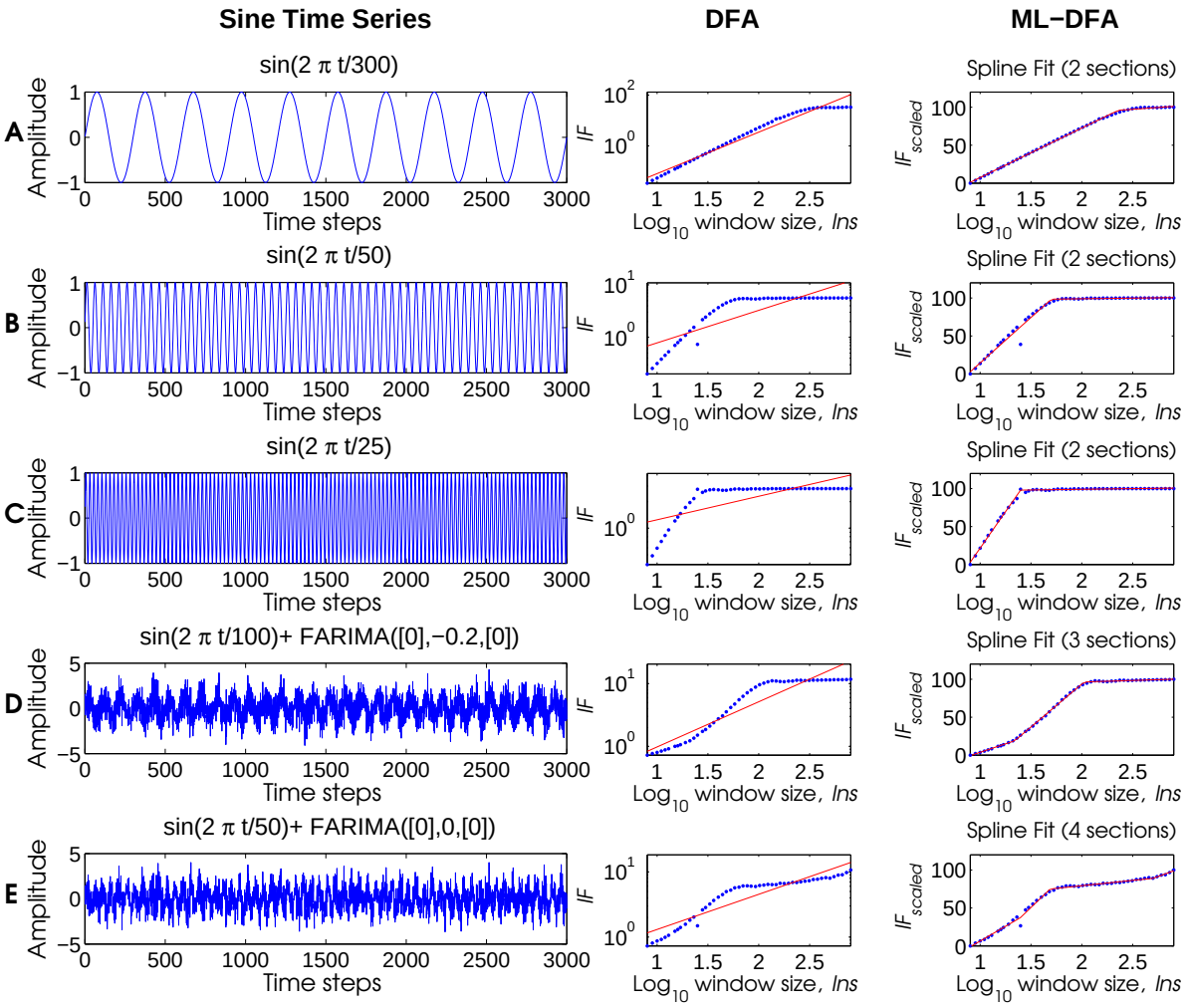


FIGURE 11.3: Simulated time series, containing 8000 innovations, and corresponding DFA fluctuation plots for 5 sinusoidal signals with varying levels of independent, additive noise. Each row A-E corresponds to a different sinusoidal function, with varying DFA fluctuation plots. In each row, the left-hand panels show a representative 3000 innovations of the time series. The middle panels show the fluctuation plots fitted using the standard DFA technique, with a linear function, with the DFA exponent $\alpha$ given above. The right-hand panels show the application of the ML-DFA technique to the same fluctuation plots, with best fit function determined by the AIC measure.

TABLE 11.1: ML-DFA results on synthetic data using AIC. From 1000 simulations of noise time series, the table gives the proportion of times that each of the alternative models was found to be the best fit, according to AIC values when ML-DFA was applied to fractional Gaussian noise, FARIMA(1,$d$,1) processes and noisy sinusoidal signals.

| | Linear | Non-linear | | | | | | | | | |
|---|---|---|---|---|---|---|---|---|---|---|---|
| Model | $x$ | $x^2$ | $x^3$ | $x^4$ | $x^5$ | $\sqrt[n]{x}$ | 4-$x$ | 3-$x$ | 2-$x$ | log | $e$ |
| FARIMA([0],0.5,[0]) | 95.9 | 3.9 | - | - | - | - | - | - | - | - | 0.2 |
| FARIMA([0],0.2,[0]) | 92.5 | 6.3 | - | - | - | - | - | - | - | - | 1.2 |
| FARIMA([0],0,[0]) | 79.7 | 17.1 | 0.1 | - | - | 0.7 | - | - | - | 0.4 | 2 |
| FARIMA([0.4],0.2,[0]) | 3.8 | 17.5 | 0.1 | - | - | 53 | - | - | - | 8.2 | 17.4 |
| FARIMA([0],0.2,[0.4]) | - | 93 | 0.3 | - | - | - | - | - | 1.1 | - | 5.6 |
| FARIMA([0.8],0.2,[0]) | 0.1 | 9.8 | - | - | - | 42.4 | - | - | - | 12.7 | 35 |
| FARIMA([0],0.2,[0.8]) | - | - | 62.7 | 0.4 | - | - | - | - | 22.8 | - | 14.1 |
| FARIMA([0.4],0.2,[0.8]) | - | 0.2 | 22 | 0.3 | - | - | - | - | 28.2 | - | 49.3 |
| FARIMA([0.8],0.2,[0.4]) | - | 46.6 | - | - | - | 18.7 | - | - | - | 0.5 | 34.2 |
| FARIMA([0],-0.2,[0])+sin($\frac{2\pi t}{100}$) | - | - | - | - | - | - | - | 100 | - | - | - |
| FARIMA([0],0,[0])+sin($\frac{2\pi t}{50}$) | - | - | - | 0.1 | 16.2 | - | 83.3 | - | 0.4 | - | - |

The fitted models are listed in the top row, alongside the proportion of best fits assigned to each one by the value of the AIC measure. The shorthand n-$x$ is used to denote a n-segment spline. The shorthand $\sqrt[n]{x}$ combines results for $n = 2, 3, 4$. The signals whose DFA fluctuation plots are analysed are described in the left-hand side column.

TABLE 11.2: ML-DFA results on synthetic data using BIC. From 1000 simulations of noise time series, the table gives the proportion of times that each of the alternative models was found to be the best fit, according to BIC values when ML-DFA was applied to fractional Gaussian noise, FARIMA(1,$d$,1) processes and noisy sinusoidal signals.

| | Linear | Non-linear | | | | | | | | | |
|---|---|---|---|---|---|---|---|---|---|---|---|
| Model | $x$ | $x^2$ | $x^3$ | $x^4$ | $x^5$ | $\sqrt[n]{x}$ | 4-$x$ | 3-$x$ | 2-$x$ | log | $e$ |
| FARIMA([0],0.5,[0]) | 96.1 | 3.7 | - | - | - | - | - | - | - | - | 0.2 |
| FARIMA([0],0.2,[0]) | 94.7 | 4.8 | - | - | - | - | - | - | - | - | 0.5 |
| FARIMA([0],0,[0]) | 89 | 10.1 | - | - | - | 0.2 | - | - | - | 0.2 | 0.5 |
| FARIMA([0.4],0.2,[0]) | 20.1 | 12.3 | - | - | - | 49.7 | - | - | - | 5.2 | 12.7 |
| FARIMA([0],0.2,[0.4]) | 0.1 | 94.2 | 0.1 | - | - | - | - | - | - | - | 5.6 |
| FARIMA([0.8],0.2,[0]) | - | 9.8 | - | - | - | 42.4 | 0.1 | - | - | 12.7 | 35 |
| FARIMA([0],0.2,[0.8]) | - | - | 30.2 | - | - | - | - | - | 13.6 | - | 56.2 |
| FARIMA([0.4],0.2,[0.8]) | - | 0.2 | 10.8 | - | - | - | - | - | 4.9 | - | 84.1 |
| FARIMA([0.8],0.2,[0.4]) | - | 46.6 | - | - | - | 18.7 | - | - | - | 0.5 | 34.2 |
| FARIMA([0],-0.2,[0])+sin($\frac{2\pi t}{100}$) | - | - | - | - | - | - | - | 100 | - | - | - |
| FARIMA([0],0,[0])+sin($\frac{2\pi t}{50}$) | - | - | - | 0.1 | 40.5 | - | 21.8 | - | 37.6 | - | - |

The fitted models are listed in the top row, alongside the proportion of best fits assigned to each one by the value of the BIC measure. The shorthand n-$x$ is used to denote a n-segment spline. The shorthand $\sqrt[n]{x}$ combines results for $n = 2, 3, 4$. The signals whose DFA fluctuation plots are analysed are described in the left-hand side column.

The reader will observe that the noisy sinusoidal signals have been altered to a different frequency. This is because, as noted in the main chapter, the oscillation frequency is closely associated with the location of the crossover in the DFA fluctuation plot, and this crossover would need to be within the range of window sizes for which DFA is performed in order to be analysable. For this reason, the two noisy sinusoidal time series have been altered to be FARIMA([0],-0.2,[0])+sin($\frac{2\pi t}{100}$) and FARIMA([0],0,[0])+sin($\frac{2\pi t}{50}$).

The proportions of simulations for which the linear model hypothesis is rejected or selected are very similar to those reported in the simulations with 100,000 innovations. Both AIC and BIC measures are less effective in fitting the FARIMA([0],0,[0]) time series to a linear model as there is indeed more stochastic variation in this (much) shorter time series. The AIC measure still shows that 79.7% of the fluctuation plots are best fit by a linear model, while the BIC measure returns a proportion of 89%.

The DFA fluctuation plot corresponding to the FARIMA([0],0,[0])+sin($\frac{2\pi t}{50}$) time series also shows a reduced proportion of simulations that were best fit by the four-segment spline model, which [129] showed to be the characteristic shape of the fluctuation plot. The AIC measure found that 83.3% of simulations were best fit by the four-segment spline model, while the corresponding figure for the BIC measure was 21.8%. The AIC measure therefore performs closer to our expectations in short simulations of noisy sinusoidal signals, thus supporting our recommendation in the main chapter.

The reader may note that, unlike in the main chapter, Tables 11.1 and 11.2 include the quintic model. This does not interfere with the likelihood of the linear model hypothesis being rejected. When performing the analysis without allowing the quintic model as a possible alternative model, those fluctuation plots that had been best fit by the quintic

model, were found to be best fit by the four-segment spline (in 154 cases out of 162), or by the two-segment spline (in 8 out of 162 cases) instead. Indeed, in all analyses that contributed to the results previously presented in the main chapter, the quintic model was included as a model to be tested. However, because no simulation of a signal was found to be best fit by a quintic model, it was not listed in the final tables presented.

Whilst it is possible in principle that the selection of models could affect the likelihood that the linear model hypothesis be accepted/rejected, the results suggest that this is very unlikely to occur due to the existing bias towards the linear model hypothesis (it having fewer parameters than most candidate models). Furthermore, it has been consistently emphasised that the results should be interpreted in terms of the linear model hypothesis not being rejected rather than the linear model hypothesis being accepted.

### 11.1.2 Hurst's Nile Data

In this section, the DFA technique is applied to the data that Hurst originally studied (see Section 1.1.8.3). This data consists of a time series of the minimum level of the River Nile between the years 622 and 1281 A.D.. DFA and ML-DFA are applied to the time series.

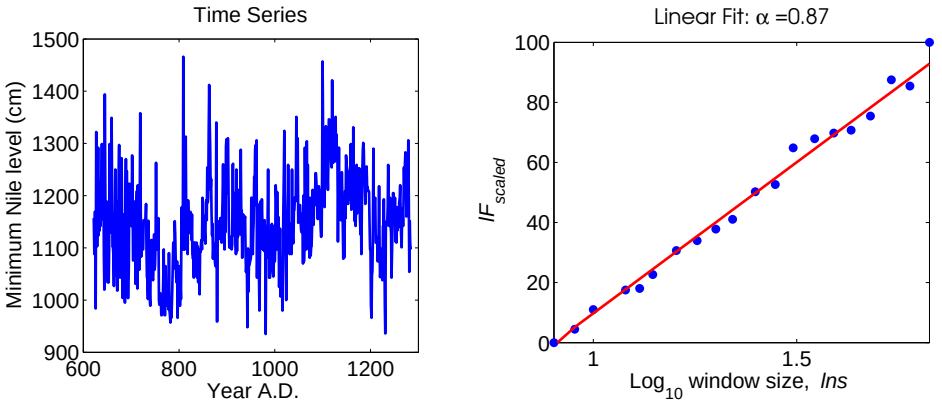


FIGURE 11.4: The annual minimum water levels of the Nile River at the Roda Gauge (622-1281 A.D.) alongside the DFA of this time series with a minimum window size of 8 data points, and a maximum of 66.

Happily, a DFA exponent of $\approx 0.85$ is obtained and a plot accepted to be linear by ML-DFA.

## 11.2 Chapter 4

### 11.2.1 Physiological Data

#### 11.2.1.1 Subjects rejected by BIC

Here, the DFA fluctuation plots of the subjects (4/20) for which the linear model was rejected by the BIC measure are shown and Figure 11.5 is produced, which contains these fluctuation plots. It was chosen not to include this figure in the main chapter because the results presented throughout the main chapter support the assertion that the AIC measure is in general more accurate at selecting the model that is (theoretically) expected to best fit the fluctuation plots of tested functions. Indeed, this is further confirmed by applying ML-DFA to shorter synthetic data of length 8000 innovations (see previous section), and by analysing noisy FARIMA signals (included in the main chapter). In the absence of compelling evidence for the benefit of BIC, it is not felt to be appropriate to include these figures.

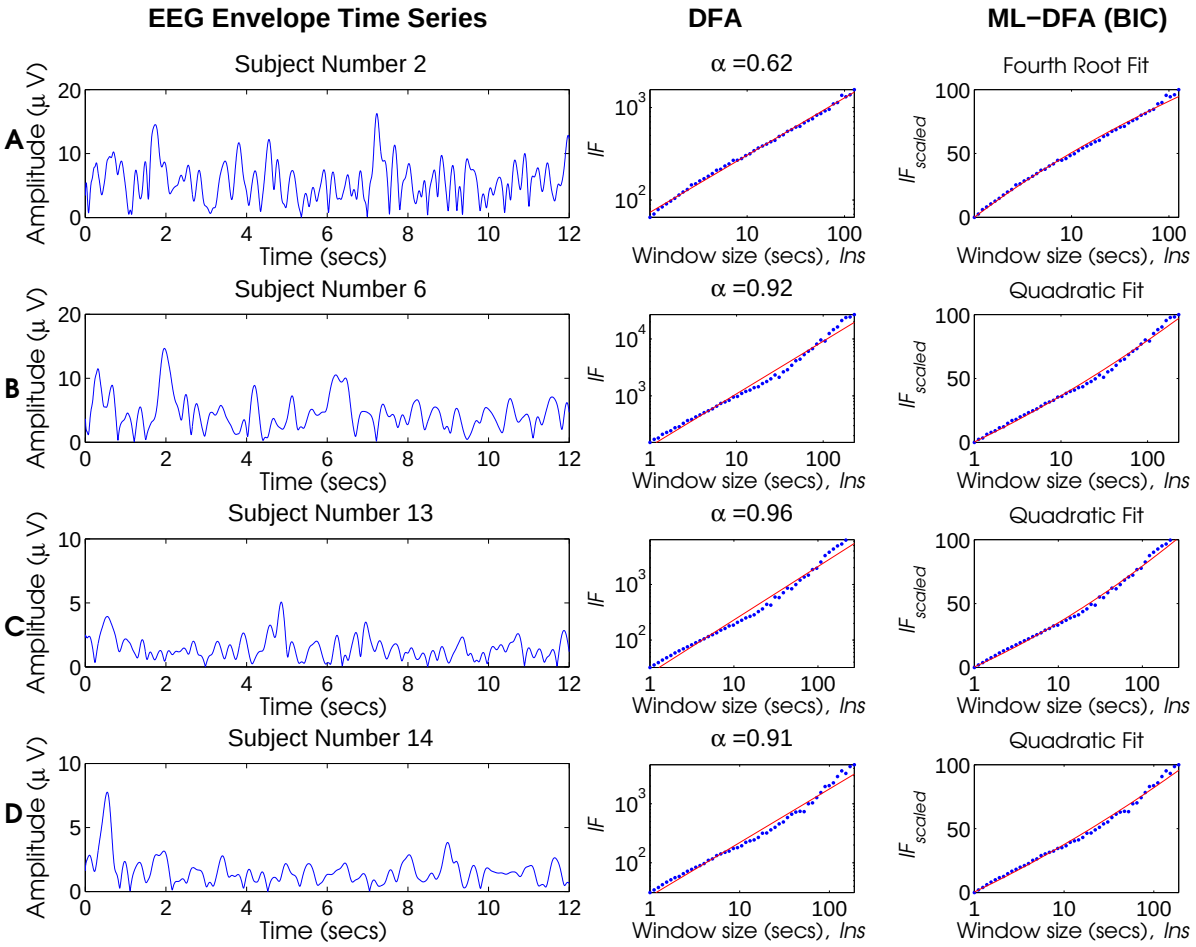


FIGURE 11.5: DFA fluctuation plots for 4 example signals from the Cz electrode of the EEG recording used in the main chapter. Specifically, the 4 rows A-D correspond to subjects 2,6,13,14. In each row, the left-hand side panel shows a representative 12 seconds of the time series, the middle panel shows the fluctuation plot fitted using standard DFA with the DFA exponent $\alpha$ given above each plot, and the right-hand side panel shows the best fit model as determined by ML-DFA using BIC.

#### 11.2.1.2 Short Time Scales

Here, the short time scales (0.1-1s) of the fluctuation plots are shown, where the filter-integration effect shows up. Figure 11.6 was produced, where these time scales are presented for a selection of 3 subjects used in the main chapter, namely subjects 2, 3 and 13. The reader will observe that the filter integration effect is very evident in the DFA fluctuation plot for time scales smaller than 100 samples, which is equivalent to approximately half a second of time.

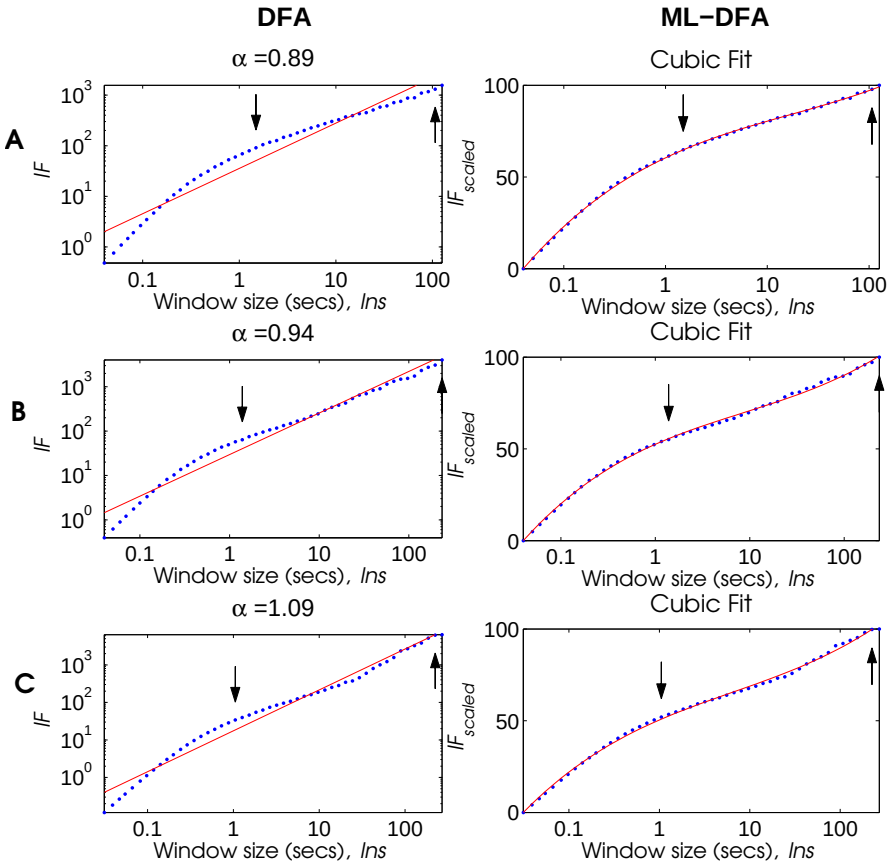


FIGURE 11.6: DFA fluctuation plots when different window lengths are used to analyse the Cz electrode signal of the EEG recording used in the main chapter for subjects 2,3 and 13. The minimum window length is 8 time steps ($\frac{8}{256} \approx 0.031$ seconds) and the maximum window length is $\frac{N}{10}$, or 187 seconds throughout. All panels show the DFA and ML-DFA analysis. Panel A shows subject 2, panel B shows subject 3 and panel C shows subject 13. In each row, the left-hand panels show the fluctuation plots fitted using the standard DFA technique, with a linear function, with the DFA exponent $\alpha$ given above each plot. The right-hand panels show the same fluctuation plots alongside the best fit function, as determined by the AIC values of the ML-DFA technique.

This figure is not included in the body of the main chapter because the short time scales presented in Figure 11.6 are also shown in Figure 8 of the main chapter in the case of one particular subject, and the appearance of the fluctuation plots in these short time scales, and the position at which the filter effect begins to be evident are very consistent across subjects.

### 11.2.2 Additional Data Set

An additional data set has also been analysed. Specifically, the clean signals available for download from the Neurophysiological Biomarker Toolbox website (http://www.nbtwiki.net/) have been studied. However, as we are not setting out to explore changes

in maintenance or loss of scaling or change in DFA exponent between two conditions or subject groups, this analysis is not included in the main chapter.

The signals were bandpass filtered between 8 and 13 Hz, consistent with the main chapter, and signals recorded both during the eyes closed and the eyes open conditions, were studied. The ML-DFA technique was then applied using the DFA window size settings of [178], namely, the minimum window size was of length five seconds, and the largest was one quarter of the full length of the data. In this case, the time series were between 239 and 291 seconds in length, making the largest window size between 59.75 and 72.75 seconds. The full set of 16 subjects available from this source was studied. Table 11.3 reports the models found to be the best fit for each DFA fluctuation plot. The proportion of subjects for which the linear model hypothesis was rejected is comparable to that obtained for the data collected and presented in the main chapter. In particular, in the eyes closed condition, 7/16 (AIC) and 9/16(BIC) were not rejected. In the eyes open condition 8/16(AIC) and 8/16 (BIC) were not rejected. Figures 11.7 and 11.8 show a selection of subjects from these data sets. In particular, subjects 1, 3, 7 and 13 are shown because they show a selection of different best-fit models using the AIC measure.

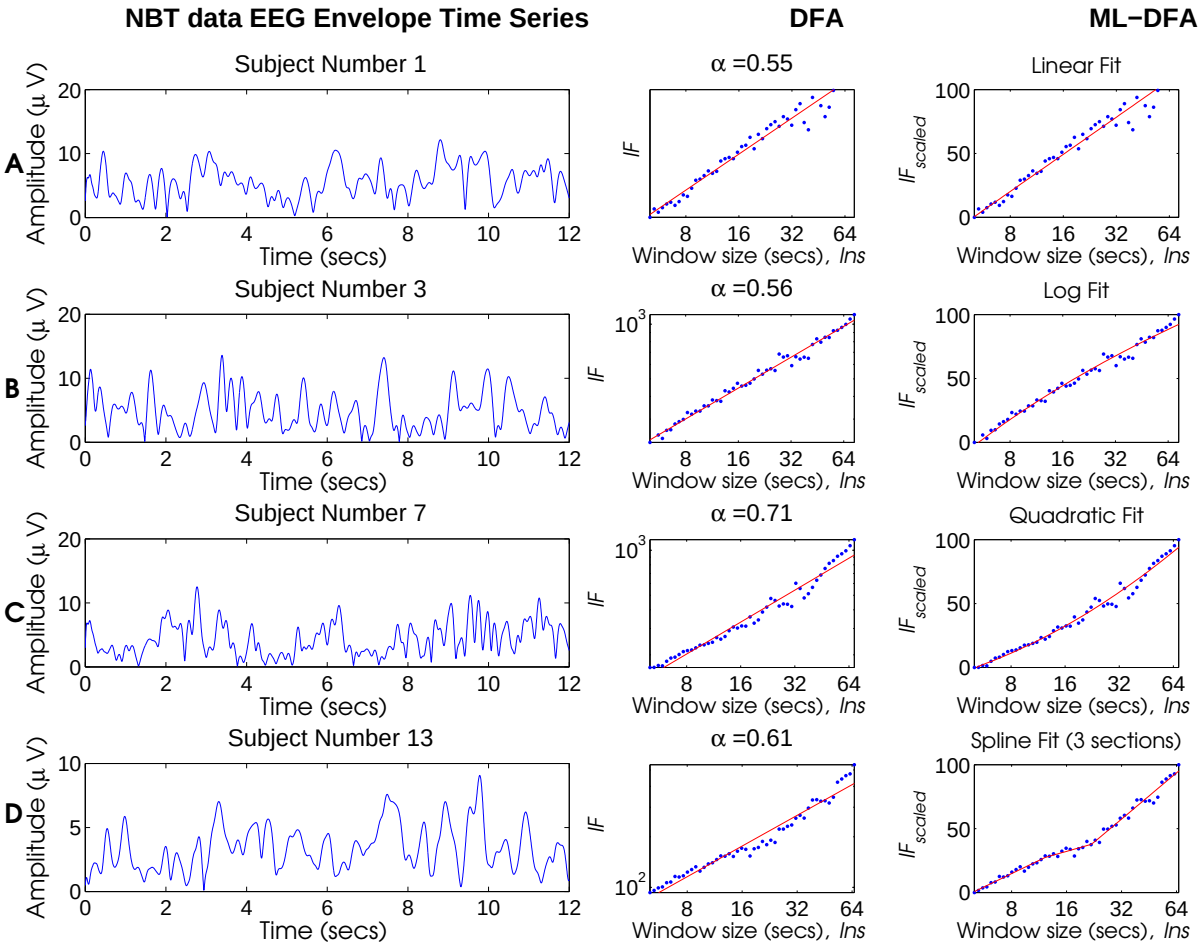


FIGURE 11.7: DFA fluctuation plots for 4 example signals taken from the NBT website (http://www.nbtwiki.net/) for the Cz electrode (channel 129) of an EEG recording made during resting state with eyes closed. Specifically, the 4 rows A-D correspond to subjects 1,3,7,13. In each row, the left-hand side panel shows a representative 12 seconds of the time series, the middle panel shows the fluctuation plot fitted using standard DFA with the DFA exponent $\alpha$ given above each plot, and the right-hand side panel shows the best fit model as determined by ML-DFA using AIC.

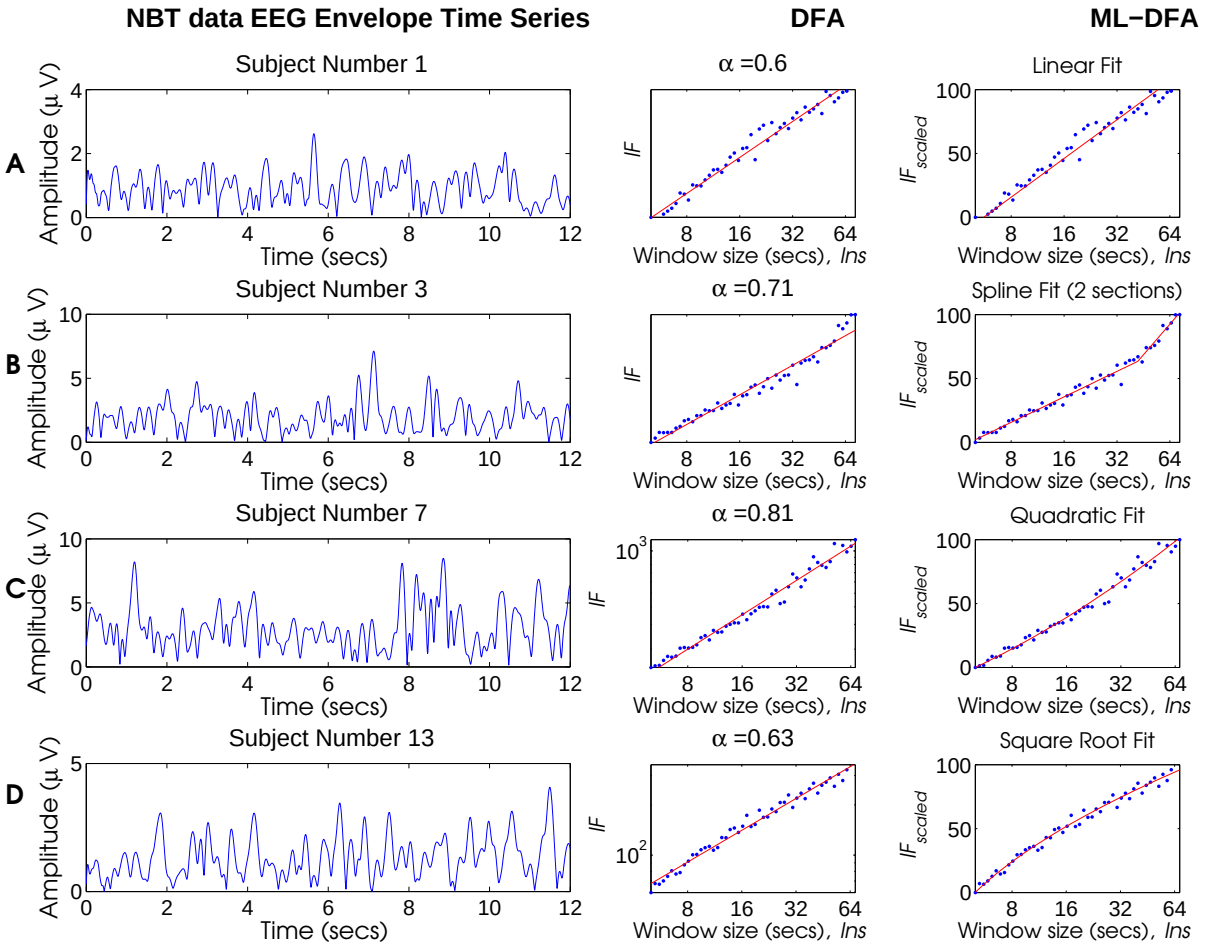


FIGURE 11.8: DFA fluctuation plots for 4 example signals from the NBT website (http://www.nbtwiki.net/) for the Cz electrode (channel 129) of an EEG recording made during resting state with eyes open. Specifically, the 4 rows A-D correspond to subjects 1,3,7,13. In each row, the left-hand side panel shows a representative 12 seconds of the time series, the middle panel shows the fluctuation plot fitted using standard DFA with the DFA exponent $\alpha$ given above each plot, and the right-hand side panel shows the best fit model as determined by ML-DFA using AIC.

TABLE 11.3: Results of ML-DFA with the EEG signal obtained from the Cz electrode (channel 129) in 16 healthy subjects during a resting state task recorded with eyes closed and eyes open (data downloaded from the Neurophysiological Biomarker Toolbox website).

| | Eyes Closed | | | Eyes Open | | |
|---|---|---|---|---|---|---|
| Subject | Slope | AIC | BIC | Slope | AIC | BIC |
| 1 | 0.554 | Linear | Linear | 0.600 | Linear | Linear |
| 2 | 0.658 | Linear | Linear | 0.693$^{\dagger}$ | Quadratic | Quadratic |
| 3 | 0.565$^{\dagger}$ | Logarithmic | Logarithmic | 0.709$^{\dagger}$ | Two-segment spline | Two-segment spline |
| 4 | 0.661$^{\dagger}$ | Quadratic | Linear | 0.519 | Linear | Linear |
| 5 | 0.798$^{\dagger}$ | Square Root | Square Root | 0.709 | Linear | Linear |
| 6 | 0.699$^{\dagger}$ | Logarithmic | Logarithmic | 0.718 | Linear | Linear |
| 7 | 0.710$^{\dagger}$ | Quadratic | Quadratic | 0.811$^{\dagger}$ | Quadratic | Quadratic |
| 8 | 0.871 | Linear | Linear | 0.693$^{\dagger}$ | Logarithmic | Logarithmic |
| 9 | 0.643$^{\dagger}$ | Fourth Root | Linear | 0.522$^{\dagger}$ | Quadratic | Quadratic |
| 10 | 0.788 | Linear | Linear | 0.620 | Linear | Linear |
| 11 | 0.740 | Linear | Linear | 0.934 | Linear | Linear |
| 12 | 0.732$^{\dagger}$ | Quadratic | Quadratic | 0.722$^{\dagger}$ | Quadratic | Quadratic |
| 13 | 0.607$^{\dagger}$ | Three-segment spline | Two-segment spline | 0.633$^{\dagger}$ | Square Root | Square Root |
| 14 | 0.628 | Linear | Linear | 0.780 | Linear | Linear |
| 15 | 0.690$^{\dagger}$ | Logarithmic | Logarithmic | 0.752$^{\dagger}$ | Square Root | Square Root |
| 16 | 0.784 | Linear | Linear | 0.678 | Linear | Linear |

Each subject is identified by number in the left-hand side column, alongside the best fit model determined by ML-DFA using AIC and BIC. The $^{\dagger}$ symbol indicates those subjects whose fluctuation plots were rejected as not being linear by at least one of the AIC or BIC measures. When the fluctuation plot is rejected by BIC, it is also rejected by AIC in all cases. The exponents provided in columns 2 and 5 were obtained using standard DFA.

The reader's attention is also drawn to the fluctuation plots of subject number 1, which, both in the eyes open and eyes closed condition, are not visually convincing as linear. However, ML-DFA finds that the linear model is the best fit. It is suggested that this plot is a specific example of the bias that ML-DFA will place in favour of the linear model.

## 11.3 Chapter 5

### 11.3.1 Analytic Derivation of $\triangle_{ij}$

The analytical solutions for $\triangle_{ij}$, the difference between phases $\phi_i$ and $\phi_j$ of oscillators $i$ and $j$, are distinct for the two cases $\frac{K}{\omega_i - \omega_j} > 1$ and $\frac{K}{\omega_i - \omega_j} < 1$ where $\omega_i$ and $\omega_j$ are the respective natural frequencies of oscillators $i$ and $j$, and $K$ is the coupling added globally to the system. Equation 5.5 can be rearranged to obtain the following integral:

$$\int dt = \int \frac{d\triangle}{(\omega_i - \omega_j) - K\sin(\triangle_{ij})}$$

where $t$ denotes time. This integral can be solved using the standard substitution of $x = \tan\left(\frac{\triangle_{ij}}{2}\right)$.

Doing so, and letting $C = \frac{K}{(\omega_i - \omega_j)}$, we get:

$$\int dt = \frac{2}{(\omega_i - \omega_j)} \int \frac{dx}{\left(1 - C^2 + (x - C)^2\right)} \tag{11.1}$$

There are two different scenarios for this integral, depending on whether $C < 1$ and $\sqrt{1 - C^2}$ is a real or imaginary number. Each case is dealt with in turn.

#### 11.3.1.1 If $C < 1$, or when coupling is smaller than the difference in natural frequency

We can rearrange 11.1 in terms of $\sqrt{1 - C^2}$ which is real and:

$$\int dt = \frac{2}{(\omega_i - \omega_j)(1 - C^2)} \int \frac{dx}{\left(1 + \left(\frac{x - C}{\sqrt{1 - C^2}}\right)^2\right)}$$

We can solve this integral using the fact that $\tan^{-1}(z) = \int \frac{dz}{1+z^2}$ to get:

$$t = \frac{2}{(\omega_i - \omega_j)\sqrt{(1 - C^2)}} \left[ \tan^{-1} \left( \frac{\tan\left(\frac{\triangle_{ij}}{2}\right) - C}{\sqrt{1 - C^2}} \right) - \tan^{-1} \left( \frac{\tan\left(\frac{\triangle_{ij}^0}{2}\right) - C}{\sqrt{1 - C^2}} \right) \right] \tag{11.2}$$

Here, $\triangle_{ij}^0$ is the value of $\triangle_{ij}$ at time $t = 0$, i.e., the initial difference in phase between oscillators $i$ and $j$.

Setting $D = \frac{2}{(\omega_i - \omega_j)\sqrt{(1 - C^2)}} \tan^{-1} \left( \frac{\tan\left(\frac{\triangle_{ij}^0}{2}\right) - C}{\sqrt{1 - C^2}} \right)$ we can rearrange Equation 11.2 to get:

$$\triangle_{ij} = 2\tan^{-1} \left( \left(\sqrt{1 - C^2}\right) \tan\left( \frac{(t - D)\,(\omega_i - \omega_j)\sqrt{(1 - C^2)}}{2} \right) + C \right)$$

#### 11.3.1.2 If $C > 1$, or when coupling is larger than the difference in natural frequency

Here, $\sqrt{1-C^2}$ is imaginary, so we rearrange 11.1 in terms of $\sqrt{C^2-1}$:

$$\int dt = \frac{2}{(\omega_i - \omega_j)(1-C^2)} \int \frac{dx}{\left(1 - \left(\frac{x-C}{\sqrt{C^2-1}}\right)^2\right)}$$

We can solve this integral using the fact that $\frac{1}{2}\left(\log^{-1}(-z-1) - \log^{-1}(z-1)\right) = \int \frac{dz}{1-z^2}$:

$$t = \frac{-1}{(\omega_i - \omega_j)\sqrt{(C^2-1)}} \log\left[A\left(\frac{1+y}{1-y}\right)\right]$$

where $A = \frac{1-y^0}{1+y^0}$ and $y^0$ is the value of $y$ at time $t = 0$.

This can be rearranged to yield:

$$\triangle_{ij} = 2\tan^{-1}\left[\sqrt{C^2-1}\left(\frac{e^{-t(\omega_i-\omega_j)\sqrt{(C^2-1)}} - A}{A + e^{-t(\omega_i-\omega_j)\sqrt{(C^2-1)}}}\right) + C\right]$$

## 11.4 Chapter 6

### 11.4.1 Surrogate Data

In the phase synchrony analysis method, DFA is applied to the rate of change of phase difference between two signals, however, it is also possible to apply DFA to the rate of change of the phase of a single time series. Analysis of rates of change of individual phases yields exponents that are in the same range of values as those of the rate of change of phase difference (not presented). The question then arises as to whether there is a relationship between the DFA exponents of the rates of change of the individual phases, and the DFA exponent of the rate of change of the resulting phase difference.

In other words, if we were to take one signal with a DFA exponent $\gamma_1$ in the rate of change of phase and another with a DFA exponent of $\gamma_2$ in the rate of change of phase, then what would be the DFA of the rate of change of their difference $\gamma_{new}$? It has previously been discussed that a FARIMA process can be used to generate time series with a known DFA exponent (Section 1.1.8.8). A FARIMA process may therefore be used to simulate two time series that are surrogate signals for the two time-varying rates of change of phase with DFA exponents $\gamma_1$ and $\gamma_2$, respectively. The question then remains how we can calculate the rate of change of their phase difference when we do not have the phases, but only their rate of change. However, by linearity, the rate of change

of phase difference is the same as the difference in the rates of change. Therefore, to calculate $\gamma_{new}$, it is necessary to take the difference of the two time series and apply DFA to this difference. The time series themselves could be reconstructed from the FARIMA time series (their rates of change of phase) by the procedure described in Section 8.3.2.1.

Specifically, 100 pairs of FARIMA time series of length $N = 100000$ innovations were generated with all the unique pairings of non-identical DFA exponents from the set $\{0.5, 0.55, 0.6, ...1.0\}$. This created $55 \times 100$ pairs of time series which represented the rates of change of phase difference. The surrogate neurophysiological signals themselves were then constructed using the procedure described in Section 8.3.2.1. The phase synchrony analysis method was then applied to these signals to recover $\gamma_{new}$, which will also be referred to as the 'new' DFA exponent here. The minimum window used for DFA was 600 innovations which was used as a nominal sampling frequency for these time series as described in Section 8.3.2.1. The maximum windows size was a tenth of the length of the data $N$, which consisted of 10000 innovations, or 16 seconds.

The DFA exponent of each of these FARIMA time series was also computed. The larger of the DFA exponents is referred to as the 'maximum' exponent here and the smaller of the two is referred to as the 'minimum' exponent.

A scatter plot of the maximum and the new DFA exponent is displayed in Figure 11.9 and a scatter plot of the minimum and the new DFA exponents is displayed in Figure 11.10. It may be observed that the relationship between the maximum and the new DFA exponents is close to being linear, while that of the minimum and new DFA exponents has no evident pattern. In particular, a given minimum DFA exponent can give rise to a new DFA exponent that belongs to the full range of exponents $\gamma \in [0.5, 1]$. On the other hand, the maximum DFA exponent is seen to be strongly related to the value of the new exponent.

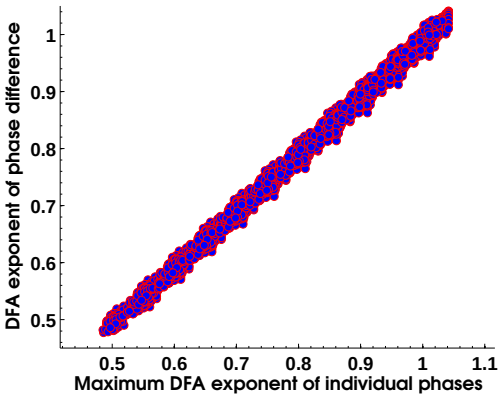


FIGURE 11.9: The relationship between the difference in DFA exponents of the individual phases and the maximum DFA exponent in contributing to the DFA exponent of their phase difference.

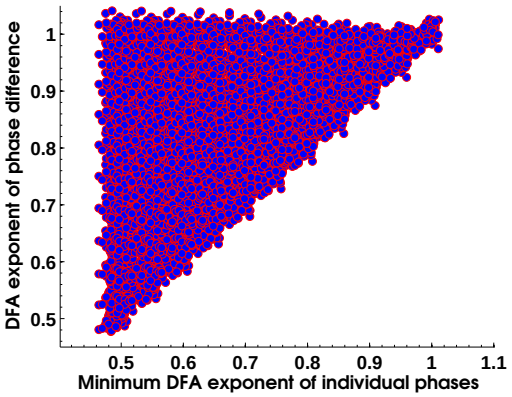


FIGURE 11.10: The relationship between the difference in DFA exponents of the individual phases and the minimum DFA exponent in contributing to the DFA exponent of their phase difference.

One explanation for this observation may come from the fact that FARIMA time series with a larger DFA exponent will tend to also have larger amplitude. This is because at each innovation of a time series with a DFA exponent $\gamma > 0.5$, a value that is greater than the mean is progressively more likely to be followed by another value that is greater than the mean, with increasing DFA exponent. The cumulative deviations from the mean will therefore be greater for time series with a larger DFA exponent.

For this reason, the effect of normalising the amplitude and standard deviation of the time series is also investigated on the relationship between the minimum, maximum and new exponents. Specifically, the mean of the time series was subtracted at each innovation and the resulting value was divided by the standard deviation of the time series.

Figure 11.11 shows a scatter plot of the maximum DFA exponent with the new DFA exponent and Figure 11.12 shows a scatter plot of the minimum and the new DFA exponent after the FARIMA time series were normalised.

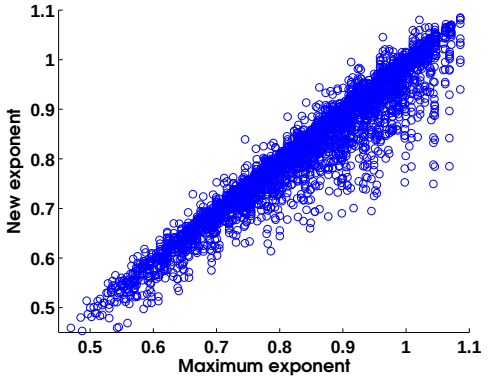


FIGURE 11.11: A scatter plot of the maximum of the DFA exponents of two normalised FARIMA time series against the DFA exponent of the rate of change of difference between the FARIMA time series

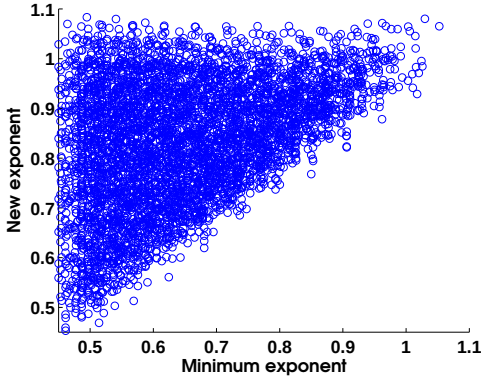


FIGURE 11.12: A scatter plot of the minimum of the DFA exponents of two normalised FARIMA time series against the DFA exponent of the rate of change of the difference between the FARIMA time series

The relationship between the maximum and the new DFA exponents is less well-defined when the time series was previously normalised, suggesting that the value of the minimum DFA exponent has more influence on the new DFA exponent in this case. In particular, when the maximum DFA exponent was high and equal to $\approx 1$, the new exponent could take a range of values from $\approx 0.7$ and above, suggesting that some combination of the two underlying time series was transferred onto the value of the new DFA exponent.

In interpreting results of the phase synchrony analysis method, there are two possible scenarios that we may consider. The first is that the two time series that we are analysing are completely independent, such as two FARIMA time series. If this is the case, then it is possible to determine whether the DFA exponents of these two time series are similar to each other by applying DFA to them separately. If these exponents are not identical or similar to each other, then the recent paper by Hu et al. demonstrates that the DFA fluctuation plot of the sum or difference between these two time series should contain a crossover. Such a crossover should be detected by ML-DFA, and if it is not then, the

stringency of this method may need to be altered. The possible routes for future work in this line will be discussed in the general discussion of this thesis. The necessity of a robust and trustworthy estimate of the DFA exponent is emphasised by this observation. On the other hand, if application of DFA shows that the exponents of the two time series are very similar, then it may be possible to apply alternative techniques such as those of mutual information to determine the independence between them.

Importantly, due to the extensive inter-connectivities between neurons in the human nervous system, it would be difficult to assert definitively that two neurophysiological time series were completely independent. Indeed, regardless of how geometrically distant two regions brain are, as long as they belong to the same nervous system, it is likely that there will be some mutual influence between their respective neuronal activity. Therefore the scenario of two independent time series may not be a realistic one for two time series from a single nervous system.

The second scenario concerns the case of the two time series being analysed are not independent of each other. In this situation, there will, by definition, be some synchronisation between the underlying time series, and the exponent obtained from applying the phase synchrony analysis method will then reflect some degree of communication. The question is whether the DFA exponent obtained would be biased by the DFA exponents of the two individual time series. In this case, it may be possible to apply a normalisation scheme to the time series before using the phase synchrony analysis method. More detail on the possible routes for such a scheme will be given in the general discussion of this thesis. This will be presented alongside further neurophysiological implications of these results in relation to characterising interactions from phase difference.

### 11.4.2 The Ising Model

Results for the sub-lattices of size $8 \times 8$ were shown in the main chapter. A small sub-lattice size permits a greater range of distances between sub-lattices to be studied. This means that long-range correlations between pairs of time series may be more likely to exist. One problem of using very small sub-lattices, however, is that the time series is then created by taking an average of a very small number of spins of value $+1$ or $-1$ (see Section 1.1.7.3). Such a time series alters very sharply at each time innovation. Application of the Hilbert transform to such signals can give rise to artefactual results of the Hilbert transform. This is avoided with sub-lattices of size $8 \times 8$, however, we aim in this section to demonstrate that the qualitative result obtained from a larger sub-lattice size is unchanged. These results are presented in Figure 11.13.


FIGURE 11.13: The average DFA exponents of rate of change of phase difference between pairs of time series generated by $16 \times 16$ sub-lattices of the $96 \times 96$ Ising model lattice. The temperature parameter, $T$, is varied on the $x$ axis. The average of the valid DFA exponents is shown in pink, and the error bars are a single standard deviation from the mean. The proportion of valid exponents, as calculated by the ML-DFA technique, is denoted by the vertical bars. The theoretical critical parameter $T_c$ is indicated by a red asterisk. A horizontal line at DFA exponent 0.5 is plotted to guide the eye. The same validity bars as in Figure 6.12 are highlighted in magenta.

It is also noted that using a smaller sub-lattice size would yield a greater number of time series and therefore a greater number of their pairwise combinations for calculating an average DFA exponent. This significantly increases the computational time required to apply the method.

### 11.4.3 The Kuramoto model

In this section, the effects of varying the standard deviation of the noise in the Kuramoto model are considered. The standard deviation $\sigma_i$ is added to the phase of the Kuramoto model in Equation 6.2.

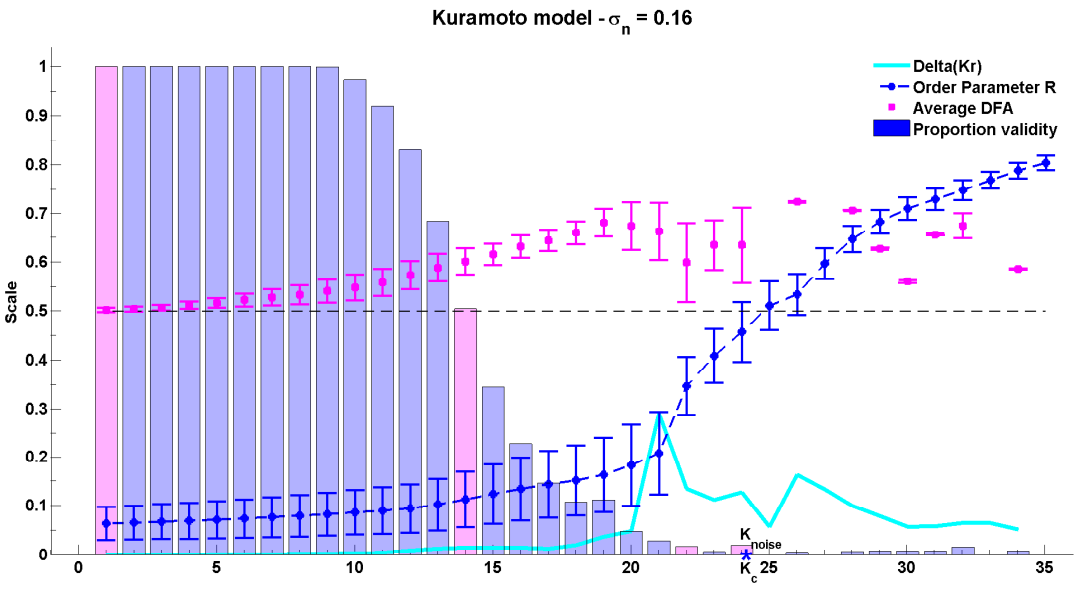


FIGURE 11.14: The average DFA exponents of phase synchrony, as a function of the coupling parameter, $K$, obtained from Kuramoto model oscillator time series. The model uses 44 oscillators, and the Gaussian white noise input has standard deviation $\sigma_i = 0.16$. The average of the valid DFA exponents are shown in pink, and the error bars are a single standard deviation from the mean. The proportion of valid exponents, as calculated by the ML-DFA technique, are indicated by bars. The Kuramoto model order parameter $r$ is in blue, and the quantity $\Delta(Kr)$ is in cyan. Its peak has been used as an indicator of the effective critical coupling. The theoretical critical coupling indicated by a red asterisk and marked as $K_c$. A horizontal line at DFA exponent 0.5 is plotted to guide the eye. The same validity bars as in Figure 6.17 are highlighted in magenta.

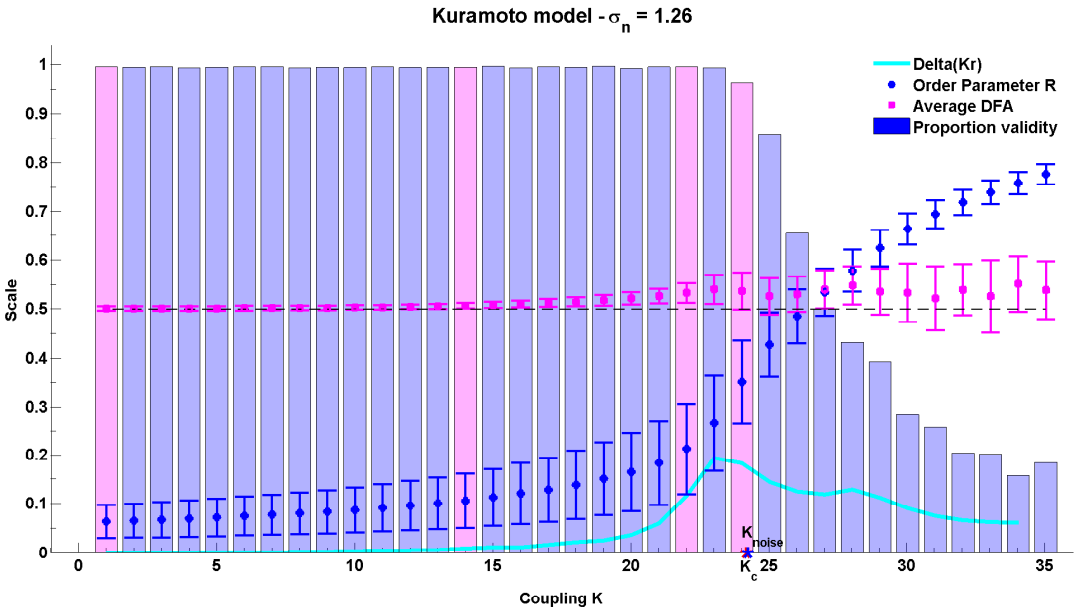


FIGURE 11.15: The average DFA exponents of phase synchrony, as a function of the coupling parameter, $K$, obtained from Kuramoto model oscillator time series. The model uses 44 oscillators, and the Gaussian white noise input has standard deviation $\sigma_i = 1.26$. The average of the valid DFA exponents are shown in pink, and the error bars are a single standard deviation from the mean. The proportion of valid exponents, as calculated by the ML-DFA technique, are indicated by bars. The Kuramoto model order parameter $r$ is in blue, and the quantity $\Delta(Kr)$ is in cyan. Its peak has been used as an indicator of the effective critical coupling. The theoretical critical coupling indicated by a red asterisk and marked as $K_c$. A horizontal line at DFA exponent 0.5 is plotted to guide the eye. The same validity bars as in Figure 6.17 are highlighted in magenta.

As the level of noise is increased, the peak DFA exponent is reduced (Figure 11.15), and the opposite happens when the noise level is reduced (Figure 11.14). However, the proportion of valid DFA exponents is increased when the noise level is greater. This is due to the fact that the phase difference time difference is similar to which noise, which will certainly have a well-defined DFA exponent.

#### 11.4.3.1 Relationship between coupling value of DFA peak difference in natural frequency

The DFA exponents of the phase difference between pairs of oscillators are dependent on the difference between their respective natural frequencies .

Figure 11.16 shows a histogram of the coupling value $K$ at which the peak value of the DFA exponent is reached for each pair.

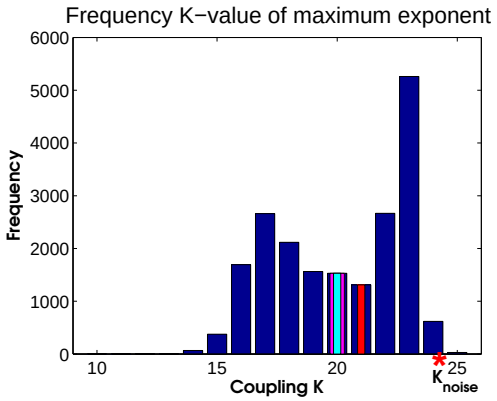


FIGURE 11.16: A histogram of the coupling parameter value $K$ that shows the peak DFA exponent, for each of the 19900 pairs of the 200 oscillators making up the Kuramoto model. The median of these values (20) is indicated by a pink bar, the mean (20) is shown by a light blue bar and the effective critical coupling indicated by the peak in $\Delta(Kr)$ (21) is shown with a red bar. The theoretical critical value of $K_{noise}$ (24) is indicated by a red asterisk.

Figure 11.17 is a histogram of the coupling parameter values $K$ at which the collapse of the DFA exponent of phase difference occurs for all pairs.

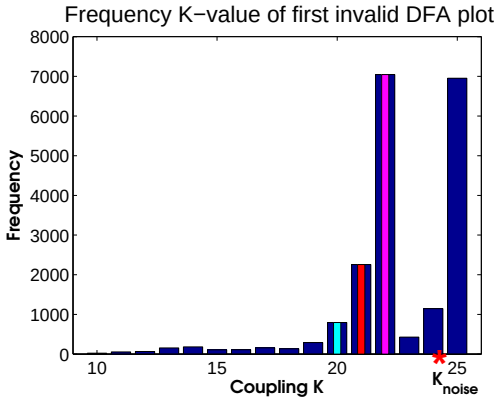


FIGURE 11.17: A histogram of the coupling parameter value $K$ at which the DFA exponent is first found to be invalid, for each of the 19900 pairs of the 200 oscillators making up the Kuramoto model. The median of these values (22) is indicated by a pink bar, the mean (20) is shown by a light blue bar and the effective coupling indicated by the peak in $\Delta(Kr)$ (21) is shown with a red bar. The critical value of $K_{noise}$ (1.95) is indicated by a red asterisk.

## 11.5 Chapter 7

### 11.5.1 List of brain regions and their associated oscillator numbers for the Cabral model

Table 11.4 provides a list of the brain regions used in the Cabral model, their abbreviated labels, which are used in plotting, and the oscillator numbers with which they are

associated.

TABLE 11.4: A list of the 66 brain regions which are represented by 66 oscillators in the Cabral model. The abbreviations, full names and oscillator numbers corresponding to the left and the right hemispheres are given for each brain region.

| | | Oscillator number | |
|---|---|---|---|
| Abbreviation | Region | Right | Left |
| ENT | Entorhinal cortex | 1 | 66 |
| PARH | Parahippocampal cortex | 2 | 65 |
| TP | Temporal pole | 3 | 64 |
| FP | Frontal pole | 4 | 63 |
| FUS | Fusiform gyrus | 5 | 62 |
| TT | Transverse temporal cortex | 6 | 61 |
| LOCC | Lateral occipital cortex | 7 | 60 |
| SP | Superior parietal cortex | 8 | 59 |
| IT | Inferior temporal cortex | 9 | 58 |
| IP | Inferior parietal cortex | 10 | 57 |
| SMAR | Supramarginal gyrus | 11 | 56 |
| BSTS | Bank of the superior temporal sulcus | 12 | 55 |
| MT | Middle temporal cortex | 13 | 54 |
| ST | Superior temporal cortex | 14 | 53 |
| PSTC | Postcentral gyrus | 15 | 52 |
| PREC | precental gyrus | 16 | 51 |
| CMF | Caudal middle frontal cortex | 17 | 50 |
| POPE | Pars opercularis | 18 | 49 |
| PTRI | Pars triangularis | 19 | 48 |
| RMF | Rostral middle frontal cortex | 20 | 47 |
| PORB | Pars orbitalis | 21 | 46 |
| LOF | Lateral orbitofrontal cortex | 22 | 45 |
| CAC | Caudal anterior frontal cortex | 23 | 44 |
| RAC | Rostral anterior cingulate cortex | 24 | 43 |
| SF | Superior frontal cortex | 25 | 42 |
| MOF | Medial orbitofrontal cortex | 26 | 41 |
| LING | Lingual gyrus | 27 | 40 |
| PCAL | Pericalcarine cortex | 28 | 39 |
| CUN | Cuneus | 29 | 38 |
| PARC | Paracentral lobule | 30 | 37 |
| ISTC | Isthmus of the cingulate cortex | 31 | 36 |
| PCUN | Precuneus | 32 | 35 |
| PC | Posterior cingulate cortex | 33 | 34 |

The labels, brain regions and oscillator numbers used in the Cabral model.

### 11.5.2 Individual oscillator pairs in the Cabral model

Results for the DFA exponent of the rate of change of phase difference between individual representative oscillator pairs are shown in Figure 11.18 for the Cabral model.

Specifically, all pairwise combinations are shown for oscillators 1,13,33,54 and 66.

Figure 11.18 shows that oscillator 33, which belongs to cluster 4 shows LRTCs at coupling value $K = 6$ when paired with all the other oscillators shown in this figure. This suggests that it drives the LRTC structure in the rate of change of phase difference in the system at this coupling value.

On the other hand, the rate of change in phase difference of oscillators 1 and 66 with other oscillators reflect the temporal structure of the oscillator with which they are paired. When paired with each other, they show a DFA exponent of 0.5 for all coupling values.

Other oscillators in the system such as 13 and 54 show LRTCs in the rate of change of their phase differences at different coupling values, but these do not correspond to the state of greatest flux in the system indicated by a peak in $\Delta(Kr)$.

It is noted that the oscillator pairs do not necessarily show valid DFA exponents continuously for coupling values. This is reflective of the fact that oscillator pairs can come in and out of synchronisation in a more complicated manner than simply with a linear increase in the coupling parameter as in the classical Kuramoto model with noise. This property of the Cabral model is a result of the richer dynamics introduced into the model by the connectivity and time delay matrices. Such dynamics may be advantageous to the human brain because they allow for the presence of inter-brain interactions containing LRTCs are a number of different coupling parameters. This might suggest that if the brain was perturbed from one 'coupling value' [1] to a slightly different one, the brain would still be able to find a regime in which LRTCs in neural synchronisation were possible, along with all their advantages (see Section 1.1.8.2).

In the next section, we shall see that when the hemispheres of the 'brain' in the Cabral model are severed, there are still coupling parameters at which LRTCs can exist. It is suggested that a modification of a 'coupling parameter' in the brain is precisely the a means by which the brain can adjust to changes in such characteristics as the network structure, and still be able to access a regime close to criticality.

### 11.5.3 The Cabral model with disconnected 'hemispheres'

In this section, the evolution of the average DFA exponent in the Cabral model is shown when connectivity between the two hemispheres has been cut.

[1] This may be an abstract parameter that modulates the interactions between brain regions in a way that we do not necessarily fully understand, or can measure

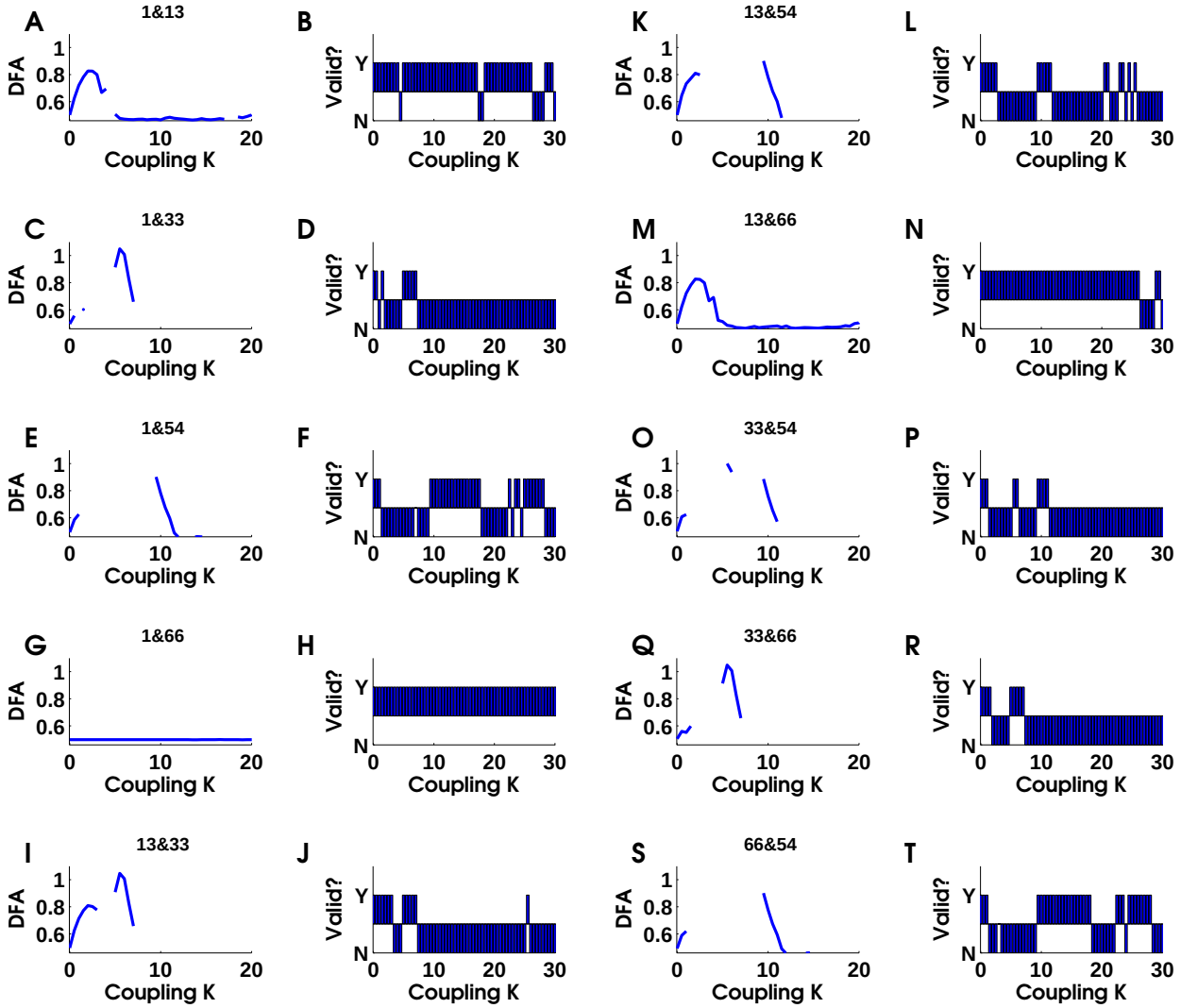


FIGURE 11.18: Panels on the left show valid DFA exponent values as coupling is increased for a representative set of oscillator pairs. The panels on the right indicate the DFA exponents that are rejected as being invalid (N) and those that are not rejected and therefore contribute to the result (Y). In particular, oscillators 1,13,33,54 and 66 are considered in all pairwise combinations. Oscillators 13, 33 and 54 are seen to give rise to LRTCs in phase synchrony for all oscillator pairings considered in this set. The peak DFA exponent occurs at consistent coupling values for each of these oscillators regardless of which oscillator they are paired with. For oscillator 13, this occurs at coupling $K = 2$, for oscillator 33 at $K = 5.5$ and for oscillator 54 at $K = 9.5$. On the other hand, oscillators 1 and 66 have a DFA exponent of 0.5 in their phase difference at all coupling values. Their phase difference takes on DFA exponent values of the oscillator they are paired with. Validity of DFA exponent for various pairings is not consistent, but those coupling values that correspond to LRTCs in the phase difference also show validity.

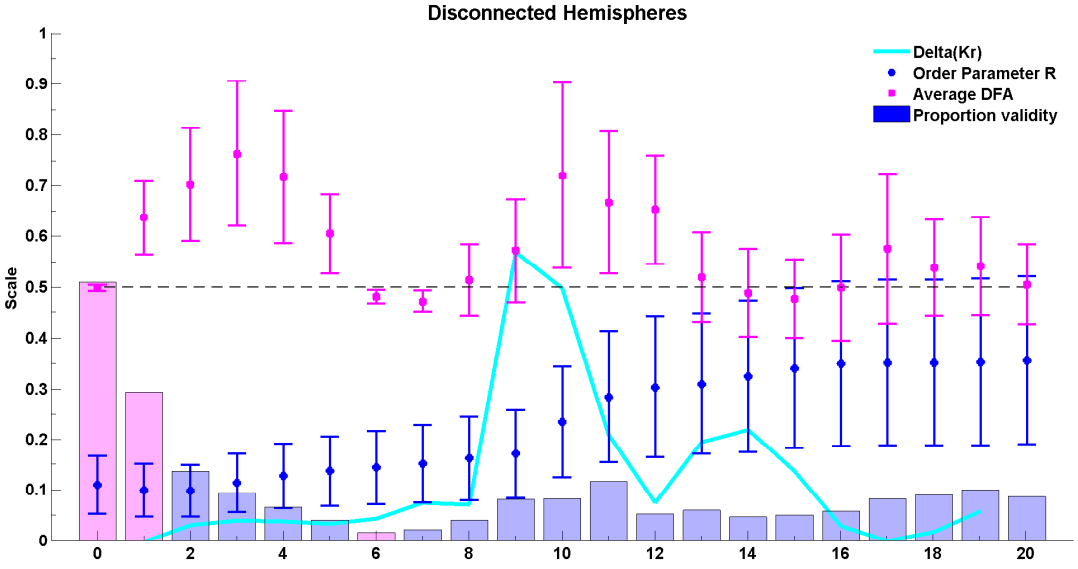


FIGURE 11.19: The average DFA exponents of phase synchrony, as a function of the coupling parameter, $K$ in the extended Kuramoto model [47]. The model includes 66 oscillators at normally distributed natural frequencies with mean 60 Hz and standard deviation $\sigma_i = 1.25$. The connectivity matrix and time delays used between oscillators correspond to empirical values in which the left and right hemispheres have been disconnected. The average of the valid DFA exponents are shown in magenta and the proportion of valid exponents, as calculated by the ML-DFA technique, are indicated by bars. The Kuramoto model order parameter $r$ is in blue, and the quantity $\Delta(Kr)$ is in cyan. Its peak has been used as an indicator of the effective critical coupling. A horizontal line at DFA exponent 0.5 is plotted to guide the eye.

The peak in the average DFA at $K = 6$, which results from the interactions of cluster 4 in the model is no longer seen. This is reflective of the fact that the connections between oscillators in this cluster are cut when the hemispheres are disconnected. We do however, still see LRTCs in the average DFA exponent at different coupling values. The peak in the change in order parameter $\Delta(Kr)$ is also changed. This may occur because phase interactions in the system are now driven by different clusters, which are contained within a single hemisphere.

## 11.6 Chapter 8

### 11.6.1 Tables

TABLE 11.5: The $p$-values obtained from a Kolmogorov-Smirnov test of normality for the comparison of each studied data set with that of human MEG recorded during resting state. Only DFA exponents determined to be valid by ML-DFA are included in the calculation.

| | Frequency Band (Hz) | | | | | | | | | | | | | | | | | |
|---|---|---|---|---|---|---|---|---|---|---|---|---|---|---|---|---|---|---|
| Task | 4-6 | 6-8 | 8-10 | 10-12 | 12-14 | 14-16 | 15-17 | 17-19 | 19-21 | 21-23 | 23-25 | 25-27 | 27-29 | 29-31 | 31-33 | 33-35 | 35-37 | 37-39 |
| Rest | 0.98 | 0.98 | 0.61 | 0.88 | 0.64 | 0.65 | 0.77 | 0.47 | 0.60 | 0.97 | 0.87 | 0.94 | 0.99 | 0.61 | 0.90 | 0.95 | 0.90 | 0.98 |
| Both | NaN | 0.95 | 0.69 | 0.96 | 0.11 | 0.87 | 0.45 | 0.91 | 0.99 | 0.97 | 0.97 | 0.80 | 0.87 | 0.91 | 0.89 | 0.88 | 0.80 | 0.96 |
| Right | 0.96 | 0.92 | 0.98 | 0.98 | 0.49 | 0.67 | 0.86 | 0.91 | 0.96 | 0.83 | 0.89 | 0.87 | 0.95 | 0.96 | 0.99 | 0.92 | 1.00 | 0.97 |
| Left | NaN | NaN | 0.93 | 0.87 | 0.53 | 0.76 | 0.92 | 0.97 | 0.99 | 0.98 | 0.32 | 0.97 | 0.98 | 0.88 | 0.67 | 0.89 | 0.99 | 0.99 |
| Gauss | 0.70 | 0.99 | 0.99 | 0.98 | 0.93 | 0.57 | 0.82 | 0.88 | 0.96 | 0.86 | 0.92 | 0.90 | 0.71 | 0.99 | 0.99 | 0.97 | 0.94 | 0.92 |
| Scanner | NaN | 0.93 | 0.91 | NaN | 0.97 | 0.50 | 0.92 | 0.75 | 0.98 | 0.91 | 0.87 | 0.89 | 0.93 | 0.95 | 0.72 | 0.91 | 0.94 | 0.97 |
| ShuffledR | 0.88 | 0.98 | 0.76 | 0.99 | 0.87 | 0.52 | 0.97 | 0.71 | 0.53 | 0.79 | 0.67 | 0.95 | 0.79 | 0.85 | 0.69 | 0.41 | 0.86 | 0.99 |
| ShuffledB | 0.81 | 0.75 | 0.68 | 0.33 | 0.83 | 0.85 | 0.51 | 0.92 | 0.56 | 0.46 | 0.93 | 0.73 | 0.74 | 0.95 | 0.48 | 0.75 | 0.90 | 0.97 |

The type of data analysed are listed in the left-hand column. The top row indicates the frequency band of the filter applied to data before it is analysed. Here the frequency bands are listed as integers to save space. Where the band is for example 4-6 Hz, this indicates that the bandpass filter was implemented from 4.5-6.5 Hz. An entry of NaN indicates that there are fewer than 2 valid DFA exponents in for the corresponding frequency band and condition, thus a standard deviation could not be found and the test could not be performed. There are no NaN entries for frequency bands above $10.5 - 12.5$ Hz. The row labelled ShuffleR indicates phase shuffled time series from recordings of resting state data. ShuffleB denotes the task of tapping both fingers. These latter rows are out of 100.

TABLE 11.6: The $p$-values obtained from a one-tailed Student's t-test for the comparison of each data set studied. Only DFA exponents determined to be valid by ML-DFA are included in the calculation.

| | Frequency Band (Hz) | | | | | | | | | | | | | | | | | |
|---|---|---|---|---|---|---|---|---|---|---|---|---|---|---|---|---|---|---|
| Data | 4-6 | 6-8 | 8-10 | 10-12 | 12-14 | 14-16 | 15-17 | 17-19 | 19-21 | 21-23 | 23-25 | 25-27 | 27-29 | 29-31 | 31-33 | 33-35 | 35-37 | 37-39 |
| Both | NaN | 0.08 | 0.31 | 0.76 | 0.02 | 0.43 | 0.29 | 0.10 | 0.20 | 0.07 | 0.01 | 0.24 | 0.33 | 0.31 | 0.21 | 0.51 | 0.06 | 0.61 |
| Right | 0.24 | NaN | 0.48 | 0.71 | 0.01 | 0.09 | 0.20 | 0.20 | 0.30 | 0.01 | 0.04 | 0.60 | 0.25 | 0.04 | 0.06 | 0.77 | 0.01 | 0.33 |
| Left | NaN | NaN | 0.58 | 0.46 | NaN | 0.40 | 0.11 | 0.58 | 0.22 | 0.10 | 0.02 | 0.02 | 0.40 | 0.37 | 0.31 | 0.69 | 0.54 | 0.28 |
| Gauss | 0.14 | 0.24 | 0.29 | 0.02 | 0.13 | 0.25 | 0.27 | 0.46 | 0.34 | 0.09 | 0.00 | 0.10 | 0.28 | 0.11 | 0.07 | 0.66 | 0.15 | 0.15 |
| Scanner | 0.30 | 0.78 | 0.17 | 0.14 | 0.03 | 0.19 | 0.19 | 0.22 | 0.05 | 0.04 | 0.00 | 0.03 | 0.86 | 0.27 | 0.09 | 0.76 | 0.30 | 0.39 |
| ShuffledR | 0.01 | 0.01 | 0.01 | 0.01 | 0.01 | 0.02 | 0.01 | 0.02 | 0.02 | 0.01 | 0.01 | 0.01 | 0.11 | 0.05 | 0.08 | 0.27 | 0.14 | 0.18 |
| ShuffledB | 0.01 | 0.02 | 0.01 | 0.01 | 0.02 | 0.03 | 0.02 | 0.07 | 0.10 | 0.11 | 0.26 | 0.05 | 0.09 | 0.07 | 0.11 | 0.33 | 0.59 | 0.15 |

The type of data analysed are listed in the left-hand column. The top row indicates the frequency band of the filter applied to data before it is analysed. Here the frequency bands are listed as integers to save space. Where the band is for example 4-5 Hz, this indicates that the bandpass filter was implemented from 4.5-6.5 Hz. The row labelled ShuffleR indicates phase shuffled time series from recordings of resting state data. ShuffleB denotes the task of tapping both fingers, however these $p$-values refer to the difference between the phase-shuffled both finger tapping task and the same task without phase-shuffling.

TABLE 11.7: The number of time series determined to be valid by ML-DFA for each frequency band and for data recorded during each task, and for each control time series. This gives the number of subjects or time series from which the averages of DFA exponents are taken.

| | Frequency Band (Hz) | | | | | | | | | | | | | | | | |
|---|---|---|---|---|---|---|---|---|---|---|---|---|---|---|---|---|---|
| Data | 4-6 | 6-8 | 8-10 | 10-12 | 12-14 | 14-16 | 15-17 | 17-19 | 19-21 | 21-23 | 23-25 | 25-27 | 27-29 | 29-31 | 31-33 | 33-35 | 35-37 | 37-39 |
| Rest | 2 | 2 | 6 | 5 | 6 | 6 | 5 | 5 | 5 | 7 | 6 | 7 | 6 | 7 | 5 | 7 | 6 | 6 |
| Both | 1 | 5 | 3 | 5 | 7 | 6 | 6 | 6 | 7 | 5 | 7 | 7 | 7 | 6 | 7 | 7 | 6 | 7 |
| Right | 4 | 4 | 2 | 2 | 5 | 6 | 5 | 6 | 4 | 6 | 7 | 5 | 7 | 6 | 6 | 7 | 7 | 7 |
| Left | 0 | 1 | 4 | 4 | 5 | 7 | 6 | 7 | 6 | 6 | 7 | 7 | 6 | 6 | 7 | 6 | 7 | 7 |
| Gauss | 3 | 2 | 6 | 4 | 3 | 6 | 6 | 4 | 7 | 5 | 7 | 4 | 6 | 7 | 7 | 7 | 7 | 6 |
| Scanner | 1 | 1 | 3 | 4 | 5 | 4 | 6 | 6 | 7 | 4 | 7 | 7 | 6 | 6 | 5 | 7 | 7 | 6 |
| ShuffledR | 97 | 95 | 98 | 97 | 95 | 96 | 97 | 96 | 97 | 94 | 94 | 95 | 97 | 93 | 96 | 95 | 96 | 95 |
| ShuffledB | 99 | 100 | 94 | 95 | 95 | 98 | 98 | 97 | 96 | 98 | 99 | 97 | 95 | 97 | 97 | 95 | 96 | 94 |

The type of data analysed are listed in the left-hand column. The top row indicates the frequency band of the filter applied to data before it is analysed. There are 7 subjects and thus 7 simulations of noise control data. However, as the data was phase-shuffled 100 times, the number of valid DFA exponents is correspondingly out of 100 rather than out of 7. Here the frequency bands are listed as integers to save space. Where the band is for example 3-5 Hz, this indicates that the bandpass filter was implemented from 3.5-5.5 Hz. The row labelled ShuffleR indicates phase shuffled time series from recordings of resting state data. ShuffleB denotes the task of tapping both fingers.

### 11.6.2 Varying the bandpass filtering range

In this section, it is verified that the results obtained in the main chapter by bandpass filtering the data into 2 Hz frequency ranges are not caused by serendipity of the filtering band. In order to do this, the data is bandpass filtered data into frequency ranges of different widths and centred at different frequency locations. More precisely, results are obtained from data bandpass filtered for all possible frequency bands in the 1-40 Hz range that can be considered as narrowband for the purposes of Hilbert transform application. In order to determine the frequencies that are sufficiently narrowband, a quantity called the frequency bandwidth is used, which is defined using the values of the limits of the bandpass filter $f_H$ and $f_L$, where $f_H$ is the upper limit and $f_L$ is the lower limit. The frequency bandwidth is then defined as :

$$fBW = 2\frac{f_H - f_L}{f_H + f_L}$$

Narrowband signals are considered to obey the condition $fBW \ll 1$ [293], however, mathematical derivations required in order for the Hilbert transform to generate a phase and amplitude for a signal is $fBW < 1/2$ [293], which is the condition that applied to the results.

#### 11.6.2.1 A note on presentation of results

DFA exponents of the rate of change of the phase difference between left and right motor cortices of the MEG data are presented in 2-dimensional plots in which the $x$-axis represents the width of the bandpass filter applied prior to applying the method ($f_H - f_L$), and the $y$-axis represents twice the central frequency of the bandpass filter ($f_H + f_L$). So that the DFA exponent found for a bandpass filter of 11-16 Hz would be located in position (5,27) of the graph.

Figure 11.20 indicates the bandpass filtering region that corresponds to the condition $fBW < 1/2$ in blue.

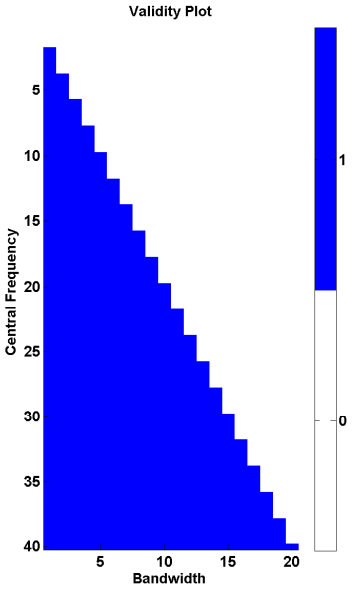


FIGURE 11.20: A plot to indicate the region of bandpass filter ranges considered in the conclusions, based on the fact that their fractional bandwidth is of size 1 or lower. The lower limit of the bandpass is along the y-axis and the upper limit is on the x-axis of the plot.

#### 11.6.2.2 Average across subjects

In Figure 11.21, DFA exponents for a number of frequency bands are shown in the resting state and during the task of tapping both fingers.

In both plots, there high DFA exponents are seen when the central frequency of the band is very low. These high exponents are consistent across different tasks, and indeed for different types of data. They occur because of artefacts in the Hilbert transform when the time series is very smooth and slow. There are also several frequencies with no value for the DFA exponent. This occurs because during very slow oscillations, the minimum

window size used for DFA of one second doesn't extend across several oscillations, as recommended. This means that many DFA exponents are invalid.

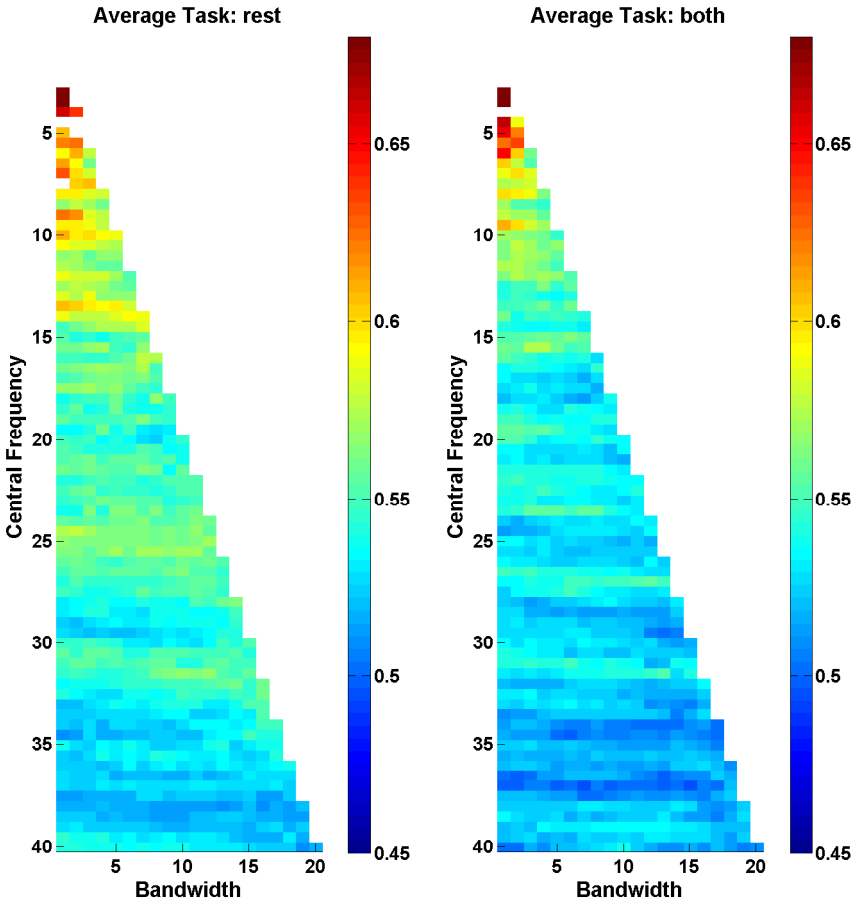


FIGURE 11.21: The average DFA of phase difference between left and right motor cortices taken across all subjects in the A. resting state and the B. both fingers tapping conditions.

For central frequencies that are greater than approximately 10 Hz, this effect is no longer evident. Instead, there are gradual rises and falls in the DFA exponents in particular frequency bands. When these are visible, they tend to extend for a number of band widths, which are centred at a particular frequency. This suggests that high (or low) DFA exponent are robustly associated with specific frequencies.

Figure 11.22 shows the differences between DFA exponents of the left and right motor cortices during resting state and while tapping both fingers. We can observe that high DFA valuesfor frequency bands centred at low frequencies cancel out for these two tasks and a low difference is observed. There are a number of frequency ranges that show a significant difference in this difference across subjects, which appear as in blue if there is significance at a 5% level. One is centred at 13.5 Hz, which is where the $\alpha$ band result is shown. There is another at 17.5 Hz and a third at 24.5 Hz. The latter of these is the

location of the result in the $\beta$ band. The difference at 17.5 Hz is not evident when the data is bandpass filtered in 2 Hz bands as in Chapter 8.

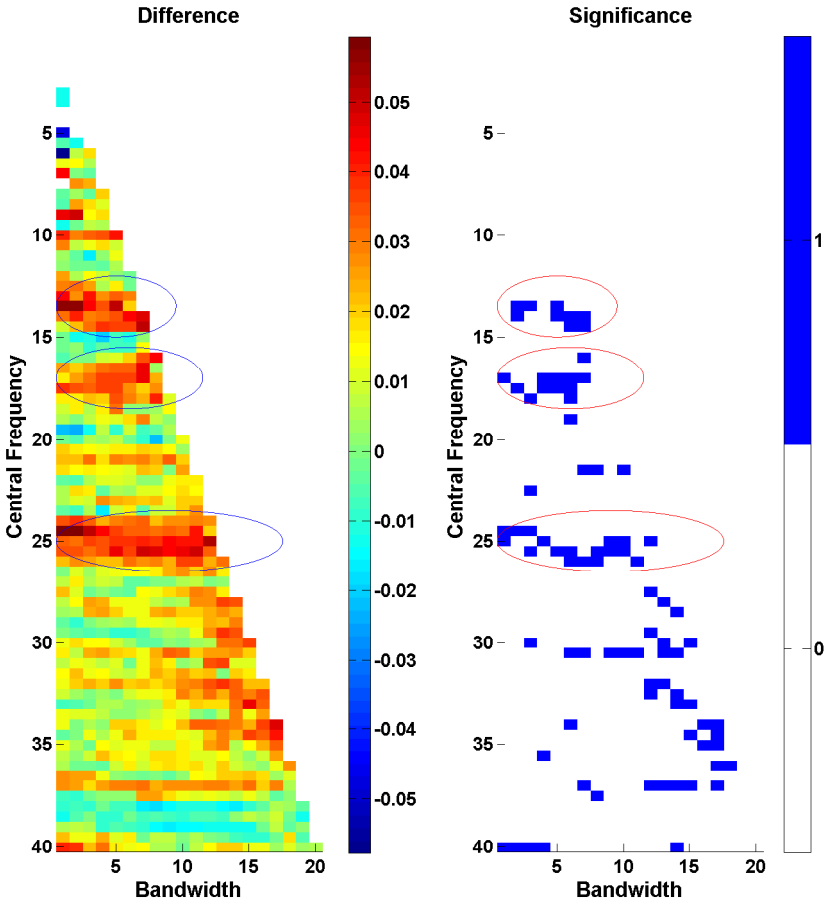


FIGURE 11.22: A. The difference between DFA exponents of phase difference between left and right motor cortices taken across all subjects in the resting state and the both fingers tapping conditions, and B. a plot of significance for these values across subjects. A point on the plot is markes as blue if it is significant at the 5% level for a pairwise t-test of those DFA exponents that are accepted as linear by ML-DFA. The t-test is perfromed across subjects as descibed in Section 8.2.1.4.

The plots in this section are an additional demonstration of the fact that the results obtained in Chapter 8 are robust because they are seen to be present for different frequency band widths centred at the frequencies in which LRTCs are observed for resting state human MEG data.

# Bibliography


[1] D. Abasolo, R. Hornero, J. Escudero, and P. Espino. A study on the possible usefulness of detrended fluctuation analysis of the electroencephalogram background activity in alzheimer's disease. *IEEE Trans. Bio-Med Eng.*, 55(9):2171–2179, 2008.

[2] Juan A. Acebrón, Conrad J. Pérez Vicente, Félix Ritort, and Renato Spigler. The Kuramoto model: A simple paradigm for synchronization phenomena. *Rev. Mod. Phys.*, 77:137 – 185, 2005.

[3] P.S. Addison. *Fractals and Chaos: An illustrated course*. Taylor & Francis, 1997.

[4] R. Adler. A Study of Locking Phenomena in Oscillators. *Proceedings of the IRE*, 34(6):351–357, June 1946.

[5] Blankenship A.G. and Feller M.B. Mechanisms underlying spontaneous patterned activity in developing neural circuits. *Nature*, 11:18–29, 2010.

[6] Hirotugu Akaike. A new look at the statistical model identification. *IEEE T. Automat. Contr.*, 19(6):716–723, 1974.

[7] Thomas Akam and Dimitri M. Kullmann. Oscillations and filtering networks support flexible routing of information. *Neuron*, 67(2):308 – 320, 2010.

[8] J. S. Anderson, I. Lampl, and D. Ferster. The contribution of noise to contrast invariance of orientation tuning in cat visual cortex. *Science*, 290:1968, 2000.

[9] F. J. Anscombe. Graphs in statistical analysis. *Amer Statist*, 27(1):17–21, 1973.

[10] Dilip N. Athreya, Guy Van Orden, and Michael A. Riley. Feedback about isometric force production yields more random variations. *Neurosci. Lett.*, 513(1):37 – 41, 2012.

[11] R. Baierlein. *Thermal Physics*. Cambridge University Press, 1999.

[12] P. Bak and M. Paczuski. Complexity, contingency, and criticality. *Proc. Natl. Acad. Sci. U S A.*, 92(15):6689–6696, 1995.

[13] Per Bak. *How Nature Works: The Science of Self-organized Criticality*. Copernicus (Springer), 1st edition, 1996.

[14] Per Bak, Chao Tang, and Kurt Wiesenfeld. Self-organized criticality: An explanation of the $1/f$ noise. *Phys. Rev. Lett.*, 59:381–384, 1987.

[15] S. N. Baker, J. M. Kilner, E. M. Pinches, and R. N. Lemon. The role of synchrony and oscillations in the motor output. *Experimental brain research. Experimentelle Hirnforschung. Expérimentation cérébrale*, 128(1-2):109–117, September 1999.

[16] S. N. Baker, R. Spinks, A. Jackson, and R. N. Lemon. Synchronization in Monkey Motor Cortex During a Precision Grip Task. I. Task-Dependent Modulation in Single-Unit Synchrony. *J. Neurophysiol.*, 85(2):869–885, February 2001.

[17] Peter A. Bandettini. Twenty years of functional mri: The science and the stories. *NeuroImage*, 62(2):575 – 588, 2012. 20 {YEARS} {OF} fMRI 20 {YEARS} {OF} fMRI.

[18] Jean-Marc Bardet and Imen Kammoun. Asymptotic properties of the detrended fluctuation analysis of long-range-dependent processes. *IEEE T. Inform. Theory*, 54(5):2041–2052, 2008.

[19] A. T. Barker, R. Jalinous, and I. L. Freeston. Non-invasive Magnetic Stimulation of Human Motor Cortex. *Lancet*, 1:1106–1107, 1985.

[20] Lionel Barnett, Joseph T. Lizier, Michael Harré, Anil K. Seth, and Terry Bossomaier. Information flow in a kinetic ising model peaks in the disordered phase. *Phys. Rev. Lett.*, 111:177203, Oct 2013.

[21] Axel Bauer, Jan W. Kantelhardt, Armin Bunde, Petra Barthel, Raphael Schneider, Marek Malik, and Georg Schmidt. Phase-rectified signal averaging detects quasi-periodicities in non-stationary data. *Physica A*, 364:423–434, 2006.

[22] Rodney J. Baxter and Physics. *Exactly Solved Models in Statistical Mechanics (Dover Books on Physics)*. Dover Publications, January 2008.

[23] John M. Beggs and Dietmar Plenz. Neuronal avalanches in neocortical circuits. *J. Neurosci.*, 23(35):11167–11177, 2003.

[24] John M Beggs and Nicholas Timme. Being critical of criticality in the brain. *Front. Fract. Physiol.*, 3:163, 2012.

[25] Jan Beran. *Statistics for long-memory processes*. Monographs on statistics and applied probability, 61. Chapman & Hall, 1994.

[26] H. Berger. Uber das elektrenkephalogramm des menschen. *Archiv fur Psychiatrie und Nervenkrankheiten*, 87:527–580, 1929.

[27] Luc Berthouze and Simon F. Farmer. Adaptive time-varying detrended fluctuation analysis. *J. Neurosci. Meth.*, 209(1):178–188, 2012.

[28] Luc Berthouze, Leon M. James, and Simon F. Farmer. Human EEG shows long-range temporal correlations of oscillation amplitude in theta, alpha and beta bands across a wide age range. *Clin. Neurophysiol.*, 121(8):1187–1197, 2010.

[29] B. Boashash. Estimating and interpreting the instantaneous frequency of a signal. I. Fundamentals. *Proc. IEEE*, 80(4):520–538, 1992.

[30] B. Boashash, P. O'Shea, and M. J. Arnold. Algorithms for instantaneous frequency estimation: A comparative study. In F. T. Luk, editor, *Advanced Signal Processing Algorithms, Architectures, and Implementations*, volume 1348 of *Proc. SPIE*, pages 126–148, 1990.

[31] Boualem Boashash and Peter O'Shea. Use of the cross wigner-ville distribution for estimation of instantaneous frequency. *IEEE Trans. Signal Proces.*, 41(3):1439–1445, 1993.

[32] Luis L. Bonilla, John C. Neu, and Renato Spigler. Nonlinear stability of incoherence and collective synchronization in a population of coupled oscillators. *J. Stat. Phys.*, 67:313–330, 1992.

[33] Stefan Bornholdt and Thimo Rohlf. Topological evolution of dynamical networks: Global criticality from local dynamics. *Phys. Rev. Lett.*, 84(26):6114–6117, 2000.

[34] M. Botcharova, S. F. Farmer, and L. Berthouze. Power-law distribution of phase-locking intervals does not imply critical interaction. *Phys. Rev. E*, 86:051920, 2012.

[35] M. Botcharova, S. F. Farmer, and L. Berthouze. A maximum likelihood based technique for validating detrended fluctuation analysis (ML-DFA). *pre-print*, 2013. arXiv:1306.5075.

[36] Michael Breakspear, Stewart Heitmann, and Andreas Daffertshofer. Generative models of cortical oscillations: neurobiological implications of the Kuramoto model. *Front. Hum. Neurosci.*, 4:190, 2010.

[37] John-Stuart Brittain, Celia Catton, Bernard A. Conway, Jens Bo Nielsen, Ned Jenkinson, and David M. Halliday. Optimal spectral tracking – with application to speed dependent neural modulation of tibialis anterior during human treadmill walking. *J. Neurosci. Meth.*, 177(2):334 – 347, 2009.

[38] John-Stuart Brittain, David M. Halliday, Bernard A. Conway, and Jens Bo Nielsen. Single-trial multiwavelet coherence in application to neurophysiological time series. *IEEE Trans. Biomed. Engineering*, 54(5):854–862, 2007.

[39] Peter J. Brockwell and Richard A. Davis. *Time series: Theory and methods.* Springer-Verlag, 1991.

[40] Matthew J. Brookes, Joanne R. Hale, Johanna M. Zumer, Claire M. Stevenson, Susan T. Francis, Gareth R. Barnes, Julia P. Owen, Peter G. Morris, and Srikantan S. Nagarajan. Measuring functional connectivity using MEG: Methodology and comparison with fcMRI. *NeuroImage*, 56(3):1082 – 1104, 2011.

[41] Peter Brown, Stephan Salenius, John C. Rothwell, and Riitta Hari. Cortical correlate of the piper rhythm in humans. *Journal of Neurophysiology*, 80(6):2911–2917, 1998.

[42] Andreas Bruns. Fourier-, hilbert- and wavelet-based signal analysis: are they really different approaches? *Journal of Neuroscience Methods*, 137(2):321 – 332, 2004.

[43] R. M. Bryce and K. B. Sprague. Revisiting detrended fluctuation analysis. *Sci Rep*, 2:315, 2012.

[44] Randy L. Buckner, Jessica R. Andrews-Hanna, and Daniel L. Schacter. The brain's default network. *Annals of the New York Academy of Sciences*, 1124(1):1–38, 2008.

[45] K. Burnham and D. Anderson. *Model selection and multimodel inference: A practical information-theoretic approach*. Springer, 2nd edition, 2002.

[46] Gyorgy Buzsaki. *Rhythms of the Brain*. Oxford University Press, USA, 1 edition, 2006.

[47] Joana Cabral, Etienne Hugues, Olaf Sporns, and Gustavo Deco. Role of local network oscillations in resting-state functional connectivity. *NeuroImage*, 57(1):130–139, 2011.

[48] J. L. Cambier and M. Nauenberg. Distribution of fractal clusters and scaling in the ising model. *Phys. Rev. B*, 34:8071–8079, Dec 1986.

[49] R. T. Canolty, C. F. Cadieu, K. Koepsell, R. T. Knight, and J. M. Carmena. Multivariate phase-amplitude cross-frequency coupling in neurophysiological signals. *IEEE T. Bio-Med Eng.*, 59(1):8–11, 2012.

[50] Robin Lester Carhart-Harris, Robert Leech, Peter John Hellyer, Murray Shanahan, Amanda Feilding, Enzo Tagliazucchi, Dante R Chialvo, and David Nutt. The entropic brain: A theory of conscious states informed by neuroimaging research with psychedelic drugs. *Front. Hum. Neurosci.*, 8(20), 2014.

[51] Andrea Cavagna, Alessio Cimarelli, Irene Giardina, Giorgio Parisi, Raffaele Santagati, Fabio Stefanini, and Massimiliano Viale. Scale-free correlations in starling flocks. *Proc. Natl. Acad. Sci. U S A.*, 107(26):11865–11870, 2010.

[52] Z. Chen, P.C. Ivanov, K. Hu, and H. Eugene Stanley. Effect of nonstationarities on detrended fluctuation analysis. *Phys. Rev. E*, 65(4 Pt 1):041107, 2002.

[53] Zhi Chen, Kun Hu, Pedro Carpena, Pedro Bernaola-Galvan, H. Eugene Stanley, and Plamen Ch. Ivanov. Effect of nonlinear filters on detrended fluctuation analysis. *Phys. Rev. E*, 71:011104, 2005.

[54] Dante R. Chialvo. Emergent complex neural dynamics. *Nat. Phys.*, 6(1):744–750, 2010.

[55] D.R. Chialvo. Critical brain networks. *Physica A*, 340:756–765, 2004.

[56] N. Chopra and M. W. Spong. On synchronization of Kuramoto oscillators. In *IEEE Decis. Contr. P.*, volume 44, pages 3916–3922. IEEE, 2005.

[57] G. Claeskens and N.L. Hjort. *Model Selection and Model Averaging*. Cambridge University Press, New York, 2008.

[58] Aaron Clauset, Cosma Rohilla Shalizi, and M. E. J. Newman. Power-law distributions in empirical data. *SIAM Review*, 51:661–703, 2009.

[59] Richard G. Clegg. A practical guide to measuring the hurst parameter. In *21st UK Performance Engineering Workshop, School of Computing Science Technical Report Series, CSTR-916, University of Newcastle*, pages 43–55, 2006.

[60] D. Cohen. Magnetoencephalography: Evidence of magnetic fields produced by alpha-rhythm currents. *Science*, 161(3843):784–786, 1968.

[61] B A Conway, D M Halliday, S F Farmer, U Shahani, P Maas, A I Weir, and J R Rosenberg. Synchronization between motor cortex and spinal motoneuronal pool during the performance of a maintained motor task in man. *J. Physiol.*, 489(Pt 3):917–924, 1995.

[62] R. Cooper, J.W. Osselton, and J.C. Shaw. *EEG technology*. Butterworth-Heinemann Limited, 1974.

[63] Glen Cowan. *Statistical Data Analysis*. Oxford University Press, USA, 1998.

[64] Lopes da Silva F. Neural mechanisms underlying brain waves: from neural membranes to networks. *Electroen. Clin. Neuro.*, 79(2):81–93, 1991.

[65] Andreas Daffertshofer and Bernadette C. M. van Wijk. On the influence of amplitude on the connectivity between phases. *Front. Neuroinform.*, 5(6), 2011.

[66] H. Daido. Intrinsic Fluctuation and Its Critical Scaling in a Class of Populations of Oscillators with Distributed Frequencies. *Progr. Theoret. Phys.*, 81:727–731, April 1989.

[67] Bryan C. Daniels. Synchronization of globally coupled nonlinear oscillators: the rich behavior of the kuramoto model. *Ohio Wesleyan Physics Dept., Essay*, 7:2, 2005. Available online.

[68] Gustavo Deco and Viktor K. Jirsa. Ongoing cortical activity at rest: Criticality, multistability, and ghost attractors. *J. Neurosci.*, 32(10):3366–3375, 2012.

[69] Nima Dehghani, Claude Bdard, Sydney S. Cash, Eric Halgren, and Alain Destexhe. Comparative power spectral analysis of simultaneous elecroencephalographic and magnetoencephalographic recordings in humans suggests non-resistive extracellular media. *J. Comput. Neurosci.*, 29(3):405–421, 2010.

[70] Mauricio R. Delgado, Elizabeth A. Phelps, and Trevor W. Robbins, editors. *Decision Making, Affect, and Learning: Attention and Performance XXIII*. Oxford University Press, 2011.

[71] Arnaud Delorme and Scott Makeig. EEGLAB: An open source toolbox for analysis of single-trial EEG dynamics including independent component analysis. *J. Neurosci. Meth.*, 134(1):9–21, 2004.

[72] Charmaine Demanuele, Christopher J James, and Edmund JS Sonuga-Barke. Distinguishing low frequency oscillations within the 1/f spectral behaviour of electromagnetic brain signals. *Behav. Brain Funct.*, 3(1):62, 2007.

[73] K. Trachenko Dima Bolmatov, V. V. Brazhkin. Thermodynamic behaviour of supercritical matter. *Nature Communications*, pages –, 2013.

[74] Sam M. Doesburg, Jessica J. Green, John J. McDonald, and Lawrence M. Ward. Rhythms of consciousness: Binocular rivalry reveals large-scale oscillatory network dynamics mediating visual perception. *PLoS ONE*, 4(7):e6142, 2009.

[75] Florian Dörfler and Francesco Bullo. On the Critical Coupling for Kuramoto Oscillators. *SIAM J. Applied Dynamical Systems*, 10(3):1070–1099, 2011.

[76] Erwan Dupont, Ileana L. Hanganu, Werner Kilb, Silke Hirsch, and Heiko J. Luhmann. Rapid developmental switch in the mechanisms driving early cortical columnar networks. *Nature*, December 2005.

[77] Srimonti Dutta, Dipak Ghosh, Shukla Samanta, and Santanu Dey. Multifractal parameters as an indication of different physiological and pathological states of the human brain. *Physica A*, 396:155 – 163, 2014.

[78] Javier Escudero, Roberto Hornero, Daniel E. Absolo, Alberto Fernndez, and Miguel Lpez Coronado. Artifact removal in magnetoencephalogram background activity with independent component analysis. *IEEE T. Bio-Med. Eng.*, 54(11):1965–1973, 2007.

[79] M. Essl and P. Rappelsberger. Eeg cohererence and reference signals: experimental results and mathematical explanations. *Medical and Biological Engineering and Computing*, 36(4):399–406, 1998.

[80] Paul Expert, Renaud Lambiotte, Dante R. Chialvo, Kim Christensen, Henrik Jeldtoft J. Jensen, David J. Sharp, and Federico Turkheimer. Self-similar correlation function in brain resting-state functional magnetic resonance imaging. *J. R. Soc. Interface*, September 2010.

[81] S. F. Farmer. Rhythmicity, synchronization and binding in human and primate motor systems. *J. Physiol.*, 509(1):3–14, 1998.

[82] SF Farmer, FD Bremner, DM Halliday, JR Rosenberg, and JA Stephens. The frequency content of common synaptic inputs to motoneurones studied during voluntary isometric contraction in man. *The Journal of Physiology*, 470(1):127–155, 1993.

[83] J. Feder. *Fractals*. Plenum Press, New York, 1988.

[84] Peter Fransson and Guillaume Marrelec. The precuneus/posterior cingulate cortex plays a pivotal role in the default mode network: Evidence from a partial correlation network analysis. *NeuroImage*, 42(3):1178 – 1184, 2008.

[85] Walter J Freeman. Origin, structure, and role of background EEG activity. Part 1. Analytic amplitude. *Clin. Neurophysiol.*, 115(9):2077–88, 2004.

[86] Walter J. Freeman. Origin, structure, and role of background EEG activity. part 2. analytic phase. *Clin. Neurophysiol.*, 115(9):2089–2107, 2004.

[87] W.J. Freeman and L.J. Rogers. Fine temporal resolution of analytic phase reveals episodic synchronization by state transitions in gamma EEGs. *J Neurophysiol*, 87(2):937–45, 2002.

[88] Nir Friedman, Shinya Ito, Braden A. W. Brinkman, Masanori Shimono, R. E. Lee DeVille, Karin A. Dahmen, John M. Beggs, and Thomas C. Butler. Universal critical dynamics in high resolution neuronal avalanche data. *Phys. Rev. Lett.*, 108:208102, May 2012.

[89] Pascal Fries. A mechanism for cognitive dynamics: Neuronal communication through neuronal coherence. *Trends Cogn. Sci.*, 9:474–480, 2005.

[90] Pascal Fries. Neuronal gamma-band synchronization as a fundamental process in cortical computation. *Annu. Rev. Neurosci.*, 32(1):209–224, 2009.

[91] Pascal Fries, Pieter R. Roelfsema, Andreas K. Engel, Peter Knig, and Wolf Singer. Synchronization of oscillatory responses in visual cortex correlates with perception in interocularrivalry. *Proc. Natl. Acad. Sci. U S A.*, 94(23):12699–12704, 1997.

[92] K. J. Friston, L. Harrison, and W. Penny. Dynamic causal modelling. *NeuroImage*, 19(4):1273–1302, 2003.

[93] Eberhard Fuchs and Gabriele Flügge. Cellular consequences of stress and depression. *Dialogues Clin. Neurosci.*, 6(2), 2004.

[94] D. Gabor. Theory of communication. *J. IEE*, 93(26):429–457, 1946.

[95] G. Gallavotti. *Statistical Mechanics: A Short Treatise*. Texts and monographs in physics. Springer, 1999.

[96] J.B. Gao, J. Hu, W.W. Tung, Y.H. Cao, N. Sarshar, and V. P. Roychowdhury. Assessment of long range correlation in time series: How to avoid pitfalls. *Phys. Rev. E*, 73:016117, 2006.

[97] José M.V. García J.A. Mathematical properties of DNA sequences from coding and noncoding regions. *Revista Mexicana de Física*, 51:122–130, 2005.

[98] M. S. Gazzaniga, J. E. Bogen, and R. W. Sperry. Some functional effects of sectioning the cerebral commissures in man. *Proceedings of the National Academy of Sciences*, 48(10):1765–1769, 1962.

[99] Douglas Georgopoulos, Voula C.; Preis. A comparison of computational methods for instantaneous frequency and group delay of discrete-time signals. *J. Audio Eng. Soc*, 46(3):152–163, 1998.

[100] Aristides Gionis, Heikki Mannila, Taneli Mielikinen, and Panayiotis Tsaparas. Assessing data mining results via swap randomization. *ACM Trans. Knowl. Discov. Data*, 1(3), 2007.

[101] Gérard Girolami and David Vakman. Instantaneous frequency estimation and measurement: a quasi-local method. *Measurement Science and Technology*, 13(6):909, 2002.

[102] Pulin Gong, Andrey R. Nikolaev, and Cees van Leeuwen. Intermittent dynamics underlying the intrinsic fluctuations of the collective synchronization patterns in electrocortical activity. *Phys. Rev. E*, 76:011904, Jul 2007.

[103] Daniel A. Goodenough and David L. Paul. Gap junctions. *Cold Spring Harb. Perspect. Biol.*, 1:a002576, Jun 20097.

[104] J. Goswami. Algorithms for estimating instantaneous frequency. *Signal Processing*, 84(8):1423–1427, 2004.

[105] C. W. J. Granger and Roselyne Joyeux. An introduction to long-memory time series models and fractional differencing. *J. Time Ser. Anal.*, 1(1):15–29, 1980.

[106] Charles M. Gray and David A. McCormick. Chattering cells: Superficial pyramidal neurons contributing to the generation of synchronous oscillations in the visual cortex. *Science*, 274(5284):109–113, 1996.

[107] Dariusz Grech and Zygmunt Mazur. Scaling range of power laws that originate from fluctuation analysis. *Phys. Rev. E*, 87:052809, 2013.

[108] Roberta Grech, Tracey Cassar, Joseph Muscat, KennethP Camilleri, SimonG Fabri, Michalis Zervakis, Petros Xanthopoulos, Vangelis Sakkalis, and Bart Vanrumste. Review on solving the inverse problem in eeg source analysis. *J. NeuroEng. Rehabil.*, 5(1):1–33, 2008.

[109] Michael D. Greicius, Ben Krasnow, Allan L. Reiss, and Vinod Menon. Functional connectivity in the resting brain: A network analysis of the default mode hypothesis. *Proc. Natl. Acad. Sci. U S A.*, 100(1):253–258, 2003.

[110] Ariel Haimovici, Enzo Tagliazucchi, Pablo Balenzuela, and Dante R. Chialvo. Brain Organization into Resting State Networks Emerges at Criticality on a Model of the Human Connectome. *Physical Review Letters*, 110(17):178101+, April 2013.

[111] D. M. Halliday, B. A. Conway, S. F. Farmer, and J. R. Rosenberg. Using electroencephalography to study functional coupling between cortical activity and electromyograms during voluntary contractions in humans. *Neurosci. Lett.*, 241(1):5–8, 1998.

[112] David M Halliday and Simon F Farmer. On the need for rectification of surface emg. *J. Neurophysiol.*, 103(6):3547; author reply 3548–9, 2010.

[113] "D.M. Halliday, J.R. Rosenberg, A.M. Amjad, P. Breeze, B.A. Conway, and S.F. Farmer". A framework for the analysis of mixed time series/point process data - theory and application to the study of physiological tremor, single motor unit discharges and electromyograms. *Prog. Biophys. and Mol. Bio.*, 64(2–3):237 – 278, 1995.

[114] Cheol E. Han, Sang Wook Yoo, Sang Won Seo, Duk L. Na, and Joon-Kyung Seong. Cluster-based statistics for brain connectivity in correlation with behavioral measures. *PLoS ONE*, 8(8):e72332, 08 2013.

[115] Sami Hanhijärvi, Gemma C. Garriga, and Kai Puolamäki. Randomization techniques for graphs. In *SDM*, pages 780–791, 2009.

[116] P. Hansen, M. Kringelbach, and R. Salmelin. *MEG: An Introduction to Methods.* Oxford University Press, USA, 1 edition, 2010.

[117] Richard Hardstone, Simon-Shlomo Poil, Giuseppina Schiavone, Rick Jansen, Vadim V Nikulin, Huibert D. Mansvelder, and Klaus Linkenkaer-Hansen. Detrended fluctuation analysis: A scale-free view on neuronal oscillations. *Front. Physiol.*, 3:450, 2012.

[118] R. Hari. Magnetoencephalography in clinical neurophysiological assessment of human cortical functions. In *Electroencephalography: Basic Principles, Clinical Applications, and Related Fields*, chapter 57, pages 1165–1197. Lippincott Williams & Wilkins, Philadelphia, PA, 2004.

[119] Caroline Hartley, Timothy J Taylor, Istvan Z Kiss, Simon F Farmer, and Luc Berthouze. Identification of criticality in neuronal avalanches: II. a theoretical and empirical investigation of the driven case. *pre-print*, 2013. arXiv:1309.3535.

[120] J. M. Hausdorff, C. K. Peng, Z. Ladin, J. Y. Wei, and A. L. Goldberger. Is walking a random walk? Evidence for long-range correlations in stride interval of human gait. *J. Appl. Physiol.*, 78(1):349–358, 1995.

[121] Donald O. Hebb. *The Organization of Behavior: A Neuropsychological Theory*. Wiley, New York, new edition edition, 1949.

[122] Arjan Hillebrand and Gareth R. Barnes. Beamformer analysis of MEG data. In Hubert Preissl, editor, *Magnetoencephalography*, volume 68 of *International Review of Neurobiology*, pages 149 – 171. Academic Press, 2005.

[123] Arjan Hillebrand, Krish D. Singh, Ian E. Holliday, Paul L. Furlong, and Gareth R. Barnes. A new approach to neuroimaging with magnetoencephalography. *Hum. Brain. Mapp.*, 25(2):199–211, 2005.

[124] B. Hjorth. An on-line transformation of EEG scalp potentials into orthogonal source derivations. *Electroen. Clin. Neuro.*, 39(5):526–530, 1975.

[125] B. Hjorth. Source derivation simplifies topographical EEG interpretation. *Am J EEG Technol*, 20:121–132, 1980.

[126] C. J. Honey, O. Sporns, L. Cammoun, X. Gigandet, J. P. Thiran, R. Meuli, and P. Hagmann. Predicting human resting-state functional connectivity from structural connectivity. *Proc. Natl. Acad. Sci. U S A.*, 106(6):2035–2040, 2009.

[127] J. J. Hopfield. Neural networks and physical systems with emergent collective computational abilities. *Proc. Natl. Acad. Sci. U S A.*, 79(8):2554–2558, 1982.

[128] J. R. M. Hosking. Fractional differencing. *Biometrika*, 68(1):165–176, 1981.

[129] Kun Hu, Plamen Ch. Ivanov, Zhi Chen, Pedro Carpena, and H. Eugene Stanley. Effect of trends on detrended fluctuation analysis. *Phys. Rev. E*, 64:011114, 2001.

[130] Y. Hua and T.K. Sarkar. Generalized pencil-of-function method for extracting poles of an em system from its transient response. *IEEE T. Antenn Propag.*, 37(2):229–234, 1989.

[131] Kerson Huang. *Statistical Mechanics*. John Wiley & Sons, 2 edition, 1987.

[132] N. E. Huang, Z. Shen, S. R. Long, M. C. Wu, H. H. Shih, Q. Zheng, N. C. Yen, C. C. Tung, and H. H. Liu. The empirical mode decomposition and the Hilbert spectrum for nonlinear and non-stationary time series analysis. *P. Roy. Soc. Lond. A Mat.*, 454(1971):903–995, 1998.

[133] H. E. Hurst. Long term storage capacity in reservoirs. *T. Am. Soc. Civ. Eng.*, 116:770–799, 1951.

[134] Clifford M. Hurvich and Chih-Ling Tsai. Regression and time series model selection in small samples. *Biometrika*, 76(2):297–307, 1989.

[135] Kai Hwang, Michael N. Hallquist, and Beatriz Luna. The development of hub architecture in the human functional brain network. *Cerebral Cortex*, 2012.

[136] Risto J. Ilmoniemi and Dubravko Kičić. Methodology for combined tms and eeg. *Brain Topography*, 22(4):233–248, 2010.

[137] Ernst Ising. Beitrag zur Theorie des Ferromagnetismus. *Zeitschrift für Physik A Hadrons and Nuclei*, 31(1):253–258, 1925.

[138] Gilad A Jacobson, Kamran Diba, Anat Yaron-Jakoubovitch, Yasmin Oz, Christof Koch, Idan Segev, and Yosef Yarom. Subthreshold voltage noise of rat neocortical pyramidal neurones. *The Journal of Physiology*, 564(Pt 1):145–160, apr 2005. PMID: 15695244.

[139] M. Jalili, E. Barzegaran, and M.G. Knyazeva. Synchronization of eeg: Bivariate and multivariate measures. *Neural Systems and Rehabilitation Engineering, IEEE Transactions on*, 22(2):212–221, March 2014.

[140] Leon M. James, David M. Halliday, John A. Stephens, and Simon F. Farmer. On the development of human corticospinal oscillations: age-related changes in EEG-EMG coherence and cumulant. *Eur. J. Neurosci.*, 27(12):3369–3379, 2008.

[141] Carlos M. Jarque and Anil K. Bera. Efficient tests for normality, homoscedasticity and serial independence of regression residuals. *Economics Letters*, 6(3):255 – 259, 1980.

[142] H. H. Jasper. The ten-twenty electrode system of the international federation. *Electroen. Clin. Neuro.*, 10:371–375, 1958.

[143] Marsden J.F., Werhahn K.J., , Ashby P., Rothwell J., Noachtar S., and Brown P. Organization of cortical activities related to movement in humans. *J. Neurosci.*, 20(6), 2000.

[144] Jerald B Johnson and Kristian S Omland. Model selection in ecology and evolution. *Trends Ecol Evol*, 19(2):101–108, feb 2004.

[145] N.F. Johnson. *Two's company, three is complexity: a simple guide to the science of all sciences*. A Oneworld book. Oneworld, 2007.

[146] G. Jones and B. Boashash. Instantaneous frequency, instantaneous bandwidth and the analysis of multicomponent signals. In *Proc. IEEE Int. Conf. Acoust. Speech. Signal Process.*, pages 2467–2470 vol.5, Apr 1990.

[147] Veikko Jousmäki and Riitta Hari. Cardiac artifacts in magnetoencephalogram. *J. Clin. Neurophysiol.*, 13(2):172–176, 1996.

[148] Dzmitry A. Kaliukhovich and Rufin Vogels. Stimulus repetition affects both strength and synchrony of macaque inferior temporal cortical activity. *J. Neurophysiol.*, 107(12):3509–3527, 2012.

[149] Jan W. Kantelhardt, Stephan A. Zschiegner, Eva K. Bunde, Shlomo Havlin, Armin Bunde, and H. Eugene Stanley. Multifractal detrended fluctuation analysis of nonstationary time series. *Physica A*, 316(1-4):87–114, 2002.

[150] T. Karagiannis, M. Molle, and M. Faloutsos. Long-range dependence: ten years of Internet traffic modeling. *IEEE Internet Comput.*, 8(5):57–64, 2004.

[151] Karmeshu and A. Krishnamachari. Sequence variability and long-range dependence in DNA: An information theoretic perspective. *Lecture Notes in Computer Science*, 3316:1354–1361, 2004.

[152] Louis H. Kauffman. Eigenform. *Kybernetes*, 34(1):129 – 150, 2005.

[153] S. Kay. Statistically/computationally efficient frequency estimation. In *Int. Conf. Acoust. Spee.*, volume 4, pages 2292–2295, 1988.

[154] Christopher T. Kello, Gordon D. A. Brown, Ramon Ferrer-i Cancho, John G. Holden, Klaus Linkenkaer-Hansen, Theo Rhodes, and Guy C. Van Orden. Scaling laws in cognitive sciences. *Trends in Cognitive Sciences*, 14(5):223–232, 2010.

[155] Jerillyn S. Kent, S. Lee Hong, Amanda R. Bolbecker, Mallory J. Klaunig, Jennifer K. Forsyth, Brian F. O?Donnell, and William P. Hetrick. Motor deficits in schizophrenia quantified by nonlinear analysis of postural sway. *PLoS ONE*, 7(8):e41808, 2012.

[156] Andrea Király, Imre Bartos, and Imre Jánosi. Correlation properties of daily temperature anomalies over land. *Tellus A*, 58(5):593 – 600, 2006.

[157] Manfred G. Kitzbichler, Richard N. A. Henson, Marie L. Smith, Pradeep J. Nathan, and Edward T. Bullmore. Cognitive effort drives workspace configuration of human brain functional networks. *J. Neurosci.*, 31(22):8259–8270, 2011.

[158] Manfred G. Kitzbichler, Marie L. Smith, Søren R. Christensen, and Ed Bullmore. Broadband criticality of human brain network synchronization. *PLoS Comput. Biol.*, 5(3):e1000314, 2009.

[159] A. Klein, T. Sauer, A. Jedynak, and W. Skrandies. Conventional and Wavelet Coherence Applied to Sensory-evoked Electrical Brain Activity. *IEEE T. Bio-Med. Eng.*, 53(3), 2006.

[160] W Klimesch, H Russegger, M Doppelmayr, and Th Pachinger. A method for the calculation of induced band power: implications for the significance of brain oscillations. *Electroen. Clin. Neuro*, 108(2):123 – 130, 1998.

[161] Andrew L. Ko, Felix Darvas, Andrew Poliakov, Jeffrey Ojemann, and Larry B. Sorensen. Quasi-periodic fluctuations in default mode network electrophysiology. *J. Neurosci.*, 31(32):11728–11732, 2011.

[162] Sh. M. Kogan. *Electronic noise and fluctuations in solids.* Cambridge University Press, Cambridge, 1996.

[163] Piotr S. Kokoszka and Murad S. Taqqu. Fractional {ARIMA} with stable innovations. *Stochastic Processes and their Applications*, 60(1):19 – 47, 1995.

[164] S. Konishi and G. Kitagawa. *Information Criteria and Statisticial Modeling.* Springer, London, 2007.

[165] Mark A. Kramer, Adriano B.L. Tort, and Nancy J. Kopell. Sharp edge artifacts and spurious coupling in EEG frequency comodulation measures. *J. Neurosci. Meth.*, 170(2):352 – 357, 2008.

[166] Periklis Y. Ktonas and Nicola Papp. Instantaneous envelope and phase extraction from real signals: Theory, implementation, and an application to eeg analysis. *Signal Processing*, 2(4):373–385, 1980.

[167] Y. Kuramoto. Self-entrainment of a population of coupled nonlinear oscillators. In H. Araki, editor, *International Symposium on Mathematical Problems in Theoretical Physics, Lecture Notes in Physics, Vol. 39,*, pages 420–422, New York, NY, USA, 1975. Springer.

[168] Y. Kuramoto. *Chemical Oscillations, Waves, and Turbulence.* Springer–Verlag, New York, 1984.

[169] Y. Kuramoto. Cooperative dynamics of oscillator community —a study based on lattice of rings—. *Progress of Theoretical Physics Supplement*, 79:223–240, 1984.

[170] Kenneth K. Kwong. Record of a single fmri experiment in may of 1991. *NeuroImage*, 62(2):610 – 612, 2012. 20 {YEARS} {OF} fMRI 20 {YEARS} {OF} fMRI.

[171] J. P. Lachaux, E. Rodriguez, J. Martinerie, and F. J. Varela. Measuring phase synchrony in brain signals. *Hum. Brain. Mapp.*, 8(4):194–208, 1999.

[172] Jean-Philippe Lachaux, Antoine Lutz, David Rudrauf, Diego Cosmelli, Michel Le Van Quyen, Jacques Martinerie, and Francisco Varela. Estimating the time-course of coherence between single-trial brain signals: an introduction to wavelet coherence. *Clin. Neurophysiol.*, 32(3):157 – 174, 2002.

[173] Ivan M. Lang, Bidyut K. Medda, and Reza Shaker. Mechanisms of reflexes induced by esophageal distension. *American Journal of Physiology - Gastrointestinal and Liver Physiology*, 281(5):G1246–G1263, 2001.

[174] L. Leocani, C. Toro, P. Manganotti, P. Zhuang, and M. Hallett. Event-related coherence and event-related desynchronization/synchronization in the 10 Hz and 20 Hz EEG during self-paced movements. *Electroen. Clin. Neuro.*, 104(3):199–206, 1997.

[175] Anna Levina, J. Michael Herrmann, and Theo Geisel. Phase transitions towards criticality in a neural system with adaptive interactions. *Phys. Rev. Lett*, 102(11):118110:1–118110:4, 2009.

[176] Ying Li, A. Papandreou-Suppappola, and D. Morrell. Instantaneous frequency estimation using sequential bayesian techniques. In *Signals, Systems and Computers, 2006. ACSSC '06. Fortieth Asilomar Conference on*, pages 569 –573, 2006.

[177] K. Linkenkaer-Hansen, S. Monto, H. Rytsälä, K. Suominen, E. Isometsä, and S. Kähkönen. Breakdown of long-range temporal correlations in theta oscillations in patients with major depressive disorder. *J. Neurosci.*, 25(44):10131–10137, 2005.

[178] K Linkenkaer-Hansen, V V Nikouline, J M Palva, and R J Ilmoniemi. Long-range temporal correlations and scaling behavior in human brain oscillations. *J. Neurosci.*, 21(4):1370–1377, 2001.

[179] Klaus Linkenkaer-Hansen, Vadim V. Nikulin, J. Matias Palva, Kai Kaila, and Risto J. Ilmoniemi. Stimulus-induced change in long-range temporal correlations and scaling behaviour of sensorimotor oscillations. *Eur. J. Neurosci.*, 19(1):203–218, 2004.

[180] V. Litvak, J. Mattout, S.J. Kiebel, C. Phillips, R.N.A. Henson, J. Kilner, G. Barnes, R. Oostenveld, J. Daunizeau, G. Flandin, W.D. Penny, and K.J. Friston. EEG and MEG data analysis in SPM8. *Comput. Intell. Neurosci.*, 2011(852961), 2011.

[181] Wei Ji Ma, Jeffrey M Beck, Peter E Latham, and Alexandre Pouget. Bayesian inference with probabilistic population codes. *Nat Neurosci*, 9(11):1432–1438, November 2006.

[182] David J. C. Mackay. *Information Theory, Inference and Learning Algorithms.* Cambridge University Press, first edition, 2003.

[183] A.D.R. MacQuarrie and C. Tsai. *Regression and time series model selection.* World Scientific Publishing, 1998.

[184] B. Mandelbrot. *Fractals: Form, Chance and Dimension.* W. H. Freeman, San Francisco, 1977.

[185] Benoit B. Mandelbrot. *The fractal geometry of nature.* W. H. Freeman, 1982.

[186] Benoit B. Mandelbrot and James R. Wallis. Noah, joseph, and operational hydrology. *Water Resour. Res.*, 4(5):909–918, 1968.

[187] Benoit B. Mandelbrot and James R. Wallis. Some long-run properties of geophysical records. *Water Resour. Res.*, 5(2), 1969.

[188] D. Maraun, H. W. Rust, and J. Timmer. Tempting long-memory - on the interpretation of DFA results. *Nonlinear Proc. Geoph.*, 11(4):495–503, 2004.

[189] Kyle E. Mathewson, Gabriele Gratton, Monica Fabiani, Diane M. Beck, and Tony Ro. To see or not to see: Prestimulus phase predicts visual awareness. *J. Neurosci.*, 29(9):2725–2732, 2009.

[190] Ali Mazaheri and Ole Jensen. Rhythmic pulsing: linking ongoing brain activity with evoked responses. *Front. Hum. Neurosci.*, 4, 2010.

[191] J.A. McEwen and G.B. Anderson. Modeling the stationarity and gaussianity of spontaneous electroencephalographic activity. *IEEE Trans. Biomed. Eng.*, 22(5):361–9, 1975.

[192] Christian Meisel, Alexander Storch, Susanne Hallmeyer-Elgner, Ed Bullmore, and Thilo Gross. Failure of adaptive self-organized criticality during epileptic seizure attacks. *PLoS Comput. Biol.*, 8(1):e1002312, 2012.

[193] David C. Mertens. *Population-specific predictions for the finite Kuramoto model and collective synchronization in a system with resonant coupling.* PhD thesis, University of Illinois at Urbana-Champaign, 2011.

[194] G. Miritello, A. Pluchino, and A. Rapisarda. Phase transitions and chaos in long-range models of coupled oscillators. *Europhys. Lett.*, 85(1):10007, 2009.

[195] Roberto A. Monetti, Wolfram Bunk, Ferdinand Jamitzky, Christoph Raeth, and Gregor Morfill. Detecting non-linearities in data sets. characterization of fourier phase maps using the weighted scaling indices. *pre-print*, 2004. arXiv:physics/0405130.

[196] Teresa Montez, Simon-Shlomo Poil, Bethany F Jones, Ilonka Manshanden, Jeroen P A Verbunt, Bob W van Dijk, Arjen B Brussaard, Arjen van Ooyen, Cornelis J Stam, Philip Scheltens, and Klaus Linkenkaer-Hansen. Altered temporal correlations in parietal alpha and prefrontal theta oscillations in early-stage Alzheimer disease. *Proc Natl Acad Sci USA*, 106(5):1614–1619, 2009.

[197] Simo Monto, Sampsa Vanhatalo, Mark D Holmes, and J Matias Palva. Epileptogenic neocortical networks are revealed by abnormal temporal dynamics in seizure-free subdural EEG. *Cereb Cortex*, 17(6):1386–1393, June 2007.

[198] Elliott W Montroll and Michael F Shlesinger. On the wonderful world of random walks. *Stud. Stat. Mech.*, 11(1), 1984.

[199] V. V. Morariu, L. Buimaga-Iarinca, C. Vamos, and S. Soltuz. Detrended fluctuation analysis of autoregressive processes. *pre-print*, 2007. arXiv:0707.1437.

[200] Paolo Moretti and Miguel A. Muñoz. Griffiths phases and the stretching of criticality in brain networks. *Nature Communications*, 4, 2013.

[201] Florian Mormann, Klaus Lehnertz, Peter David, and Christian E. Elger. Mean phase coherence as a measure for phase synchronization and its application to the EEG of epilepsy patients. *Physica D*, 144(3-4):358 – 369, 2000.

[202] Radhakrishnan Nagarajan. Surrogate testing of linear feedback processes with non-gaussian innovations. *Physica A: Statistical Mechanics and its Applications*, 366:530–538, July 2006.

[203] Vadim V. Nikulin, Erik G. Jnsson, and Tom Brismar. Attenuation of long-range temporal correlations in the amplitude dynamics of alpha and beta neuronal oscillations in patients with schizophrenia. *NeuroImage*, 61(1):162–169, 2012.

[204] V.V. Nikulin and T. Brismar. Long-range temporal correlations in electroencephalographic oscillations: Relation to topography, frequency band, age and gender. *Neuroscience*, 130(2):549 – 558, 2005.

[205] P.L. Nunez and R. Srinivasan. *Electric Fields of the Brain: The Neurophysics of EEG*. Oxford University Press, 2006.

[206] S. Ohara, A. Ikeda, T. Kunieda, S. Yazawa, K. Baba, T. Nagamine, W. Taki, N. Hashimoto, T. Mihara, and H. Shibasaki. Movement-related change of electrocorticographic activity in human supplementary motor area proper. *Brain*, 123(6):1203–1215, 2000.

[207] L. Onsager. Crystal statistics. I. A two-dimensional model with an order-disorder transition. *Phys. Rev.*, 65(3-4):117–149, Feb 1944.

[208] Angela Onslow, Rafal Bogacz, and Matthew W. Jones. Quantifying phase-amplitude coupling in neuronal network oscillations. *Prog. Biophys. Mol. Bio.*, 105:49–57, 2011.

[209] I. Orovic, S. Stankovic, T. Thayaparan, and LJ. Stankovic. Multiwindow s-method for instantaneous frequency estimation and its application in radar signal analysis. *IET Signal Processing*, 4(4):363–370, 2010.

[210] Sanderson J. & Fryzlewicz P. Locally stationary wavelet coherence with application to neuroscience. In *Proceedings of the 56$^{th}$ session of the International Statistical Institute*, Lisbon, Portugal, 22-29 August 2007.

[211] B R Parnas. Noise and neuronal populations conspire to encode simple waveforms reliably. *IEEE Trans Biomed Eng*, 43(3):313–8, 1996.

[212] C-K Peng, S V Buldyrev, S Havlin, M Simons, H E Stanley, and A L Goldberger. Mosaic organization of DNA nucleotides. *Phys. Rev. E*, 49(2):1685–1689, 1994.

[213] C.-K. Peng, S. Havlin, J.M. Hausdorff, J.E. Mietus, H.E. Stanley, and A.L. Goldberger. Fractal mechanisms and heart rate dynamics: Long-range correlations and their breakdown with disease. *J. of Electrocardiol.*, 28, Supplement 1:59 – 65, 1995.

[214] C. K. Peng, Shlomo Havlin, H. Eugene Stanley, and Ary L. Goldberger. Quantification of scaling exponents and crossover phenomena in nonstationary heartbeat time series. *Chaos*, 5(1):82–87, 1995.

[215] Donald B. Percival and Andrew T. Walden. *Wavelet Methods for Time Series Analysis (Cambridge Series in Statistical and Probabilistic Mathematics)*. Cambridge University Press, 2000.

[216] Ernesto Pereda, Rodrigo Q. Quiroga, and Joydeep Bhattacharya. Nonlinear multivariate analysis of neurophysiological signals. *Prog. Neurobiol.*, 77(1-2):1–37, 2005.

[217] T. H. Petersen, M. Willerslev-Olsen, B. A. Conway, and J. B. Nielsen. The motor cortex drives the muscles during walking in human subjects. *The Journal of Physiology*, 590(10):2443–2452, 2012.

[218] G Pfurtscheller. Graphical display and statistical evaluation of event-related desynchronization. *Electroen. Clin. Neuro.*, 43:757 – 760, 1977.

[219] G. Pfurtscheller. Event-related synchronization (ERS): an electrophysiological correlate of cortical areas at rest. *Electroen. Clin. Neuro.*, 83(1):62 – 69, 1992.

[220] G Pfurtscheller and A Aranibar. Event-related cortical desynchronization detected by power measurements of scalp EEG. *Electroen. Clin. Neuro.*, 42(6):817–826, 1977.

[221] G. Pfurtscheller and A. Aranibar. Evaluation of event-related desynchronization (ERD) preceding and following voluntary self-paced movement. *Electroen. Clin. Neuro.*, 46(2):138–146, 1979.

[222] G. Pfurtscheller and A. Berghold. Patterns of cortical activation during planning of voluntary movement. *Electroen. Clin. Neuro.*, 72(3):250–258, 1989.

[223] G. Pfurtscheller and Lopes da Silva F.H. Event-related EEG/MEG synchronization and desynchronization: basic principles. *Clin. Neurophysiol.*, 110(11):1842–1857, 1999.

[224] G. Pfurtscheller and C. Neuper. Event-related synchronization of mu rhythm in the EEG over the cortical hand area in man. *Neurosci. Lett.*, 174:93–96, 1994.

[225] J. C. Phillips. Scaling and self-organized criticality in proteins: Lysozyme *c*. *Physical Review E*, 80:051916, 2009.

[226] Angkoon Phinyomark, Montri Phothisonothai, Chusak Limsakul, and Pornchai Phukpattaranont. Effect of trends on detrended fluctuation analysis for surface electromyography (emg) signal. In *PEC 8: 8th PSU-Engineering Conference*, pages 333–338, 2010.

[227] Belinda Phipson and Gordon K Smyth. Permutation p-values should never be zero: Calculating exact p-values when permutations are randomly drawn. *Stat. Appl. Genet. Molec.*, 9(1):1–16, 2010.

[228] A. Pikovsky, M. Rosenblum, and J. Kurths. *Synchronization: A Universal Concept in Nonlinear Science*. Cambridge Nonlinear Science Series. Cambridge University Press, 2003.

[229] Dietmar Plenz and Dante R. Chialvo. Scaling properties of neuronal avalanches are consistent with critical dynamics. *pre-print*, December 2009. arXiv:0912.5369.

[230] Simon-Shlomo Poil, Richard Hardstone, Huibert D. Mansvelder, and Klaus Linkenkaer-Hansen. Critical-State Dynamics of Avalanches and Oscillations Jointly Emerge from Balanced Excitation/Inhibition in Neuronal Networks. *J. Neurosci.*, 32(29):9817–9823, 2012.

[231] W. H. Press. Flicker Noises in Astronomy and Elsewhere. *Comments on Astrophysics*, 7(4):103–119, 1978.

[232] Roland Priemer. *Introductory Signal Processing*. World Scientific Publishing, River Edge, NJ, USA, 1990.

[233] V Priesemann, MHJ Munk, and M Wibral. Subsampling effects in neuronal avalanche distributions recorded in vivo. *BMC Neuroscience*, 2009:1 – 20, 2009.

[234] D. Purves, D. Fitzpatrick, L.C. Katz, A.S. Lamantia, J.O. McNamara, S.M. Williams, and G.J. Augustine. *Neuroscience*. Sinauer Associates, 2001.

[235] M. Le Van Quyen, J. Foucher, J. Lachaux, E. Rodriguez, A. Lutz, J. Martinerie, and F. J. Varela. Comparison of hilbert transform and wavelet methods for the analysis of neuronal synchrony. *J. Neurosci. Meth.*, 111(2):83–98, 2001.

[236] B.S. Raghavendra and D.N. Dutt. A study of long-range correlations in schizophrenia eeg using detrended fluctuation analysis. In *International Conference on Signal Processing and Communications (SPCOM)*, pages 1–5, 2010.

[237] Marcus E Raichle, Ann Mary MacLeod, Abraham Z Snyder, William J Powers, Debra A Gusnard, and Gordon L Shulman. A default mode of brain function. *Proceedings of the National Academy of Sciences*, 98(2):676–682, 2001.

[238] C. Rau, C. Plewnia, F. Hummel, and C. Gerloff. Event-related desynchronization and excitability of the ipsilateral motor cortex during simple self-paced finger movements. *Clin. Neurophysiol.*, 114(10):1819–1826, 2003.

[239] Gary M. Raymond and James B. Bassingthwaighte. Deriving dispersional and scaled windowed variance analyses using the correlation function of discrete fractional gaussian noise. *Physica A*, 265(1-2):85–96, 1999.

[240] Tiago L. Ribeiro, Mauro Copelli, Fbio Caixeta, Hindiael Belchior, Dante R. Chialvo, Miguel A. L. Nicolelis, and Sidarta Ribeiro. Spike avalanches exhibit universal dynamics across the sleep-wake cycle. *PLoS ONE*, 5(11):e14129, 11 2010.

[241] A. Riehle and E. Vaadia. *Motor Cortex in Voluntary Movements: A Distributed System for Distributed Functions.* Taylor & Francis, 2004.

[242] Fred Rieke, Davd Warland, Rob de Ruyter van Steveninck, and William Bialek. *Spikes: Exploring the Neural Code.* MIT Press, Cambridge, MA, USA, 1999.

[243] G. Rilling and P. Flandrin. One or Two Frequencies? The Empirical Mode Decomposition Answers. *Trans. Sig. Proc.*, 56(1):85–95, 2008.

[244] Peter M. Robinson, editor. *Time series with long memory.* Oxford University Press, 2003.

[245] R. Saab, M.J. McKeown, L.J. Myers, and R. Abu-Gharbieh. A wavelet based approach for the detection of coupling in eeg signals. In *Neural Engineering, 2005. Conference Proceedings. 2nd International IEEE EMBS Conference on*, pages 616–620, March 2005.

[246] O. Sacks. *The Man Who Mistook His Wife For A Hat: And Other Clinical Tales.* Simon & Schuster, 1998.

[247] V. Sakkalis. Review of advanced techniques for the estimation of brain connectivity measured with eeg/meg. *Comput. Biol. Med.*, 41(12):1110–1117, December 2011.

[248] "Stephan Salenius and Riitta Hari". Synchronous cortical oscillatory activity during motor action. *Current Opinion in Neurobiology*, 13(6):678 – 684, 2003.

[249] Gennady Samorodnitsky. Long range dependence. *Found Trends Stoch Syst*, 1(3):163–257, 2006.

[250] Jan-Mathijs Schoffelen, Robert Oostenveld, and Pascal Fries. Neuronal Coherence as a Mechanism of Effective Corticospinal Interaction. *Science*, 308(5718):111–113, 2005.

[251] Gideon Schwarz. Estimating the Dimension of a Model. *Ann Statist*, 6(2):461–464, 1978.

[252] I. W. Selesnick. The design of approximate Hilbert transform pairs of wavelet bases. *IEEE T. Signal Proces.*, 50(5):1144–1152, 2002.

[253] R. Shalbaf, P.T. Hosseini, and M. Analoui. Epilepsy detection using detrended fluctuation analysis. In *International Conference on Wavelet Analysis and Pattern Recognition*, pages 235–240, 2009.

[254] Woodrow L. Shew, Hongdian Yang, Thomas Petermann, Rajarshi Roy, and Dietmar Plenz. Neuronal avalanches imply maximum dynamic range in cortical networks at criticality. *J. Neurosci.*, 29(49):15595–15600, 2009.

[255] Oren Shriki, Jeff Alstott, Frederick Carver, Tom Holroyd, Richard N A Henson, Marie L Smith, Richard Coppola, Edward Bullmore, and Dietmar Plenz. Neuronal avalanches in the resting MEG of the human brain. *J. Neurosci.*, 33(16):7079–7090, 2013.

[256] W. Singer. Neuronal synchrony: a versatile code for the definition of relations? *Neuron*, 24(1):49–65, 1999.

[257] I. Soltesz and K. Staley. *Computational Neuroscience in Epilepsy*. Elsevier Science, 2011.

[258] Didier Sornette. *Critical Phenomena in Natural Sciences: Chaos, Fractals, Self-Organization and Disorder: Concepts and Tools*. Springer, 2nd edition, 2006.

[259] O. Sporns. *Networks of the Brain*. MIT Press, 2011.

[260] C.J. Stam and E.C.W. van Straaten. The organization of physiological brain networks. *Clin. Neurophysiol.*, 123(6):1067 – 1087, 2012.

[261] Cornelis J. Stam and Eveline A. de Bruin. Scale-free dynamics of global functional connectivity in the human brain. *Hum. Brain. Mapp.*, 22(2):97–109, 2004.

[262] Cornelis J. Stam, Guido Nolte, and Andreas Daffertshofer. Phase lag index: Assessment of functional connectivity from multi channel EEG and MEG with diminished bias from common sources. *Hum. Brain. Mapp.*, 28(11):1178–1193, 2007.

[263] H.E. Stanley, S.V. Buldyrev, A.L. Goldberger, Z.D. Goldberger, S. Havlin, Rosario Nunzio Mantegna, S.M. Ossadnik, C.-K. Peng, and M. Simons. Statistical mechanics in biology: how ubiquitous are long-range correlations? *Physica A*, 205(1):214–253, 1994.

[264] Stilian Stoev and Murad S. Taqqu. Simulation methods for linear fractional stable motion and FARIMA using the fast Fourier transform. *Fractals*, 12:95–121, 2004.

[265] S. H. Strogatz. From Kuramoto to Crawford: exploring the onset of synchronization in populations of coupled oscillators. *Physica D*, 143(1-4):1–20, 2000.

[266] Steven H. Strogatz and Renato E. Mirollo. Stability of incoherence in a population of coupled oscillators. *J. Stat. Phys.*, 63(3):613–635, 1991.

[267] Enzo Tagliazucchi, Pablo Balenzuela, Daniel Fraiman, and Dante R Chialvo. Criticality in large-scale brain fmri dynamics unveiled by a novel point process analysis. *Frontiers in Physiology*, 3(15), 2012.

[268] Murad S. Taqqu, Vadim Teverovsky, and Walter Willinger. Estimators for long-range dependence: An empirical study. *Fractals*, 3:785–798, 1995.

[269] MikaP. Tarvainen, J.-P. Niskanen, J.A. Lipponen, P.O. Ranta-aho, and P.A. Karjalainen. Kubios HRV – A software for advanced heart rate variability analysis. In Jos Sloten, Pascal Verdonck, Marc Nyssen, and Jens Haueisen, editors, *4th European Conference of the International Federation for Medical and Biological Engineering*, volume 22 of *IFMBE Proc*, pages 1022–1025. Springer Berlin Heidelberg, 2009.

[270] P. Tass, M. G. Rosenblum, J. Weule, J. Kurths, A. Pikovsky, J. Volkmann, A. Schnitzler, and H. J. Freund. Detection of n:m phase locking from noisy data: Application to magnetoencephalography. *Phys. Rev. Lett.*, 81:3291, 1998.

[271] Timothy J. Taylor, Caroline Hartley, Peter L. Simon, Istvan Z Kiss, and Luc Berthouze. Identification of criticality in neuronal avalanches: I. a theoretical investigation of the non-driven case. *J. Math. Neurosci.*, 3(5):1–26, 2013.

[272] James Theiler, Stephen Eubank, André Longtin, Bryan Galdrikian, and J. Doyne Farmer. Testing for nonlinearity in time series: the method of surrogate data. *Physica D*, 58(1-4):77–94, September 1992.

[273] Emmanuelle Tognoli and J. A. S. Kelso. Enlarging the scope: grasping brain complexity. *pre-print*, oct 2013. arXiv:1310.7277.

[274] Jonathan Touboul and Alain Destexhe. Can power-law scaling and neuronal avalanches arise from stochastic dynamics? *PLoS ONE*, 5(2):e8982, 2010.

[275] P. Turchin. *Complex Population Dynamics: A Theoretical / Empirical Synthesis*. Princeton University Press, 2003.

[276] R.E. Turner and M. Sahani. Demodulation as probabilistic inference. *IEEE Audio, Speech, Language Process*, 19(8):2398 –2411, 2011.

[277] Richard E. Turner and Maneesh Sahani. Probabilistic amplitude and frequency demodulation. In J. Shawe-Taylor, R.S. Zemel, P. Bartlett, F.C.N. Pereira, and K.Q. Weinberger, editors, *Advances in Neural Information Processing Systems 24*, pages 981–989. Curran Associates, Inc., 2011.

[278] A B Vallbo and J Wessberg. Organization of motor output in slow finger movements in man. *The Journal of Physiology*, 469(1):673–691, 1993.

[279] Hanneke van Dijk, Jan-Mathijs Schoffelen, Robert Oostenveld, and Ole Jensen. Prestimulus oscillatory activity in the alpha band predicts visual discrimination ability. *J. Neurosci.*, 28(8):1816–1823, 2008.

[280] W. van Drongelen. *Signal Processing for Neuroscientists: An Introduction to the Analysis of Physiological Signals*. Elsevier Science, 2006.

[281] J. L. van Hemmen and W. F. Wreszinski. Lyapunov function for the kuramoto model of nonlinearly coupled oscillators. *J. Stat. Phys.*, 72:145–166, 1993.

[282] B.D. van Veen, W. van Drongelen, M Yuchtman, and A. Suzuki. Localization of brain electrical activity via linearly constrained minimum variance spatial filtering. *IEEE Trans. Biomed. Eng.*, 44:867–880, 1997.

[283] C. Varotsos and D. Kirk-Davidoff. Long-memory processes in ozone and temperature variations at the region $60°S - 60°N$. *Atmos Chem Phys*, 6(12):4093–4100, 2006.

[284] Dimitri Van De Ville, Juliane Britz, and Christoph M. Michel. EEG microstate sequences in healthy humans at rest reveal scale-free dynamics. *Proc. Natl. Acad. Sci. U S A.*, 107(42):18179–18184, 2010.

[285] J. Ville. Theorie et Applications de la Notion de Signal Analytique. *Cables et Transmission*, 1:61–74, 1948.

[286] E. J. Wagenmakers, S. Farrell, and R. Ratcliff. Estimation and interpretation of 1/alpha noise in human cognition. *Psychonomic Bulletin and Review*, 11(4):579–615, 2004.

[287] Gilles Wainrib, Michle Thieullen, and Khashayar Pakdaman. Reduction of stochastic conductance-based neuron models with time-scales separation. *Journal of Computational Neuroscience*, 32(2):327–346, 2012.

[288] A. Wald and J. Wolfowitz. On a test whether two samples are from the same population. *The Annals of Mathematical Statistics*, 11(2):147–162, 1940.

[289] Chien-Chih Wang and Wen-Hung Yang. Using detrended fluctuation analysis (DFA) to analyze whether vibratory insoles enhance balance stability for elderly fallers. *Arch. of Gerontol. and Geriat.*, 55(3):673 – 676, 2012.

[290] Fengzhong Wang, Kazuko Yamasaki, Shlomo Havlin, and H. Eugene Stanley. Scaling and memory of intraday volatility return intervals in stock market. *pre-print*, 2005. arXiv:physics/0511101.

[291] Xiao-Jing J. Wang. Neurophysiological and computational principles of cortical rhythms in cognition. *Physiological reviews*, 90(3):1195–1268, 2010.

[292] Nicholas J. Ward, Simon F. Farmer, Luc Berthouze, and David M. Halliday. Rectification of emg in low force contractions improves detection of motor unit coherence in the beta-frequency band. *J. Neurophysiol.*, 110(8):1744–1750, 2013.

[293] Professor Charles L. Weber. Waveform representations and narrowband signals. In *Principles of Radar Systems Design*, Lecture Notes, chapter 4, pages 59–76. University of South Carolina, 1984.

[294] Marijke Welvaert and Yves Rosseel. On the definition of signal-to-noise ratio and contrast-to-noise ratio for fmri data. *PLoS ONE*, 8(11):e77089, 11 2013.

[295] Gerhard Werner. Fractals in the nervous system: conceptual implications for theoretical neuroscience. *pre-print*, 2009. arxiv:0910.2741.

[296] Gerhard Werner. Fractals in the nervous system: conceptual implications for theoretical neuroscience. *Front. Physiol.*, 1:1–15, 2010.

[297] Gerhard Werner. Letting the brain speak for itself. *Front. in Physiol.*, 2:1–15, 2011.

[298] Brandon J. Whitcher and Peter F. Craigmile. Multivariate spectral analysis using hilbert wavelet pairs. *International Journal of Wavelets, Multiresolution and Information Processing (IJWMIP)*, 2(4):567–587, 2004.

[299] Brandon J. Whitcher, Peter F. Craigmile, and Peter Brown. Time-varying spectral analysis in neurophysiological time series using hilbert wavelet pairs. *Signal Processing*, 85(11):2065–2081, 2005.

[300] Andreas Widmann and Erich Schröger. Filter effects and filter artifacts in the analysis of electrophysiological data. *Front. Psychol.*, 3(233), 2012.

[301] E. R. Williams and S. N. Baker. Circuits generating corticomuscular coherence investigated using a biophysically based computational model. i. descending systems. *J. Neurophysiol.*, 101:31–41, 2009.

[302] Claire L. Witham, C. Nicholas Riddle, Mark R. Baker, and Stuart N. Baker. Contributions of descending and ascending pathways to corticomuscular coherence in humans. *J. of Physiol.*, 589(15):3789–3800, 2011.

[303] Zhaohua Wu and Norden E. Huang. A study of the characteristics of white noise using the empirical mode decomposition method. *P. Roy. Soc. Lond. A Mat.*, 460(2046):1597–1611, June 2004.

[304] Okada Y. *Biomagnetism: an Interdisciplinary Approach*, chapter Neurogenesis of evoked magnetic fields, pages 399–408–121. Plenum Press, New York, 1983.

[305] Yuhong Yang. Can the strengths of AIC and BIC be shared? A conflict between model identification and regression estimation. *Biometrika*, 92(4):937–950, 2005.

[306] Nick Yeung, Rafal Bogacz, Clay B. Holroyd, Sander Nieuwenhuis, and Jonathan D. Cohen. Theta phase resetting and the error-related negativity. *Psychophysiology*, 44(1):39–49, 2007.

[307] Randy K. Young. *Wavelet theory and its applications*. Kluwer international series in engineering and computer science. Kluwer Academic Publishers, Boston, 1993.

[308] A. Zeman. *A Portrait of the Brain*. Byword Books Private Limited, 2011.

[309] Adam Zeman. Consciousness. *Brain*, 124(7):1263–1289, 2001.

# Glossary

**$\frac{1}{f}$ noise** A time series in which the power spectrum has a slope of $-1$. $1/f$ noise is also sometimes called pink noise. The Hurst exponent of $1/f$ noise is 1.

**AIC** Akaike's information criterion may be used to compare the evidence for one model against another. It is based on a maximum likelihood measure and penalises the number of parameters in the model.

**amplitude envelope** The amplitude envelope $A$ of a bandpassed signal is a convex hull formed by the peaks in amplitude in a time-varying signal.

**angular frequency** The angular frequency $\omega$ is the angular speed of evolution of an oscillatory signal. It is defined by $\omega = 2\pi f$ where $f$ is the frequency.

**autocorrelation function** The autocorrelation function quantifies the correlation between the amplitude of a signal separated by different time lags.

**bandpass filter** A bandpass filter can be used to isolate a specific frequency band in a time series.

**BIC** Bayesian information criterion may be used to compare the evidence for one model against another. It is based on a maximum likelihood measure and penalises the number of parameters in the model. The BIC is stricter than the AIC on penalising the number of parameters.

**Brownian noise** The cumulative sum of a white noise time series. Brownian noise has a slope of $-2$ in its power spectrum and a Hurst exponent of 1.5.

**CNS** The central nervous system includes the brain, the spinal chord and the retina.

**coherence** The coherence provides a single time-averaged scalar value of oscillatory synchronisation, used to correlate components in the frequency domain.

**cross-correlation function** The cross-correlation function quantifies the correlation between the amplitudes of two signals, which are separated by different time lags .

**DFA** Detrended fluctuation analysis (DFA) is a technique used to estimate the Hurst exponent. The exponent obtained by DFA is denoted by $\gamma$.

**EEG** Electroencephalography (EEG) is the non-invasive recording of electrical activity produced by the neuronal activity of the brain. The recording produced in called an electroencephalogram and is sometimes also abbreviated by the acronym EEG.

**EMG** Electromyography (EMG) is a technique for recording the electrical activity produced by muscles whose activity depends on motorneuronal discharge. The recording produced in called an electromyogram and is sometimes also abbreviated by the acronym EMG.

**EPSP** An excitatory post-synaptic potential (EPSP) is a temporary depolarisation of post-synaptic membrane potential caused by the flow of positively charged ions into the post-synaptic cell due to ion channel opening.

**ERD** Event-related desynchronisation (ERD) is the de-synchronisation (loss of power in a given frequency band) in motor control amplitude change in the $\mu$ and $\beta$ bands as a result of the onset of movement [218].

**ERS** Event-related synchronisation (ERS) is the synchronisation (increase of power in a given frequency band) in motor control amplitude change in the $\mu$ and $\beta$ bands as a result of the onset of movement [223].

**FARIMA** A Fractionally Integrated Moving Average (FARIMA) model can be used to generate time series with a pre-determine Hurst exponent and varying levels of shirt and long range temporal correlations.

**fMRI** functional magnetic resonance imaging is a neuroimaging technique that tracks the BOLD signal of a time series).

**frequency** The frequency $f$ is the number of cycles completed by an oscillatory signal in a time period. If the time period is 1 second, then the unit of frequency is Hertz (Hz). Frequency can also be time-varying $f(t)$ in signals that do not always evolve at the same speed.

**Gaussian white noise** A time series in which has equal power at all frequencies, represented by a flat power spectrum. Each value in this time series is drawn at random from a Gaussian distribution. Gaussian white noise has a Hurst exponent of 0.5.

**GLS** Global lability of synchronisation is the change in the number of time series in a system for which a coherence measure generated using Hilbert wavelet transforms is in the interval $[-\pi, \pi]$. The probability distribution of GLS was shown in be a power law in Ising, Kuramoto, MEG and fMRI data in [158].

**Hurst exponent** The Hurst exponent is a measure of self-similarity in a time series. Denoted by $H$.

**IPSP** An inhibitory post-synaptic potential (IPSP) is a kind of synaptic potential that makes a post-synaptic neuron less likely to generate an action potential. The opposite of an inhibitory post-synaptic potential is an excitatory post-synaptic potential EPSP, which is a synaptic potential that makes a post-synaptic neuron more likely to generate an action potential.

**LRD** Long-range dependence (LRD) is defined by a decay in the autocorrelation function of a time series that is slower than an exponential decay.

**LRTCs** Long-range temporal correlations (LRTCs) are defined by a power law decay in the autocorrelation function of a time series.

**MEG** Magnetoencephalography (MEG) is a non-invasive neuro-imaging technique that records the magnetic fields produced by the electric currents produced by neuronal activity in the brain. The recording produced in called an magnetoencephalogram and is sometimes also abbreviated by the acronym MEG.

**ML-DFA** A technique that we have developed that can be used to validate the exponent obtained by DFA.

**OST** Optimal spectral tracking (OST) is a series of techniques introduced by [37] for determining the time-varying characteristics such as phase information for a time series and calculating the coherence between two time series.

**phase** The phase $\phi$ is the position of an oscillatory signal in its cycle. Phase is typically defined to evolve in the range $[-\pi, \pi]$.

**phase synchrony analysis method** A method that I have developed to assess the presence of LRTCs in the rate of change of phase difference between two time series.

**pink noise** A time series in which the power spectrum has a slope of $-1$. Pink noise is also sometimes called $1/f$ noise. The Hurst exponent of pink noise is 1.

**PLI** A phase-locked interval was defined by [158] as a time period for which the difference in a coherence measure generated using Hilbert wavelet transforms is in the interval $[-\pi/4, \pi/4]$. The probability distribution of PLIs was shown in be a power law in Ising, Kuramoto models and MEG and fMRI data in [158].

**PNS** The peripheral nervous system includes all regions of the nervous system that are not the brain, the spinal chord or the retina. It contains the neurons that connect the CNS to muscles and organs..

**power law** A function where the dependent variable is the independent variable taken to a power $y = Cx^{-\alpha}$.

**power spectrum** The power spectrum quantifies the power/amplitude of a signal as a function of frequency.

**RMSE** Root mean square error is the square root of the average of the squared error obtained when .

**self-similarity** A property of objects under which their constituent parts are smaller replicas of the larger whole on all scales.

**signal** A time-series. The terms time series and signal are often used interchangeably in this thesis.

**SOC** Self-organised criticality (SOC) was a concept introduced by Bak [14] to explain the complexity that we observe in the world around us. It is described by a dynamical system with a critical point as the attractor, which bypasses the need to have an external force to organise the behaviour of the system, or the need to tune any parameters to the correct values.

**synchronisation** Synchronisation is sometimes referred to as the collective activity of neurons belonging to a neuronal pool to produce increased amplitude (such as in ERS and ERD), but it is also a term that refers to the synchronisation between two time series such as neurophysiological signals. In this thesis, synchronisation is used more commonly to refer to the latter phenomenons, and when it is not, this is stated explicitly.

**time series** A time-series is a set of values, which are associated with a point in time. The terms time series and signal are often used interchangeably in this thesis.

**white noise** A time series in which has equal power at all frequencies, represented by a flat power spectrum. White noise has a Hurst exponent of 0.5.